AMPEROMETRIC STUDY OF MICROSCOPIC BAND AND CYLINDER ARRAY ELECTRODES

Brian Jeffrey Seddon, December 1989.

A thesis submitted for the degree of Doctor of Philosophy

at the University of Edinburgh.

Abstract

AMPEROMETRIC STUDY OF MICROSCOPIC BAND AND CYLINDER ARRAY ELECTRODES

The amperometric characteristics of a large scale interdigitated microband device was studied. Of particular interest to analytical application is the differential (anode-cathode) mode of operation. The device operated in this way delivered a steady state current of approximately 11nA μM^{-1}, corresponding to 0.5nA μM^{-1} for a $1mm^2$ device. The time taken for the current to reach a steady state value, response time, was of the order of 2s for the present device operated with a system containing equiconcentration of a redox couple (O/R system). The interdigitated device was utilised in the voltammetric analysis of ferricyanide in aqueous potassium chloride solution. The current versus concentration plots were linear over a wide concentration range, 1μM to 1mM, with detection limit in the nanomolar range.

The current-time transients leading to steady state were modelled by computer simulation using symplifying grid boundary conditions. Reasonable correlation was found between simulated chronoamperometric data and experiment.

An approximate expression is presented for the steady state current at interdigitated microband array electrodes. This equation was found to be a satisfactory estimation of the current for values of the bandwidth to band gap ratio greater than ca. 5, and is therefore readily applicable to many practical devices.

The fabrication and characterisation of platinum and carbon fibre dual microcylinder electrodes was considered. These devices were found to behave in analogous way to the interdigitated microband device, i.e. shielding and feedback current phenomena are observed. An equation was derived for the steady state current at microcylinder anode-cathodes. This expression was verified by chronoamperometry for devices of different electrode radius and separation.

A brief review of the application of interdigitated microband array electrodes and microcylinder anode-cathode devices to electroanalysis is presented with emphasis to immunoassay.

Acknowledgement

I would like to acknowledge Dr. M. J. Eddowes and Dr. H. H. J. Girault for their contribution to this work. I am grateful to those concerned at Thorn EMI Central Research Laboratories for the microfabrication of interdigitated electrodes. To the members of the Edinburgh electrochemistry group, 1986–1989, I express kind regards.

This post-graduate studentship was funded by the SERC and Thorn EMI Central Research Laboratories under a CASE award scheme.

Declaration

I declare that the work presented in this thesis is my own unless otherwise stated by reference.

Symbols and units.

The following list of symbols and units have been used throughout,

w_e band electrode width, bandwidth, m.

w_g electrode spacing, band or cylinder gap, m.

l electrode length, m.

r^o radius of cylinder electrode, m.

C^b bulk solution concentration, mol m^{-3} (mM).

δ diffusion field thickness, µm.

D diffusion coefficient, $m^2\ s^{-1}$.

A electrode area, m^2.

i diffusion current, A.

i/CA Current density per unit concentration, A m^{-2} mM^{-1}.

i/C current per unit concentration, sensitivity, A mM^{-1}.

Other symbols which have been adopted are specifically refered to in the text.

A unit of particular interest to microdetector design was used throughout this work for ease of conversion in terms of electrode area and analyte concentration. The current density refered to in the text is the current per unit area per unit concentration and is symbolised i/CA. The unit has been written in a discrete manner to aid reference and will be given as A m^{-2} mM^{-1}. This unit of current per unit area per unit concentration may be reduced by those who wish to A m mol^{-1}.

Contents

CHAPTER 1

INTRODUCTION

1.1 MICROSENSORS.

Microelectrodes arranged as discrete units within a larger network address a fundamental problem of sensitivity in amperometric trace analysis. Extension of this basic concept to microdetector/sensor design introduces new constraints concerning spacial configuration. Questions now raised include: which are the most useful microelectrode geometries and how are they to be arranged in order to optimise the important analytical parameters? Both of these geometric considerations will depend upon the function of the device and are currently restricted by contemporary microfabrication technology. There are now two planar formats recognised for regular microelectrode ensembles. They are fundamentally different because they rely on different operating principles. In one form, the microelectrodes are operated at a common electric potential, and must be distributed such that the electrochemical processes occurring at individual electrodes remain independent. The diffusion current response is then an amplification of one microelectrode. For this design one can appreciate that electrode sites must be sufficiently distanced in order that diffusional transport remains mutually independent. In a second electrode distribution, (and more recent in terms of the planar geometry) microelectrodes are operated at different electric potentials such that microanode and microcathode surfaces are placed in intimate association in terms of perimeter to electrode area. This format relies on the presence of a reversible redox species for operation. The most important microelectrode arrangement of the latter is the interdigitated microband device.

1.2 INTERDIGITATED MICROBAND ELECTRODES.

The extensive research into a reliable amperometric oxygen probe to overcome undesireable convective and media influence lead to the development of the microband electrode in a laminate format. Saito, in a series of articles dated from the 1960s, [1-3] detailed the analytical application

of Pt band electrodes of bandwidth 0.01μm to 0.05μm, for oxygen measurement. He described the relevant fabrication problems for electrodes based on platinum thin films and showed that sensitivity enhancement and convectional stability could be gained in chronoamperometric experiments with electrodes of submicrometer dimension. Saito went on to describe the first theoretical model for the steady state amperometric response of a microband electrode based on a convective-diffusion mass transport model.

The amperometric characteristics of laminate band electrodes were reconsidered by Wightman et al. in 1985 [4] for both micrometer and submicrometer scale bandwidth. Their work demonstrated the correspondence between cylindrical and band geometies in terms of chronoamperometic behaviour and reaffirmed earlier inferences pertaining to convection influence on electrode performance in flow situations. Furthermore, these workers defined the general application of analytical linear sweep voltammetry with submicron band electrodes for the detection of $Ru(NH_3)_6^{3+}$ at nanomolar concentration.

Aoki et al. [5-7] have developed the theory for the chronoamperometric and cyclic voltammetry response of single microband electrodes and have formulated empirical equations suitable for general experimentation.

Much attention has been paid recently to the amperometric properties of single microband electrodes, in particular the current amplification as a consequence of one macroscopic dimension. Further moves to increase the amperometric signal, whilst preserving the transient characteristics of the microelectrode current, have culminated in theoretical and experimental studies on regular ensembles of microelectrodes.

The amperometric interdigitated microband array electrodes of concern in the present study is a device composed of two coplanar electrodes. Each electrode consists of a number of microscopic elements of strip or band geometry arranged such that each band of one electrode is flanked by two bands of the second electrode. More is said about the geometrical characteristics of the interdigitated device in chapter 3. Electrodes may be controlled at common or differential electric potentials relative to a reference electrode. This independent voltage control of two microscopically displaced surfaces gives rise to some of the most interesting amperometric effects in

microelectrode research.

Interdigitated devices can be classified in terms of geometrical dimensions; band length l, bandwidth w_e, and band gap w_g. Geometric parameters such as bandwidth and band gap are specific to the form of the current-time characteristic, and are referred to here as specific dimensions. Micrometer scale devices may be arbitrarily subdivided according to the specific dimensions into small scale, where bandwidth and band gap are less than 10μm and large scale devices with specific dimensions greater than 10μm. Alternatively where overall device size is paramount the interdigitated device may be defined in terms of the number of bands per electrode (hence triple band array etc), or band length. In this work it is proposed that the term interdigitated microband array electrodes be reserved only for the case of anode-cathode operation. The alternate potentiostatic mode will be considered as a microband array electrode; this will be elaborated further in chapter 4.

The origins of the amperometric interdigitated microband array electrodes are firmly entrenched in planar microfabrication technology where precision control over microscopic structure, necessary to device specification, can be made. The device, described in its present form, has come to diffusion controlled chronoamperometric studies from various investigations carried out in the late 1970s which made use of the fabrication developments in the microelectronics industry. These studies include; amperometric detection systems in liquid chromatography and isotachophoresis [8], microdielectrometers and surface acoustic wave devices [9]. One of the first applications of the device involved conductivity measurement, and has since been used in the development of chemiresistor devices [10]. The interdigitated structure was favoured in these studies on account of the large perimter to band gap ratio, which allowed the measurement of a current signal of convenient size using a low applied voltage. This effectively demonstrated that device geometry had important consequences to analytical sensitivity.

Mansfield [11] has recently (1988) applied the characteristics of the interdigitated device as a probe for the monitoring of corrosion effects of acid rain etc. by measuring a polarisation resistance and equating this to corrosion rate. The devices discussed were made from nickel or zinc with a bandwidth of 600μm and a band gap of 200μm. The superior performance of small scale

devices to be discussed in this work with reference to amperometric response will no doubt find application in this particular area.

Interdigitated microband array electrodes have evolved in the field of liquid chromatography as an amperometric detection system. This development was in a response to the need for extension of amperometric detection to selective multi-analyte sensing and to improve other analytical parameters such as sensitivity and detection limit. The interdigitated device in anode-cathode operation was developed by Anderson et al. [12-14] for use in flow systems. The device operated by arranging bands normal to the flow with an upstream generator band (say anode) affording the oxidised form of a reversible redox couple which was transported downstream to a collector (detector) electrode. This principle of operation was not new, it had been the basis of several earlier detectors using macroscopic electrodes. Moreover, the flow stream anode-cathode had been developed from the stationary solution experiments of reversible redox species in thin layer cells by Reilley et al. in 1960s [15].

Some of the first experiments concerned with the amperometric behaviour of interdigitated devices for reversible redox species in quiescent solution were carried out in studies primarily concerned with the performance of molecular based electronic devices. The interdigitated structure in such experiments functioned only as support electrodes.

Wrighton et al. [16] demonstrated the effects of bipotentiostatic control (analogous to ring-disc electrodes experiments) in cyclic voltammetry experiments of the $Ru(NH_3)_6^{3+/2+}$ couple using a dual band device with bandwidth 1-2μm and band gap 0.3μm. The device characteristics showed the typical effects of recycling or "feedback" diffusion known to thin layer anode-cathode studies. Diffusional transport collection efficiency determined in these studies was of the order of 80%. The device operated by reduction of $Ru(NH_3)_6^{3+}$ to $Ru(NH_3)_6^{2+}$ at a Pt cathode by sweeping the voltage from 0.0V to -0.6V versus asaturated calomel electrode (SCE), while the anode was held at 0.0V relative to SCE and functioned to reconvert $Ru(NH_3)_6^{2+}$ back to $Ru(NH_3)^{3+}{}_6$. The operational mechanism of this device relied on diffusional mass transport and could only have been observed for the planar geometry when electrode dimensions and separation were miniaturised to a size comparible to that of the diffusion field.

The first reported study on the amperometic properies of an interdigitated microband array device for reversible redox species under quiescent conditions was presented by Anderson and Sanderson in 1985 [17]. Their device consisted of 25 anode and cathode bands with 50μm bandwidth, 5mm band length and 50μm band gap. The device was arranged within a 70μm optically transparent thin layer cell for spectroelectrochemical studies. These workers verified steady state voltammetry and chronoamperometry and outlined an empirical expression for the limiting current in terms of specific dimensions of the device. The authors drew attention to the important dimensional features, viz bandwidth and gap, affecting device response including the magnitude of steady state current and response time. Furthermore these authors described a mechanism of operation involving the limitation of a diffusion field by the recycling nature of close spaced collector electrodes.

Experimental and numerical characterisation of amperometric interdigitated electrodes has followed for microscopic devices (50μm band length, 2.3μm bandwidth) in dual and triple band formats, for both shielding and feedback experiments [18]. The study highlighted the effects of band gap on the diffusion current and collection efficiency. In the case of feedback current experiments the enhancement of current density for small scale devices over that of the larger scale is most noticeable. The device operated as a band array electrode demonstrated the basic effect of close spaced electrodes, i.e. the observed limiting current was not the sum of individual electrodes.

Laminate techniques reappeared for the construction of dual microband electrodes which are individually addressable [19] and therefore can be operated in common or differential potential modes. The work of Bartelt et al. [20] illustrated the salient voltammetric characteristics of a dual microband electrode in three different operation modes, namely, single band anode, dual band anode and as anode–cathode. The device used was a laminate type with specific dimensions, w_g=4μm, w_e=4.6μm and band length 5mm. In these experiments, using ferrocene, the peak current for the dual anode mode was only ca. 35% of the single band mode, while for the anode–cathode operation a steady state current response was observed. A triple band laminate device further showed the operating effects of feedback diffusion for a $CoCp_2^+$ species in dilute solutions of support electrolyte. Using the central band as generator (cathode) for $CoCp_2^+ \rightarrow CoCp_2$, and two collector band anodes

$CoCp_2 \rightarrow CoCp_2^+$, the steady state current was 1.3μA mM^{-1}, an enhancement of 82% over that of single band operation for 20mM support electrolyte. In the case of 0.02mM support electrolyte, the current enhancement was even greater, with the generation of a steady state current of 2.5μA mM^{-1}. These experiments illustrate the effects of electric conduction on the mass transport process at interdigitated microband electrodes and are as yet to be theoretically treated.

Over very recent times (1988-89) there has been major emphasis on a mathematical description of the chronoamperometric properties of the interdigitated device with reference to the important geometrical parameters. Aoki et al. [21,22] have made a significant contribution to the theoretical and experimental development of the new amperometric device. They have fabricated and characterised a series of small scale devices clarifying the importance of bandwidth and gap features to the transient and steady state feedback current. Additionally, they have expounded a rigorous theoretical treatment of the steady state flux problem associated with the interdigitated device, and arrived at an empirical formula with general application. These studies will be discussed in chapters 2 and 6, in the light of the present work detailing the operation of interdigitated microband electrodes.

The current work described in this text introduces an approximate formulation for the feedback diffusion current at interdigitated microband array electrode which is found applicable to most practical detector designs, see appendix 1. The model proposed is based on simplifing assumptions concerning the steady state diffusion field boundary conditions, approximating lines of mass flux with a confocal elliptic function and equiconcentration surfaces with a confocal hyperbolic function. The theoretical treatment given to this system is discussed in detail in chapter 2, and has been derived from the analogous heat conduction problem. The study focuses on the operational characteristics of a large scale interdigitated device with bandwidth of 95μm and band gap of 18μm, with emphasis on analytical performance. The chronoamperometric response of the device in common and differential potential operation is discussed in terms of diffusion field theory. Time dependent diffusion fields for the different operating modes were modelled for the simulation of i-t characteristics using an explicit finite difference method with uniform two dimensional space co-ordinates. The theoretical treatments and experimental

data presented for interdigitated microband array electrodes lead to the corollary that the submicrometer dimension is the important scale for chemical detector application. In an attempt to design and fabricate devices with specific dimensions less than 1μm a thin laminate approach was taken. The submicrometer band electrodes developed were characterised using an analogous theoretical treatment for the cylindrical electrode. The potential application of interdigitated microband electrodes to immunoassay has been briefy outlined in chapter 6.

1.3 DUAL MICROCYLINDER ELECTRODES.

The quantitative aspects of the diffusion current for electrodes of cylindrical geometry were investigated as long ago as 1931 by Glasstone and Reynolds. These workers equated a diffusion controlled current at a platinum wire electrode (r=265μm) with Fick's equation for linear flux and verified a proportionality between the current, analyte concentration and electrode area. A systematic study followed for the diffusion controlled electrolysis at microcylindrical electrodes by Kolthoff and Laitenin, 1939 [24], where the chronoamperometric response was measured. These early experiments, although not purely under diffusion control, demonstrated the utility of cylindrical electrodes for application to analytical amperometry, such as titrimetry, and were of particular value in the field of oxygen electrode research.

Davies and Brink in 1942 [25] demonstrated the applicability of platinum microwire electrodes (25μm<r<100μm) for the physiological measurement of oxygen and discussed the potential of such probes for the monitoring of in vivo environments with a view to mapping oxygen concentration within tissue.

Advances in carbon fibre technology lead to the manufacture of highly uniform micrometer fibers and in so doing created interest in the material as an electrode [26] and refs therein. In the 1970s physiological experiments were conducted for the in vivo measurement of catecholamines using carbon fibre electrodes. Studies in this area gave impetus to ideas for further utilisation of miniaturised amperometric electrodes in microanalysis.

Along with the advent of microelectrode research over recent times (1980s), stimulated by the availability of quality micrometer wires and fibres, there has

been renewed interest in microscopic platinum wire and carbon fibre electrodes as a versatile amperometric electrode in detector/sensor designs. Recent applications include enzyme electrodes, liquid chromatography [27,28], capillary zone electrophoresis detectors and probe electrodes for in vivo measurements. In step with experimental developments in microwire research [29,30] a re-examination of the theoretical basis of chronoamperometry and cyclic voltammetry at microscopic cylinder electrodes was attempted. In these studies various electrochemical conditions were considered including, reversible and quasi-reversible redox systems and combined migration-diffusion mass transport [31-34].

The principles of single microwire electrode fabrication have been considered throughout the relevant literature. Generally this involves sealing a micrometer diameter wire in glass or epoxy resin. The wire protrudes from a support (rod) to a given distance which is usually measured after fabrication. Although such fabrication methods have several drawbacks, they have benefited the amperometric study of the single microwire electrode. The methods prescribed are of limited application to the design and construction of regular microcylinder array devices. However, this methodology could be used to assemble dual arrangements of microwires with such precision as to allow characterisation, as described in chapter 3.

To the present time an amperometric study of the diffusion current characteristics of dual microcylinder electrodes for reversible redox species has not been documented. This is partly due to fabrication difficulties, but also arises from a limited awareness of the response characteristics and potential useage of such devices. The microcylinder electrodes discussed here consist of two parallel microscopic metal wires or carbon fibres separated by a microscopic gap. The parallel wire device can be operated in one or two electrode mode, or alternatively as an anode and cathode, cf. microband electrodes.

Diffusion controlled chronoamperometry experiments for reversible redox species at a dual microcylinder anode-cathode device show similar behaviour to that discussed for the microband system in terms of shielding and feedback current effects. The feedback diffusion current at this device was modelled for the case of a steady state response using the bilinear transformation of space

co-ordinates. In the transformed space the lines of mass flux and concentration surfaces are represented by orthogonal circular functions. The diffusion theory developed for this system follows analogous descriptions of stationary field behaviour in electric, magnetic and heat conduction disciplines. The experimental and theoretical data for dual microcylinder anode-cathode devices highlight the importance of electrode radius and spacing to the current response. The potential applications of dual microcylinder anode-cathode devices are reviewed in chapter 6 with specific reference to in vivo monitoring.

CHAPTER 2

THEORY FOR DIFFUSION PROCESSES AT AMPEROMETRIC MICROBAND AND CYLINDER ARRAY ELECTRODES.

2.1 BASIC CONCEPTS OF DIFFUSION MASS TRANSPORT [35,36].

Diffusion is a mass transport phenomenon involving the movement of a substance in response to a gradient of concentration. For solutions, this process may be envisaged microscopically in terms of a resultant force, F, experienced by a solute species originating from molecular perturbations of the solvent. This can be expressed as the variation of Gibbs energy for an elementary displacement,

$$F = -1/N_A.\partial G/\partial x \qquad (2.1)$$

where N_A is Avogadro's number.

For isotropic media, the diffusional flux, J, of a species i, at any instant in the diffusion process, i.e. the number of molecules per second passing a plane of unit area, is given by,

$$J_i = -D_i \mathrm{grad} C_i \qquad (2.2)$$

where, D_i, is the diffusion coefficient of the diffusant and $\mathrm{grad}C_i$, the concentration gradient operating.

Equation (2.2) shows the rate of mass flow is proportional to a gradient of concentration and hence any parameters which affect this gradient will have concomitant effects on mass flux.

Diffusion induced by electrochemical means is initiated from a perturbation of the interfacial electrode-electrolyte layer. This takes the form of an electrochemical process at the electrode which instantaneously changes the local concentration of electroactive species. A concentration field is thus established which is a function of space coordinates and time, and is refered

to as a transient field.

$$C = f(x,y,z,t) \tag{2.3}$$

For a uniform diffusion (concentration) field, where surfaces of equiconcentration lie parallel to the electrode and lines of mass flux project normally to the electrode surface, the flux lines can be considered as the direction along which the diffusion force acts. This field pattern as shown in figure 2.1 describes diffusional mass transport of species to and from a macroscopic planar surface The diffusion layer thickness, δ, can be pictured as a time dependent boundary with bulk solution, where,

$$C_i = C^b_i \tag{2.4}$$

Therefore in the case of a diffusion field of uniform geometry, the number of lines of flux to an electrode remains constant as the field extends into solution. This condition has a direct influence on the electrode current; it will be shown for non-uniform fields generated at microelectrodes that the diffusion field surface expands with time, changing the current response from that of a linear field response.

The intensity of the field at a given concentration surface and time is defined as the number of flux lines per unit area. Pertinent to electrode mass flux is the field intensity or more usually, flux density, at the electrode surface. This quantity relates the flux linkage between bulk solution and electrode surface as the field evolves.

For macroscopic electrodes the mass flux to the electrode is linear, and eqn. (2.2) reduces to a one dimensional expression, viz. Fick's first equation.

$$J = -D(\partial C/\partial x) \tag{2.5}$$

Equating the electrode mass flux and the rate of charge flow with time gives,

$$i = nFAJ_{x=0} \tag{2.6}$$

and realising, after a given electrolysis time the field will extend a distance δ, such that $dC/dx = C^b/\delta$, the corresponding diffusion current is given by,

$$i = nFDAC^b_i/\delta \tag{2.7}$$

where, for the Cottrell equation,

$$\delta = \sqrt{\pi Dt} \qquad (2.8)$$

2.2 CHRONOAMPEROMETRY: A TECHNIQUE FOR STUDYING TRANSIENT AND STEADY STATE DIFFUSION FIELDS OF ELECTROACTIVE SPECIES.

Chronoamperometry is an electrochemical method for monitoring the time variation of an electrode current. The current may be governed by a charge transfer process including adsorption phenomena. Equally the current may be controlled by the rate of mass transport. By judicious control of experimental parameters such as the type of redox species and electrode, electrode polarisation, electrolyte conditions etc., it is possible to discriminate between these various current limiting processes. This work is concerned primarily with the diffusion controlled chronoamperometry at arrangements of microscopic electrodes and the effects of the diffusion field on i-t response.

Voltammetric data for a redox species provides information for potential step experiments. For investigations into the effects of mass transport on amperometric behaviour it is usual to select a potential step from a region where no faradaic current is observed to a region where the current is mass transport limited, see figure 2.2. The duration of the potential step, τ, is the time period during which the current is measured; in figure 2.3, τ=10s. The time window for purely diffusion controlled current is dependent on the various experimental conditions used. This may be generalised for quiescent aqueous systems relying on the capacitive decay time and the onset of convectional mass transport. Diffusion currents in such systems are typically measured over the time period of 50ms to 10s.

2.3 THE DIFFUSION CURRENT AT ISOLATED MICROSCOPIC CYLINDER ELECTRODES.

The mathematical treatment of heat conduction at cylindrical surfaces initiated analogous theory for a diffusion process in terms of a microscopic concentration field of cylindrical geometry. Ruis et al. [37] approached this transport problem showing the significance of field geometry to the diffusional flux and hence chronoamperometric behaviour of microcylinder electrodes.

For a diffusion controlled electrolysis of species O to a cylinder electrode of

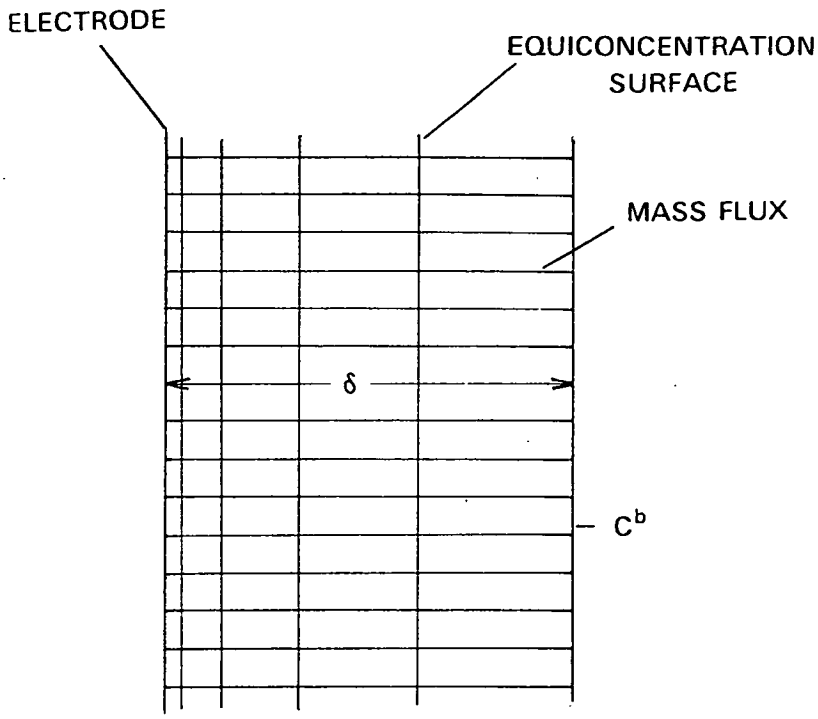

Figure 2.1 Illustration of a transient diffusion field at a macroscopic electrode.

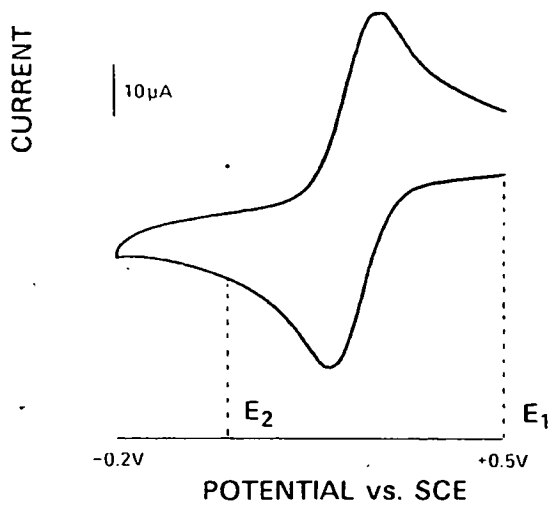

Figure 2.2 Cyclic voltammetry for a reversible redox species ($Fe(CN)_6^{3-}$)at conventional large scale electrode.

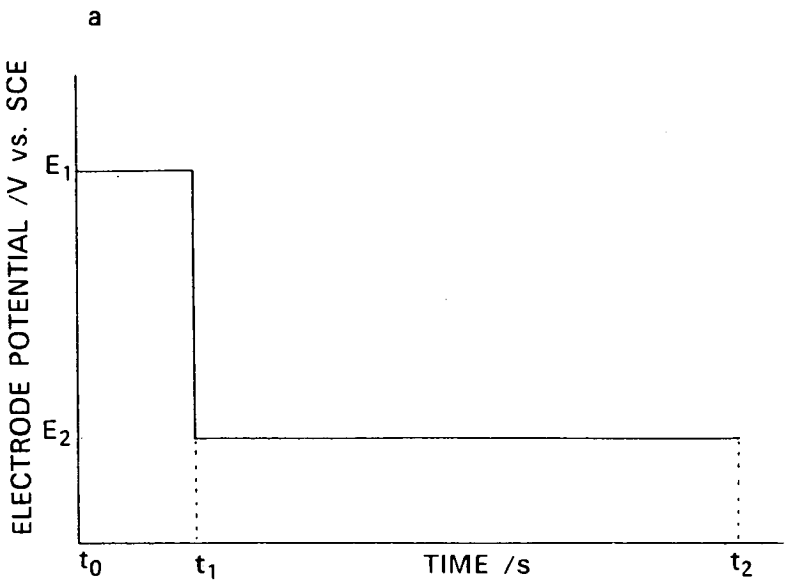

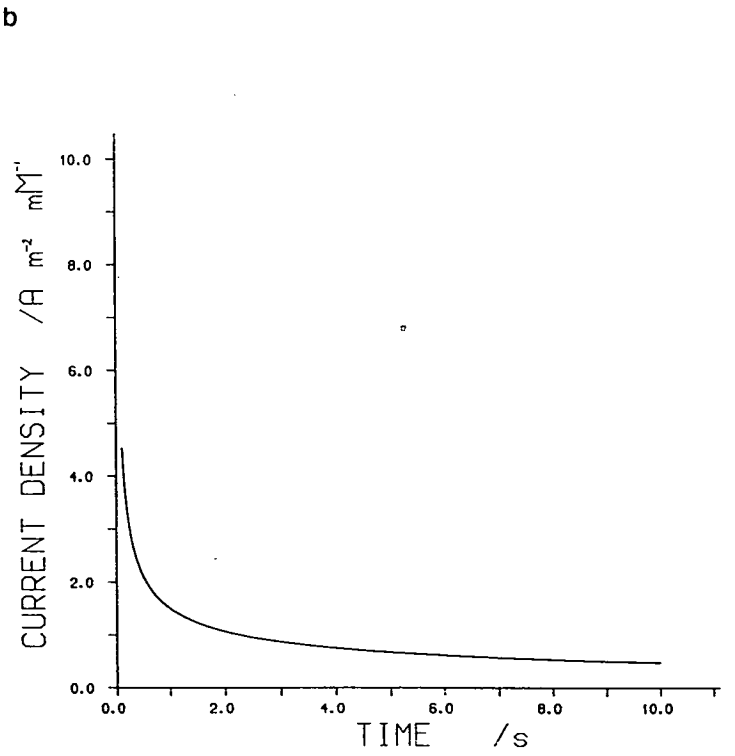

Figure 2.3 Chronoamperometric experiment corresponding to fig. 2.2. a. electrode potential vs. time b. current vs. time curve.

radius, r^o and infinite length given by,

$$O + ne \rightleftharpoons R$$

the diffusion expression in cylindrical co-ordinates is,

$$\partial C/\partial t = D\left[\partial^2 C/\partial r^2 + 1/r\partial C/\partial r + 1/r^2\partial^2 C/\partial\theta^2 + \partial^2 C/\partial l^2\right] \quad (2.9)$$

for a very long cylinder $\partial C/\partial l = 0$, (2.10)

and $C_R = 0,\ r_o \leqq r \leqq \infty,\ t=0$ (2.11)

$$C_R = 0,\ r\rightarrow\infty, \qquad t>0 \quad (2.12)$$

$$C_R = C_O{}^b,\ r = r^o, \quad t>0 \quad (2.13)$$

if no angular concentration gradient exists, $\partial C/\partial\theta = 0$. (2.14)

Applying the treatment from the heat conduction problem discussed by Carslaw and Jaeger et al. [38,39], an analogous expression for the diffusion current, i, can be derived subject to the boundary conditions of eqns.(2.9) to (2.14),

$$i = 4nFDCIf(\theta)/\pi \quad (2.15)$$

where, $$f(\theta) = \int_0^\infty e^{-\theta u}/\left[J_o{}^2(u) + Y^2{}_o(u)\right]u\ du \quad (2.16)$$

and $\theta = Dt/r^{o2}$, and $J_o(u)$, $Y_o(u)$ are Bessel functions of the first and second kinds with zero order.

The integral term in eqn.(2.16) has two important limiting analytical forms which are a function of the non-dimensional parameter θ.

For small values of θ,

$$Lim_{\theta\rightarrow 0} f(\theta) = (1/(\pi\theta)^{1/2} + 1/2 - 1/4(\theta/\pi)^{1/2} + \theta/8 + \ldots) \quad (2.17)$$

and for large θ,

$$Lim_{\theta\rightarrow\infty} f(\theta) = \frac{1}{\ln(4\theta)-2\gamma} - \frac{\gamma}{(\ln(4\theta)-2\gamma)^2} \ldots \quad (2.18)$$

where γ is Euler's constant, 0.5772.

For a value of θ less than ca. 10^{-4} (small t or large r) equation (2.15) approximates the chronoamperometric response of a macroscopic electrode indicating the curvature of the electrode is of little importance to the mass flux. The function, $f(\theta)$ then reduces to $1/(\pi\theta)^{1/2}$. For example, the Cottrell equation adequately describes the behaviour of a cylinder electrode of radius 8.72 mm and taking $D(FeCN)_6^{3-}=7.6\times10^{-10}m^2\ s^{-1}$ for $t\leqq10s$.

The early theoretical treatment of the diffusion current at cylinder electrodes formulated some important results concerning the behaviour of a microscopic cylindrical diffusion field and its consequences to chronoamperometry. The dimensionless factor θ takes small values at short electrolysis time. Then the diffusion field thickness δ, is not extensive in comparison with r^o, the radial flux lines are then approximated by a linear field pattern. For large θ, the diffusion field is extensively distributed within the medium relative to the electrode radius, i.e. at long electrolysis time eqn. (2.18) approximates the chronoamperometric response. Neglecting all but the first term in this series, eqn.(2.18) reduces to,

$$i = 4\pi nFDCl/\ln(4\theta)-2\gamma \qquad (2.19)$$

Equation (2.19), where applicable, is an interesting result because it shows that the diffusion current at a cylinder electrode is time dependent, however this dependence is an inverse logarithmic function, suggesting relative insensitivity to this quantity. Under such conditions the current is described as varying in virtual or quasi steady state. Eqn.(2.19) also indicates the weak dependence of the diffusion current on the electrode dimension, r^o.

A re-examination of the cylindrical diffusion current problem has taken place over recent years following general interest in microelectrode research [30,32]. Aoki et al. have analysed the integral in eqn.(2.16) for values of θ important to micrometer scale cylinder electrodes. They expressed more clearly the limitations for θ in eqns.(2.17) and (2.18). For eqn.(2.17) to apply, θ must be smaller than 0.18. Therefore an electrode of radius 12.5µm, and taking $D=7.6\times10^{-10}m^2\ s^{-1}$, eqn.(2.17) predicts the i-t response for electrolysis times t, less than 0.21s. While for a radius of 100µm, the equation applies for $t<2.4s$. Equation (2.18) is applicable when $\theta\geqq1200$. Hence for an electrode of radius,

r^{o}=12.5 eqn.(2.18) is suitable for electrolysis times greater than 246.7s. Therefore, convective effects render expression (2.19) useless to wire electrodes of conventional micrometer scale.

2.4 HEMICYLINDRICAL DIFFUSION FIELD APPROXIMATION FOR SUBMICROMETER BAND ELECTRODES.

2.4.1 EQUIVALENCE OF THE HEMICYLINDER AND BAND ELECTRODES AT THE SUBMICRON DIMENSION.

This section applies the limiting case for eqn.(2.18), $\theta \rightarrow \infty$, from cylindrical diffusion theory to an approximate description of the field at a submicron scale band electrode. In this way it is therefore possible to obtain greater understanding of the amperometric behaviour of such electrodes.

Equation (2.19) can be used to estimate the chronoamperometric characteristics of submicrometer scale band electrodes. Important as regards to amperometric microsensor design is information on the time response of the diffusion current, sensitivity to bandwidth and the time development of the diffusion field. This latter point is important for application of submicron band electrodes in particulate or convective media, and also provide information for the fabrication of band array electrodes on the submicrometer scale.

The hemicylindrical diffusion current expression is one half that of eqn.(2.19) and can be restated for a band of equivalent area, $w_e l = \pi r l$.

Whence, $w_e = \pi r$ (2.20)

Therefore, an equivalent expression for the diffusion current at a band electrode is,

$$i = 2\pi nFDCl \Big/ \left(\ln(4\pi^2 Dt/w^2) - 2\gamma \right) \qquad (2.21)$$

Simplifying eqn.(2.21) by eliminating the 2γ term gives,

$$i = 2\pi nFDCl / \ln(4\pi^2 Dt/w^2) \qquad (2.22)$$

The general applicability of eqn.(2.22) to a description of chronoamperometry at submicrometer band electrodes can be considered with reference to a

limiting condition, e.g. $\theta > 1200$. Taking $D = 10 \times 10^{-10} m^2 s^{-1}$ and for an electrode of bandwidth of 100nm, eqn.(2.22) will estimate i-t behaviour for electrolysis time greater than ca. 12ms. Table 2.1 shows the theoretical amperometric characteristics of a submicron band electrode, most noticeable is the magnitude of the current density which increase with diminishing bandwidth.

3.4.2 AN EXPRESSION FOR THE DIFFUSION LAYER THICKNESS.

The extent to which the hemicylindical diffusion field at a submicron band electrode evolves into the solution with time can be estimated from eqn.(2.22). The diffusion current at a hemicylinder electrode is given by,

$$i = nFDlr^{o} \int_{\theta=0}^{\theta=\pi} (\partial C/\partial r) d\theta \qquad (2.23)$$

Approximating r with the size of the diffusion field, i.e. the diffusion layer thickness, δ.

then, $$i = \pi nFDC^{b} r^{o}/\delta \qquad (2.24)$$

From eqn.(2.22) and eqn.(2.24), we have the following identity for a hemicylinder electrode,

$$2\delta/r = 1/\ln(4\theta) \qquad (2.25)$$

Hence an approximate expression for the time dependent diffusion field thickness, δ at a submicron band electrode is,

$$\delta = w \ln(4\theta)/2\pi \qquad (2.26)$$

If eqn.(2.18) is considered, then taking into account eqn.(2.24), δ becomes,

$$\delta = \frac{w}{2\pi(1/\ln(4\theta) - 2\gamma - \gamma/\ln(4\theta) - 2\gamma)^2} \qquad (2.27)$$

Figure 2.4 illustrates the growth of a diffusion field at a band electrode of 100nm bandwidth. The hemicylindrical diffusion field evolves on a very short time scale, 10ms, gradually extending to size ca. 0.27µm after 10s. Using eqn.(2.26), it is possible to compare the diffusion field characteristics as a function of bandwidth for submicroscopic band electrodes. Table 2.2 shows data for a 50nm and 100nm electrode. The ratio of the diffusion layer surface

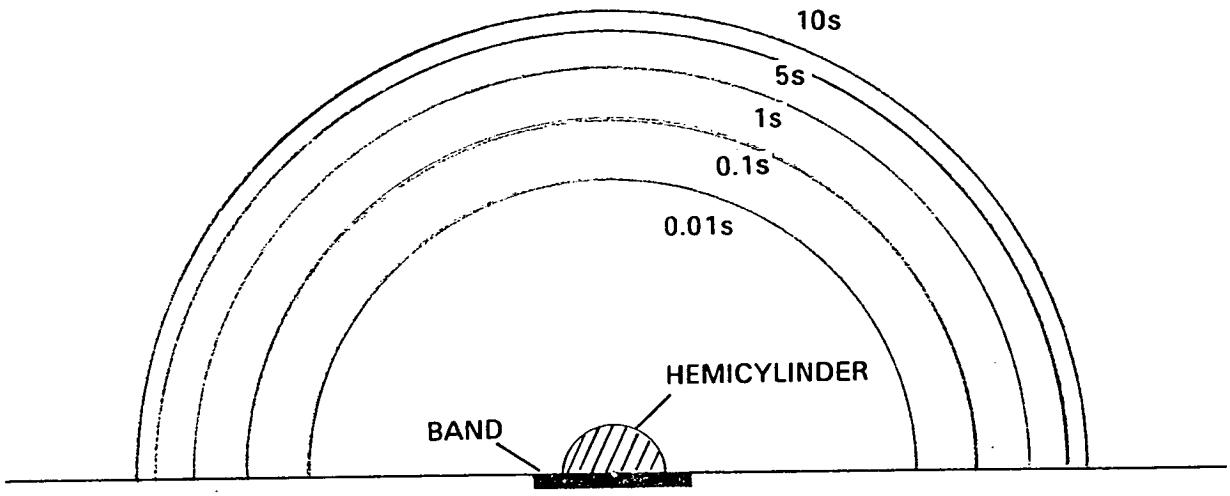

Figure 2.4 Illustration of diffusion field development at a submicroscopic cylinder electrode and approximation to an equivalent band geometry. Diffusion layer thickness was calculated from eqn.(2.22) taking $D=7.6\times10^{-10}m^2\ s^{-1}$, and w=100nm.

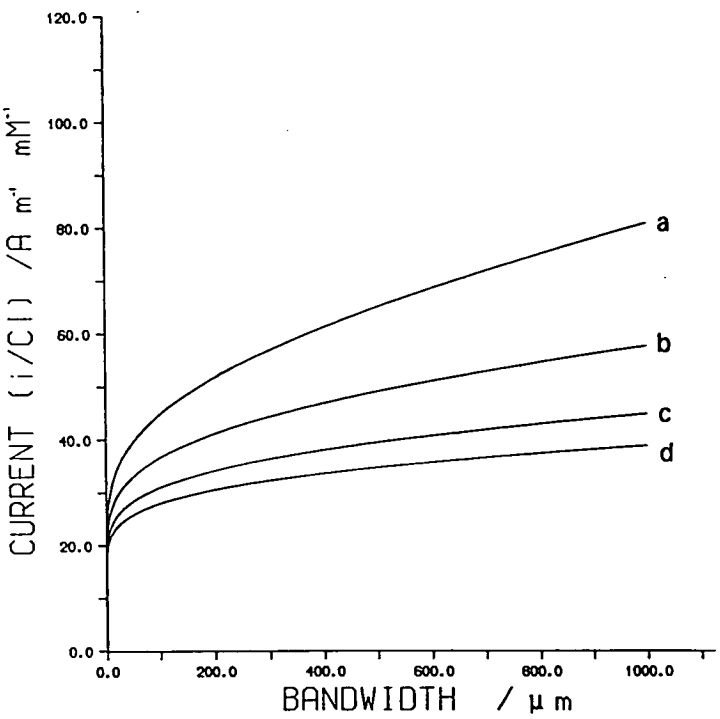

Figure 2.5 Diffusion current vs. bandwidth curves for submicrometer band electrodes. Data calculated from eqn.(2.22) taking $D=7.6\times10^{-10}m^2\ s^{-1}$. a. 0.01s, b. 0.1s, c. 1.0s, d. 5.0s.

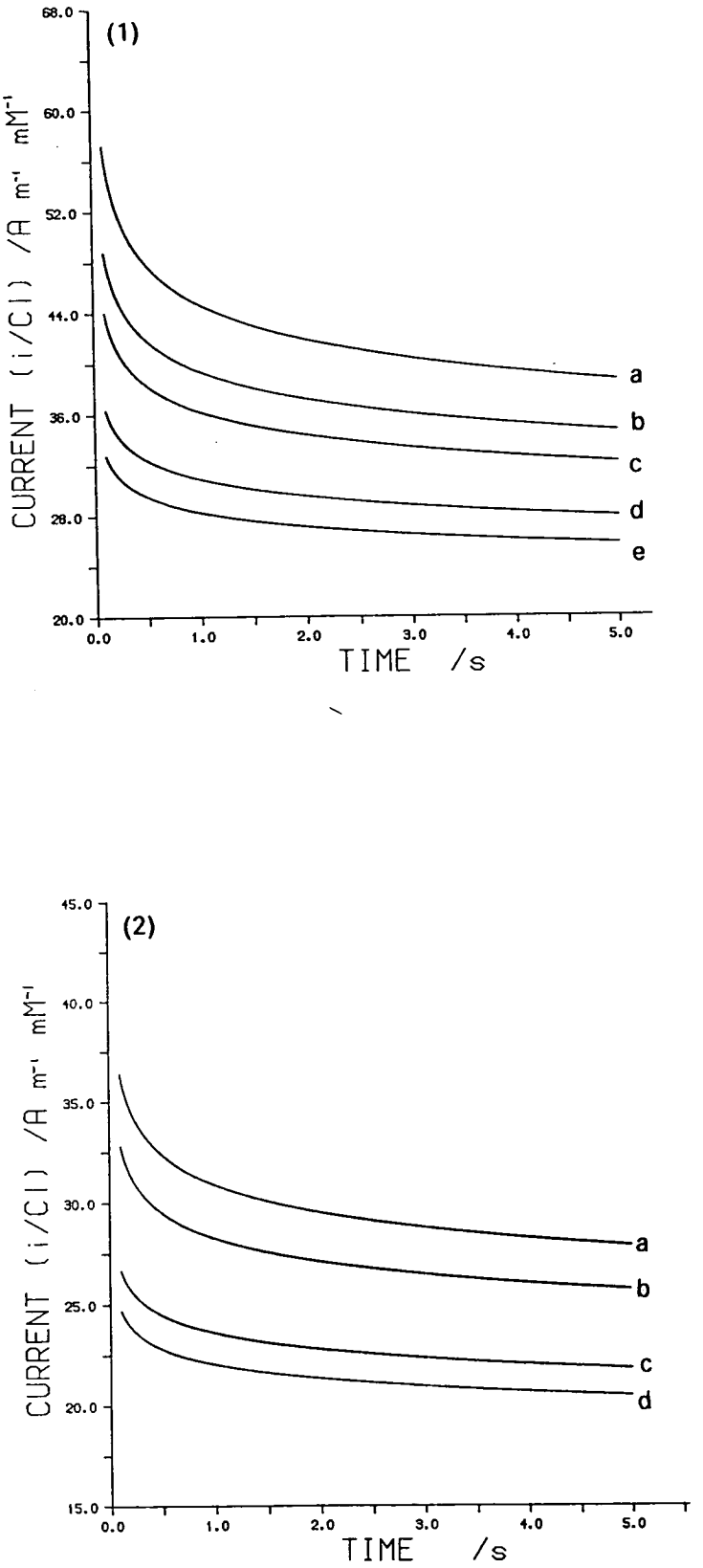

Figure 2.6 Theoretical chronoamperometric curves for micron/submicron band electrodes. Data calculated from eqn.(2.22) taking $D=7.6\times10^{-10}m^2\ s^{-1}$.

(1) a. 1μm, b. 0.5μm, c. 0.3μm, d. 0.1μm, e. 0.05μm.

(2) a. 100nm, b. 50nm, c. 10nm, d. 5nm.

to the electrode area represents the total flux linkage at any instant in the development of the field. This parameter is found to increase for electrodes of submicroscopic dimension as bandwidth is reduced. Furthermore, as w is decreased the size of the diffusion field at a given time is also diminished resulting in higher field strength, i.e. C^b/δ. Field parameters such as diffusion layer thickness and surface have an important bearing on the diffusion controlled chronoamperometry at submicroscopic band electrodes, this will be expanded in chapter 5.

2.4.3 THE DIFFUSION CURRENT DEPENDENCE ON BANDWIDTH.

Figure 2.5 shows the variation of diffusion current with bandwidth for submicrometer electrodes. The current, at a given time, increases with bandwidth owing to the enlargening electrode area. Unlike for the linear diffusion field where there is a direct proportionality between current and electrode area, for the case of hemicylindrical field geometry we have,

$$i = f(A/w\ln(b/w^2)), \qquad \text{where } b=\pi^2 Dt \tag{2.28}$$

By differentiation of eqn.(2.22) with respect to w, the relative sensitivity of a diffusion current to variations in bandwidth, (di/dw)/i, at submicrometer band electrodes can be obtained;

$$(di/dw)/i = 2/w\ln(4\theta) \tag{2.29}$$

The i-w curves in fig. 2.5, plotted for different t, indicate the sensitivity of the diffusion field to changes in bandwidth; the current is a strong function of bandwidth at short time, as suggested from eqn.(2.29).

2.4.4 DIFFUSION CURRENT DEPENDENCE ON ELECTROLYSIS TIME.

The weak dependence of diffusion current on electrolysis time as evident from eqn.(2.22) leads to the condition of virtual steady state chronoamperometry. Figure 2.6 shows a series of i-t curves for submicrometer band electrodes plotted for varying bandwidth. The rate of change of current with time can be used to define a response time for the quasi steady state signal.

Differentiation of eqn.(2.22) with respect to time yields,

$$di/dt = -2\pi nFDCl/t(\ln(4\pi^2 Dt/w^2))^2 \tag{2.30}$$

Dividing eqn.(2.30) by eqn.(2.22) allows calculation of the rate of change of the amperometric signal with time,

hence, $(di/dt)_i = -1/t\ln(4\pi^2 Dt/w^2)$ (2.31)

This function is a measure of the gradient of the chronoamperogram at any given time.

2.5 AN APPROXIMATE EXPRESSION FOR THE STEADY STATE DIFFUSION CURRENT AT INTERDIGITATED MICROBAND ARRAY ELECTRODES.

The following discussion focuses on the steady state mass transport problem of diffusion for the recycling of reversible redox species between parallel coplanar microanodes and cathodes of band geometry positioned with a microscopic spacing. The derivation follows an analogous treatment for heat flux between a heat source and sink, and as been dealt with elsewhere [38]. The expression derived in the present work and published in ref.[23] (see appendix 1), attempts to predict the steady state current response of the interdigitated microband array electrodes reported in this study. The model proposed could also serve other interdigitated devices where band gap is small relative to the bandwidth.

The derivation supposes a quiescent electrolyte solution composed of an electochemically reversible redox couple and excess electroinactive (support) electrolyte. The simple electrode process is considered;

$$O + ne \rightleftharpoons R$$

where species O and R are initially present in equiconcentration, C^b.

The above mentioned restriction remove the necessity for convective and migration considerations and simplify the mass transport problem to a two dimensional diffusion between parallel coplanar surfaces. The electrode system illustrated in figure 3.2. is redrawn in fig. 2.7 showing a band anode-cathode pair in cross-section with the condition of the diffusion field at steady state. The time invariant diffusion field considered assumes total recycling of species by a feedback diffusion process i.e. 100% collection efficiency, hence the device should be considered as an infinite array with no edge losses. The anode is shown in cross-section bounded by X_1 and X_2, and the cathode $-X_1$

and $-X_2$ at Y=0, which for an interdigitated device represents one half bandwidth. The region between $-X_1$ and X_1 is the band gap.

The anode is polarised at a potential E_a, and the cathode E_c, such that the following boundary conditions hold;

At the anode,

$$C_O/C_R = \exp(nF/RT(E_a-E^{o/}) \quad X_1 \leqq X \leqq X_2 \quad Y=0 \tag{2.32}$$

At the cathode,

$$C_O/C_R = \exp(nF/RT[E_c-E^{o/}) \quad -X_1 \geqq X \geqq -X_2, \quad Y=0 \tag{2.33}$$

where $E^{o/}$ is the formal standard potential for the redox couple.

The boundary conditions for this system reads,

$$C_R=C_R^{\,b},\ C_O=C_O^{\,b} \qquad Y=\infty \tag{2.34}$$

$$(\partial C/\partial y)=0, \quad -X_1<X<X_1 \qquad Y=0 \tag{2.35}$$

$$(\partial C/\partial x)=0, \quad X=\pm X_2 \qquad 0 \leqq y \leqq \infty \tag{2.36}$$

Fick's equation (2.38) describing the two dimensional diffusion transport of O and R between the band electrodes in cartesian co-ordinates is,

$$\frac{\partial C}{\partial t} = D\left[\frac{\partial^2 C}{\partial^2 x} + \frac{\partial C^2}{\partial y^2}\right] \tag{2.37}$$

For a steady state diffusion process ($\partial C/\partial t=0$) eqn.(2.37) reduces to the Laplace expression. For species O,

$$D_O\left[\frac{\partial^2 C_O}{\partial x^2} + \frac{\partial^2 C_O}{\partial y^2}\right] = 0 \tag{2.38}$$

Let E_a and E_c have values such that the current at the anode and cathode are under diffusion control. The boundary conditions at the interdigitated microband electrodes become,

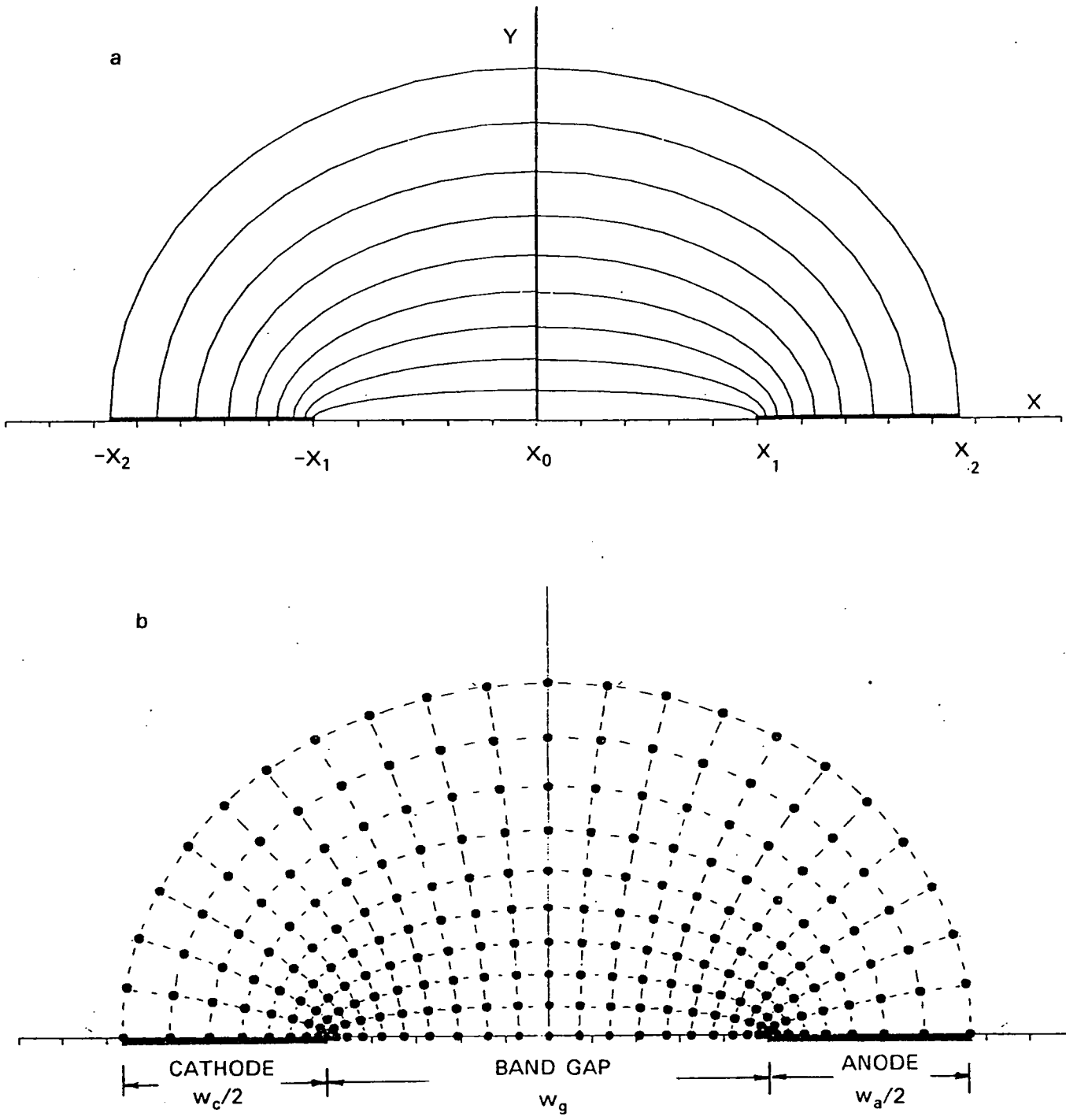

Figure 2.7 a. Steady state flux field at interdigitated microband array electrodes. b. Steady state diffusion field illustrating equiconcentration and flux surfaces.

At the anode, $C_O=2C_O^b$, $X_1 \leqq X \leqq X_2$ (2.39)

At the cathode, $C_O=0$, $-X_1 \geqq X \geqq -X_2$ (2.40)

The important function to be determined is the surface flux over the interval X_1 to X_2. In terms of per unit band length and assuming, $D_O=D_R$, the steady state flux to the band electrode is given by;

$$J/I = \int_{X1}^{X2} D\left(\frac{\partial C}{\partial y}\right)_{y=0} dx \qquad (2.41)$$

recognising $I/nFI = J/I$, where I is the current density, (2.42)

the steady state current per unit band length may be derived from eqn.(2.41) by solving the integral term.

Applying the theorem for complex conjugate transformation [38] to the stationary field problem,

$$u+iv = \cosh^{-1}(x+iy)/X_1 \qquad (2.43)$$

We can define x and y as,

$$x = \text{coshu cosv} \qquad (2.44)$$

$$y = \text{sinhu sinv} \qquad (2.45)$$

Where x and y are dimensionless variables given by,

$$x = X/X_1 \qquad (2.46)$$

$$y = Y/X_1 \qquad (2.47)$$

Defining a dimensionless concentration, v, for species O,

$$v = \pi C/2C_O^b \qquad (2.48)$$

Now, the confocal hyperbolic and elliptic lines illustrated in fig. 2.7 are representations of the concentration and flux fields respectively, established at steady state. The anode and cathode therefore behave as equiconcentration surfaces and are limiting hyperbola.

The concentration surfaces are then given by,

$$\frac{x^2}{\cos^2 v} - \frac{y^2}{\sin^2 v} = 1 \qquad (2.49)$$

and the flux lines (surfaces),

$$\frac{x^2}{\cosh^2 u} + \frac{y^2}{\sinh^2 u} = 1 \qquad (2.50)$$

In order to solve eqn.(2.41) for the flux function and hence derive an expression for the steady state current it is necessary to transform the geometric variables (concentration- flux field) from a rectangular co-ordinate (x-y) space to an hyperbolic-eliptical co-ordinate (u-v) space.

Differentiating 2.44 and 2.45 with respect to x and y respectively yields,

$$\cos(v)\sinh(u)(du/dx) - \sin(v)\cosh(u)(dv/dx) = 1 \qquad (2.51)$$

$$\sin(v)\cosh(u)(du/dx) + \cos(v)\sinh(u)(dv/dy) = 1 \qquad (2.52)$$

For the condition y=0, $X_1 > X > X_2$, and v=0 (C_O=0),

$$\sinh(u)\,(du/dx)_{y=0,\ X1 \leqq X \leqq X2} = 1 \qquad (2.53)$$

$$\sinh(u)\,(dv/dy)_{y=0,\ X1 \leqq x \leqq X2} = 1 \qquad (2.54)$$

giving the identity,

$$(du/dx)_{y=0, X1 \leqq x \leqq X2} = (dv/dy)_{y=0, X1 \leqq x \leqq X2} \qquad (2.55)$$

The integral of interest then becomes,

$$2C_O{}^b/\pi \int_{2X1}^{X} \left(\partial u/\partial x\right)_{y=0} dx = \left[u\right]_{x=x1,y=0}^{x=x2,y=0} \qquad (2.56)$$

hence from eqn.(2.41) and (2.43) an expression for the steady state current at an interdigitated device consisting of m anode-cathode pairs is,

$$i = 2mnFDC_O{}^b l \cosh^{-1}(X_2/X_1)/\pi \qquad (2.57)$$

where l is the band length.

Equation (2.57) can be transformed into the following form, noting $y = \cosh^{-1}(x) = \ln(x+\sqrt{(x^2-1)})$.

Therefore the steady state current at interdigitated microband array electrodes is given by,

$$i = 2mnFDC^b_O \ln(X_2/X_1+((X_2/X_1)^2-1)^{1/2})/\pi \quad (2.58)$$

For a repeat anode-cathode system, where $w_e = w_a = w_c$

hence $$X_2 = w_e/2+w_g/2 \quad (2.59)$$

and $$X_1 = w_g/2 \quad (2.60)$$

therefore, $$X_2/X_1 = w_e/w_g + 1 \quad (2.61)$$

substituting into eqn.(2.57) and allowing $P = w_e/w_g$

an expression in terms of w_e and w_g follows,

$$i = 2mnFDC_O{}^b l \ln(P+1+\sqrt{P^2+2P})/\pi \quad (2.62)$$

Equation (2.62) can be rearranged for a dual band system, assuming total redox recycling,

$$i = 2mnFDC_O{}^b l \ln(2P+1+\sqrt{4P^2+4P})/\pi \quad (2.63)$$

For a reversible redox system initially containing only one form of the couple equations (2.62) and (2.63) reduce by one half owing to the change in boundary conditions, cathode $C_O=0$, anode $C_O=C_O{}^b$.

The above theory for the steady state current has assumed compliance with the Laplace equation and the stationary field boundary conditions. The latter however is only an approximation. Figure 2.8 shows the model upon which the above derivation is based. It assumes that the bandwidth is infinitely large. The error introduced by this approximation for devices with large w_e/w_g ratios will require comparison with the analytical/numerical solution.

Equation (2.62) indicates that the feedback current is not a strong function of either bandwidth or band gap. Figure 2.9 plots the current function, $i/2mnFDCl$ against w_e/w_g illustrating the dependence of the steady state current on this

ratio. Fig. 2.10 shows the variation of current density with band gap for a device of bandwidth, 95μm. It will be observed that current density increases with diminution of band gap; sharp increases in steady state current are found for small values of band gap. Figure 2.11 shows the variation in current density with band gap for a device with submicrometer specific dimensions. The plot illustrates the potential enhancement of sensitivity for microsensors operating on the principle of feedback diffusion.

Aoki et al. [21] have formulated a rigorous solution to the feedback diffusion problem at interdigitated microband electrodes with a polygonal boundary analysis using a Schwarz–Christoffel transformation, a treatment analogous to field problems found in electrostatics and magnetics. The empirical expression derived by these workers (2.64) is reported to approxmiate the solution to within 2% for $w_e/w_g > 0.18$.

$$i = mnFDCl(0.637ln(2.55(1+w_e/w_g))-0.19/(1+w_e/w_g)^2) \qquad (2.64)$$

Table 2.3 compares the current values from eqn.(2.62) and (2.64) for micrometer bandwidth devices. It is found that the approximation presented here tends to the empirical equation given by Aoki et al. for large values of the ratio w_e/w_g, e.g. eqn.(2.62) underestimates the current in eqn.(2.64) by 5% for w_e/w_g = 50. This would correspond to a device of bandwidth 100μm and band gap of 2μm. For the interdigitated device considered in this work eqn.(2.62) is in error of eqn.(2.64) by −8.8%. It is therefore clear that the approximation made in this derivation provide a good estimation of the current to better than ca. 10% for values of w_e/w_g greater than about 5.

2.6 THEORY FOR THE STEADY STATE DIFFUSION CURRENT AT A PARALLEL MICROCYLINDER ANODE AND CATHODE.

Consider an electrolytic system as proposed above for the interdigitated microband electrodes where both forms of a reversible redox species are present. The problem considered here is the steady state diffusional transport between a parallel microcylinder anode and cathode of radii r_a and r_c, as illustrated in figure 2.12. Analysis of this stationary field problem has been considered in other disciplines, including heat conduction, magnetism and electrostatics. The field is simplified by transformation from a system of exterior cylinders with circular flux and equiconcentration surfaces to one of

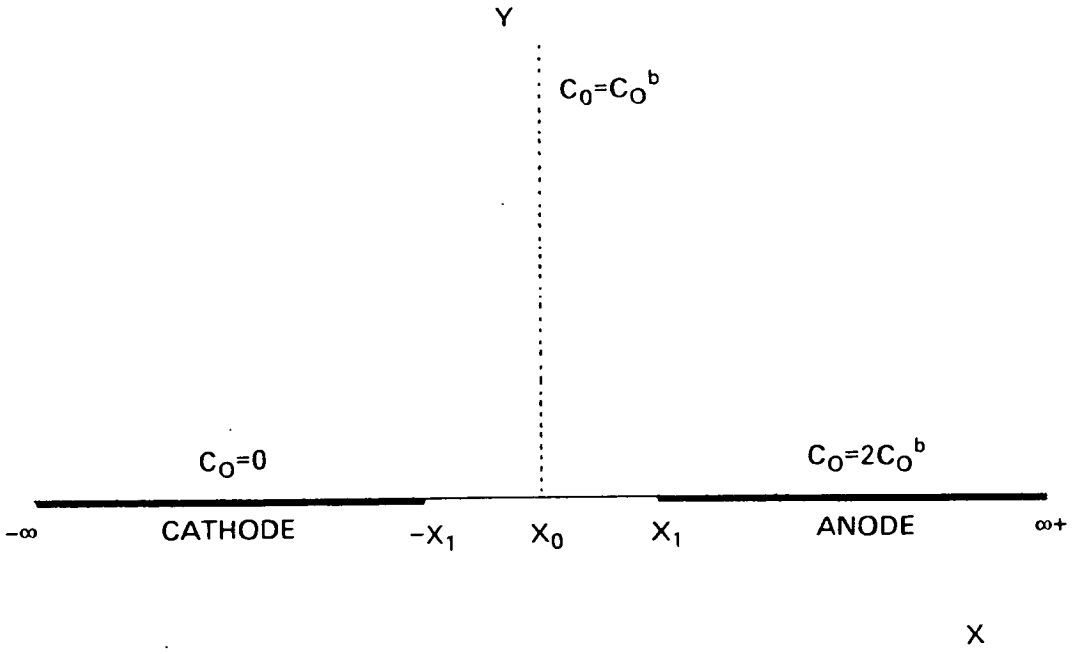

Figure 2.8 Theoretical steady state flux model for interdigitated microband array electrodes.

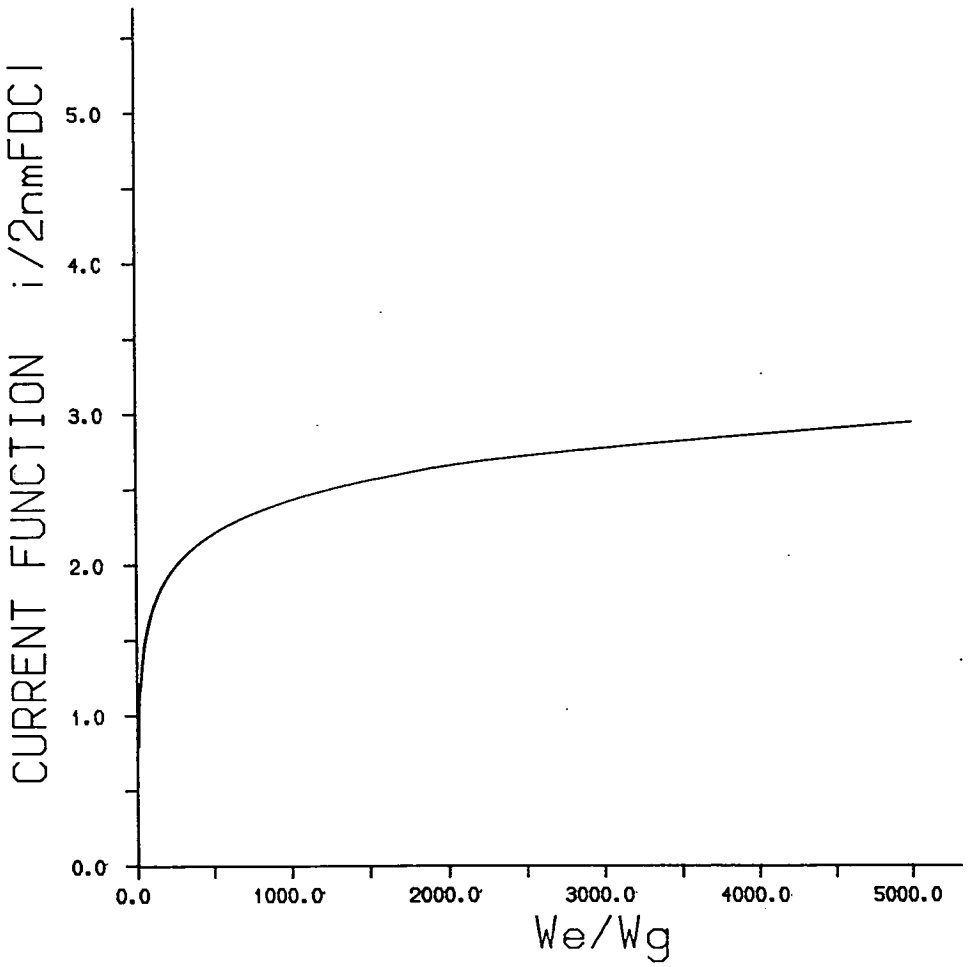

Figure 2.9 Variation of current function with the ratio w_e/w_g. Data calculated from eqn.(2.62) taking $D=7.0\times10^{-10}m^2\ s^{-1}$.

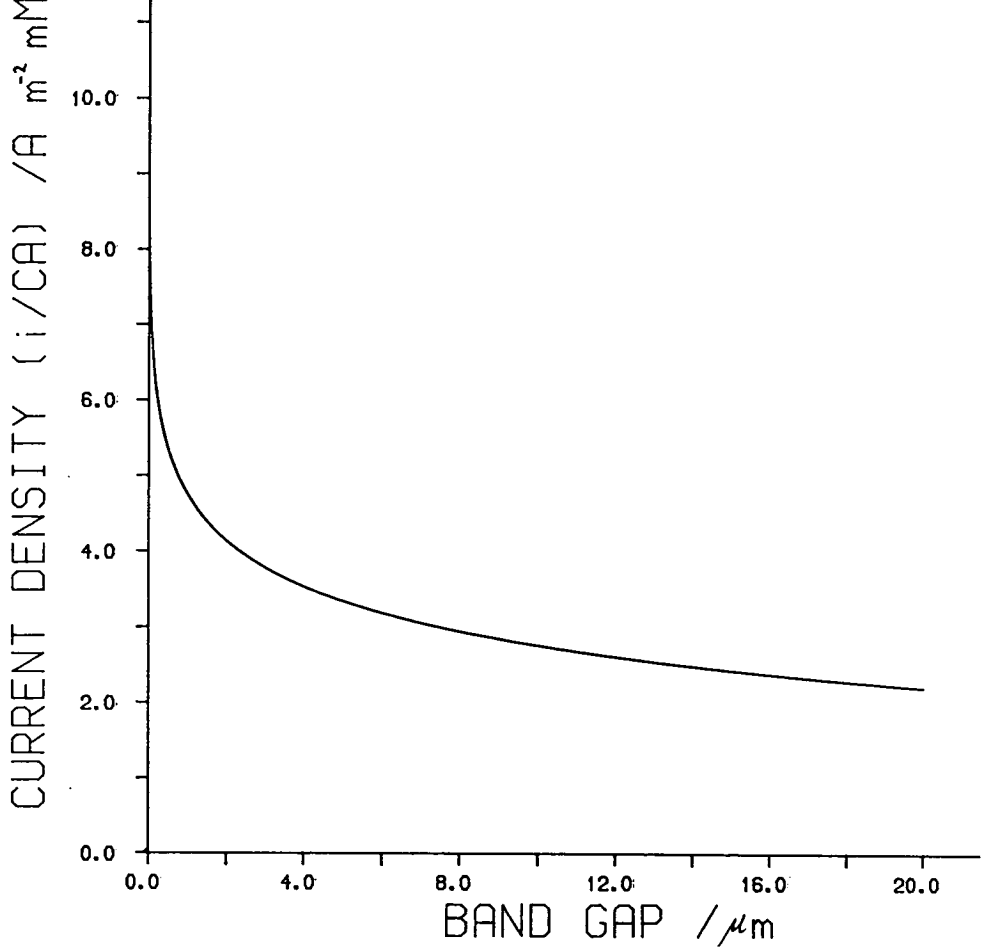

Figure 2.10 Current density versus bandwidth for an interdigitated microband array electrode of bandwidth, 95μm.

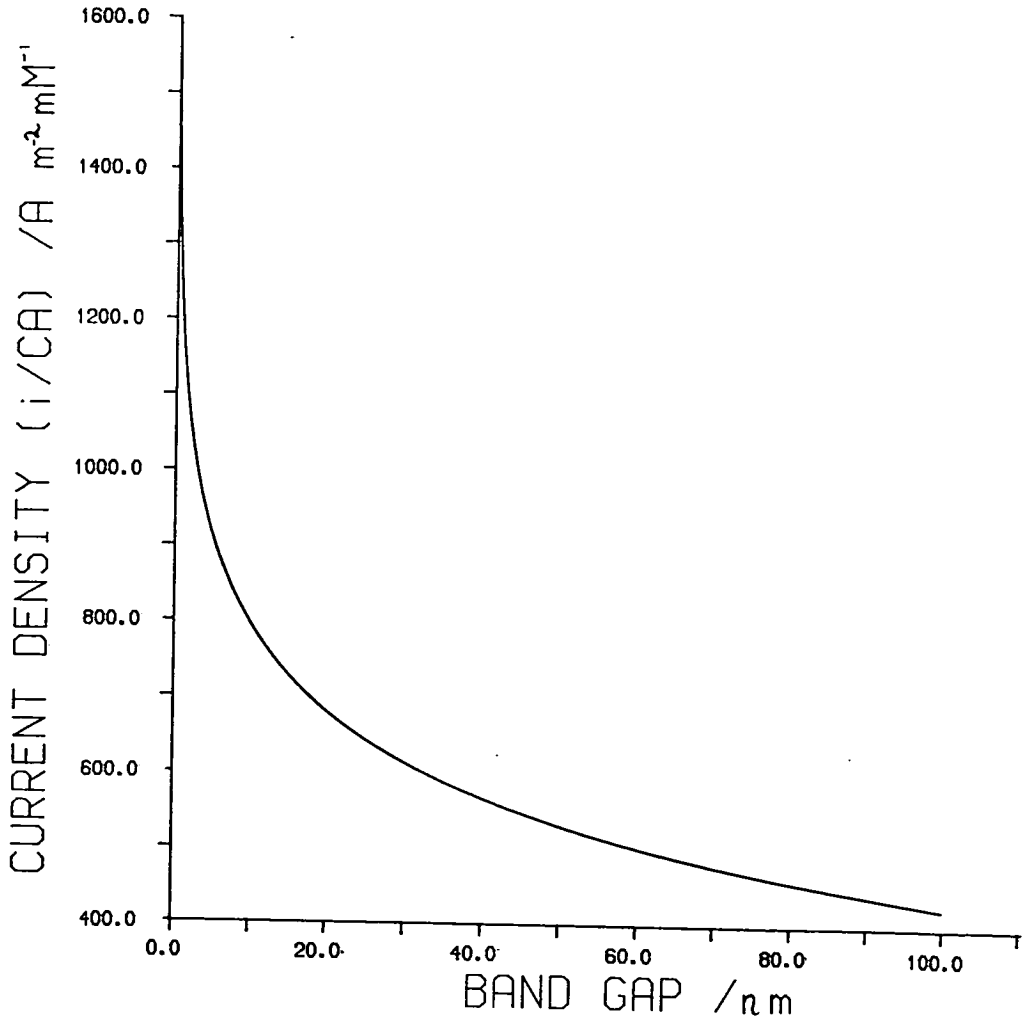

Figure 2.11 Current density versus bandwidth for a submicrometer interdigitated microband device, w_e=500nm .

concentric cylinders where flux is now described by a radial function, as depicted in figure 2.13.

The transformation from cartesian coordinates can be written;

$$u+iv = i(\ln(x+c)+iy)/((x-c)+iy) \tag{2.65}$$

such that equiconcentration surfaces are described by v, and given by the relation,

$$v = \ln(p_1/p_2) \tag{2.66}$$

and lines of flux are described by,

$$u = \theta_2 - \theta_1 \tag{2.67}$$

where p and θ are defined by reference to figure 2.13,

When steady state mass flux is reached between the electrodes the following boundary conditions exist,

at the anode, $C_R = 0, \quad C_O = 2C^b_O$ (2.68)

at the cathode, $C_O = 0, \quad C_R = 2C^b_O$ (2.69)

and for species O the diffusion equation becomes,

$$\partial^2 C_O/\partial x^2 + \partial^2 C_O/\partial y^2 = 0 \tag{2.70}$$

The steady state current per unit length at the microcylinder anode is given by,

$$i/l = nFD\int_{\theta=0}^{\theta=2\pi} \left(\partial C_O/\partial r\right)_{r=ra} d\theta \tag{2.71}$$

For this system it is possible to define any equiconcentration surface in terms of a radius r, and distance d, from the origin X=0, Y=0.

For any circle the condition holds,

$$p_1/p_2 = (d_1 + \sqrt{d_1^2 - r_1^2})/\, r_1 \tag{2.72}$$

The flux and equiconcentration surface of interest are those at the electrode.

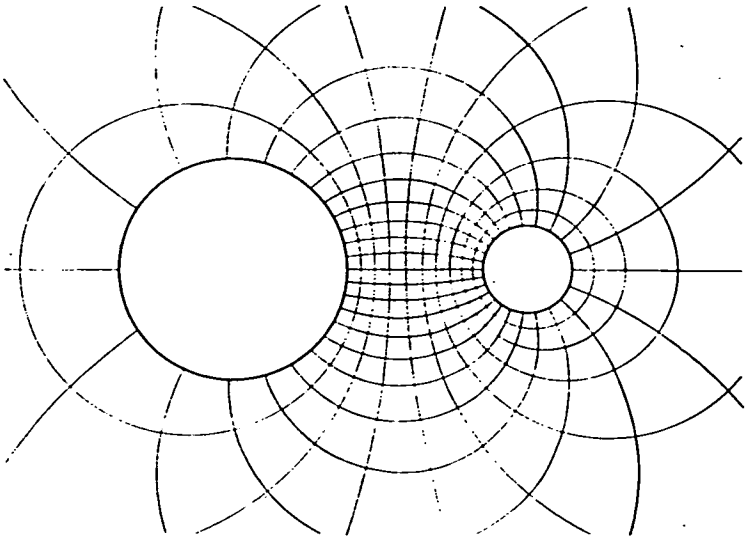

Figure 2.12 Illustration of the steady state diffusion field at a dual microcylinder anode–cathode.

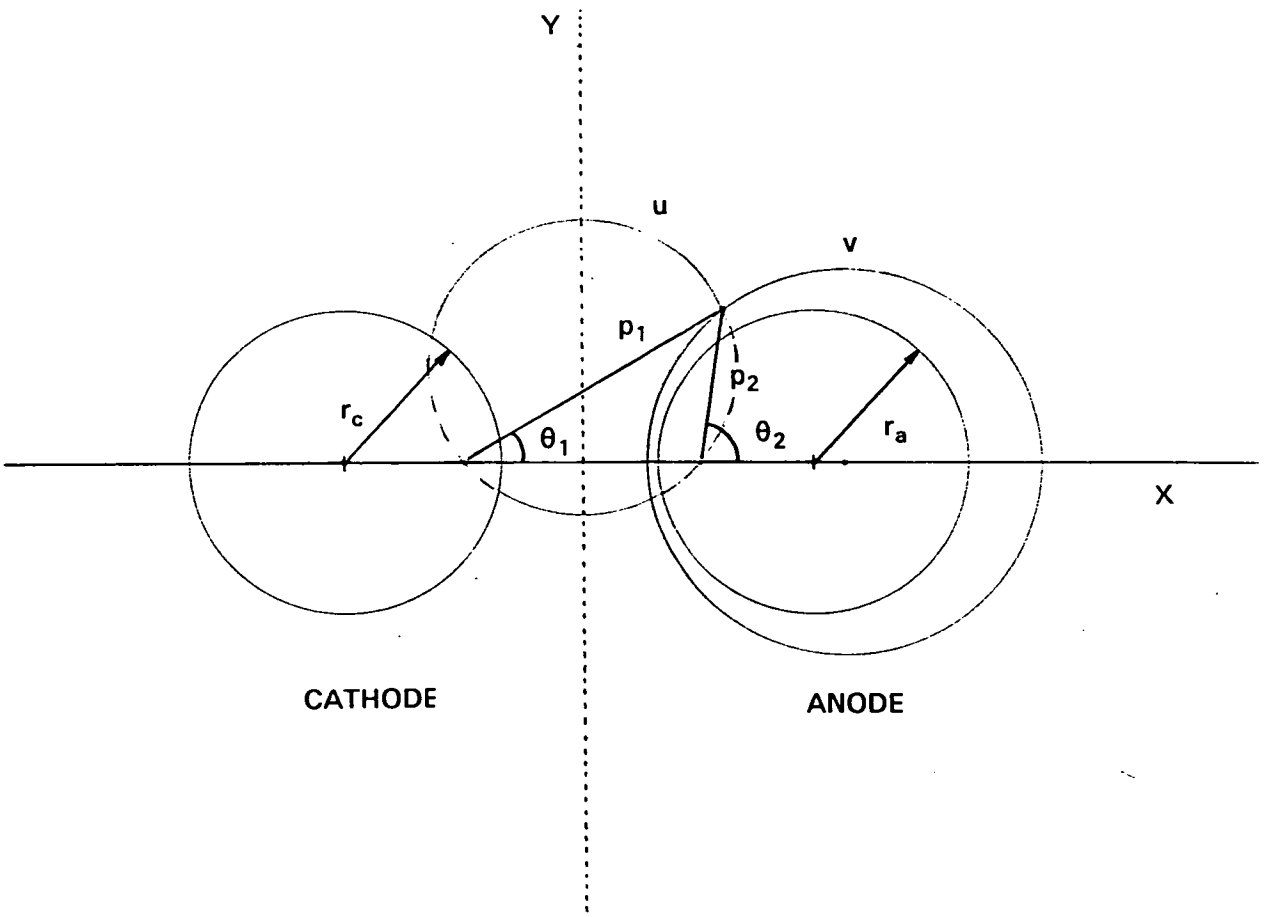

Figure 2.13 Lines of mass flux and equiconcentration surfaces in a steady state diffusion field at a dual microcylinder anode–cathode.

For the cathode, from eqn.(2.66)

$$v_c = \ln((d_c + \sqrt{d_c^2 - r_c^2})/ r_c) \tag{2.73}$$

hence, $$v_c = \cosh^{-1}(d_c/r_c) \tag{2.74}$$

and for the anode,

$$v_a = \ln((d_a + \sqrt{d_a^2 - r_a^2})/ r_a) \tag{2.75}$$

$$v_a = \cosh^{-1}(d_a/r_a) \tag{2.76}$$

The rate of mass flow across the equiconcentration surface of the anode is given by,

$$J/I = D\int_{s1}^{s2} \partial u/\partial s \, ds \tag{2.77}$$

i.e. the integral becomes, $$\left[u\right]_{u1}^{u2} \tag{2.78}$$

where u_1 and u_2 are values of the mass flux at s_1 and s_2.

since for orthogonality,

$$\partial u/\partial s = -\partial v/\partial r \tag{2.79}$$

The steady state current is given by,

$$i/I = 2\pi nFDC^b/(v_2-v_1) \tag{2.80}$$

When $r_a=r_c$ ($d_a=d_c$) eqn.(2.80) reduces to the symmetric case, eqn.(2.81).

$$i = 2\pi nFDC_O^b/\cosh^{-1}(d/r) \tag{2.81}$$

Equation (2.81) leads to the conclusion that the steady state diffusion current at symmetrical microcylinder anode-cathode devices is dependent on the cylinder radius, r, and the centre to centre separation, d.

Figure 2.12 illustrates an asymmetrical dual microcylinder anode and cathode, where $r_c>r_a$. Analysis of this electrode system for the steady state condition outlined above leads to the following expression for the feedback current.

$$i = \frac{4\pi nFDCl}{\cosh^{-1}(d_a/r_a) + \cosh^{-1}(d_c/r_c)} \tag{2.82}$$

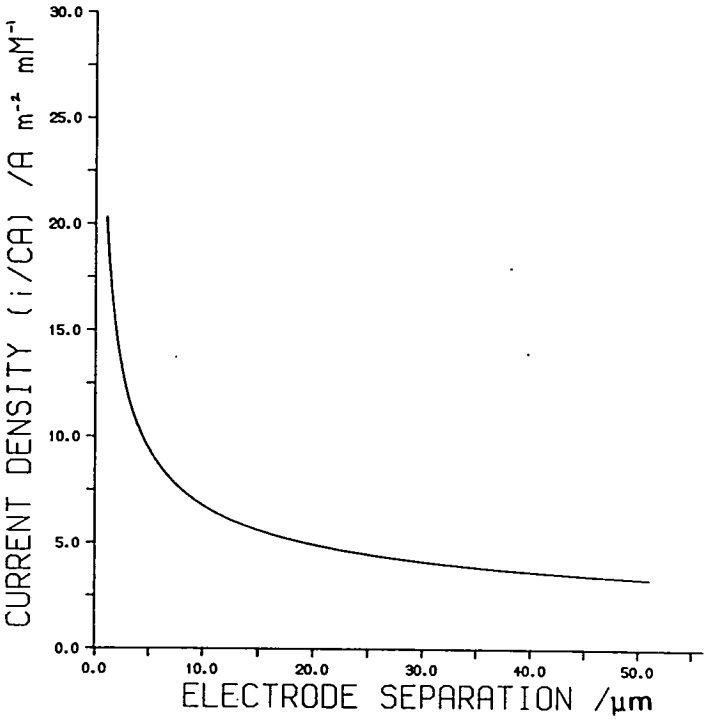

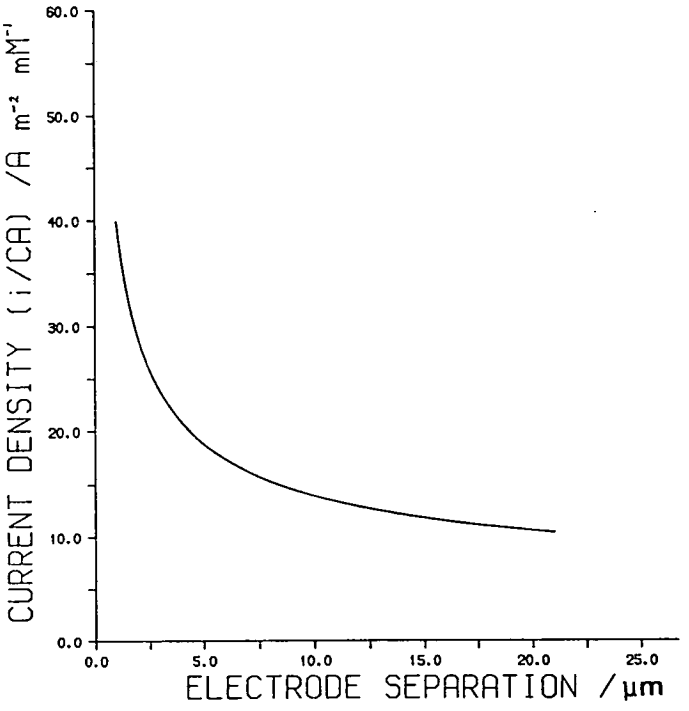

Figure 2.14 Plot of steady state current density against electrode separation (2d) for dual microcylinder anode-cathode devices. a. r=12.5µm, b. r=3.4µm.

Equation (2.82) predicts for the condition $r_c >> r_a$ and $d_c = d_a$ an enhancement of the steady state current with respect to the symmetric system. This effect occurs in response to a shift in the C^b equiconcentration surface to a position closer the anode surface invoking a greater diffusion field strength resulting in higher flux.

2.7 SIMULATION OF CHRONOAMPEROMETRY AT INTERDIGITATED MICROBAND ARRAY ELECTRODES.

This section describes briefly the numerical computation of the diffusion current-time characteristic for regular large scale microband array electrodes under different operating conditions, i.e. the interdigitated microband device operated as a ensemble of microbands at a common applied potential and as an alternate series of anodes and cathodes.

The method involves simulation of the concentration field in the solution region above the electrode system. From the concentration profiles at the electrode surface, the mass flux for a given species at any instant can be calculated, and hence current-time data.

An explicit finite difference method is used with uniform rectangular space and time co-ordinates in order to compute two dimensional diffusional transport to the microscopic electrode assembly, subject to grid boundary conditions. All programs were written in standard Fortran and executed on the mainframe computer at Edinburgh University Computer Service, see appendix 2. Two dimensional concentration profiles were plotted by mean of a Symvu graphics package (EUCS).

Chronoamperometry at an isolated microband electrode was used to verify the accuracy of the simulation model before application to microband arrays.

The diffusion to a microband electrode may be expressed by the two dimensional Fick equation in cartesian co-ordinates;

$$\frac{\partial C}{\partial t} = D\left[\frac{\partial^2 C}{\partial x^2} + \frac{\partial^2 C}{\partial y^2}\right] \qquad (2.83)$$

The difference equation is derived by Taylor expansion of concentration C, along a given co-ordinate, refer to fig. 2.15.

For the x co-ordinate,

$$C = C_0 + (\partial C/\partial x)_0(x-x_0) + 1/2!(\partial C^2/\partial x^2)_0(x-x_0)^2 + 1/3!(\partial C^3/\partial x^3)_0(x-x_0)^3 + \ldots \quad (2.84)$$

Hence the transformation for $\partial^2C/\partial x^2$ to a difference equation, neglecting terms of power 3 or more in eqn.(2.84).

$$\partial^2C/\partial x^2 = 1/\Delta x^2(C_1^t + C_3^t - 2C_0^t) \quad (2.85)$$

and in y,

$$\partial^2C/\partial y^2 = 1/\Delta y^2(C_2^t + C_4^t - 2C_0^t) \quad (2.86)$$

where the superscript, t, indicates the value of the variable, C, at time t.

Noting, $\partial C/\partial t = (C_0^{t+\Delta t} - C_0^t)/\ \Delta t$ (2.87)

For a uniform square grid, $\Delta x = \Delta y$, and the finite difference form of eqn.(2.84) in general notation, x(i) and y(j), is given by,

$$C_{i,j}^{t+\Delta t} = C_{i,j}^t + D\Delta t/\Delta x^2(C_{i-1,\,j}^t + C_{i+1,j}^t + C_{i,j-1}^t + C_{i,j+1}^t - 4C_{i,j}^t) \quad (2.88)$$

where $D\Delta t/\Delta x^2=\lambda$ and was assigned a value 0.25.

By assiging grid values for C at a given time t, it is possible by eqn.(2.83) to compute the value of C at any point in the concentration field at a later time $t+\Delta t$.

The finite difference expression approximates the partial differential equation (2.83) for small values of the grid parameter Δx.

The electrode current is given by,

$$i = nFDAC^b(\partial C/\partial y)_{y=0} \quad (2.89)$$

where the electrode lies parallel to the x direction and normal to the y co-ordinate, as in fig. 2.16.

For a microband electrode of bandwidth w_e and length l,

$$i = nFDC^b l \int_{x=o}^{x=w_e} (dC/dY)dy/\ \delta \qquad (2.90)$$

by assigning the non-dimensional space increment, $dY = dy/\delta$ (2.91)

where δ is some distance in dimensional space.

The integral term in finite difference notation becomes,

$$\int_{x=0}^{x=w_e} (dC/dY)\ dx = w_e \sum_1^N (\Delta C/\Delta Y)/N \qquad (2.92)$$

where N is the number of volume elements (boxes) covering the electrode. The current at a microband electrode can therefore be computed from the concentration field at the electrode surface at any given time by,

$$i = nFDC^b l w_e/\delta N \sum_1^N \Delta C/\Delta Y \qquad (2.93)$$

2.7.1 ISOLATED MICROBAND ELECTRODE.

Figure 2.16 illustrates the two dimensional space grid used for the simulation of the concentration field at a single microband electrode. The grid system is simplified to account for the smallest repeat pattern (unit cell). In this instance a plane of symmetry is found parallel to the point $w_e/2$, hence figure 2.16 shows the cross-section of one half band and the distance extending above the electrode, the y coordinate and in the plane of the electrode, the x coordinate. Simulation parameters such as grid dimensions and iteration size are given in table 2.4.

2.7.2 MICROBAND ARRAY ELECTRODE.

The unit cell shown in figure 2.16 was modified to simulate converging diffusion fields at close spaced microband electrodes. The modification involved restating the boundary condition in the x coordinate, i.e. for $\delta \geqq w_g/2$, $C_O(w_g/2) < C_O^b$. The simplest repeat pattern for this electrode system includes one half band and one half band gap, however a grid arrangement similar to that in fig. 2.17 was adopted in certain instances, where neighbouring bands are set at a common potential. This grid was informative for the mapping of a complete concentration field within the band gap region but unfortunately doubles the computation amount.

2.7.3 INTERDIGITATED MICROBAND ARRAY ELECTRODES.

The concentration field at a large scale interdigitated microband device can be computed and the corresponding feedback flux simulated for a system as described below. The grid pattern for the interdigitated device is shown in figure 2.17 The unit cell in this case is composed of one half anode and cathode separated by a band gap. This grid, subject to the boundary conditions listed, can only be applied to a system containing both forms of a reversible redox couple present at equiconcentration. This system is computationally the simplest of the feedback simulations to implement. The following assumption are made,

1. Electrolyte contains a reversible redox couple which undergoes the simple electrochemical process, $O + ne \rightleftharpoons R$.

2. O and R species are initially present at equiconcentration.

3. Equality of diffusion coefficients, $D_O=D_R$

4. Current is diffusion controlled, C_O(cathode)=0.

5. The interdigitated device is a regular structure, $w_a=w_c$.

6. The microband array is infinite, $n=\infty$.

7. The bandwidth is much smaller than band length.

8. Existence of a Nernst plane at w_g, where $C_O=C_O^b$.

9. Semi-infinite diffusion in the y coordinate, $C_O^{y\rightarrow\infty}= C_O^b$.

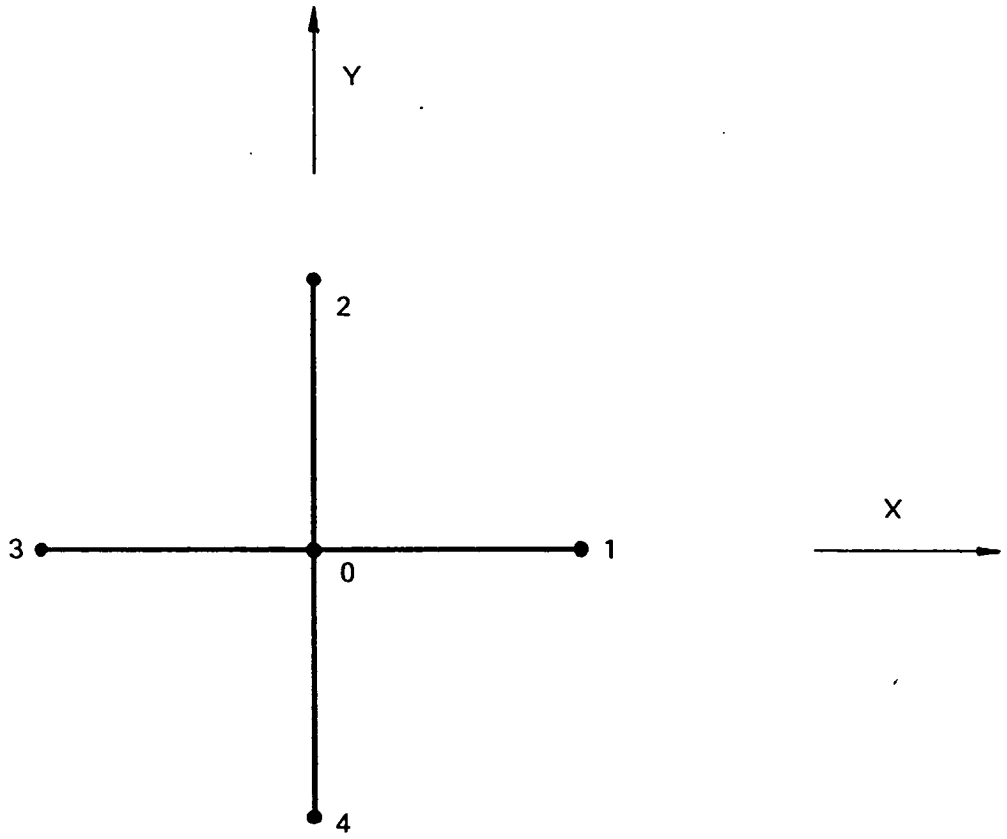

Figure 2.15 Uniform two dimensional square grid.

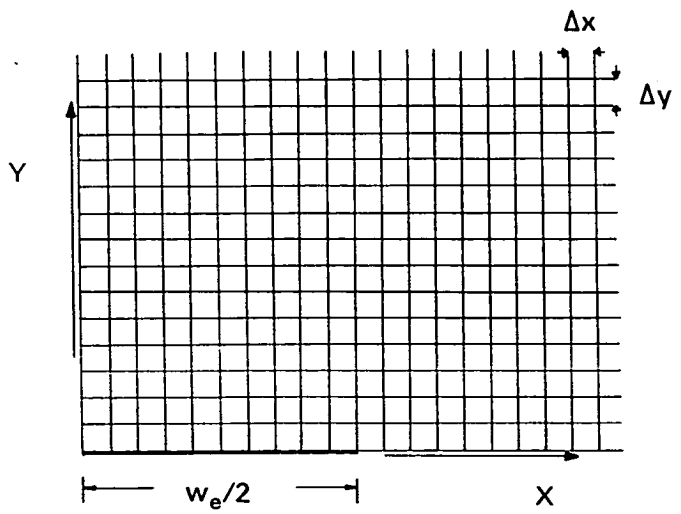

Figure 2.16 Uniform two dimensional space grid for the simulation of the diffusion field at a microband electrode.

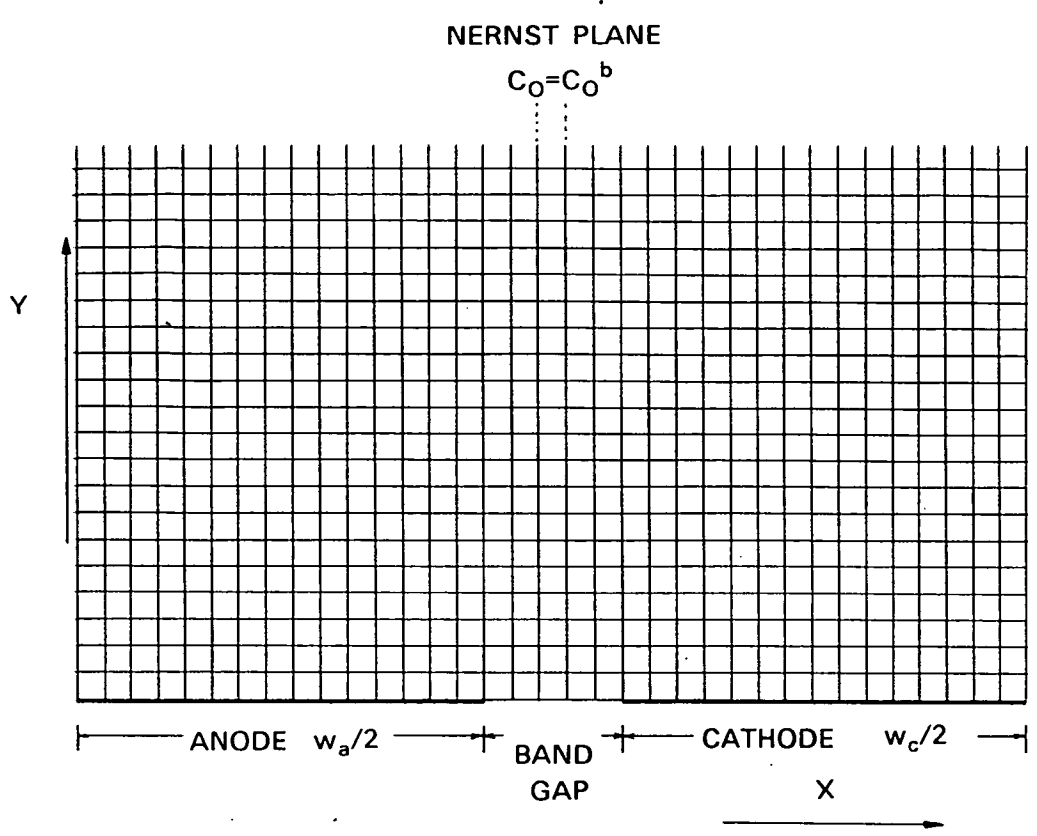

Figure 2.17 Uniform two dimensional space grid for the simulation of the diffusion field at interdigitated microband array electrodes.

TABLE 2.1 THEORETICAL DIFFUSION CURRENT DATA FOR A SUBMICROMETER BAND ELECTRODE USING THE HEMICYLINDRICAL EXPRESSION.

Band length l,mm	Band width w,μm	Area A, mm^2	Current i/C $nAmM^{-1}$	Current density Am^2mM^{-1}	$\theta^{\#}$ t=10s
1.0	1.0	1.0	36.5	36.5	0.0076
1.0	0.5	0.5	32.9	65.8	0.030
1.0	0.1	0.1	26.8	267.6	0.76
1.0	0.05	0.05	24.8	495.3	3.04
1.0	0.01	0.01	21.1	2111.3	76.0

#Taking $D=7.6\times10^{-10}m^2\ s^{-1}$.

TABLE 2.2 DIFFUSION FIELD PARAMETERS FOR SUBMICROSCOPIC BAND ELECTRODES

Band width,w /nm	$\delta(t=10s)$ /nm	δ/w	Nernst surface,S /nm	S/w
50	148	3.0	465	9.3
100	274	2.74	861	8.6

TABLE 2.3 COMPARISON OF APPROXIMATE EQUATIONS FOR THE STEADY STATE CURRENT AT INTERDIGITATED MICROBAND ARRAY ELECTRODES OF MICROMETER SCALE BANDWIDTH.

w_e /μm	w_g /μm	w_e/w_g	i/C^1 /nAmM^{-1}	i/C^2 /nAmM^{-1}	% DIFF.
3.0	2.0	1.5	96.4	110.9	-13.1
10.0	2.0	5.0	152.2	167.1	-8.9
50.0	2.0	25.0	242.7	257.8	-5.9
100.0	2.0	50.0	284.1	299.2	-5.0
100.0	0.5	200.0	368.3	383.5	-4.0
100.0	0.1	1000	466.9	482.1	-3.2
95.0	18.0	5.3	155.0	170.0	-8.8

Data calculated from eqn.(2.62) (1),and eqn.(2.64) (2),taking $D=10\times10^{-10}m^2\ s^{-1}$, n=1, C=1mM, l=1mm and m=10.

	λ	NUMBER OF BOXES (J)	J(MAX) /μm	NUMBER OF BOXES (I)	I(MAX) /μm	dx,dy /μm	ELECTRODE BOXES	TIME ITERATIONS	SIMULATION TIME /s
SINGLE BAND	0.25	151	238.6	151	238.6	1.58	30	10^4	8.2
MICROBAND ARRAY	0.25	121	191.2	variable	variable	1.58	30	10^4	8.2
INTERDIGITATED ANODE-CATHODE	0.25	201	317.6	variable	variable	1.58	30	10^4	8.2

TABLE 2.4 GRID PARAMETERS FOR THE SIMULATION OF CHRONOAMPEROMETRY AT LARGE SCALE INTERDIGITATED MICROBAND ARRAY ELECTRODES.

CHAPTER 3

MICROELECTRODE FABRICATION

3.1 FABRICATION OF THE INTERDIGITATED MICROBAND ARRAY ELECTRODES.

The interdigitated microband device was constructed using standard optical lithographic methodology. The microfabrication process, as outlined below and illustrated in figure 3.1, involves the following stages:

a. mask design and fabrication providing a two dimensional microscopic pattern with appropriate size specifications.

b. thin film metal deposition.

c. photoresist and metal etching techniques.

Cleaned silicon wafers (0.25mm-0.50mm thickness, 76.2mm dia.) were oxidised in an oxygen atmosphere with the formation of a SiO_2 layer less than 1μm thickness. The oxide film provides insulation between the electrodes and the silicon support. Two forms of device sublayer were used in fabrication, they included, chromium and polyimide. The criteria for use was based on $Au/SiO_2/Si$ adhesion characteristics in addition to suitable electrical and chemical properties. A cyclic voltammetry study was carried out on the anodic behaviour of vacuum deposited gold electrodes with Cr sublayer using an aqueous KCl solution at pH=3. These electrodes performed identically to solid gold electrodes with the onset of oxidation occurring at ca. +0.8V vs. SCE; potential sweeps beyond +1.0V generated a passivating black film of gold oxides.

A chromium thin film, ca. 10nm was applied via vacuum deposition while devices based on polyimide relied on spin coating for a uniform submicrometer insulation/adhesion film.

Interdigitated microband devices were defined on such preconditioned wafers with high feature uniformity and accuracy. Gold of ca. 100nm film thickness was vacuum deposited at 10-20Å s^{-1} onto a polyimide or chromium Si coated wafer. The gold film was then spin coated at 3000rpm for 30s with filtered

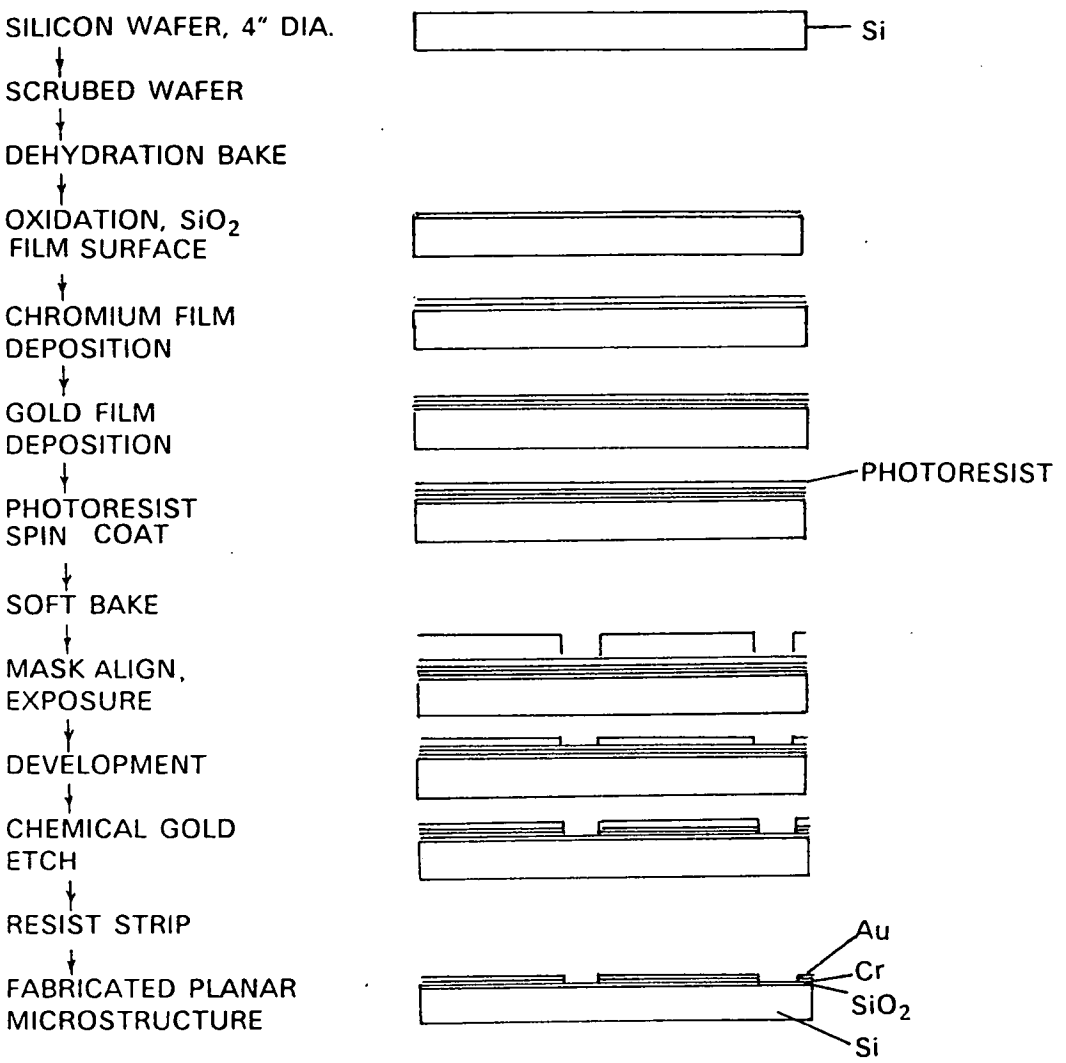

Figure 3.1 Photolithographic process for microfibrication of the interdigitated band electrodes.

negative photoresist to produce a cover of less than 1μm. The wafer then underwent a pre-exposure bake at 90 °C for 20min. in order to temporarily secure the resist layer.

A negative emulsion mask was used in this work with a total size of 62.5mm x 62.5mm, and designed with specific device dimensions of band length, width and number, in addition to electrode spacing and overall device area. The mask described here had a capacity for 20 devices per wafer. The mask was aligned onto a treated wafer prior to exposure with near u.v. radiation at 3.8W m^{-2} for 2.1s. This treatment rendered exposed resist chemically unstable to certain solvents. The wafer was then developed in toluene for 45s followed by n-butyl acetate for 45s to remove exposed resist. This was followed by air drying. The device pattern was made by a wet chemical etch process to remove exposed metal e.g. aqueous I_2, KI etchant. The remaining photoresist was dissoved from the gold sublayer by toluene, n-butyl acetate developer.

Each wafer was sectioned manually using a diamond scriber. Specific dimensions of the interdigitated device such as bandwidth and band gap, illustrated in figures 3.2-3.4, were determined by scanning electron microscopy and found to be equal to, 95.0±1.0μm and 18.0±1.0μm respectively. A list of device dimensions can be found in table 3.1. Devices were examined by optical microscopy before use for electrode quality is viz surface markings and deformations including metal bridging. A single severed band within the array can introduce as much as 10% error the in estimation of the electrode area. The resistance between electrodes for working devices ranged from 20MΩ to 124MΩ depending on the fabrication process conditions (SiO_2, polyimide thickness etc). Suitable devices were then mounted as outlined below. The voltammetric response of each electrode was measured to provide a useful and expedient indication for certain abnormal characteristics indiscernible by visible inspection, such as partial resist covering.

3.2 INTERDIGITATED DEVICE MOUNTING.

Electrode mounting formats used to study the electrochemical performance of the amperometric interdigitated device allowed some flexibility in operating conditions, such as electrode configuration and cell volume. Figure 3.5 illustrates a convenient device mounting, incorporating several features, including isolation of microelectrodes and ancillary electrical connections,

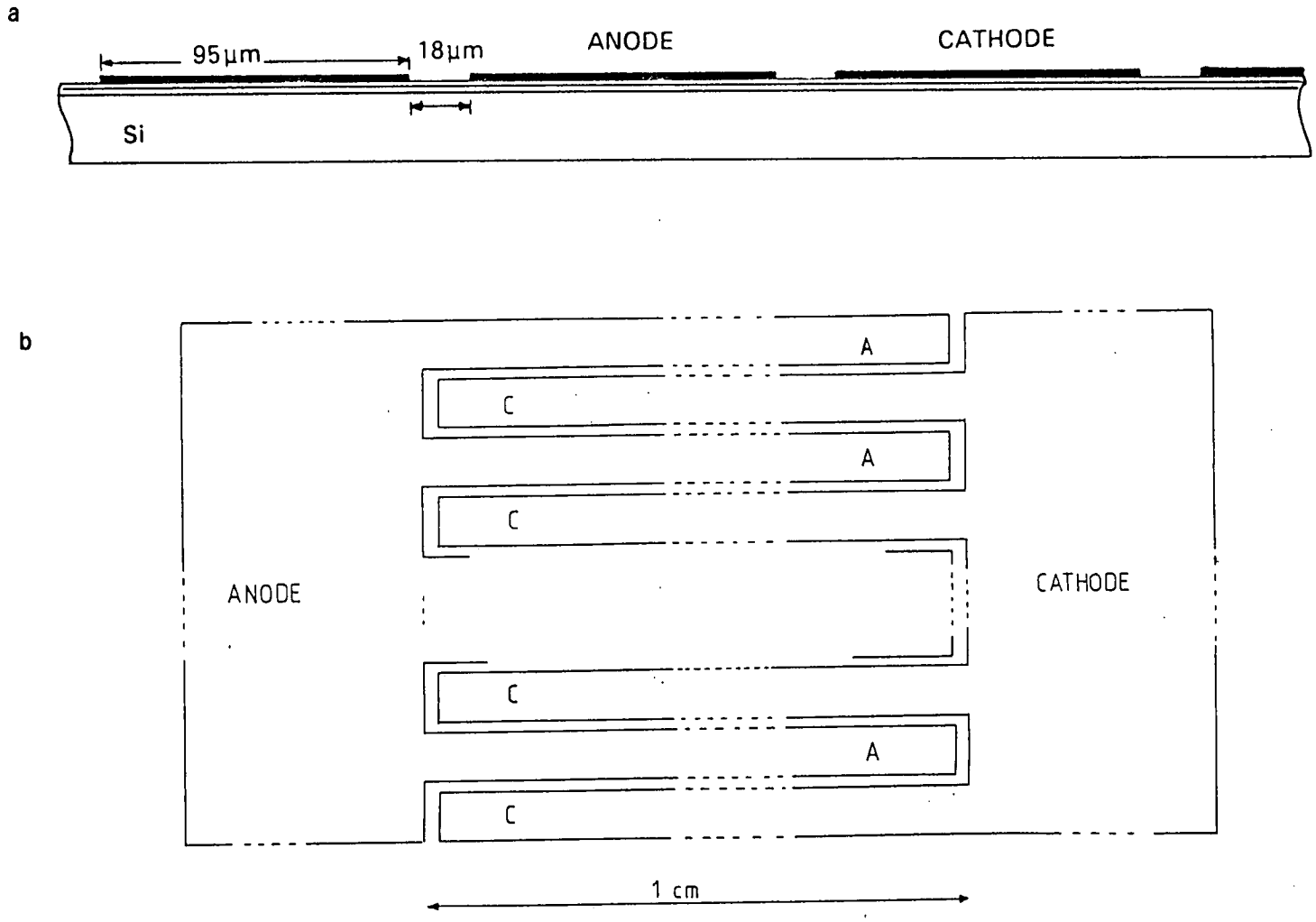

Figure 3.2 Interdigitated microband array electrodes.

a. Cross-sectional view showing part of the array structure and silicon support.

b. face view of the device illustrating the interdigitated design.

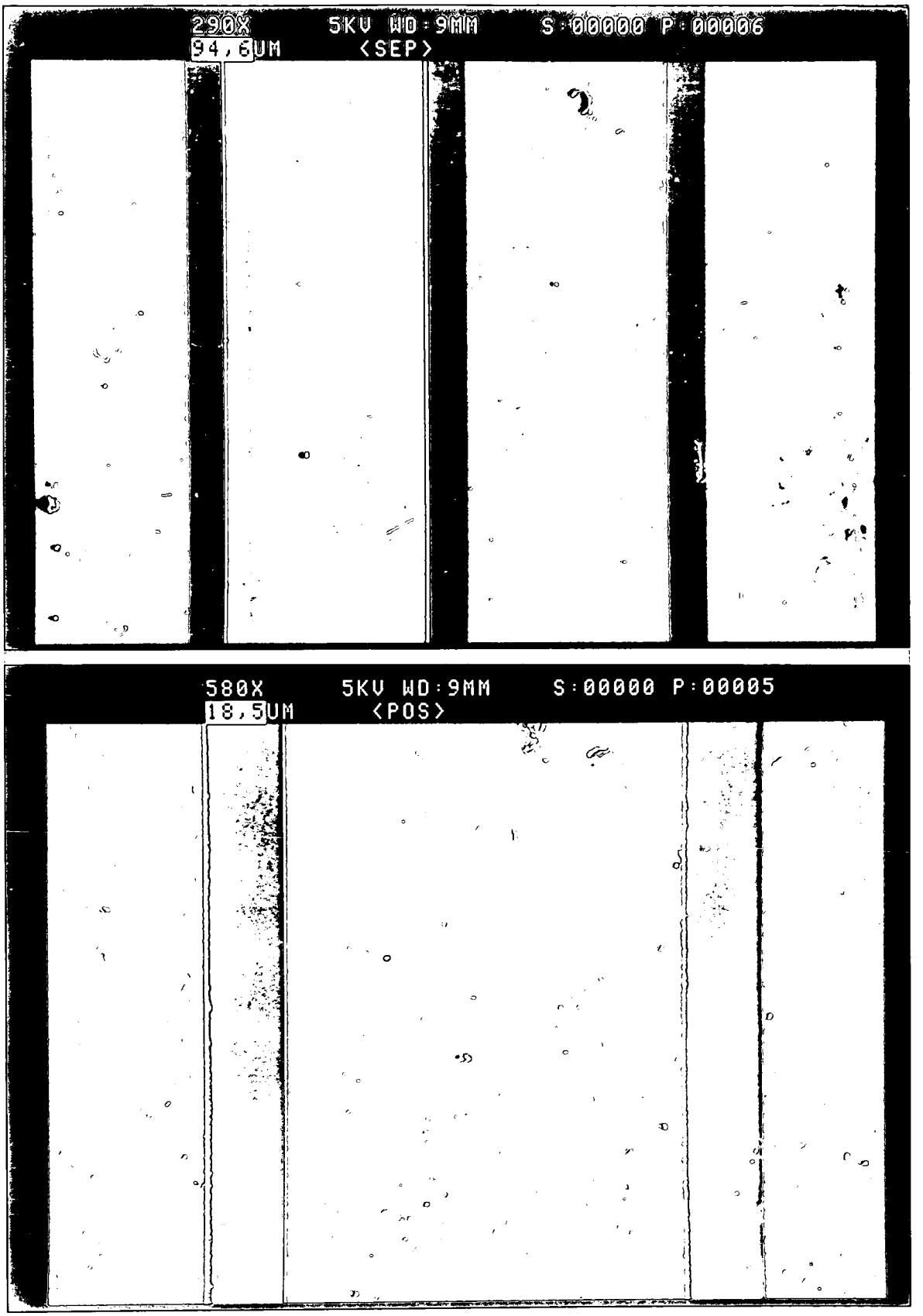

Figure 3.3 Electron micrographs of interdigitated microband array electrodes showing bandwidth and band gap dimensions.

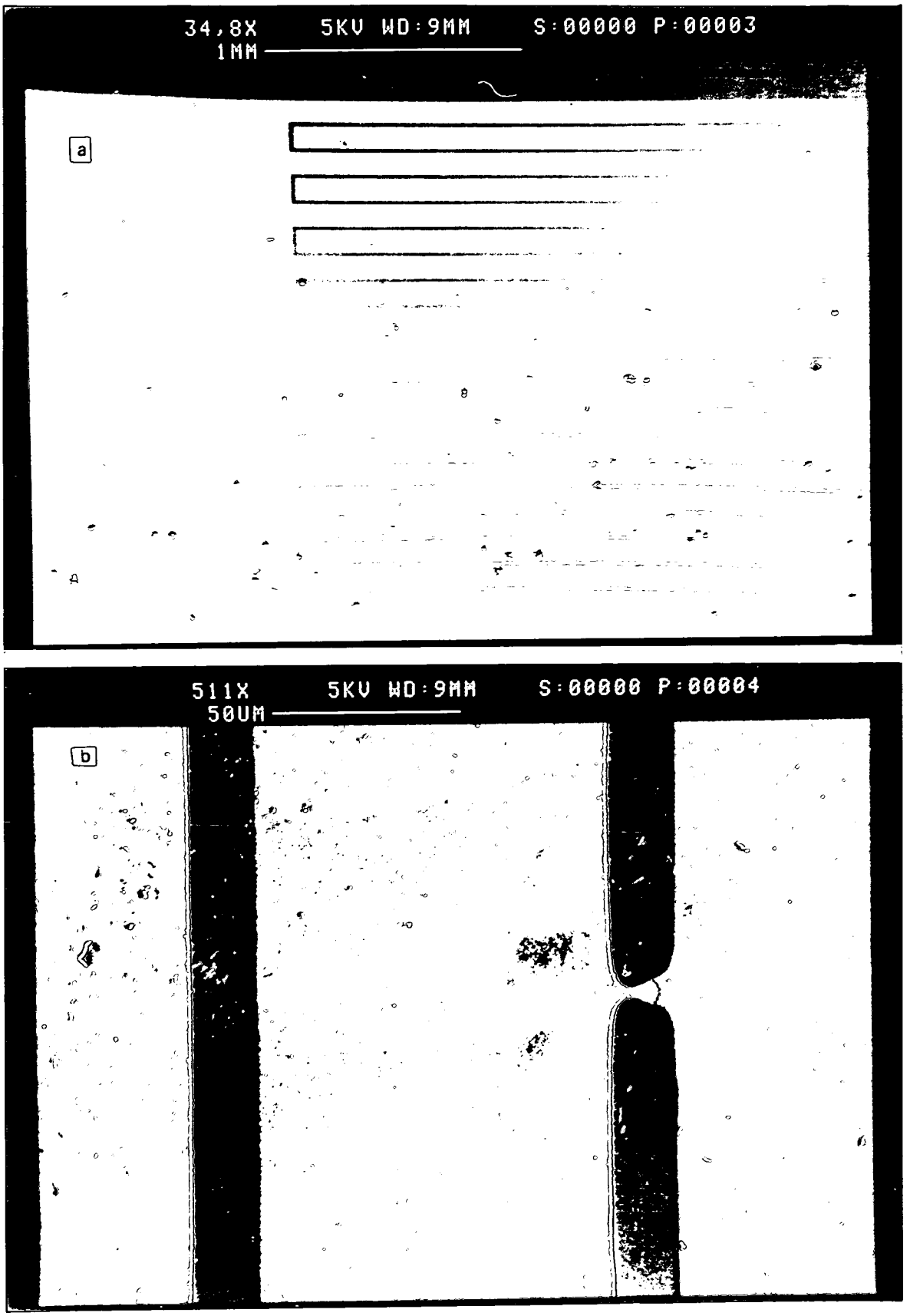

Figure 3.4 a. Electron micrograph of the interdigitated electrodes illustrating device end structure.

b. Bridging fault arising from lithographic processing

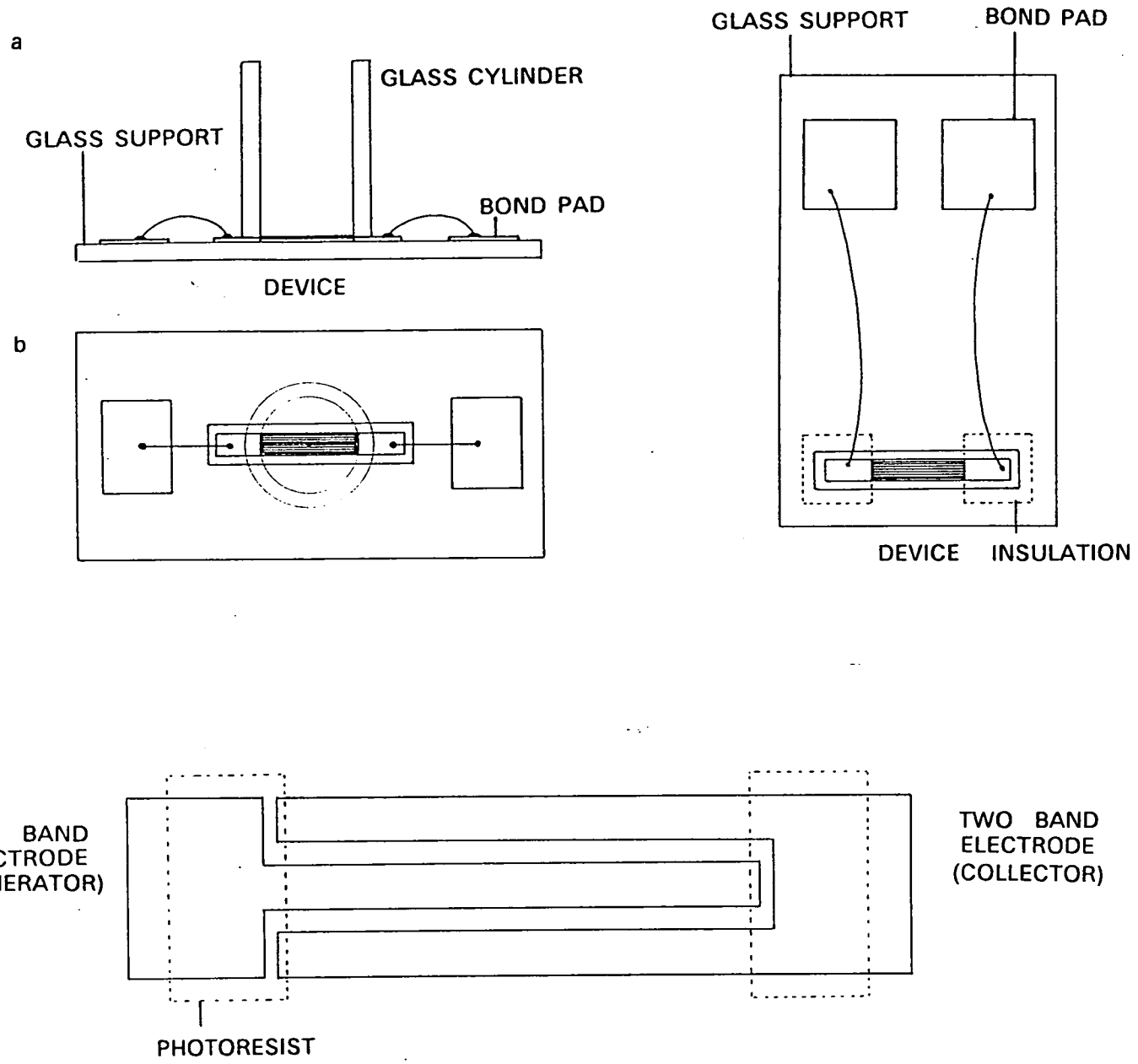

Figure 3.5 Cylindrical cell mounting for the interdigitated device. a. side view b. top view.

Figure 3.6 Interdigitated microband array electrodes mounted on a microscope slide.

Figure 3.7 A triple band interdigitated device illustrating a photolithographic insulation process.

together with an integrated cell housing. A single chip measuring 5mm x 22mm, and holding one interdigitated device was cleaned in the following solvent series: water, acetone and iso-propanol, to remove grease and other surface contamination, prior to fixing onto a clean microscope slide (25mm x 100mm).

The chip was bonded to the glass support with an epoxy resin or a silicone rubber sealant. At each side of the chip a gold plated Cu bond pad was positioned. Device bond pads were then insulated in the region nearest to the band array using insulating varnish or silicone rubber sealant. This insulation procedure was gauged by eye: on microscopic examination the inadequacy of this manual operation was apparent, leading to errors in electroactive area of the order of ±5%. An open ended glass cylinder with internal diameter 1.2mm was placed over the microelectrode region such that the band array was centralised over the tube as shown in figure 3.5. This arrangement was then made water tight with silicone sealant. Electrical connection was made from the exposed device bond pad to the external pad areas using silver conducting paint. This was then followed by a mild bake at 90°C for two hours.

This arrangement was found convenient for low volume electrochemistry i.e. 0.2ml of sample could be handled even when using additional reference and counter electrodes.

A further mounting procedure for the laboratory operation is illustrated in figure 3.6. In this arrangement the device was mounted onto a glass flat and the bond pad areas insulated as previously described, leaving the microband array exposed. The method does not include a mounted cell and thus larger electrolyte volume is required, typically greater than 10ml in amperometric experiments.

3.3 FURTHER DEVELOPMENT OF THE AMPEROMETRIC INTERDIGITATED MICROBAND ARRAY DEVICE.

The main problems associated with the amperometric testing of the present interdigitated device have been recognised. The inclusion of an interdigitated end structure, as illustrated in figure 3.2, limits the horizontal overlap of neighbouring bands to $l-2w_g$ per anode-cathode band pair. This results in a total "end error" of $20w_g$ i.e. 360µm: however this is insignificant considering

the total band length ,l, per electrode of 100mm. A much improved band array insulation procedure is depicted in figure 3.7, this could be secured by photolithographic processing a resist pattern around the microband structure. This procedure would mean accurate determination of band length, eliminating anomalies owing to interdigitated end structure with the present device. Additionally, the inclusion of a further photoresist step in the microlithography could also include isolation of bond pads allowing interdigitated devices to be used on the wafer.

The presence of a finite number of anodes and cathodes, here $n_a=n_c=10$, incorporates an edge error whereby the process of feedback diffusion is modified from the ideal case of $n_a=n_c=\infty$, which is the theoretical assumption dealt with in chapter 2. Miniturisation of the interdigitated device would allow for large values in n, reducing the effects of this asymmetry.

Although interdigitated microband devices have been fabricated almost entirely as a regular pattern, where $w_a=w_c$, it is possible to design devices with non-uniform geometry to include a collector bandwidth larger than the generator, and in so doing optimise collection efficiency and, where appropriate, the feedback current [18]. However, certain operational effects could arise from a larger collector surface such as higher background current owing to the diffusion of redox interferents from the collector to the generator.

To the present time, interdigitated microband array electrodes used in electrochemical studies have relied on established microfabrication technology. Optical lithography is particularly suitable for construction of planar structures of microscopic dimension in a controlled manner with high accuracy, uniformity and reproducibility. Interdigitated microband devices with bandwidth and band gap features ranging from 2μm to 100μm have been used almost exclusively in feedback amperometry.

Attempts have been made to reduce device features particularly the band gap to the submicoscopic scale by electroplating Pt onto prefabricated interdigitated gold electrodes. However the plating procedure used was not amenable to controlled microfabrication owing to non-uniform current distribution at the band edge which generated a thick Pt deposition, although a submicron band gap was achieved [16].

Coplanarity of the anode and cathode bands need not be the rule. It has been recently shown that optical lithography can be used to fabricate a non-coplanar device with micrometer size bandwidth and 0.5µm band gap [40]. An undulating interdigitated microband array electrode consists of a series of coplanar microanodes and a similar series of microcathodes separated by a vertical distance, h: where h can be controlled using photoresist technology from 0.2µm to several micrometers. Using chemical vapour deposition or sputter deposition methods insulation thicknesses below 0.1µm are envisaged. Such methodology would allow micron scale band electrodes to be positioned accurately with a submicron spacing.

The submicroscopic interdigitated device, where the bandwidth/gap features are typically less than 0.5µm, can be approached from available planar technology. X-ray[43] and electron beam[44,45] lithographies are capable of feature definition on the nanometer scale. Current communications in this area suggest that interdigitated microband array devices could be fabricated with a bandwidth 100nm and band gap 50nm or less. At such feature dimensions overall device size could then be reduced to low micron or even submicrometer scale.

Interdigitated microband electrodes have been fabricated in dual and triple band format using laminate techniques [20]. The method although inexpensive is not easily controlled in terms of feature uniformity. However, the technique in the form of a thin laminate mounting, utilising thin film metal deposition and photoresist techniques, could be more easily applied. The next section deals specifically with the fabrication and characterisation of single band thin laminate electrodes for extension to submicrometer band array devices.

BAND WIDTH w_e /m	BAND GAP w_g /m	BAND LENGTH l /m	BAND HEIGHT /m	NUMBER OF ELECTRODES	NUMBER OF BANDS PER ELECTRODE N_e	NUMBER OF BANDS PER DEVICE N_d	AREA PER BAND /m^2	AREA PER ELECTRODE /m^2	ACTIVE AREA PER DEVICE /m^2	DEVICE WIDTH /m	TOTAL AREA PER DEVICE /m^2	INACTIVE AREA PER DEVICE /m^2
95.0 $\pm 1.0\times10^{-6}$	18.0 $\pm 1.0\times10^{-6}$	10.0×10^{-3}	ca. 150×10^{-9}	2	10	20	0.95×10^{-6}	9.5×10^{-6}	19.0×10^{-6}	2.24×10^{-3}	22.42×10^{-6}	3.45×10^{-6}

Table 3.1 Specifications for the amperometric interdigitated microband device.

3.4 FABRICATION OF THIN LAMINATE SUBMICROMETER BAND ELECTRODES.

Thin films of gold (99.999%m/m), 7nm-100nm, were vacuum evaporated at $1x10^{-6}$mbar onto clean polymer sheets, 5cmx5cm with a thickness ranging from 12µm to 25µm. A 5cm tungsten coil was used as target with a deposition rate less than 0.1nm s^{-1} in order to prevent sample overheating and consequent laminate deformation. Metal film thickness was estimated by a calibrated quartz crystal oscillator. Metallised laminates were then spin coated with photoresist to afford uniform insulation between 1µm and 4µm as required. By judicious selection of spin coating conditions, solvent thinner, spin speed etc. photoresist layers can be applied below 1µm to thin polymer substrates e.g. <0.5µm can be attained with some negative resists at 9000rpm with film uniformity of 1%. The resulting laminate was heat cured at 90 °C for 20 min. This mild bake ensured a stable and resistive insulation suitable for aqueous electrochemical applications. In certain instances a simple mask was constructed from 125µm thickness polyester sheet. This mask was suitable for the fabrication of nine film electrodes 10mm x 15mm and served to locate electrode terminals in single and multiple metal film laminates, see figure 3.8.

Electrical contact with the metal film was achieved by removing the insulator resist covering terminal areas with acetone. Exposed metal film was coated with silver conducting paint. The terminal was then sufficiently robust to take a metal pad and crocodile clip. A band electrode of submicrometer dimension was made from such metallised laminate films by surgical blade sectioning.

Nanometer films of gold evaporated under high vacuum onto thin polyester substrates show similar resistive behaviour to silicon supported thin films. Figure 3.9 illustrates how film resistance of a polyester based laminate becomes considerable below 10nm film thickness and for films greater than 60nm there is negligible resistance. Gold film laminates based on polyester and polyimide were found to be robust with good flexibility. These composite materials were stable to shearing by the action of a blade i.e. the laminates appeared to have an intact metal-insulator edge on microscopic examination. Electrode reproducibility however, was found to depend on cutting action, which includes blade size and cutting angle. A considerable reduction in edge burring was found for laminates sectioned from the support side.

Scanning electron microscopy revealed the surface effects of laminate

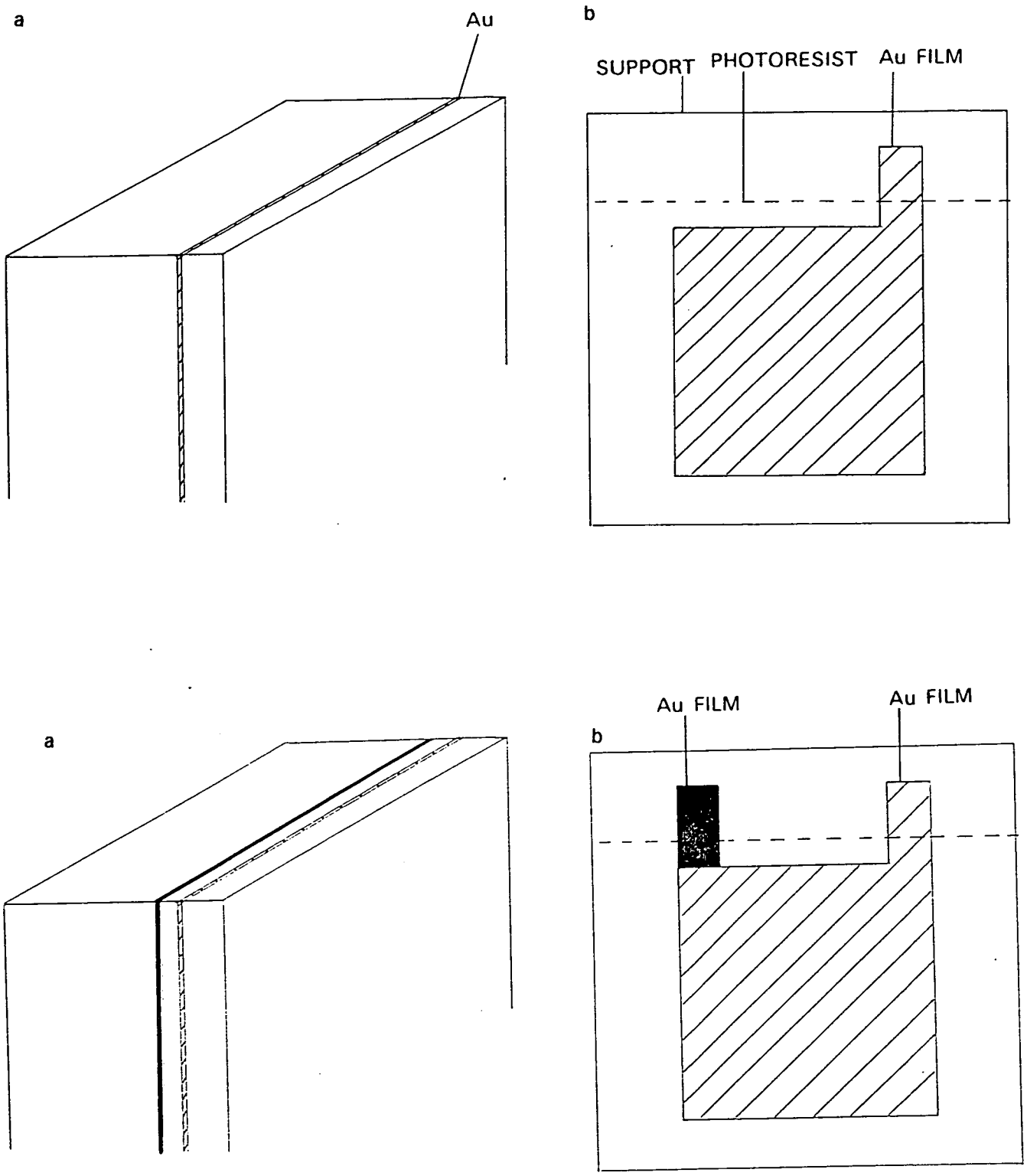

Figure 3.8 Structure of the thin film laminate (single and dual metal film)

a. side view of a polyester-gold film (0.1µm)-photoresist (1µm) laminate

b. face view showing the extent of the metal film, photoresist and electrical contact areas.

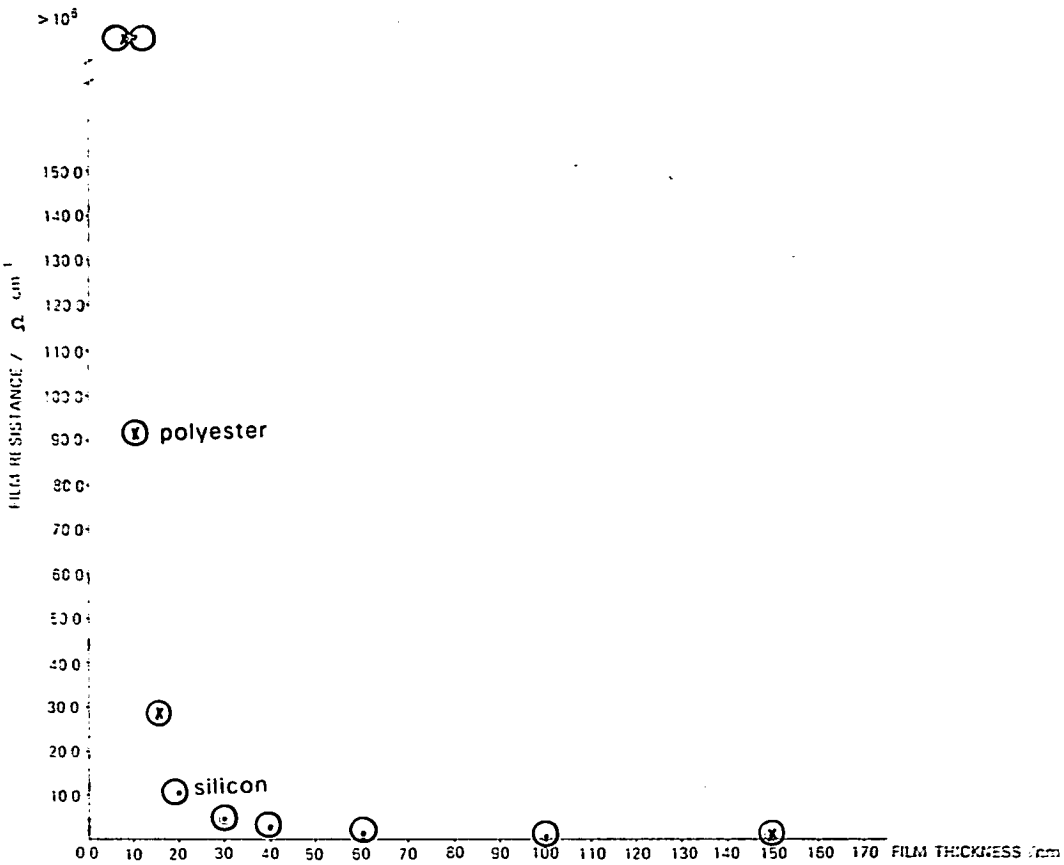

Figure 3.9 Plot of gold film resistance against film thickness for gold- polyester and gold-silicon laminates. For Au film on Si support the metal was deposited at a rate 0.5 A s^{-1}, p=10^{-3} torr.

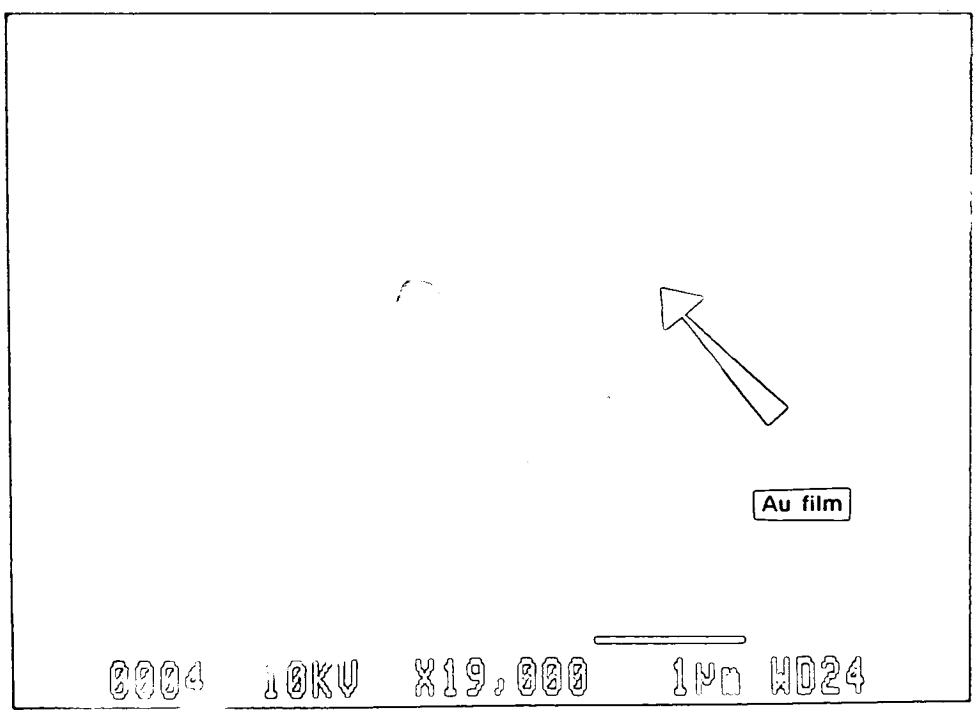

Figure 3.10 Electron micrograph of the photoresist edge of a polyimide-gold -photoresist(+ve) laminate. The resist was spin coated for film thickness less than 1µm; with a support thickness of 25µm.

sectioning. For both types of support laminates the striated nature of the material prevented clear identification of the metal film. Figure 3.10 shows the photoresist edge of one metallised polyester laminate with nominal metal film thickness 100nm. The region demarking the support-insulator boundary appears grooved. At x19000 magnification this depressed line structure appears uniform and approximately 150nm wide for 100nm metal film thickness with a 1μm photoresist surface. In general SEM examination of laminate boundary edge was inconclusive for thin films untreated by etching procedures, although a clear boundary between insulation layers was observed. The microscopic study did reveal abundant surface debris at the electrode face, possibly artefacts of the sectioning process.

Sectioned gold film laminates, insulated by a micrometer thickness photoresist are suitable for use as submicrometer band electrodes in amperometry. This aspect is discussed further in chapter 5. Insulating photoresist films ($10^6\Omega$) can be applied with submicrometer thickness as mentioned above. This feature has currently found importance as a possible fabrication route for submicrometer dual (or array) band electrodes. However, the risk of pinhole effects at this dimension is a major fabrication problem becoming more apparent for multi-metal film laminates, clean room facilities then become necessary. The density of micrometer pinholes can be minimised in various ways including reduction of total metal film coverage, pinhole etching or use of multiple polymer layers.

3.5 FABRICATION OF DUAL MICROCYLINDER ELECTRODES.

Parallel arrangements of dual platinum wire, r=12.5μm and carbon fibre, r=3.4μm, electrodes were constructed by microscopic manipulation using conventional light microscopy and micrometer needles (50μm dia.). The micrometer scale wires were positioned in a parallel coplanar geometry, extending across a slit (1mm x 4-10mm) cut into a polyester support with several micrometer spacing between wires. In this design, the slit size defined the electrode length. A dual microcylinder device is illustrated in figure 3.11 showing the important dimensional parameters for a symmetric device. Electrode positioning and insulation was effected using semi-cured epoxy resin. It was found that applying the resin in this manner reducted flow along the wire and within the microscopic gap, hence preventing partial electrode blockage.

Electrical contact was made to individual wires and bond pads sited above the electrode assembly using silver conducting paint. Epoxy resin and conducting paint was cured at low temperature ca. 40°C, owing to differences in thermal expansion coefficients of the various materials involved in the fabrication. A high temperature treatment (T >90°C), resulted in permanent wire deformation with poor device uniformity. Insulation of wire endings could be made by this technique to good precision resulting in devices of known length to 50μm. The electrical resistance between wires was typically several MΩ.

Electrode separation was determined using optical microscopy at high magnification fitted with a calibrated vernier eye piece (graticule 50 x 2μm). Several measurements for interelectrode separation were taken along the length of the wire system; it was found that spacing uniformity could be controlled to better than 4μm. From a series of five measurements an average inter-electrode spacing was calculated (cf. table 3.3.). Such values were used in calculations of the theoretical diffusion current at dual microcylinder anode-cathode devices.

Platinum devices were washed in a water/acetone/isopropyl alcohol solvent series and examined by optical microscopy for imperfections, particularly the quality of the insulation. Preliminary characterisation by cyclic voltammetry as shown in figure 3.12 was convenient for highlighting structural abnormalities.

Carbon fibre electrodes were electrolytically preconditioned before application. Such treatments have been mentioned elsewhere [29]. The treatment given here involved sweeping the potential from 0.0V to +1.5V vs. SCE in a 0.2M Na_2HPO_4/NaH_2PO_4 electrolyte (pH 7.0), as shown in fig. 5.13. This anodic treatment was essential for the generation of reversible voltammetric behaviour of redox species such as ferrocene carboxylic acid, see fig. 5.14, and catechol.

3.6 DEVELOPMENT OF MICROCYLINDER ARRAY ELECTRODES.

The method of fabrication described here for a dual microcylinder device where the wires are held taut across a millimeter slit is of limited scope for the construction of well defined microcylinder array electrodes. The development of the interdigitated microcylinder array device will require the application of advanced three dimensional engineering on a microscopic scale with similar precision to that of contemporary planar technology. However, the current method proposed is suitable for the construction of individual dual microwire probes which may which may find use for in vivo "feedback" amperometric studies: more is said about the possible applications of this device in chapter 6.

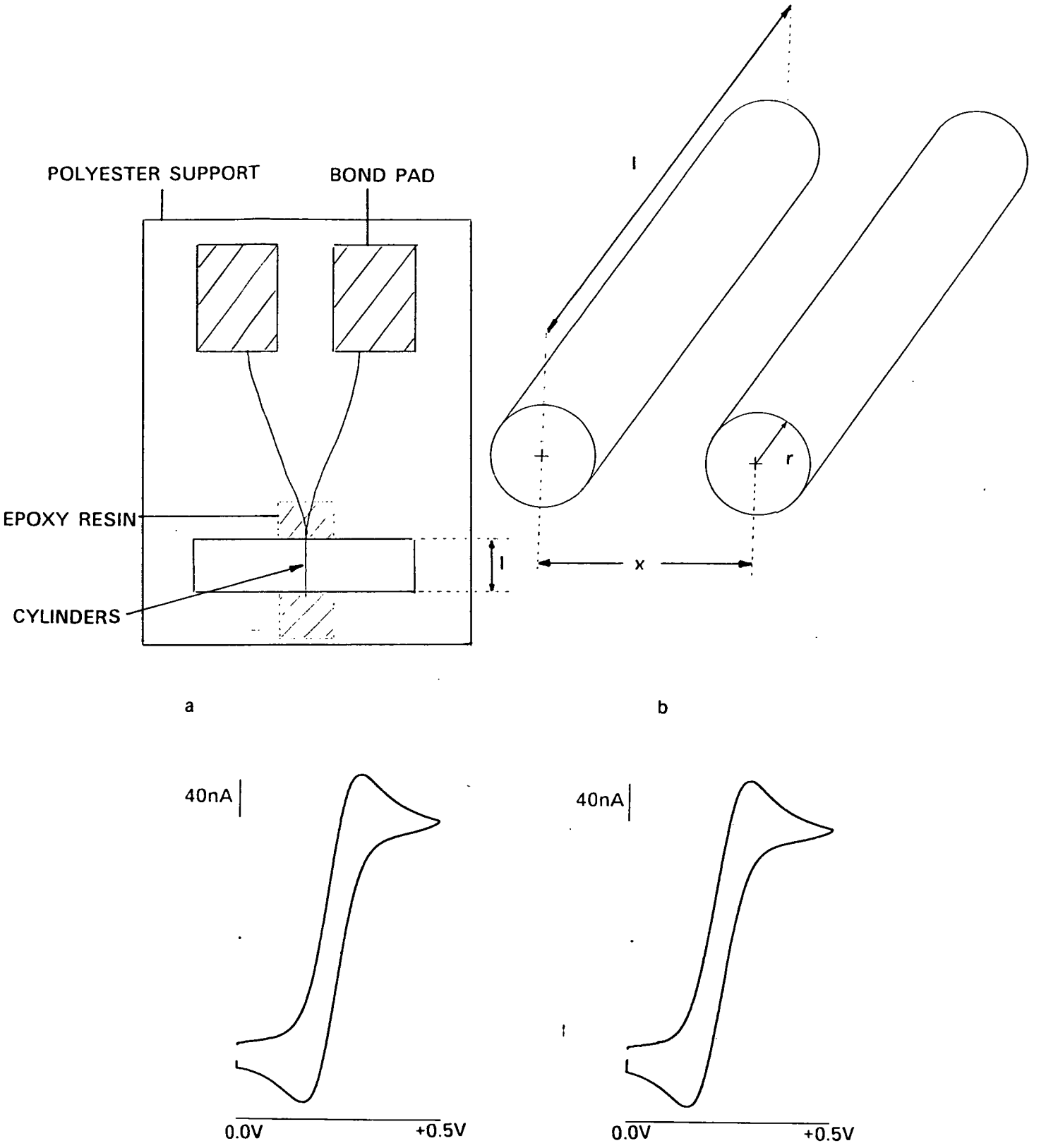

Figure 3.11 Mounting strategy for the dual microcylinder electrodes. Inset; dimensions of parallel coplanar wires.

Figure 3.12 Cyclic voltammetry of ferri/ferrocyanide (1mM) in KCl (1M) solution at Pt dual microcylinder electrodes. a. electrode 1, b. electrode 2.

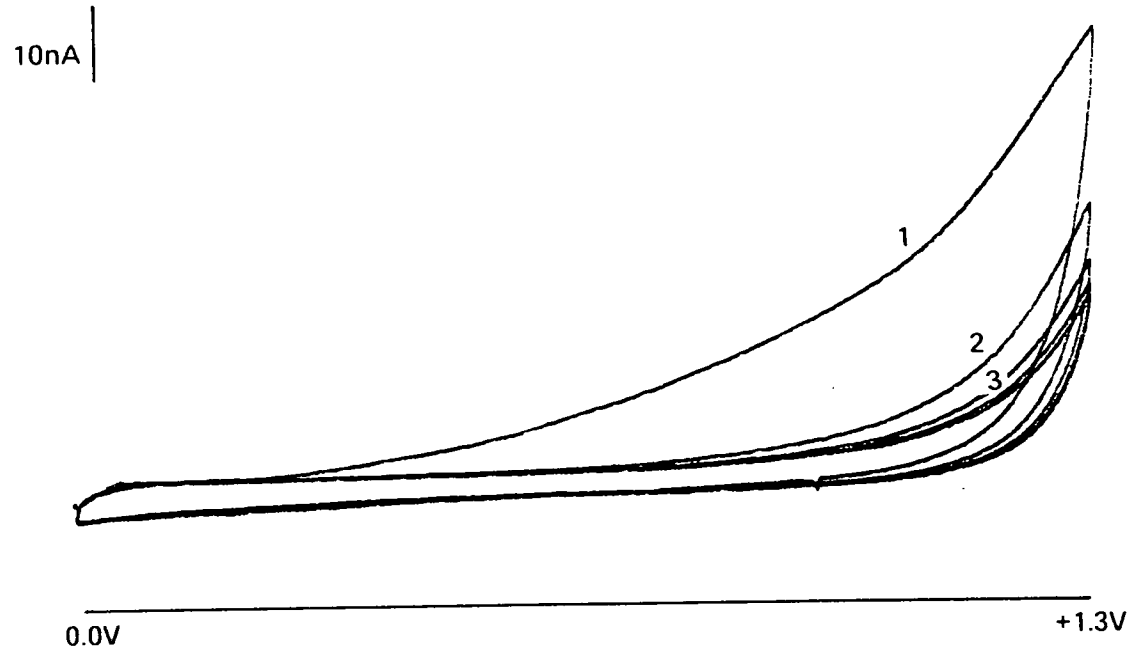

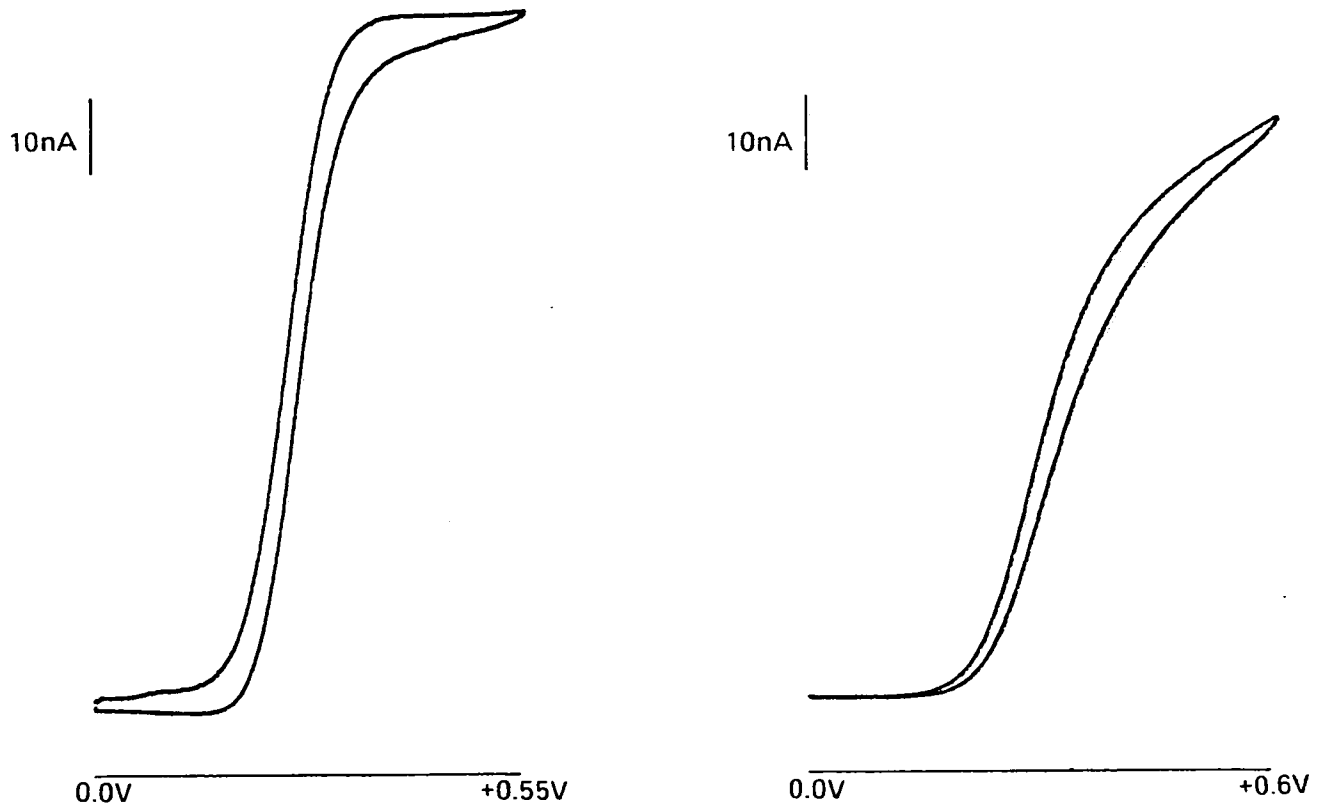

Figure 3.13 Anodic conditioning of a carbon fibre electrode. Cyclic voltammetry of aqueous NaH_2PO_4, Na_2HPO_4 (0.2M,pH=7), potential sweep from 0.0V to +1.3V vs. SCE, v=100mV s^{-1}, showing repeat scan cycles 1,2,3, etc.

Figure 3.14 Cyclic voltammetry of ferrocene carboxylic acid (0.66mM) in aqueous NaH_2PO_4 . ,Na_2HPO_4 (0.2M,pH=7) at a carbon fibre electrode, r=3.4 µm l=1.8mm. a. anodic preconditioned carbon fibre, potential sweep 0.0V to +0.55V vs. SCE, v=10mV s^{-1}. b. carbon fibre without conditioning.

TABLE 3.2 DIMENSIONS OF DUAL MICROCYLINDER ELECTRODES.

ELECTRODE MATERIAL/CODE	ELECTRODE LENGTH /μm	ELECTRODE RADIUS /μm	ELECTRODE SEPARATION /μm
Platinum PT1	10.0	12.5	25
Platinum PT2	0.65	12.5	36.3
Platinum PT3	0.60	12.5	2.7
Platinum PT4	1.8	12.5	14.0
Platinum PT5	0.55	12.5	13.5
Carbon C1	1.0	3.4	7
Carbon C2	1.0	3.4	17

CHAPTER 4

CELL ARRANGEMENT AND INSTRUMENTATION.

4.1 GENERAL CONSIDERATIONS.

The operational characteristics of an electrochemical cell consisting of an arrangement of microelectrodes for use as a microsensor or assay microdetector for the determination of redox species at low concentration (<μM) is of principle concern here. Planar microfabrication technology allow for a precise and reproducible cell format to be achieved on the microscopic scale. Therefore the potential exists for the design of microcells with well characterised properties. Detector response parameters such as the response time, sensitivity and the level of background current are linked to the electrode configuration. Moreover, accuracy and precision of the amperometric measurement are dependent on the cell performance.

The current response, as a function of time or applied potential for an electrochemical cell containing an electrochemically reversible redox species, where convection is reduced by short time measurement in quiescent solution, and electrical conduction (migration) of analyte is minimised by the presence of a large excess (>100X) of an inert electrolyte, is then dependent on the diffusion mass transport. The following cell parameters are important:

a. area of working electrode: the magnitude of the current is a function of electroactive area. For macroscopic electrodes there is direct proportionality between the diffusion current and electrode area. However, for microelectrodes the current is a more complex function of the electrode dimensions, and is influenced by geometrical form.

b. working electrode geometry: for macroscopic electrodes, the form of the current-time transient is independent of geometry. As the dimension of the electrode approaches that of the diffusion field however, the current then becomes a function of the electrode geometry.

c. cell geometry: the arrangement of electrodes within the cell has fundamental affects on the current response. This is particularly important for

cells composed of microanodes and cathodes arranged with a microscropic separation. The current-time transient of such cells is then determined by the spacial distribution of the microelectrodes.

In constant potential experiments, the uncompensated resistance (R_u) affects both the current and electric potential distributions within the cell. Furthermore, the cell time response is also dependent on the magnitude of R_u. Experimentation with macroscopic electrodes have traditionally employed Haber-Luggin probe techniques to reduce uncompensated resistance effects. More recently, and especially in interfacial liquid-liquid electrochemistry, electronic methods of dealing with cell resistance have been used. However, for experiments utilising microelectrodes, including ensembles, the measured current is typically submicroamp and hence the effects of uncompensated resistance within such cells are less important.

d. analyte properties: the electrochemical characteristics of the electroactive substance are important to the cell response, i.e. concentration, mass transport (diffusion coefficient) and charge transfer properties.

The interdigitated device can be operated in two fundamental modes, a. all bands are set at the same applied potential (common potential mode). For the device described in this study, one electrode may be used which provides a system of 10 microbands of bandwidth of 95µm and band gap of 131µm. Two electrode operation at common potential implies a 20 microband device of 95µm bandwidth and with band gap of 18µm. b. alternate bands are set at different applied potential (differential potential mode) with an anode-cathode bandwidth of 95µm and band gap of 18µm.

4.2 MICROBAND ARRAY ELECTRODE.

A simplifying cell arrangement for the study of ensembles of microband electrodes is shown in figure 4.1 a&b. The experimental configuration consists of two electrodes, one electrode is a microband array, whilst the second is a gold plate, typically 3cm x 3cm. The electrolyte consisted of aqueous $K_3Fe(CN)_6$ (1mM), $K_4Fe(CN)_6$ (1mM) and KCl (1M). For two parallel macroscopic electrodes as depicted in fig. 4.1d, the electric and current field distributions are uniform across the cell. However, with the interdigitated device operated as a microband array electrode, there exist regions of insulating surfaces

between the electrode units (bands). Such discontinuity results in non-uniform electric fields in the band gap region close to the microband array.

4.3 INTERDIGITATED MICROBAND ARRAY ELECTRODES.

Studies with interdigitated microband electrodes were previously carried out using bipotentiostatic circuitry [21,22]. In these experiments the potential control of individual electrodes is possible using a four electrode cell configuration, where the current is passed through two working electrodes (interdigitated device) and a single counter electrode. The collection and feedback efficiencies reported for interdigitated devices are dependent on the specific dimensions for the device, and the number of bands within the array. For dual band devices for example, the collection efficiency is generally greater than 50%. High collection efficiency (>80%) is found for large array devices with low micrometer spaced bands.

The present study considers the two electrode cell operation of an interdigitated device. The device is characterised for an electrolyte system containing an equiconcentration of $Fe(CN)_6^{3-/4-}$ redox couple as mentioned above. Such experimental conditions not only simplifies the instrumentation, but ensures 100% collection efficiency for close spaced microelectrodes. The electric potential scale in this experimental arrangement is then relative to $Au/Fe(CN)_6^{3-/4-}$. Conventional three electrode potentiostatic experiments have also been carried out, where the interdigitated device sufficied as the working electrode and counter electrode.

The interdigitated microband array electrodes, where neighbouring bands are operated as anode and cathode arranged with coplanar geometry are shown in figure 4.1c. In this instance the electric field distribution is totally non-uniform, high electric field strength is envisaged across the band gap, cf. the thin layer parallel plate anode and cathode system. The schematic circuit shown in figure 4.1 illustrates the potential control and current measurement stages use in the two electrode experiments.

Chronoamperometry was performed using a voltage waveform generator (HiTek PPR1) and a home-built picoammeter based on a high input impedence FET operational amplifier (Burr-Brown OAP 104) in two electrode cell arrangement. Potassium ferricyanide and potassium ferrocyanide (BDH) were of

analytical grade; micromolar solutions of the above were freshly prepared.

Although the above cell arrangement and conditions sufficed for investigative purposes of the i-t and i-E characteristics of interdigitated microband array electrodes it is of limited practical value. For sensor design other considerations become necessary such as the inclusion of a solid state reference electrode.

4.4 THIN LAMINATE SUBMICROMETER BAND ELECTRODES.

For submicrometer band electrodes, chronoamperometry and cyclic voltammetry were performed using a conventional three electrode cell configuration. The thin film electrode, $10mm < l < 60mm$, was placed several millimeters away from a reference electrode (SCE), positioned to the centre of the band. The counter electrode consisted of a large gold plate arranged parallel to the working electrode. Chronoamperometric experiments were carried out using a potential step of +0.5V to 0.0V versus SCE for the reduction of ferricyanide. The i-t curves were recorded directly with a Gould series 60000 x-y-t chart recorder. Chronoamperograms were repeatable to within 2%. The chronoamperometric determination of ferricyanide in aqueous KCl solution at low micromolar concentration was carried out using a commercial potentiostat, 100mA, 15V, without further current amplification or resort to noise elimination.

4.5 DUAL MICROCYLINDER ELECTRODES.

The dual microcylinder devices could be operated in an identical manner to that of the interdigitated microband device, i.e. at common potential in one and two electrode operation, or as an anode and cathode device. Three electrode steady state potentiostatic experiments only are considered.

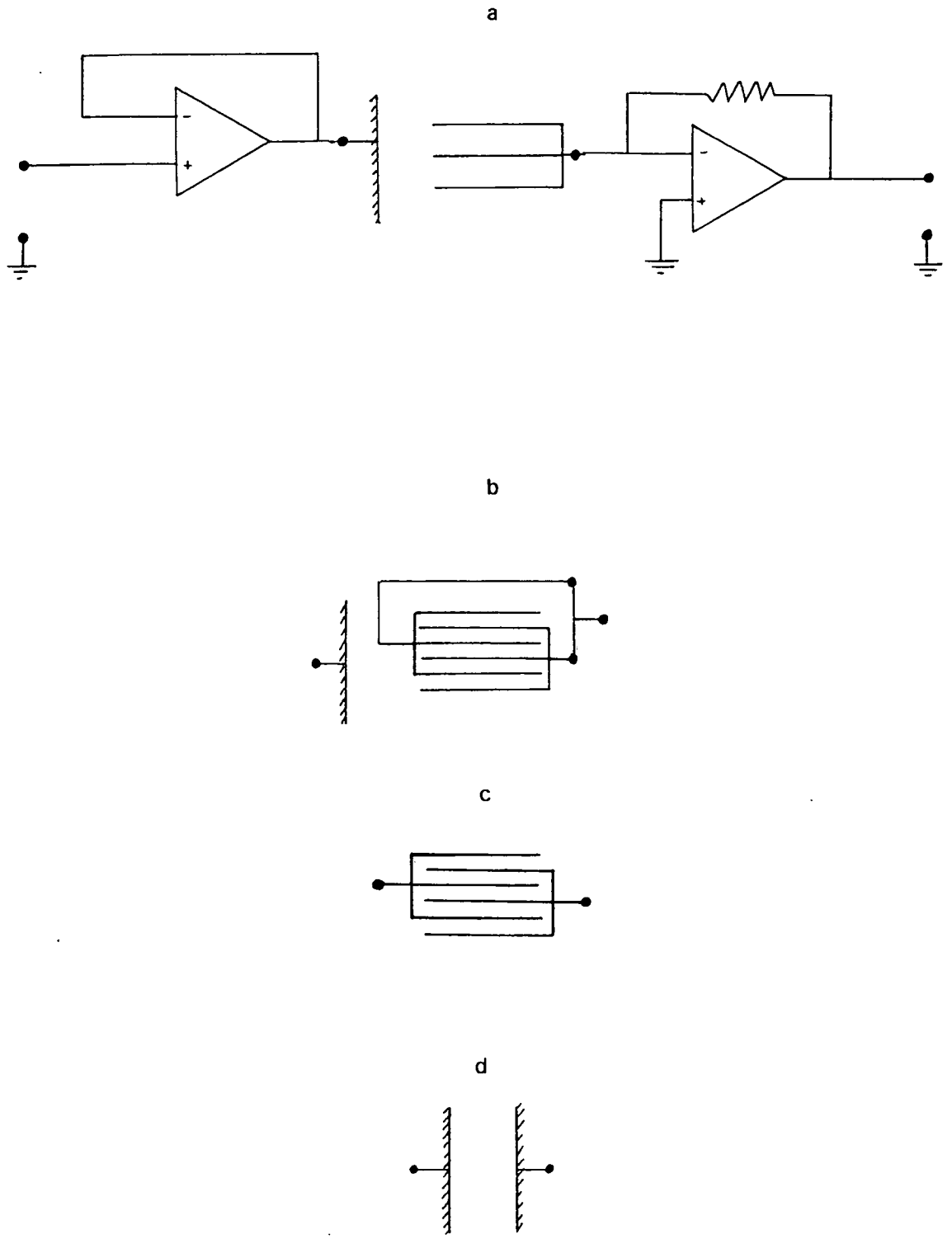

Figure 4.1 Interdigitated device operation in a two electrode cell configuration. a. one electrode, b. two electrode, c. interdigitated microband array electrodes, d. equivalent parallel plate electrodes.

CHAPTER 5

5.1 AMPEROMETRIC RESPONSE OF THE INTERDIGITATED MICROBAND DEVICE.

5.1.1 INTERDIGITATED MICROBAND DEVICE OPERATED AT A COMMON APPLIED POTENTIAL: A MICROBAND ARRAY ELECTRODE.

5.1.1.1 CYCLIC VOLTAMMETRY.

Cyclic voltammetry for the $Fe(CN)_6^{3-/4-}$ redox couple using the interdigitated device as a microband array electrode is presented in figure 5.1. The i-E waves for each electrode of this device show similar characteristics in terms of peak current, i_p, and position of peak potential. The data listed in table 5.1 demonstrates the voltammetric differences exhibited by these electrodes, eg. % variation of $i_{p,a}$ is 8.6, which is a consequence of errors introduced at the lithographic, insulation or mounting stages of fabrication. From the Randles-Sevcik equation[46] the peak current for a macroscopic electrode of area equal to one microband array electrode, i.e. dimensions, 10mm x 0.95mm, is 9.1μA mM^{-1} compared with 14.0 μA mM^{-1} delivered by a microband array electrode of bandwidth, w_e=95μm and band spacing of (w_e+2w_g) 131μm, see table 5.1. The increase in observed peak current derives from contributions made to the flux by non-linear mass transport as the diffusion layer extends beyond the width of the band electrode.

In two electrode operation (equivalent to decreasing band separation from 131μm to 18μm) the anodic peak current increases by only 29% compared to the 100% increase expected by doubling the electrode area, see fig. 5.1. A plot of current density against applied potential for the two voltammetric experiments illustrates the salient operating characteristics for microband array electrodes underlining the importance of electrode spacing, cf. fig.5.2. The linear potential sweep voltammograms indicate the following;

a. the peak current density is a function of electrode spacing.

b. the rate of change of diffusion current with respect to applied potential is reduced as band gap increases.

5.1.1.2 CHRONOAMPEROMETRY.

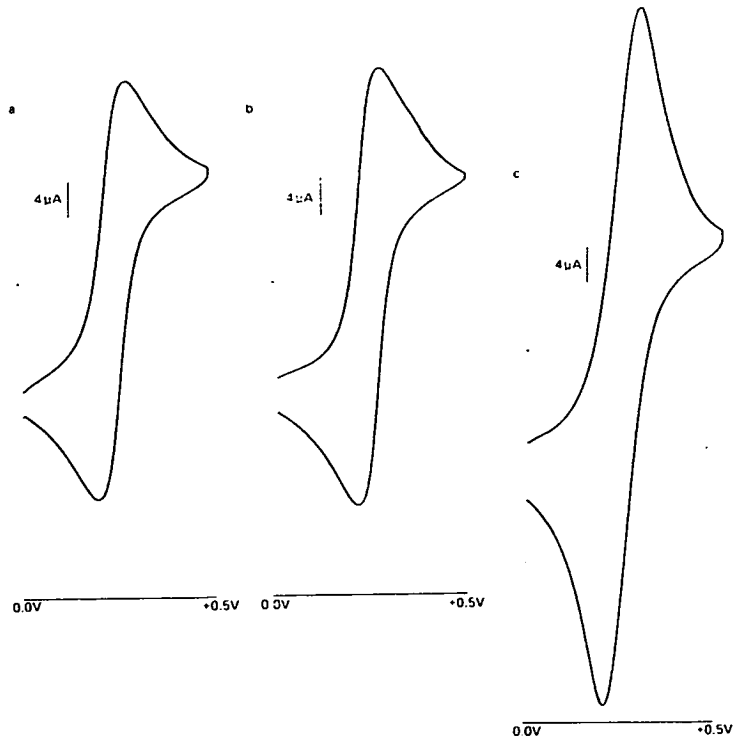

Figure 5.1 Cyclic voltammetry for $Fe(CN)_6^{3-/4-}$ at a microband array electrode. $K_3Fe(CN)_6$ (1.0mM), $K_4Fe(CN)_6$ (1.0mM) in aqueous KCl (1.0M). Potential sweep 0.0V to +0.5V vs. SCE, v=20mV s^{-1}.

a. one electrode operation, band gap 131μm, electrode 1 of the device.

b. as for a. electrode 2 of the device.

c. two electrode operation, band gap 18μm, electrodes 1&2.

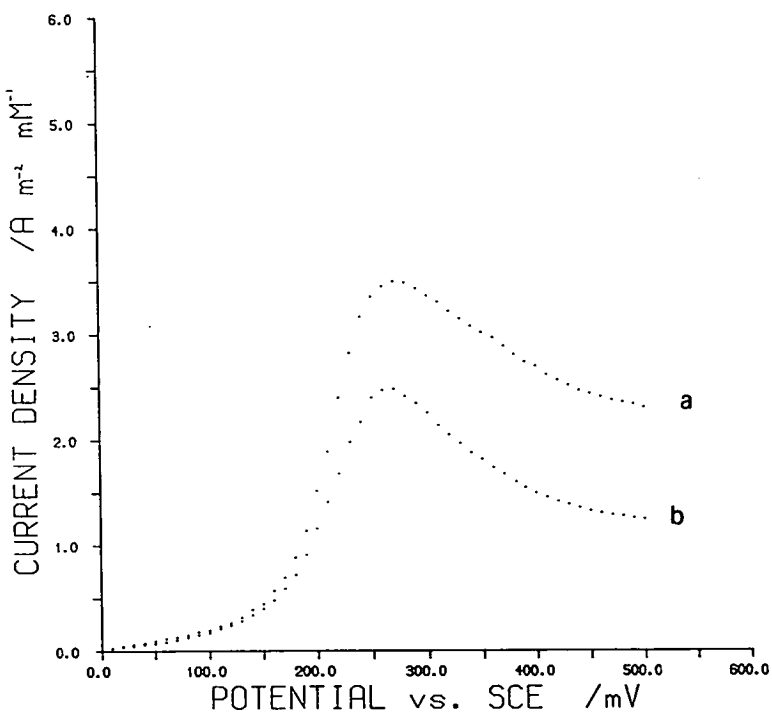

Figure 5.2 Linear potential sweep voltammetry for the oxidation of $Fe(CN)_6^{4-}$ at the microband array electrode. $K_4Fe(CN)_6$ (1.0mM), $K_3Fe(CN)_6$ (1.0mM) with KCl (1.0M) supporting electrolyte. Potential sweep from 0.0V to +0.5V vs. SCE, v=20mV s^{-1}.

a. one electrode operation, band gap 131μm.

b. two electrode operation, band gap 18μm.

The time dependence of the diffusion current, plotted here as current density, for the oxidation of ferrocyanide at the microband array electrode is shown in figures 5.3 & 5.4. The current-time characteristics for this electrode geometry when compared with a macroscopic electrode demonstrate the effects of a finite microscopic dimension (w_e) upon response. The main chronoamperometric features are:

a. the current is a function of time for microband array electrodes of bandwidth, 95µm and with band gap of 131µm and 18µm, i.e. no steady state current is observed.

b. the observed current decay is less for the microband electrode than a macroscopic electrode (Cottrell curve).

c. the current enhancement for one electrode operation over the Cottrell response is marginal, i.e. the edge effect for a 95µm band is comparitively small.

d. the current is a function of electrode spacing, reducing the band gap from 131µm to 18µm causes a reduction in the diffusion current density.

e. deviation from the macroelectrode response for the one electrode operation occurs on a time scale less than 100ms. For two electrode operation an initial deviation is observed which then conforms to the Cottrell curve at time approaching 1s.

5.1.1.3 SIMULATION OF CHRONOAMPEROMETRY AT A MICROBAND ARRAY ELECTRODE.

Two dimensional concentration profiles simulated for the diffusion controlled oxidation of $Fe(CN)_6^{4-}$ at a single or isolated microband array electrode following a potential step are shown in figure 5.5. The grid boundary parameters for this concentration field were mentioned in chapter 2. The corresponding chronoamperometric curve is compared with experimental data in fig. 5.6. The simulated i-t data overestimates the experimental data by ca. 15%.

The concentration profiles for an electrode of close spaced microbands are given in fig. 5.8, illustrating the effects of diffusion field interaction (shielding)

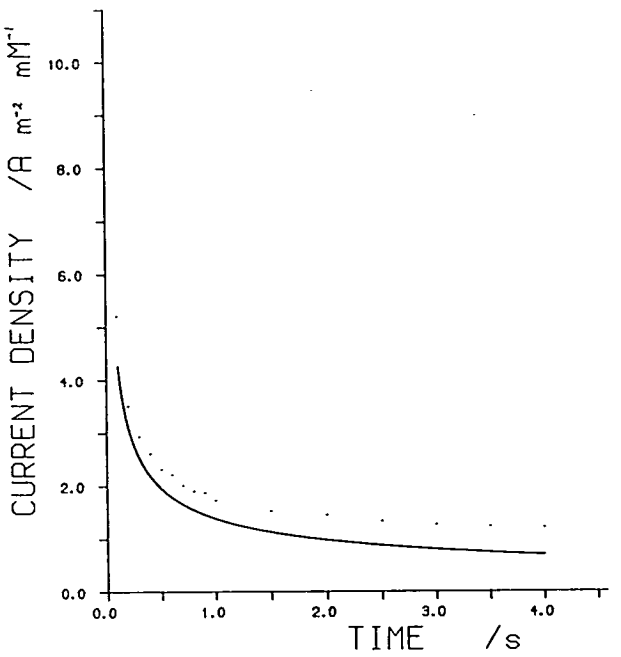

Figure 5.3 Chronoamperometry for the oxidation of $Fe(CN)_6^{4-}$ in aqueous KCl at the microband array electrode. Potential step 0.0V to +0.5V vs. $Au/Fe(CN)_6^{3-/4-}$. Solution: $K_3Fe(CN)_6$ (1.0mM), $K_4Fe(CN)_6$ (1.0mM) and KCl (0.6M).

dot curve, experimental data for a one electrode operation, w_e=95μm , w_g=131μm .

solid curve, Cottrell curve taking $D=6.4\times10^{-10}m^2\ s^{-1}$.

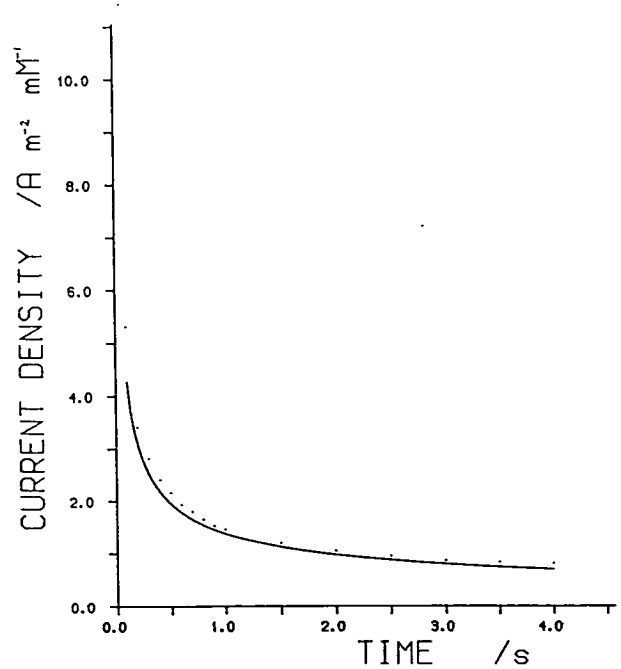

Figure 5.4 Chronoamperometry at a close spaced microband array electrode. Conditions as for fig. 5.3.

dot curve, experimental data for two electrode operation, w_e=95μm , w_g=18μm .

solid curve, Cottrell curve taking $D=6.4\times10^{-10}m^2\ s^{-1}$. 49.

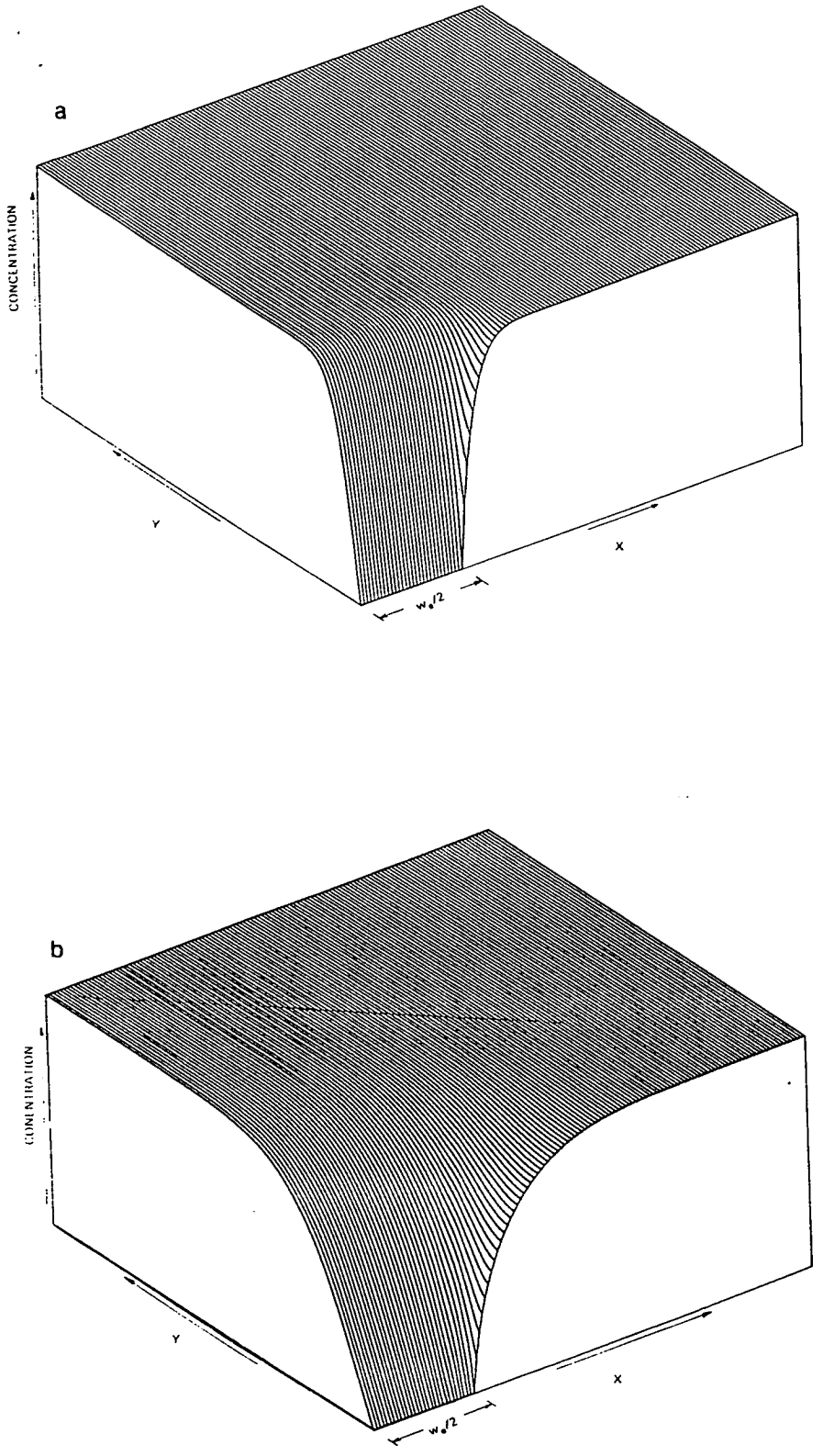

Figure 5.5 Two dimensional concentration profiles for a single microband electrode of bandwidth 95μm. a. short time b. long time.

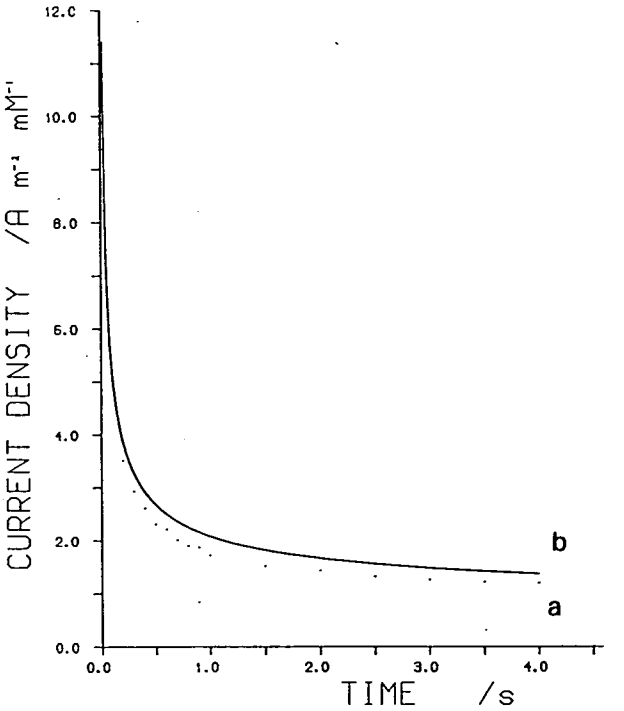

Figure 5.6 Chronoamperometry for $Fe(CN)_6^{4-}$ at a microband array electrode, conditions as in fig. 5.3. a. experimental data for a single (isolated) microband electrode. b. simulated data for a microband electrode, w_e=95μm, using $D=6.4\times10^{-10}m^2\ s^{-1}$.

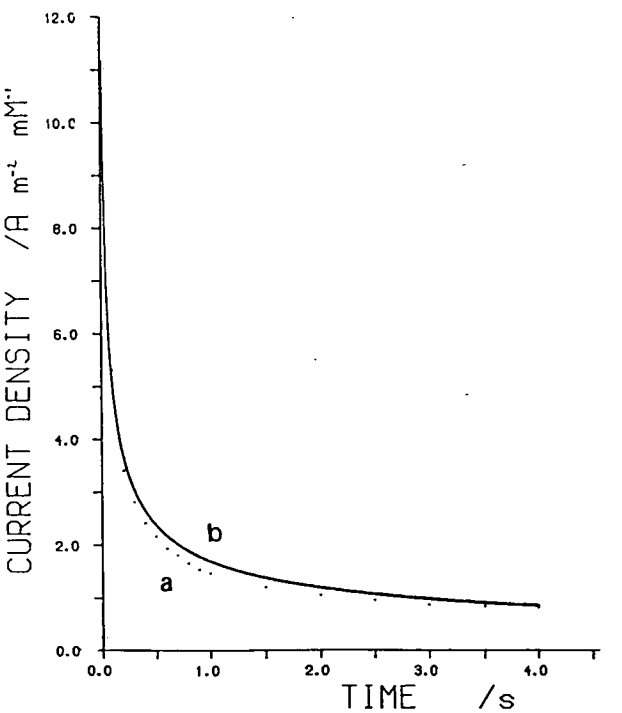

Figure 5.7 Chronoamperometry at a microband array electrode of bandwidth 95μm a. experimental data, conditions as in fig. 5.4. b. simulated data for a close spaced array, w_g=19μm. Taking $D=6.4\times10^{-10}m^2\ s^{-1}$.

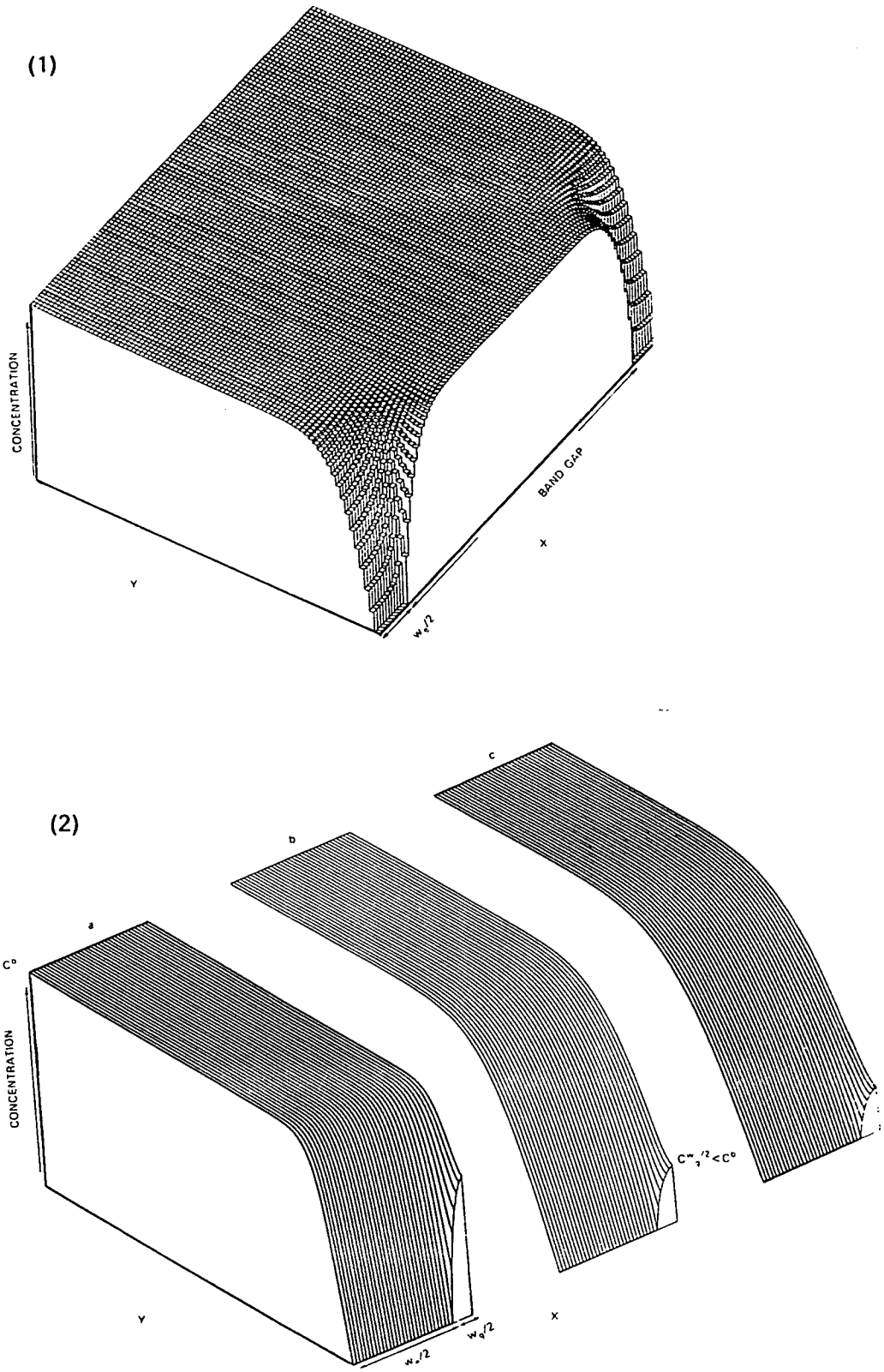

Figure 5.8 Two dimensional concentration profiles at microband array electrodes, (1) isolated array (2) close spaced array, w_e=95μ, w_g=18μm; for electrolysis time, a.83ms b.413ms c.825ms.

on the concentration field within the band gap region. The simulated i-t response for this electrode system is compared with experimental data in fig. 5.7. The simulation model for the chronoamperometric response of large scale microband array electrodes therefore approximates the experimental behaviour within acceptible fabrication errors. Figure 5.9 contrasts the simulated chronoamperometric response for an isolated microband array electrode of bandwidth, 95µm with a close spaced band configuration with band gap, 19µm. The simulation predicts an increase in current density for widely spaced bands, and indicates the time dependent nature of the response. This behaviour is further illustrated by figure 5.10, showing the variation in diffusion current with time as a function of band gap. The simulation shows for a band of 95µm bandwidth, the i-t behaviour approaches that of an isolated array at separation ca. 120µm, for a current sampled at 2.0s, cf. fig. 5.11.

5.1.1.4 BEHAVIOUR OF THE DIFFUSION FIELD AT MICROBAND ARRAY ELECTRODES.

The observations described above may be rationalised in terms of a diffusion boundary layer and field concept. Figure 5.12 illustrates qualitatively the dynamics of diffusion layer development at the microscopic band array electrode. At short electrolysis time, <100ms the diffusion layer extends into solution a short distance, ca. 11µm, relative to the size of the bandwidth. At this moment edge flux is a small contribution of the total mass flux to the electrode. As such, the concentration and flux surfaces approximate a linear model and the current-time response therefore follows Cottrell behaviour. As electrolysis proceeds transport of species from regions beyond the electrode edge becomes more significant and strong deviations from the linear flux field are observed, i.e. the microelectrode edge effect is realised. This property of the diffusion field to change symmetry, in this case (owing to bandwidth size) from a linear to flattened elliptic hemicylindrical geometry, is responsible for the enhancement in current density. The number of lines of flux established per unit time increases with an expanding diffusion field at microscopic electrodes, unlike the constant lines of flux set up at macroscopic electrodes.

The above description of a diffusion layer is applicable to a single or an ensemble of large scale microbands where individual bands are isolated by a large gap distance. However, when a microelectrode is placed within the

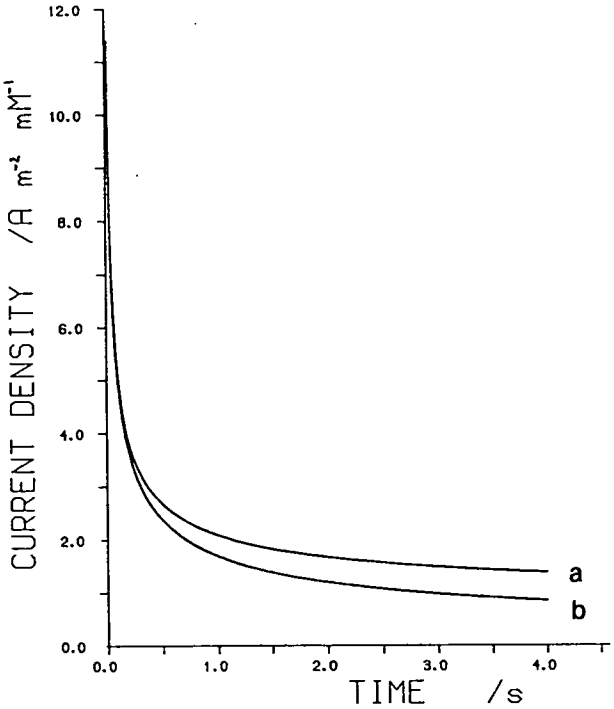

Figure 5.9 Simulated i-t curve for the oxidation of $Fe(CN)_6^{4-}$ at a. an isolated microband array electrode, b. close spaced microband array electrode w_e=95µm, w_g=19µm. D=6.4×10^{-10}m^2 s^{-1}.

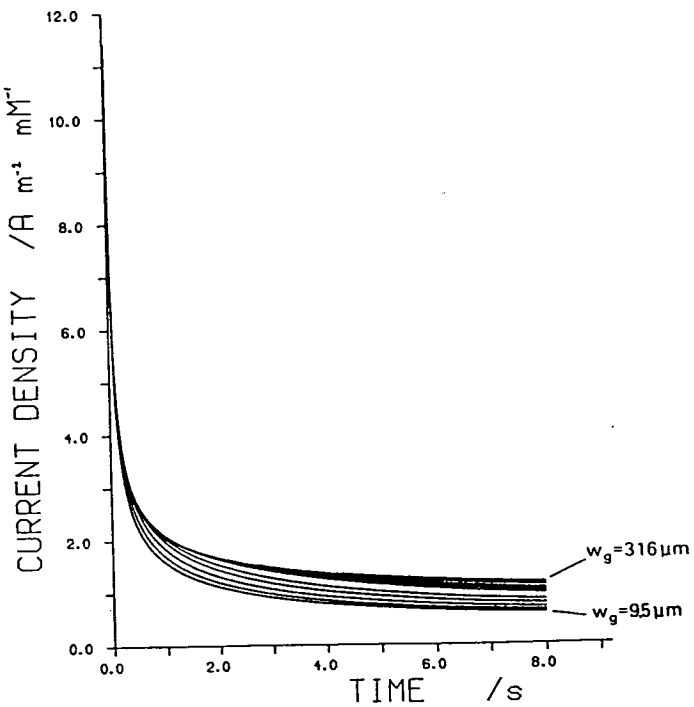

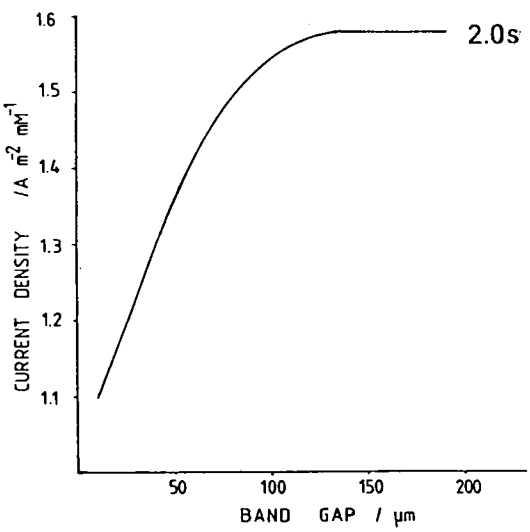

Figure 5.10 Simulated chronoamperometry at a close spaced microband array electrode, bandwidth, 95µm, D=6.4×10^{-10}m^2 s^{-1}, showing band gap dependence. Simulation parameters are given in chapter 2.

Figure 5.11 Plot of simulated diffusion current against band gap for microband array electrodes.

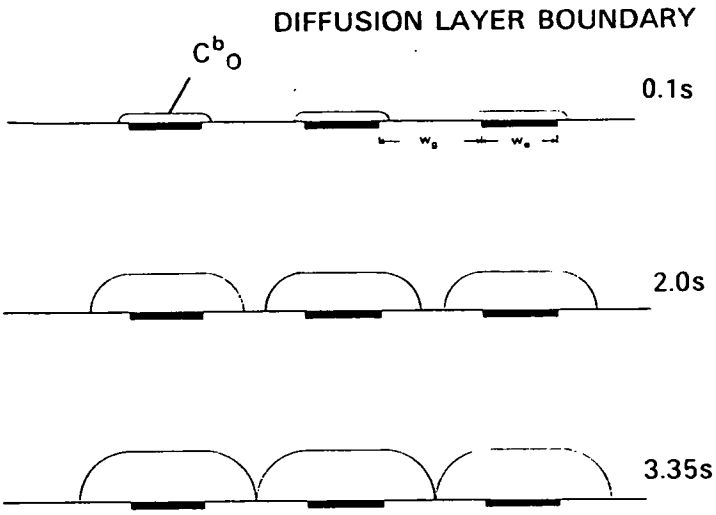

Figure 5.12 Qualitative representation of the diffusion field at a microband array electrode of bandwidth, 95µm and band gap, 131µm. The expression $\delta=\sqrt{2Dt}$, was used to estimate the diffusion layer thickness. The solid line indicates the diffusion surface taking $D=6.4\times10^{-10}m^2\ s^{-1}$.

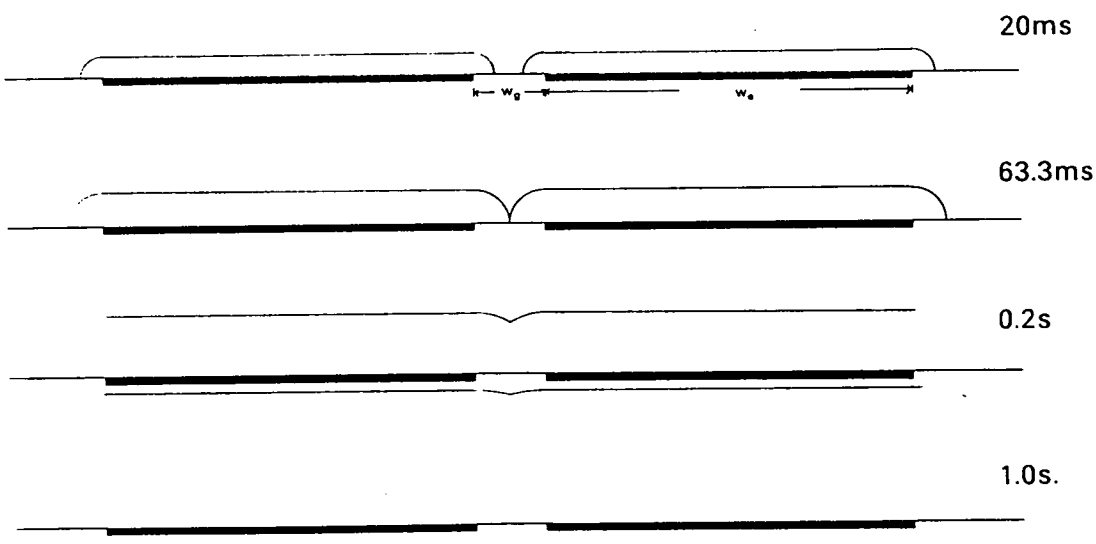

Figure 5.13 Illustration of the diffusion field at a close spaced microband array electrode. Condition as for fig.5.12, band gap 18µm.

diffusion layer of a second microelectrode the overall field geometry changes as the field at any individual electrode is influenced by the flux to neighbouring electrodes. This has concomitant effects on mass flux to the electrode surface and therefore the amperometric properties. For the microband device described here, where w_e=95μm with a band spacing of w_g=131μm, the diffusion layer must extend a distance $w_g/2$ before interaction with a neighbouring field, i.e. 65.5μm. Using $\delta=\sqrt{2Dt}$, this would take 3.35s. Further extension of the diffusion layer would lead to the shielding effect. Figure 5.13 depicts the time dependent changes to the diffusion layer surface as it extends beyond a distance $w_g/2$, for a microband spacing of 18μm. For this device the expanding diffusion layers are expected to interact on a shorter time scale (ms) with the formation of a linear field pattern after 1s. The linearising of encroached fields effectively reduces the diffusion layer surface, with the divergence of nonlinear edge flux to a the more linear form.

5.1.2 INTERDIGITATED MICROBAND DEVICE OPERATED AT A DIFFERENTIAL APPLIED POTENTIAL: THE INTERDIGITATED MICROBAND ARRAY ELECTRODES.

5.1.2.1 CYCLIC VOLTAMMETRY

The effects on the voltammetric wave of arranging the interdigitated microband array device as an alternate series of anodes and cathodes microscopically displaced are demonstrated in figure 5.14. This is equivalent to connecting the second electrode of the interdigitated device as counter electrode in a three electrode potentiostatic experiment. The outstanding difference for the anode-cathode device, as opposed to the isolated microband array electrode, for reversible redox species is the observed increase in diffusion current. Indeed, the steady state current obtained in the interdigitated case is equal to $i_{s.s.}$=21.4μA mM^{-1}, compared with a peak current of 6.8μA mM^{-1}. The form of the i-E characteristic is markedly different for the anode-cathode device; from a peaked wave typical of mass transport limitation to a constant current indicative of high rate of mass transport. This invariation of diffusion controlled current with applied potential for a reversible redox couple is a consequence of the exchange of redox forms between the working electrode and counter electrode. This implies that the steady state condition originates from an inter-electrode diffusion process and will therefore be dependent upon geometrical parameters of the device.

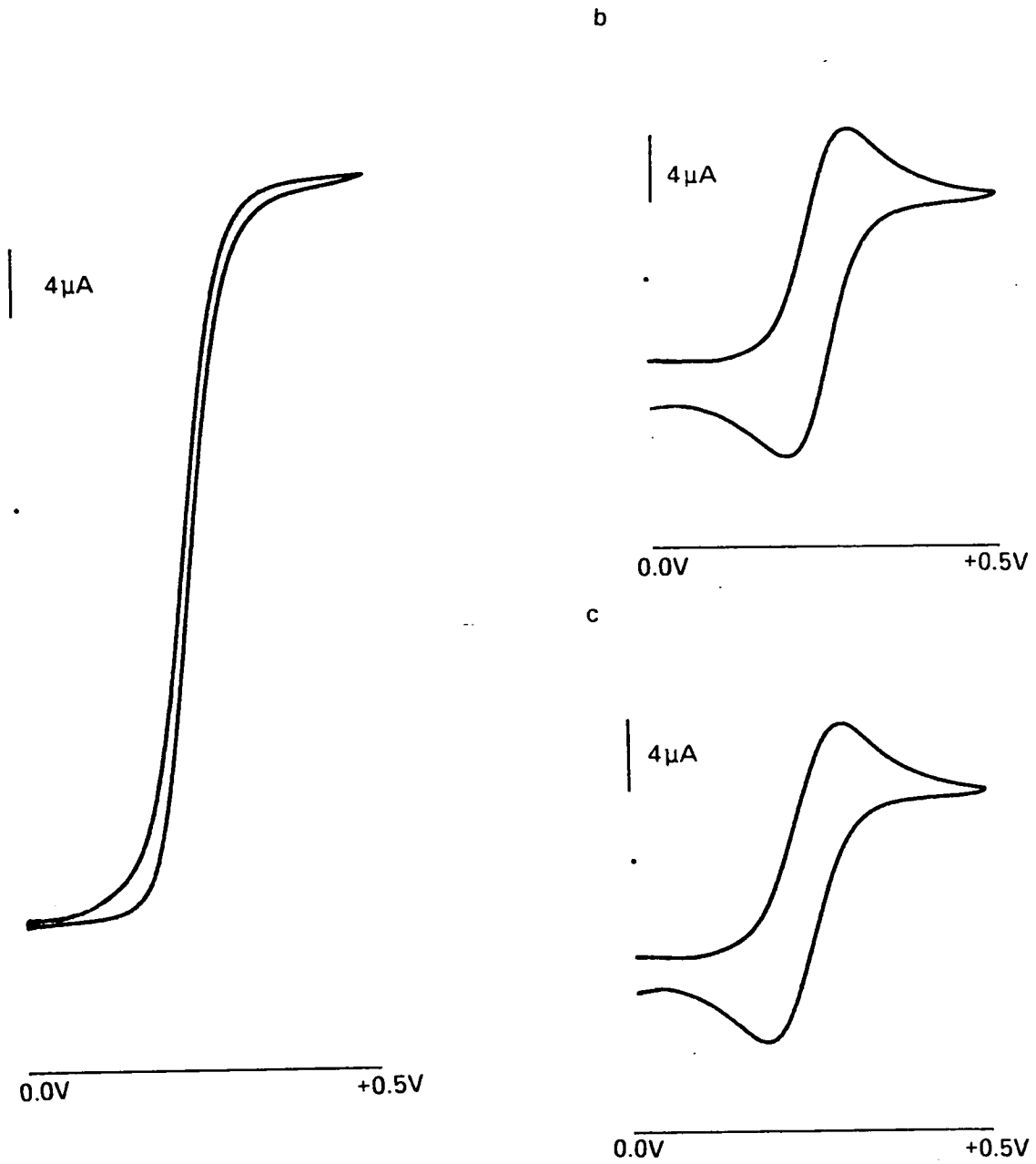

Figure 5.14 Cyclic voltammetry for $Fe(CN)_6^{3-/4-}$ at the interdigitated device. $K_4Fe(CN)_6$ (1.0mM), $K_3Fe(CN)_6$ (1.0mM) in KCl (1.0M). Potential sweep 0.0V to +0.5V vs. SCE, $v=2mV\ s^{-1}$. a. anode-cathode, b. one electrode, electrode 1., c. one electrode, electrode 2.

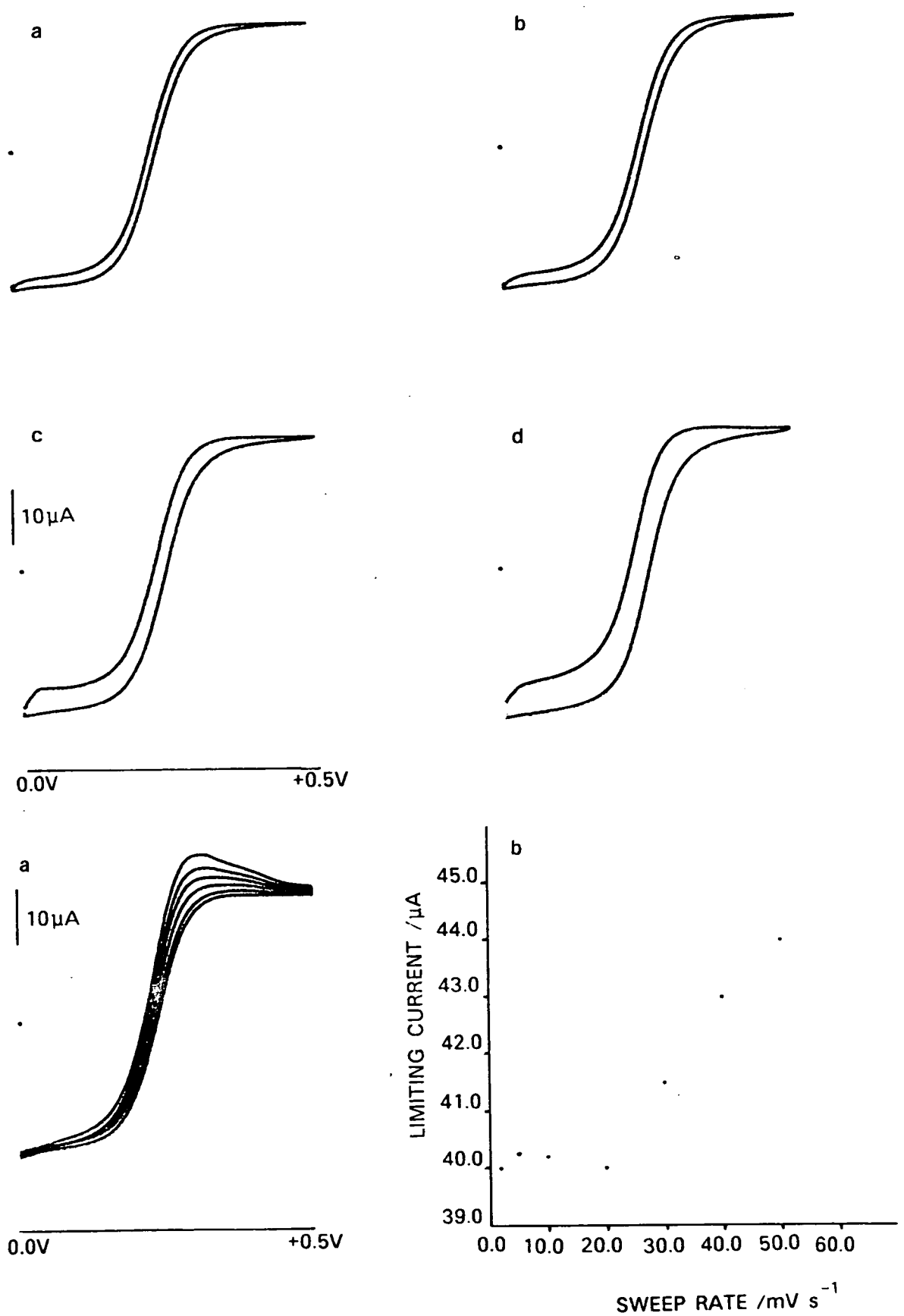

Figure 5.15 Cyclic voltammetry of the $Fe(CN)_6^{3-/4-}$ redox couple at the interdigitated microband array electrodes: sweep dependence characteristic. $K_3Fe(CN)_6$ (1.0mM), $K_4Fe(CN)_6$ (1.0mM) in aqueous KCl (1.0M). Potential sweep from 0.0V to +0.5V vs. SCE. sweep rate, mV s^{-1}, a. 2, b. 5, c. 10, d. 20.

Figure 5.16 a. Linear potential sweep voltammetry using the interdigitated device: experimental conditions as in fig. 5.15.

b. Plot of limiting current (peak current or steady state current) against sweep rate.

The potential sweep rate dependence of the votammetric response is given in figure 5.15. Cyclic voltammetry for $Fe(CN)_6^{3-/4-}$ exhibits background current effects as the sweep rate is increased from 2mV s^{-1} to 20mV s^{-1}. The origin of this background current is both faradaic and capacitive leading to an increased baseline slope and hysteresis. The magnitude of the capacitive component can be diminished by reducing the electrode bandwidth (generator area), from, i=CAv, where C is the double layer capacitance. The faradaic background current may have several sources including impurities in solution or adsorbed onto the electrode, solvent and supporting electrolyte contributions. For solution impurities the background current may originate by direct diffusion to the generator electrode or via an interelectrode process. The appearance of peak character at sweep rates approaching 20mV s^{-1} as shown in fig. 5.15 is indicative of changes occurring to the inter-electrode diffusion flux. For sweep rate values smaller than 20mV s^{-1}, the magnitude of the steady state current, $i_{s.s}$, is independent of sweep rate. The peak shape characteristic becomes more prominent as the mass transport process can no longer maintain high electrode flux for a steady state current. A further point to note about the sweep rate dependence of linear potential sweep voltammetry is shown in figure 5.16. These series of waves illustrate the balance of mass transport and charge transfer processes at interdigitated electrodes, showing that for high rates of mass transport the i-E wave is shifted on the potential scale.

The voltammetric behaviour of quasi-reversible redox species such as quinol and catechol was examined at the gold interdigitated microband array electrodes with intension to highlight the consequences of inter-electrode diffusion on slower charge transfer reactions.

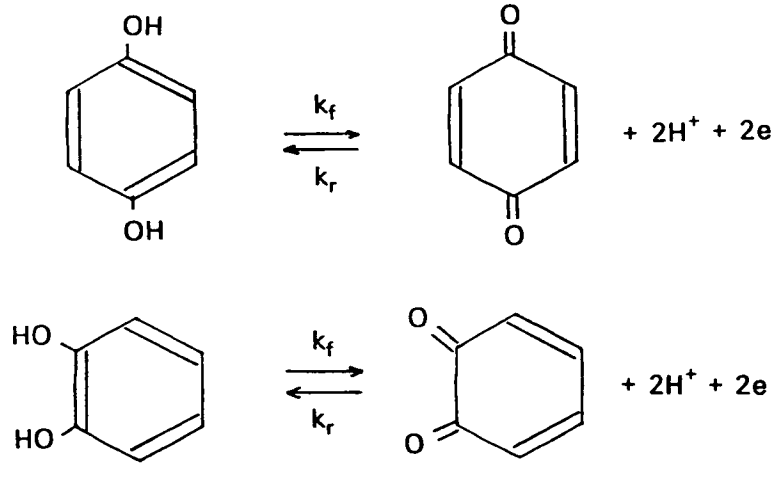

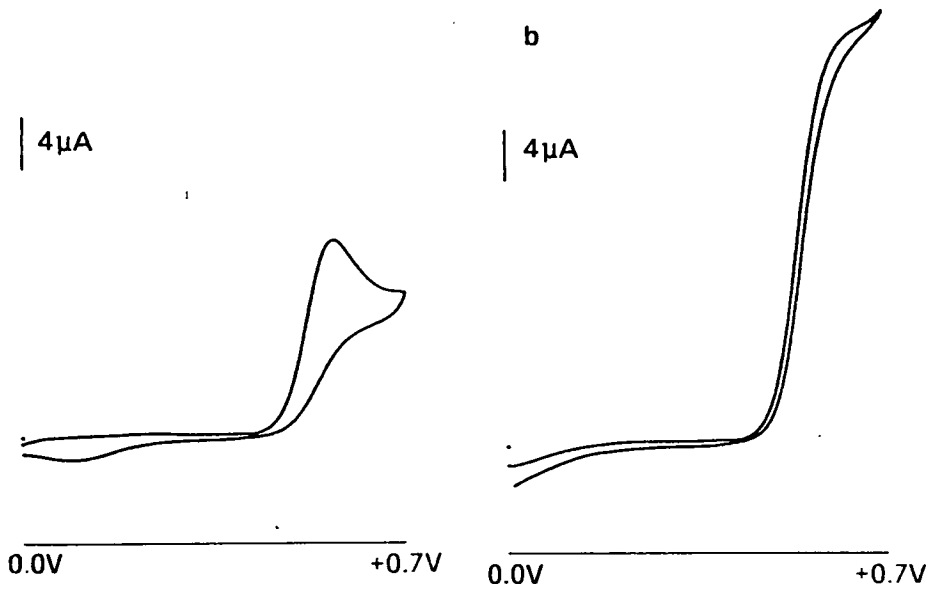

Figure 5.17 Cyclic voltammetry for the oxidation of hydroquinone (1.0mM) in aqueous KCl (1.0M) at pH=1, using a gold interdigitated microband array electrodes. Potential sweep from 0.0V to +0.7V vs. SCE. a. one electrode operation, v=2mV s^{-1}, b. interdigitated microband anode-cathode, v=2mV s^{-1}.

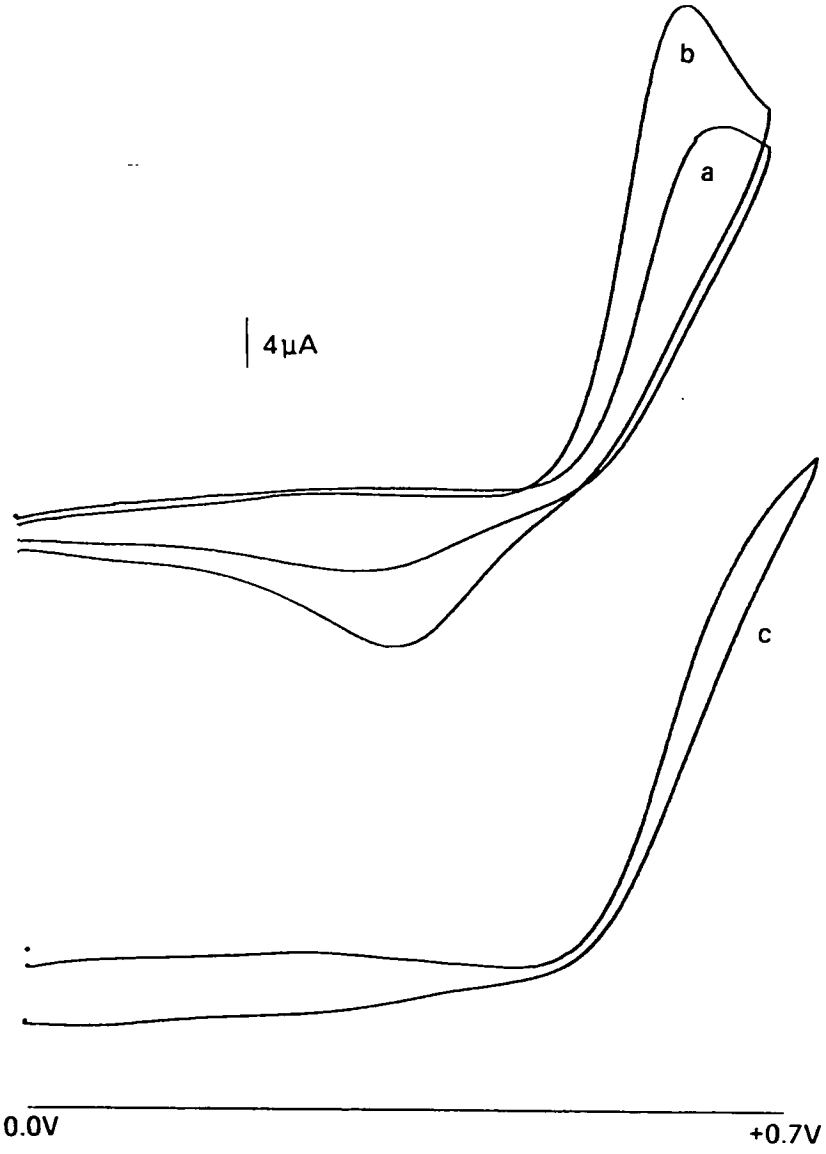

Figure 5.18 Cyclic voltammetry for catechol at the interdigitated device. Solution: catechol (1.2mM), KCl (1.0M) pH=1. Potential sweep from 0.0V to +0.7V vs. SCE, v=10mV s^{-1}. a. one electrode operation,b. two electrode operation,c. anode-cathode.

The cyclic voltammetry of hydroquinone in aqueous KCl solution, pH=1, at an interdigitated anode-cathode is compared with a microband array electrode in figure 5.17. Again, an increased current is observed with the interdigitated anode-cathode device, $i_{s.s}$=31.4μA mM^{-1} over the microband array $i_{p,a}$=14.5μA mM^{-1}. The position of the plateau current however, is shifted on the potential scale from $E_{p,a}$ +0.57V vs. SCE, for a microband array anode to ca. +0.65V. Similar, but more contrasting behaviour was found for the oxidation of catechol at gold electrodes, see figure 5.18. The i-E waves show the quasi-reversible nature of the charge transfer for quinol and catechol at gold electrodes. Since the operation of the anode-cathode device is dependent on the rate of forward and reverse charge transfer, if one is a slow process, as here k_r, the current response of the device is then limited by this process and voltammetric wave shift can occur as observed.

5.1.2.2 CONCENTRATION DEPENDENCE OF THE DIFFUSION CURRENT AT INTERDIGITATED MICROBAND ARRAY ELECTRODES.

Interdigitated microband array electrodes were used in cyclic and linear sweep voltammetry (feedback voltammetry) for the determination of $Fe(CN)_6^{3-/4-}$ at submillimolar concentration. The approach followed involved the measurement of a limiting current from the voltammogram and correlating this with the analyte concentration. Figure 5.19 compares the cyclic voltammetry of micromolar concentration of $Fe(CN)_6^{3-/4-}$ redox couple at the interdigitated device with a macroscopic electrode. The voltammograms in fig. 5.19 illustrate the effects of electrode design (geometry and configuration) on the i-E characteristic for a system containing a reversible redox species. The conventional electrode exhibits peaked i-E behaviour with, $i_{p,a}$=0.85μA ($i_{p,a}$/C=18.1nA μM^{-1}) and significant background current. The voltammetric response of the interdigitated device by contrast is quite different, generating a steady state diffusion current, $i_{s.s.}$=1.2μA at sweep rate of 20mV s^{-1} with improved sensitivity, $i_{s.s.}$/C=24.6nA μM^{-1} and diminished backround effects. The concentration dependence of this steady state voltammetry at the interdigitated microband array electrodes is shown in fig. 5.20. The range of ferri/ferrocyanide concentration measured with this device was from 0.5mM down to 0.5μM, with a limit of detection at the nanomolar level, see fig. 5.21-5.23.

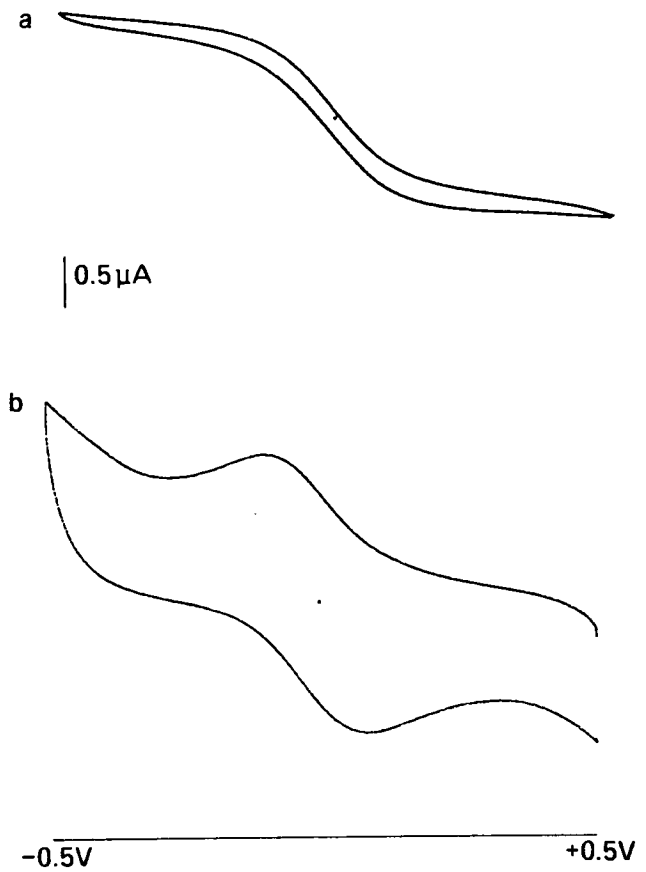

Figure 5.19 Cyclic voltammetry of $Fe(CN)_6^{3-/4-}$ (50μM) in KCl (0.6M) solution for a two electrode cell configuration. Potential sweep from +0.5V to -0.5V vs. $Au/Fe(CN)_6^{3-/4-}$, $v=20mV\ s^{-1}$. a. interdigitated device b. macroscopic gold electrode 2mm×6.5mm.

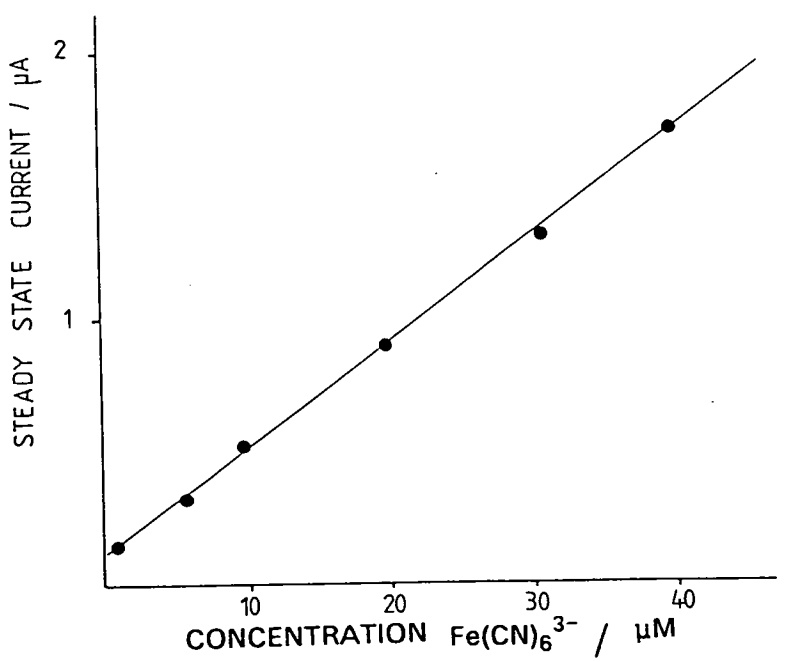

Figure 5.20 Steady state current vs. concentration for the system described in fig. 5.19.

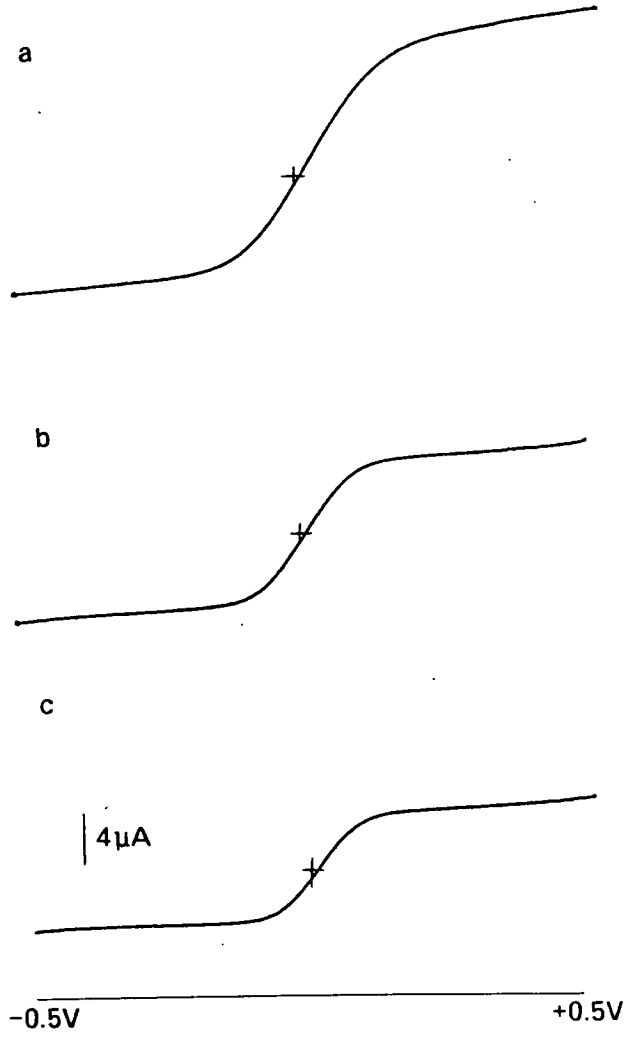

Figure 5.21 Linear potential sweep voltammetry for $Fe(CN)_6^{3-/4-}$ in a two electrode cell configuration. Conditions as for fig. 5.19. a. 0.5mM, b. 0.3mM, c. 0.2mM.

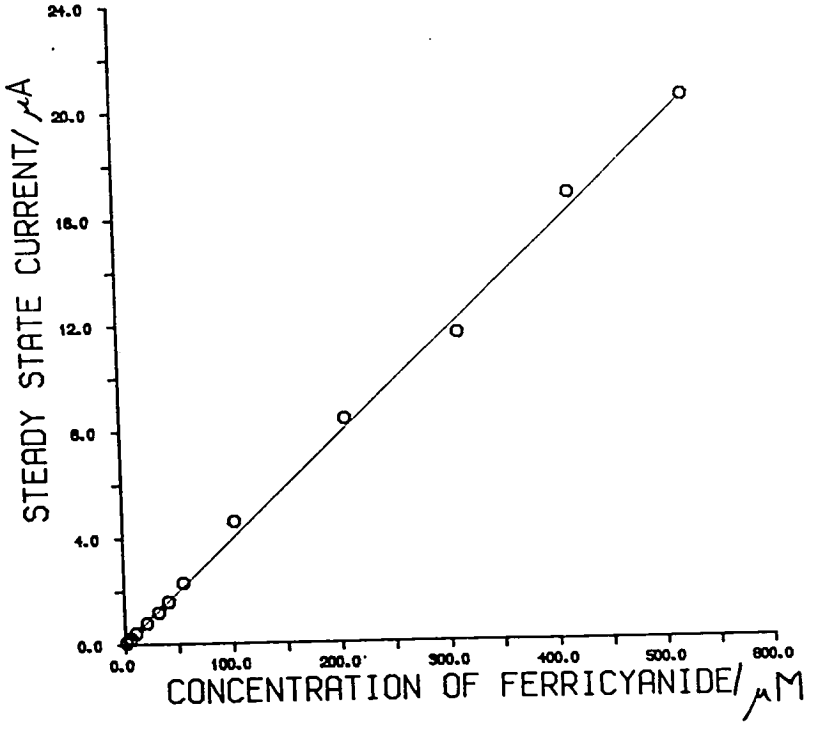

Figure 5.22 Plot of steady state current against concentration for the system as described in fig. 5.19

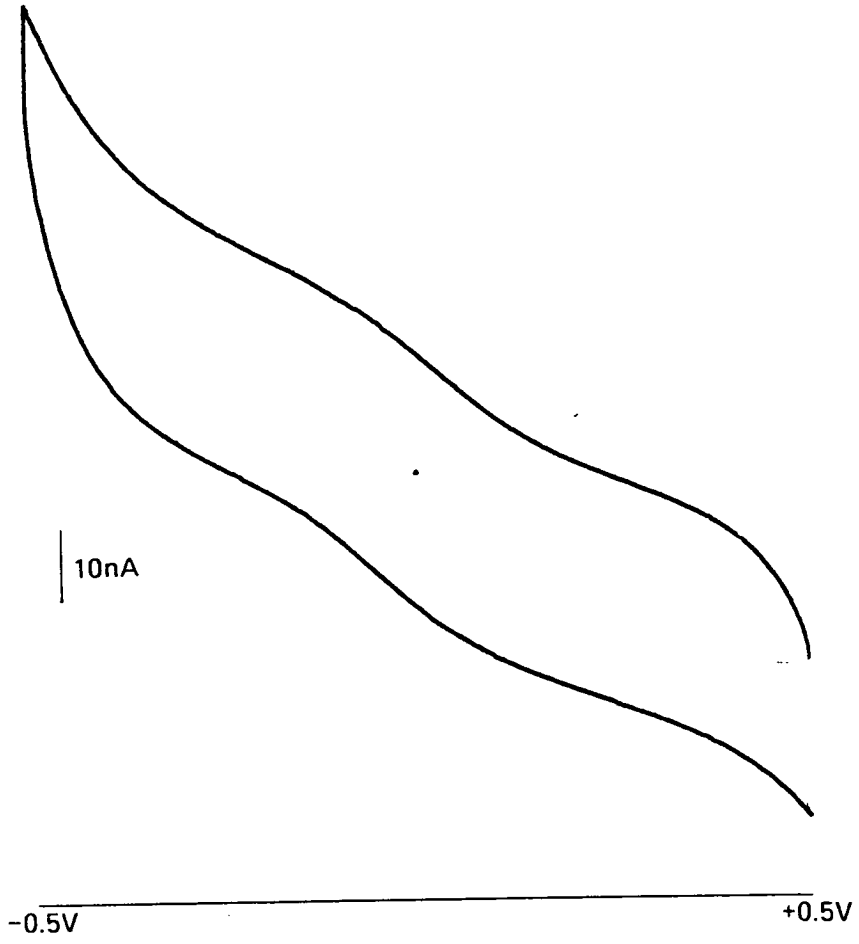

Figure 5.23 Cyclic voltammetry for $Fe(CN)_6^{3-/4-}$ (100nM) in KCl (0.6M). Conditions as for fig. 5.19.

5.1.2.3 CHRONOAMPEROMETRY

Chronoamperometry for the oxidation of $Fe(CN)_6^{4-}$ using the interdigitated device in a two electrode cell is shown in figure 5.24. The i-t data shows that deviation from microband behaviour occurs on a short time scale (<100ms), with the establishment of an amplified steady state diffusion current of ca. 25.3μA (20μAmM^{-1}) after approximately two seconds electrolysis. After about 4 seconds, the current at the interdigitated electrodes is more than double that of the microband array electrode (one electrode operation). The interdigitated device generates an average current density of 2.5A m^{-2} mM^{-1} for a O/R system, which is almost 2 times greater than a macroscopic electrode of similar area (0.69A m^{-2} mM^{-1}). Feedback chronoamperometry is also achieved with only one form of a redox couple initially present. Figure 5.25 shows the response of the interdigitated device for ferricyanide indicating a lower steady state current (ideally half the O/R case) and slower response time. These observations are directly related to differences in the feedback mechanism and are discussed further below.

5.1.2.4 SIMULATION OF CHRONOAMPEROMETRY AT INTERDIGITATED MICROBAND ARRAY ELECTRODES.

The two dimensional concentration profiles for an anode-cathode microband assembly are illustrated in figure 5.26 showing the consequences of an inter-electrode mass flux on the band gap concentration. The system depicted is that of an equiconcentration of a reversible redox couple, O and R. It will be appreciated from these profiles that the point, $w_g/2$ is maintained at concentration, $C_{O/R}^b$, i.e. a fixed Nernst plane dependent on w_g.

Simulated chronoamperometry for this system is compared with experimental data in figure 5.27. The simulation appears to approximate (within 10%) the i-t behaviour of the interdigitated device in terms of the transient response and the magnitude of the steady state current over the time period examined. Figure 5.28 shows the simulated chronoamperometric behaviour for several interdigitated devices of bandwidth, 95μm and variable band gap. As the band separation is decreased, the limiting current density increases and there is an accompanying diminution in response time. For such a device, with a band gap of 4.7μm the simulation predicts a steady state current response within 1.5s.

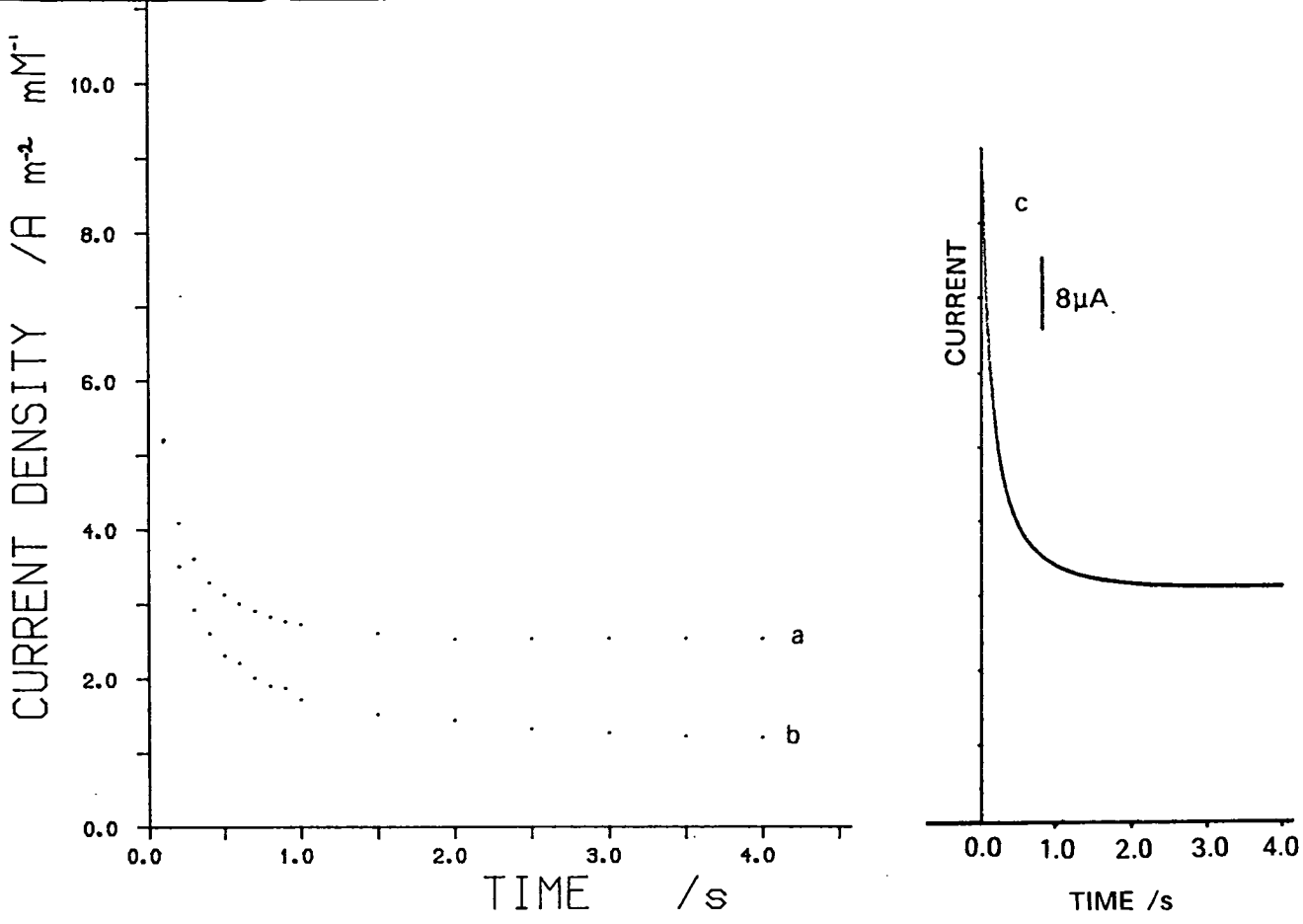

Figure 5.24 chronoamperometry of $Fe(CN)_6^{3-/4-}$ (1.3mM) in KCl (1.0M) solution at the interdigitated microband array electrodes. a/c. anode-cathode operation, b. one electrode operation. Potential step 0.0V to +0.5V vs. $Au/Fe(CN)_6^{3-/4-}$.

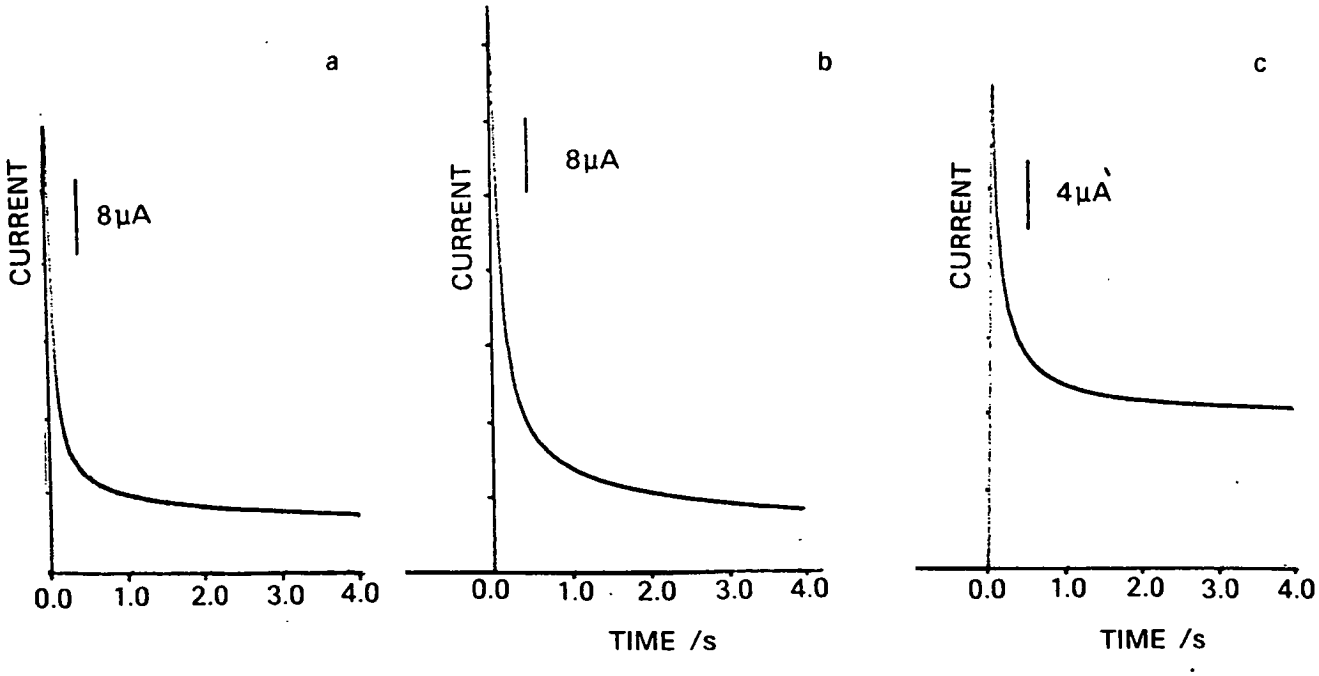

Figure 5.25 Chronoamperometry for ferricyanide (1.0mM) in KCl (0.6M) at the interdigitated device. Potential step +0.5V to 0.0V vs. $Au/Fe(CN)_6^{3-}$.

a. one electrode, b. two electrode, c. anode-cathode. 2

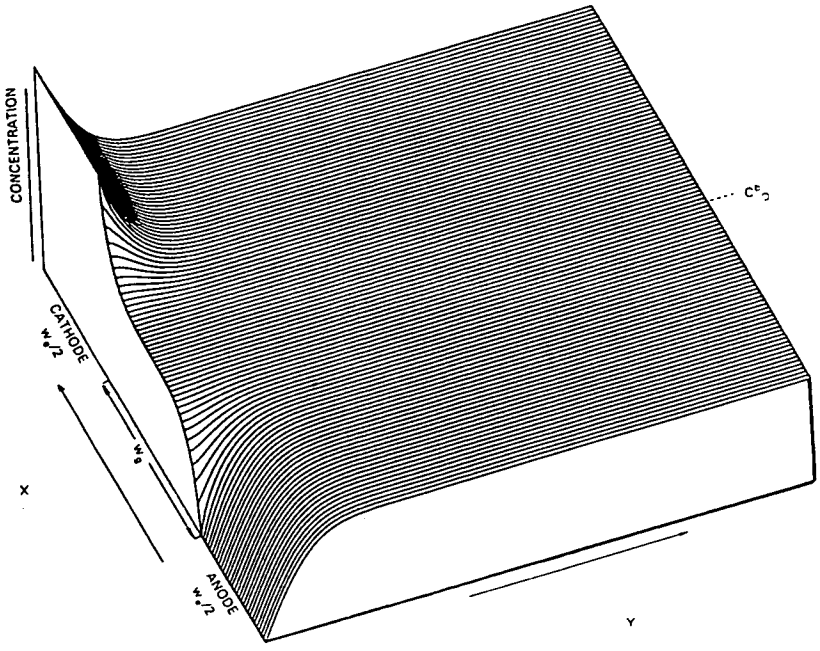

Figure 5.26 Two dimensional concentration profiles at an interdigitated device for a system containing $C^b_O=C^b_R$. Simulation parameters are given in chapter 2.

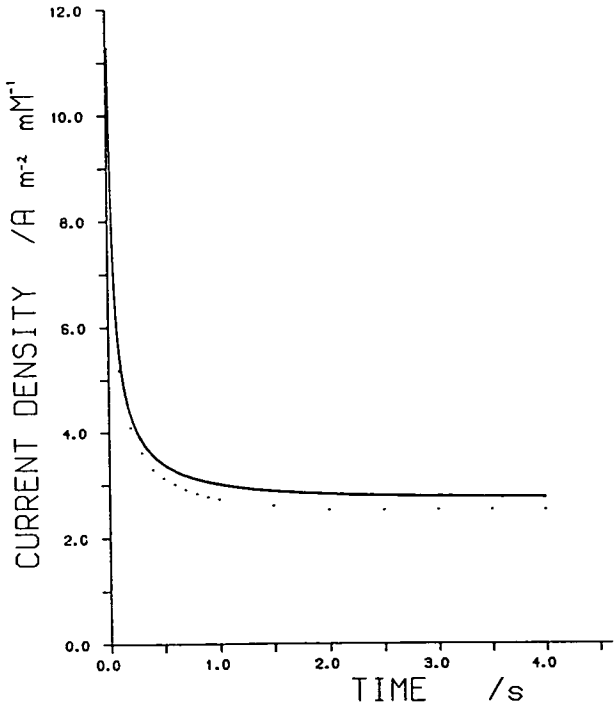

Figure 5.27 Chronoamperometry for the $Fe(CN)_6^{3-/4-}$ redox couple at the interdigitated device. $K_4Fe(CN)_6$ (1.0mM) $K_3Fe(CN)_6$ (1.0mM) in KCl (1.0M). Potential step 0.0V to +0.5V vs. $Au/Fe(CN)_6^{3-/4-}$.

dot curve: experimental data.

solid curve: simulated data for a device of bandwidth 95µm and band gap 17.4µm, taking $D=7.0\times10^{-10}m^2\ s^{-1}$.

5.1.2.5 VERIFICATION OF THE STEADY STATE CURRENT EXPRESSION FOR INTERDIGITATED MICROBAND ARRAY ELECTRODES.

Equation (2.62) derived in chapter 2 for the steady state current delivered by an interdigitated microband device for an O/R redox system was verified by plotting the steady state current, determined from linear potential sweep voltammetry, against the concentration of $Fe(CN)_6^{3-}$. A plot of the $i_{s.s.}$ vs. concentration is shown in figure 5.20. A gradient of $i_{s.s.}/C=20.25nA\ \mu M^{-1}$, was calculated which is in good agreement with the theoretical expression. Taking $D=7.0x10^{-10}m^2\ s^{-1}$, then $i_{s.s.}/C(theor.)=21.70nA\ \mu M^{-1}$, a difference of -6.9%. Chronoamperometry for the $Fe(CN)_6^{3-/4-}$ redox couple gives a steady state current of $20nA\ \mu M^{-1}$. As mentioned in chapter 2, the theoretical equation derived in this work should approximate, within 10%, the experimental data of this device, where w_e/w_g ratio is 5.28. Table 5.2 shows the limiting current data derived from cyclic voltammetry for the $Fe(CN)_6^{3-/4-}$ system and for quinol, the $i_{s.s}$ values are in agreement with theory. Table 5.3 compares theoretical feedback current with simulation for variable band gap. The theoretical data underestimate simulation by ca 20%. The error between these approaches should diminish as the ratio w_e/w_g increases, unfortunately with the present numerical model, simulation error increases with diminishing w_g for existing grid dimensions.

Table 5.4 compares experimental steady state current data determined by Aoki et al. [21] for a series of interdigitated devices, with the equation (2.62). Better agreement between theory and experiment is found for high values of the ratio w_e/w_g which is a consequence of the boundary value approximations made in the derivation of eqn.(2.62). For $w_e/w_g=5$ the difference is ca. 10% and eqn.(2.62) is a reasonable estimate for the steady state current. Table 5.5 shows the experimental data of Wrighton et al. [18] for their dual and triple band devices of microscopic band length. Agreement with theory in this case is generally poor owing to the low collection efficiency, but this is in part due to three dimensional nature of the diffusion field established at these electrodes.

5.1.2.6 BEHAVIOUR OF THE DIFFUSION FIELD AT INTERDIGITATED MICROBAND ARRAY ELECTRODES.

An explanation of the diffusion controlled current time behaviour at

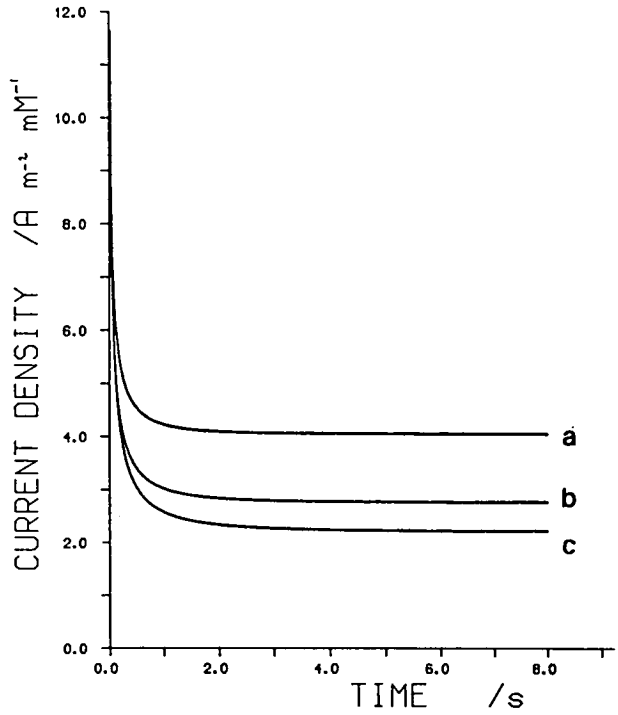

Figure 5.28 Simulated chronoamperometry at the interdigitated microband array electrodes. Bandwidth 95μm and variable band gap, $D=7.0\times10^{-10}m^2\ s^{-1}$. Simulation parameters are given in chapter 2. a. w_g=4.7μm, b. 17.4μm, c. 33.2μm.

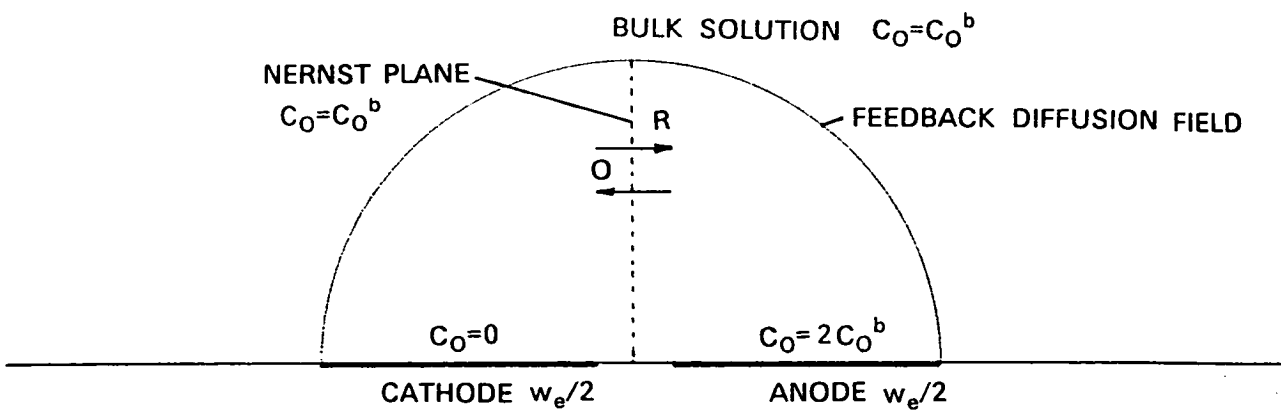

Figure 5.29 Mechanism for feedback diffusion at interdigitated microband anodes and cathodes.

interdigitated microband devices for an electrolyte system initially containing both forms of a reversible redox species may be attempted from diffusion field theory. However, it is informative to consider a molecular view of the relevant transport processes. Following electrode polarisation the oxidised form O of the redox couple is transported from the anodic band by a diffusion mechanism across the microscopic gap to the cathode where it is electrochemically reconverted back to the reduced form R. Species R then flows towards the anode; the converse is true for the cathodic process. The net effect is the establishment of a recycling (feedback) mass flux process between anode and cathode, The mechanism, depicted in figure 5.29, maintains the local concentration of both redox forms at respective electrodes modifying the chronoamperometric characteristics of the microband array electrode with the production of a stable and enhanced diffusion current. It can be appreciated from this mechanism that the important i-t characteristics are linked to the transit time for a species to traverse the inter-electrode space. For the device in this work, a species must travel a distance at least w_g before striking the opposite electrode, taking w_g=18μm and D=7.0x$10^{-10}$$m^2$ s^{-1} and using $\delta=\sqrt{2Dt}$, the minimum transport time is 231ms. The experimental data for the O/R system shows that strong deviation occurs from microband array on the time scale less than 200ms, and that the onset of steady state current is ca 2s.

The current-time response for an interdigitated microband device can be qualitatively appreciated by considering the feedback response relative to that of an isolated microband electrode. The current signal passes through various time phases, the form of the response is dependent on the diffusion regime in operation. The duration of each phase is a complex function of the device geometry. At very short time the diffusion current obeys the Cottrell equation corresponding to a linear diffusion pattern with insignificant contribution from nonlinear flux. Edge effect is observable as electrolysis proceeds affording increased current density. Typical microband electrode response is followed until the interaction of neighbouring diffusion layers i.e. for the equiconcentration O/R case diffusion interaction occurs when fields reach $w_g/2$. This interaction will continue enhancing the current, until the onset a of steady state signal.

The diffusion processes occurring at neighbouring anodes and cathodes are

independent while the diffusion field is less than $w_g/2$, hence the flux and concentration surfaces are identical to that existing at a microband electrode. However, once the condition $\delta > w_g$ is satisfied flux linkage occurs and flux lines are established which extend from the cathode surface to the anode. A transient inter-electrode flux mechanism then co-exists with a bulk diffusional flux process. This inter-electrode flux linkage continues to develop over a time phase which is dependent on the specific dimensions of the device. Total flux linkage is established when the steady state current is observed. Figure 5.30 illustrates the transient behaviour of the feedback diffusion field leading to a total recycling mass flux.

The properties of the interdigitated microband array electrodes have until now been extolled for a system possessing both forms of a reversible redox couple. This was pursued in an attempt to simplify the experimental and simulation conditions, and clarify the major characteristics of device performance. It has been shown in this work and elsewhere that interdigitated microband devices operate for the case when only one form of a redox couple is initially present. A description of this transient feedback diffusion system in terms of a concentration and flux field is involved. For a system containing initially a species O, which undergoes reduction at a microband cathode and oxidation at a neighbouring anodes, the return diffusion field of O must develop with the encroaching cathode field of the reduced form R. This mechanism will therefore include a time lag before species R is detected at the anode. In bipotentiostat experiments the i-t transients of the anode and cathode will be different, and are a function of electrode bandwidth and band gap. A simplified diagramatic representation of the diffusional dynamics of this process is given in figure 5.31.

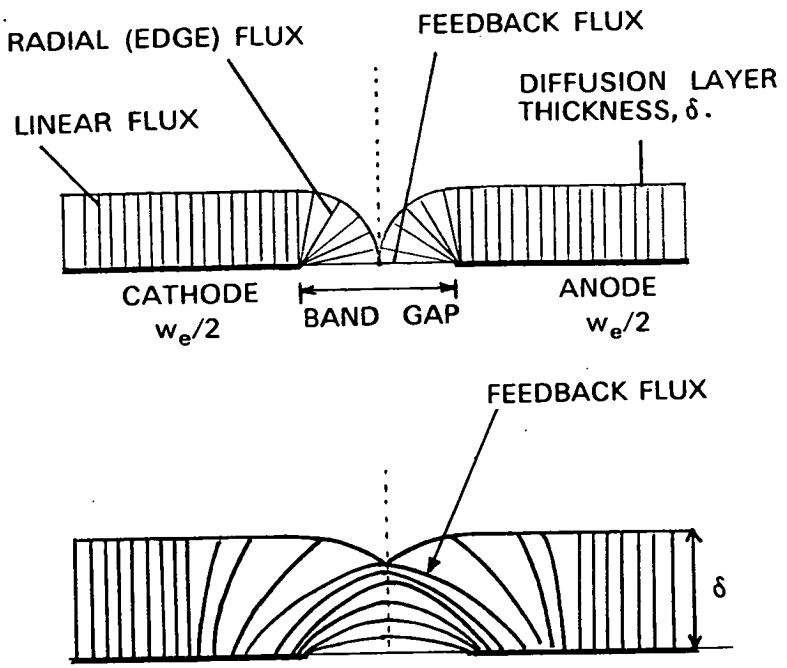

Figure 5.30 Development of the feedback flux at interdigitated microband electrodes for a system initially containing O and R species.

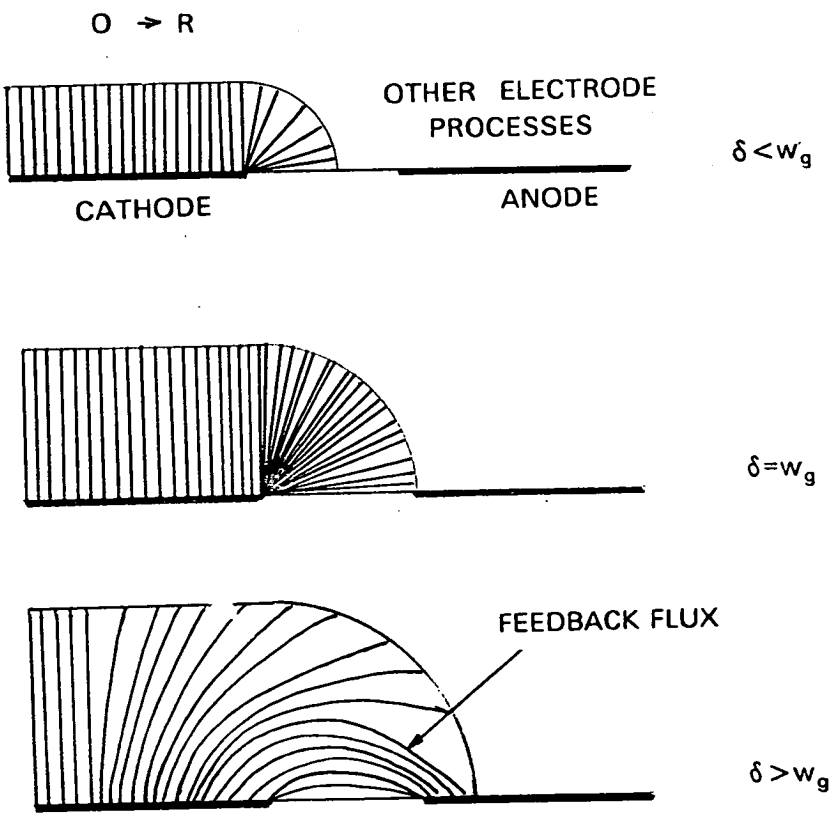

Figure 5.31 Development of the feedback flux at interdigitated microband electrodes for a system initially containing O.

TABLE 5.1 CYCLIC VOLTAMMETRY DATA FOR $FE(CN)_6^{3-/4-}$ AT MICROBAND ARRAY ELECTRODES: EXPERIMENTAL CONDITIONS IN FIG. 5.1.

PARAMETER	ELECTRODE 1	ELECTRODE 2	ELECTRODES 1&2
$E_{p,a}$/mV	265	265	270
$E_{p,c}$/mV	196	205	210
ΔE_{p-p}	69	60	60
$i_{p,a}$/μA	26.6	29.0	40.7
$i_{p,c}$/μA	27.4	28.8	42.0
$i_{p,c}/i_{p,a}$	0.97	1.0	0.97
$i_p(macro)^1$/μAmM^{-1}	9.1	9.1	18.3

1. Data for a macroscopic electrode taking $D=6.4\times10^{-10}m^2\ s^{-1}$ and $v=20mV\ s^{-1}$.

TABLE 5.2 STEADY STATE CURRENT AT THE INTERDIGITATED MICROBAND ARRAY ELECTRODES

CURRENT, i/C /μA μM^{-1}	$Fe(CN)_6^{3-/4-}$	Quinol	$i_{s.s.}/i_p$.
EXPTAL.	21.7	31.0	2.18
THEOR.	21.4	31.4	2.15

Experimental data taken from fig. 5.14 and fig. 5.17. Theoretical current calculated from eqn.(2.62) taking $D=7.0\times10^{-10}m^2\ s^{-1}$.

TABLE 5.3 COMPARISON OF THEORETICAL AND SIMULATION DATA FOR THE STEADY STATE CURRENT AT THE INTERDIGITATED MICROBAND ARRAY ELECTRODES.

w_e /μm	w_g /μm	w_e/w_g	i/CA(SIM.) Am^2mM^{-1}	i/CA(THEOR.) Am^2mM^{-1}	% DIFF.
95.0	33.2	2.9	2.22	1.84	-20.7
95.0	17.4	5.5	2.75	2.31	-19.0
95.0	4.7	20.0	4.04	3.38	-19.5

Taking $D=7.0\times10^{-10}m^2\ s^{-1}$.

TABLE 5.4 STEADY STATE CURRENT FOR INTERDIGITATED MICROBAND ARRAY ELECTRODES.

w_e/μm	w_g/μm	l/mm	w_e/w_g	n	i(exptal.) /μA mM^{-1}	i(theor.) /μA mM^{-1}	% diff.
10.0	2.0	2.0	5	25	20.3	18.3	-10.1
5.0	2.0	2.0	2.5	50	33.9	22.5	-33.6
3.0	2.0	2.0	1.5	50	29.6	18.3	-38.0

Experimental data was taken from Aoki et al. [21]. The theoretical current was calculated from eqn.(2.62) taking $D=24\times10^{-10}m^2\ s^{-1}$.

TABLE 5.5 COMPARISON OF EXPERIMENTAL AND THEORETICAL CURRENT AT DUAL AND TRIPLE INTERDIGITATED DEVICES.

n_c	n_g	w_e /μm	w_g /μm	l /mm	w_e/w_g	i/C (THEOR.) /μAmM^{-1}	i/C (EXPTAL.) /μAmM^{-1}
2	1	2.3	1.0	50	2.3	4.1	7.4
2	1	2.3	4.7	50	0.49	2.1	5.1
2	1	2.3	8.3	50	0.28	1.6	4.6
1	1	3.15#	0.2	50	15.8	9.1	15.4

Experimental data was taken from reference 18. The theoretical data was calculated using eqn.(2.62).

#Mean value of bandwidth.

5.2 AMPEROMETRIC RESPONSE OF THIN LAMINATE BAND ELECTRODES.

5.2.1 AMPEROMETRIC CHARACTERISATION OF THIN LAMINATE SUBMICROMETER BAND ELECTRODES.

The cyclic voltammetry for the reduction of $Fe(CN)_6^{3-}$ in aqueous KCl solution at nanometer bandwidth laminate band electrodes is compared with the behaviour for a macroscopic electrode in figures 5.32 & 5.33. The sigmoidal i-E response observed for such small scale electrodes is typical of an enhanced diffusional transport process to a finite microscopic electrode surface; details are in tables 5.6 & 5.7.

Figure 5.34 shows the dependence of voltammetric characteristics with voltage sweep rate, v, for a reversible redox species at a submicroscopic band electrode. At slow sweep rate the limiting diffusion current remains independent of electrode potential. However, peak behaviour becomes more pronounced for $v > 100mV\ s^{-1}$, indicative of symmetry changes occurring to the diffusion field. Other noteworthy voltammetric features for the laminate electrode include, background current effects in the form of increased base line slope and i-E hysteresis. There is no noticeable shift in $E_{p,c}$ with v compared to the macroscopic electrode, where currents of the order 30μA pass giving rise to observed iR_u effects. For the submicron band electrode there is no change in the limiting current with sweep rate over the range $10mV\ s^{-1}$ to $1V\ s^{-1}$.

Observations such as these earmark the amperometric differences with macroscopic electrodes and are a direct consequence of the nature of the diffusion field, i.e. size and geometry relative to the electrode geometic features. The independence of the limiting current with sweep rate for submicron band electrodes at fast sweep rate results from the high rate of diffusional flux predominating.

A hemicylindrial diffusion field is quickly established (ca. 100ms) at band electrodes of submicron dimension; a field pattern which maintains high mass flux to the electrode. Only until the voltage sweep rate reaches a critical value, is there an observed sweep rate dependence. At this value of sweep rate, the diffusion field does not evolved on the voltammetric time scale to a hemicylindrial field (perhaps elliptic hemicylinder). Only at very high sweep

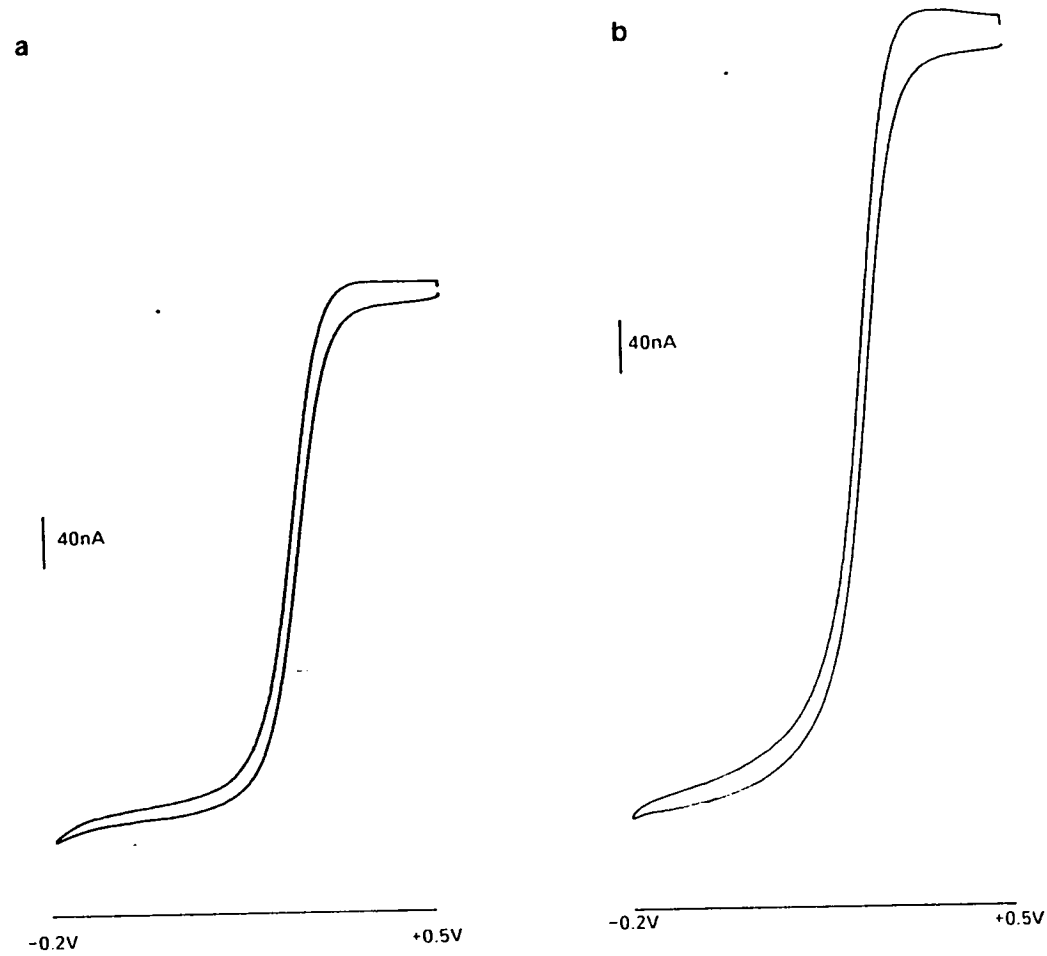

Figure 5.32 a. Cyclic voltammetry of potassium ferricyanide (1.18mM) in aqueous KCl (1.3M) at a thin laminate band electrode, v=10mV s^{-1}, potential sweep +0.5V to -0.2V vs. SCE.

Polyimide laminate, gold film 100nm, laminate length 11.6mm with 2µm negative photoresist.

b. Cyclic voltammetry of potassium ferricyanide (1.18mM) in aqueous KCl (1.3M) at a thin laminate band electrode v=20mV s^{-1}, potential sweep +0.5V to -0.2V vs. SCE.

Polyester laminate, gold film 50nm, laminate length 18.3mm with 2-3µm positive photoresist.

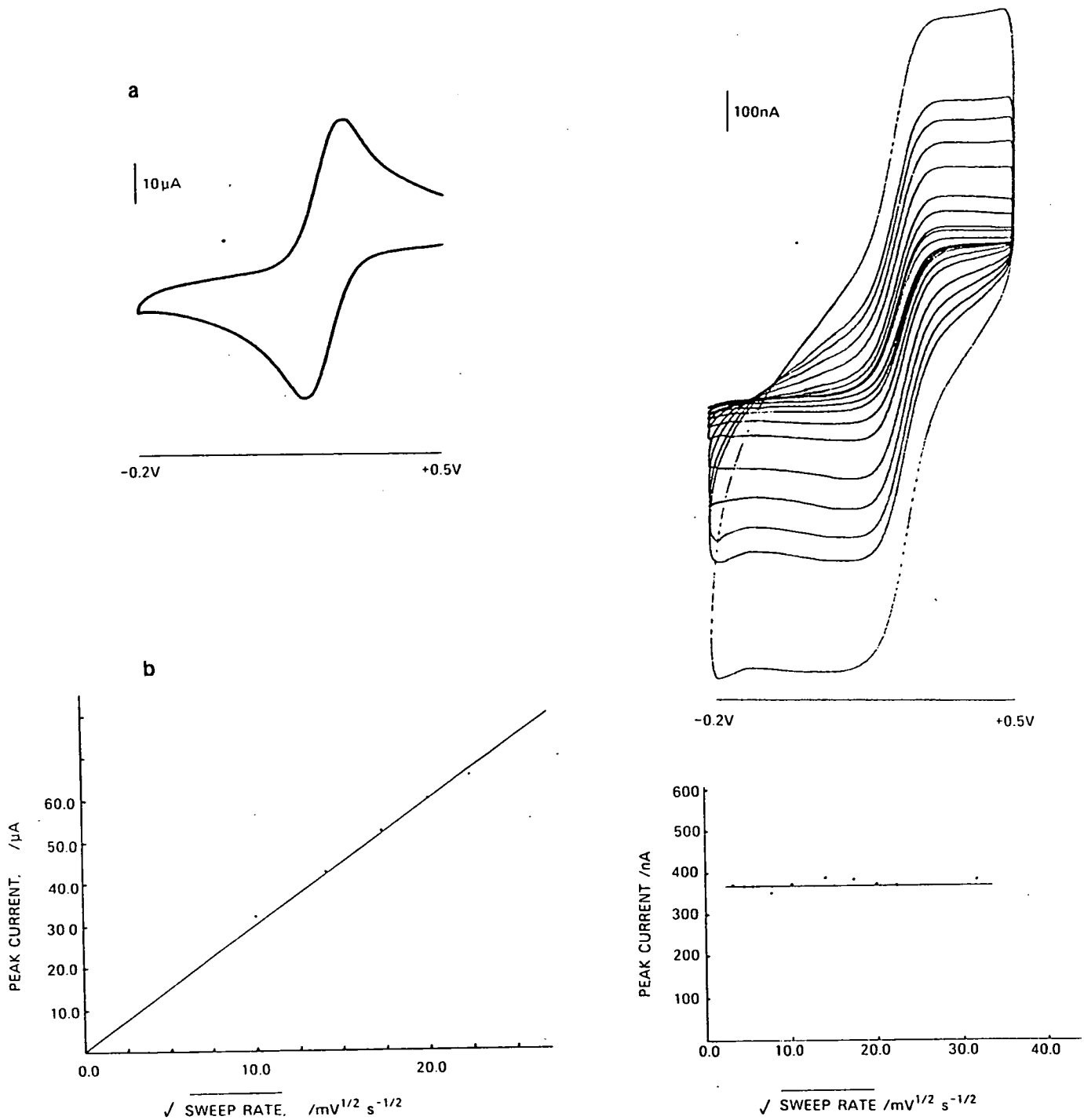

Figure 5.33 a. Cyclic voltammetry of $K_3Fe(CN)_6$ (1.0mM) in KCl (1.0M) at a macroscopic gold electrode 6.5mm × 2mm. Potential sweep from +0.5V to −0.2V vs. SCE, v=100mV s^{-1}. b. plot of i_p against $\sqrt{v}$.

Figure 5.34 Potential sweep rate dependence of peak current for a submicron band electrode: voltammetric conditions as for fig. 5.32a, v=10mV s^{-1} to 1000mV s^{-1}.

rate, which is a function of bandwidth, will the diffusion field approximate a linear field; over such values of sweep rate the voltammetric behaviour of a microband electrode is then equivalent to a macroscopic electrode.

The diffusion controlled current–time response following a potential step for the reduction of $Fe(CN)_6^{3-}$ at gold band electrodes of bandwidth, w_e=50nm and 100nm are shown in figure 5.35. The current after 5s electrolysis at such electrodes is 486nA mM^{-1} and 330nA mM^{-1} respectively . For electrodes of nominal area 915μm^2 and 1160μm^2, this corresponds to current densities of 531A m^2 mM^{-1} and 285A m^2 mM^{-1}. The corresponding current density for a macroscopic electrode is 0.68A m^2 mM^{-1}. The experimental i–t data illustrate the relative insensitivity of the diffusion current to bandwidth, as discussed for the theoretical case in chapter 2. In this instance a twofold reduction in bandwidth leads only to a 7% drop in the diffusion current at t=5s.

The higher flux density evident at the surface of submicroscopic band electrodes by comparison with macroscopic electrodes is interpreted in terms of diffusion field geometry. The large flux per unit electrode area is a result of an extensive diffusion layer surface formed after several seconds electrolysis. As the diffusion field at a submicrometer band electrode evolves, cf. fig.2.4, initially from a planar geometry on a very short time scale (which is a function w_e), and at later time as edge effect increases, through an elliptic and then hemicylindrical field pattern, the number of flux lines linking the diffusion surface and electrode increases. This field phenomenon is not found for the linear field at macroscopic electrodes where flux linkage remains constant affording a greater rate of current decay with time. A further predominating feature of the diffusion field is the size of the diffusion layer thickness, δ resulting in high concentration gradients at the electrode.

Chronoamperometric behaviour of a gold band electrode w_e=50nm, l=56.3mm at long electrolysis time, for the oxidation of $Fe(CN)_6^{4-}$, was found to exhibit a virtual steady state over an extended period, 4min., without convectional disturbance. This observation was reported previously for submicroscopic band electrodes by Saito et al. [2]. The effect again originates with the properties of the diffusion field, in this case the finite microscopic size, $\delta <$ 0.3μm for t < 10s. Influence of solution motion originating from density gradients induced from various sources, including external thermal effects and vibration, etc have less influence on a small diffusion field and hence the

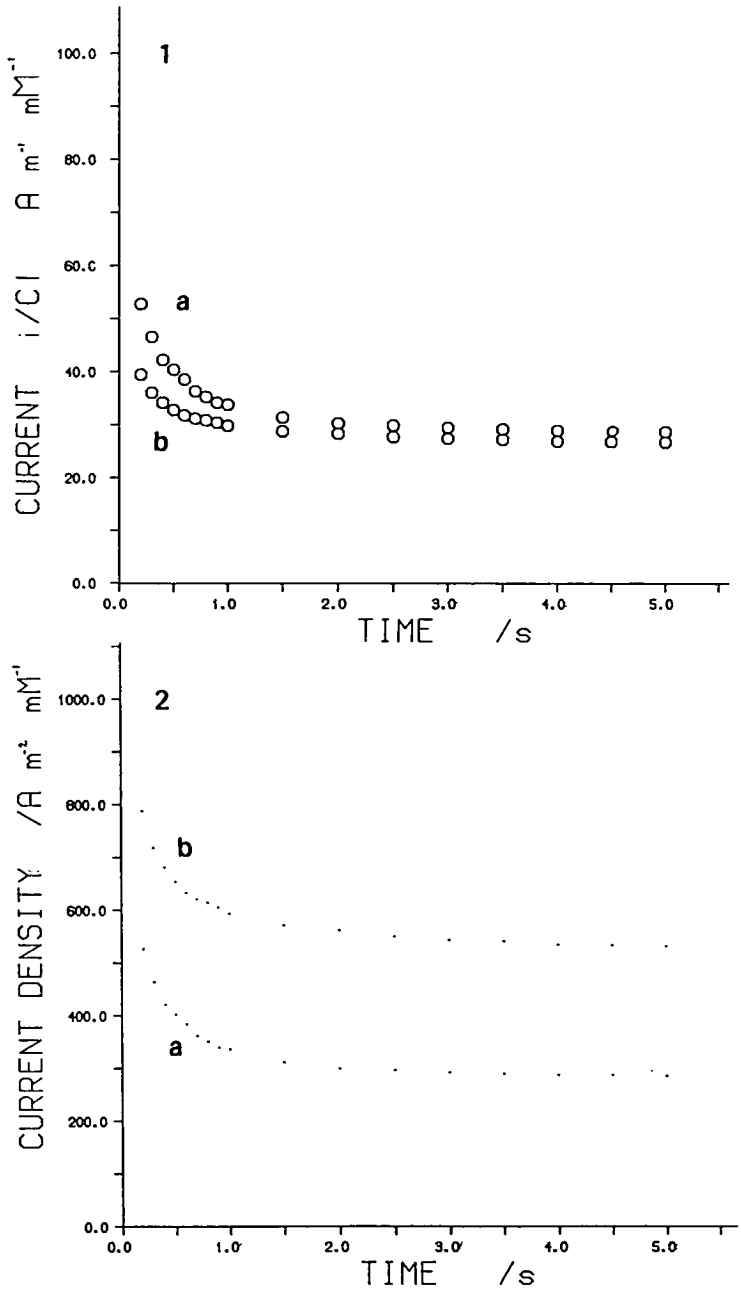

Figure 5.35 1. Chronoamperometry for reduction of $K_3Fe(CN)_6$ (1.18mM) in KCl (1.3M) at submicroscopic band electrodes. Potential step +0.5V to 0.0V vs. SCE. a. w_e=100nm, b. w_e=50nm.

2. current density-time plot, conditions as for fig. 5.3 5 .1.

diffusion current at submicroscopic electrodes.

5.2.2 THE HEMICYLINDRICAL FLUX EXPRESSION AS AN APPROXIMATION FOR THE CHRONOAMPEROMETRIC RESPONSE OF SUBMICROMETER BAND ELECTRODES.

The limiting expression described in chapter 2, eqn.(2.16) describing the i-t behaviour for a theoretical submicrometer cylinder electrode approximates the response of equivalent band geometry for electolysis time 0.01s to 10s. The applicability of eqn.(2.22) for the i-t response of submicron band electrodes has been reported elsewhere [36]. The aim here is to verify the approximation for thin laminate based electrodes. Experimental chronoamperometric data are compared with the theoretical curves for a 50nm and 100nm band electrode, in figure 5.36, showing good long time agreement within the bounds of fabrication errors. The discrepency observed at short time electrolysis (greater for larger w_e) however, may be a result of the inadequacy of the hemicylindrical approximation or indicative of electrode condition (error in bandwidth). The diffusion current density measured by cyclic voltammetry using laminate electrodes are listed in table 5.6, along with data from the hemicylindrical flux expression.

Diffusion current verses concentration plot, illustrated in figure 5.38, shows a direct proportionality for micromolar analyte concentration. The slope of this plot is in good agreement with theory and is discussed below.

5.2.3 AMPEROMETRIC ANALYSIS USING SUBMICROSCOPIC BAND ELECTRODES.

Figure 5.37 compares the cyclic voltammetry for ca. 60µM potassium ferricyanide at a macroscopic gold disc electrode with a 100nm band electrode. The effects of background current at macroscopic electrodes are most evident at micromolar analyte concentration. The application of thin laminate submicron band electrodes to the amperometric determination of reversible redox substances at low micromolar level was demonstrated using quasi-steady state chronoamperometry for $Fe(CN)_6^{3-}$ in aqueous molar KCl solution.

For analyte concentration above 10µM the i-t response is clearly discerned above the faradaic background current. For aqueous KCl (1.3M) the background current at t=10s was 1.5nA compared to an analyte current of 5.7nA, C=10µM.

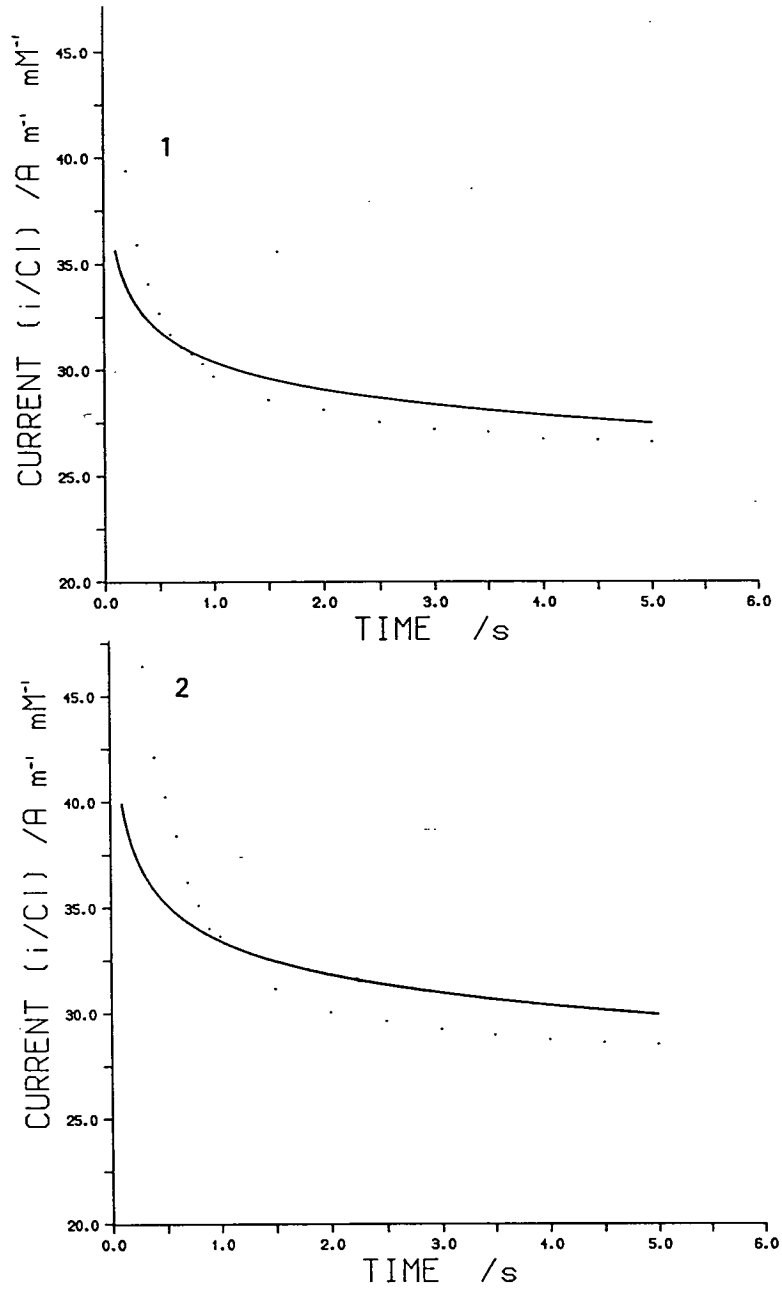

Figure 5.36. Chronamperometry for the reduction of $K_3Fe(CN)_6$ (1.18mM) in KCl (1.3M) at laminate band electrodes, (1) w_e=50nm,(2) w_e=100nm.

dot curve: experimential data, conditions as for 5.35.1.

solid curve: theoretical data from eqn.2.19taking $D=7.6\times10^{-10} m^2\ s^{-1}$.

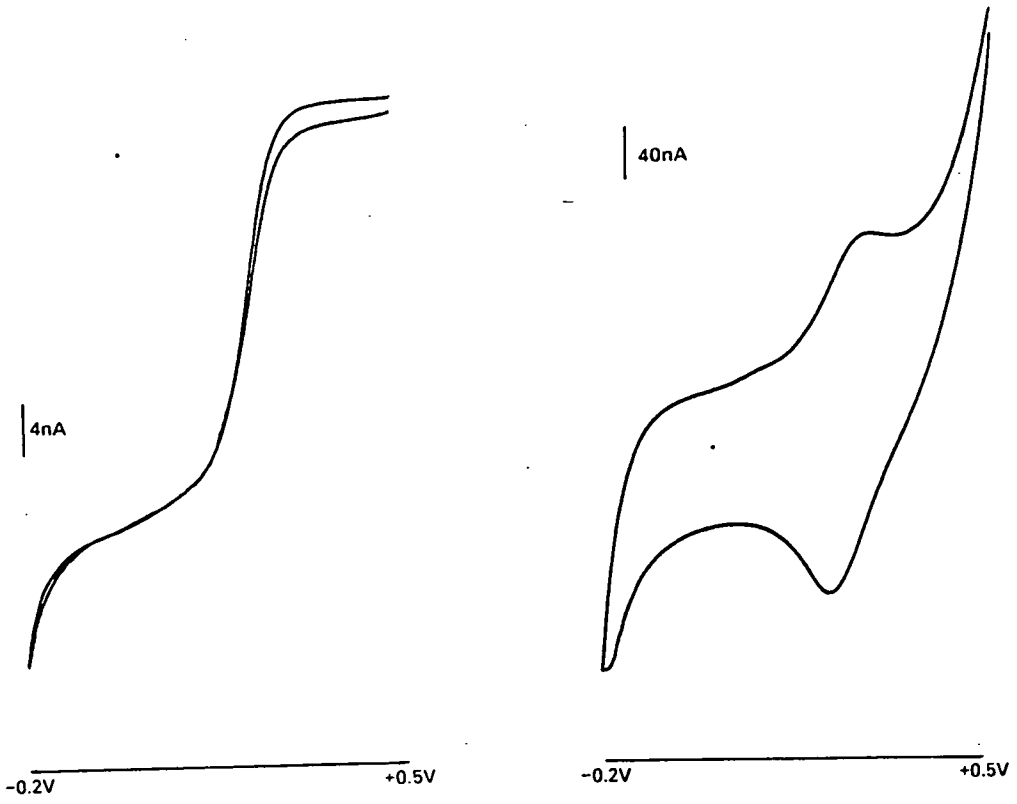

Figure 5.37 a. Cyclic voltammetry of $K_3(CN)_6$ at micromolar concentration (60.7μM) in aqueous KCl (1.0M) using a 100nm band electrode, l=11mm. Potential sweep, +0.5V to -0.2 vs. SCE, v=2mV s^{-1}. b. as for a. using a gold disc electrode of radius 0.5mm.

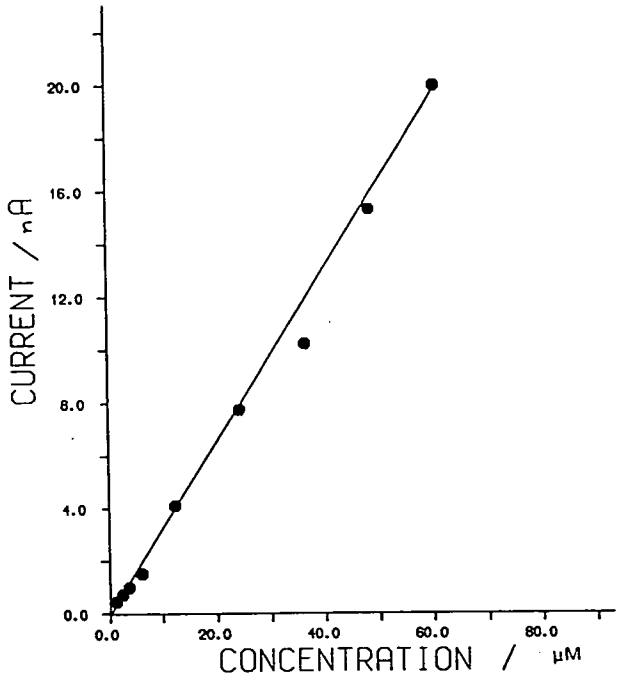

Figure 5.38 Plot of diffusion current against concentration for $K_3Fe(CN)_6$ in aqueous KCl (1.0M) at a 100nm band electrode polyimide laminate, l=11mm. The diffusion current sampled at t=10s following a potential step, +0.5V to 0.0V vs. SCE.

A plot of diffusion current against concentration was linear in $C(Fe(CN)_6^{3-})$ from 1.2μM to 61μM with slope i(t=10s)/C, 0.329nA mM^{-1}. This compares favourably with the theoretical value of 0.294nA mM^{-1}, taking $D=7.6x10^{-10}m^2$ s^{-1}, see fig. 5.38. The lowest concentration measured using the 100nm band electrode was 0.5μM, however the noise levels observed for the measurement of subnanoampere current with the present instrumentation was appreciable, limiting detection levels above 1μM. Figure 5.39 shows the i-t curves for the reduction of 0.97μM $Fe(CN)_6^{3-}$ in aqueous KCl and the background. In this work the amperometric sensitivity of the technique was 329pA μM^{-1}, with background currents typically 1.3nA at t=10s: a background current density of 2.7A m^{-2} compared with 0.01A m^{-2} for macroscopic electrodes.

5.2.4 THE EFFECTS OF BANDWIDTH ON THE VOLTAMMETRIC RESPONSE OF SUBMICROSCOPIC BAND ELECTRODES.

The voltammetric behaviour of reversible redox species at submicroscopic band electrodes, exemplified by $Fe(CN)_6^{3-/4-}$, for bandwidth greater than 50nm exhibit a sigmoidal i-E wave illustrating the presence of a diffusion limiting current in the voltage region scanned. Furthermore, the obeyence of the limiting current to a diffusion expression suggests that within this voltage region the measured current is diffusion controlled. This condition no longer applies as the bandwidth is diminished. Figure 5.40 shows the cyclic voltammetry of $Fe(CN)_6^{3-}$ at a 10nm band electrode. The i-E wave over the voltage range used previously for larger bands no longer demonstrates a mass transport limitation. Figures 5.41 and 5.42 illustrate the effects of the submicron bandwith on the reversible voltammetric behaviour of quinol and catechol. For macroscopic electrodes the oxidation wave is evident within the voltage window, however for a 100nm gold band electrode, the voltammetric wave is shifted to greater positive potential. This behaviour may have origin with the high flux density which influences the charge transfer process. It is likely that a correlation will exist between the rate of charge tranfer and bandwidth for submicroscopic band electrodes.

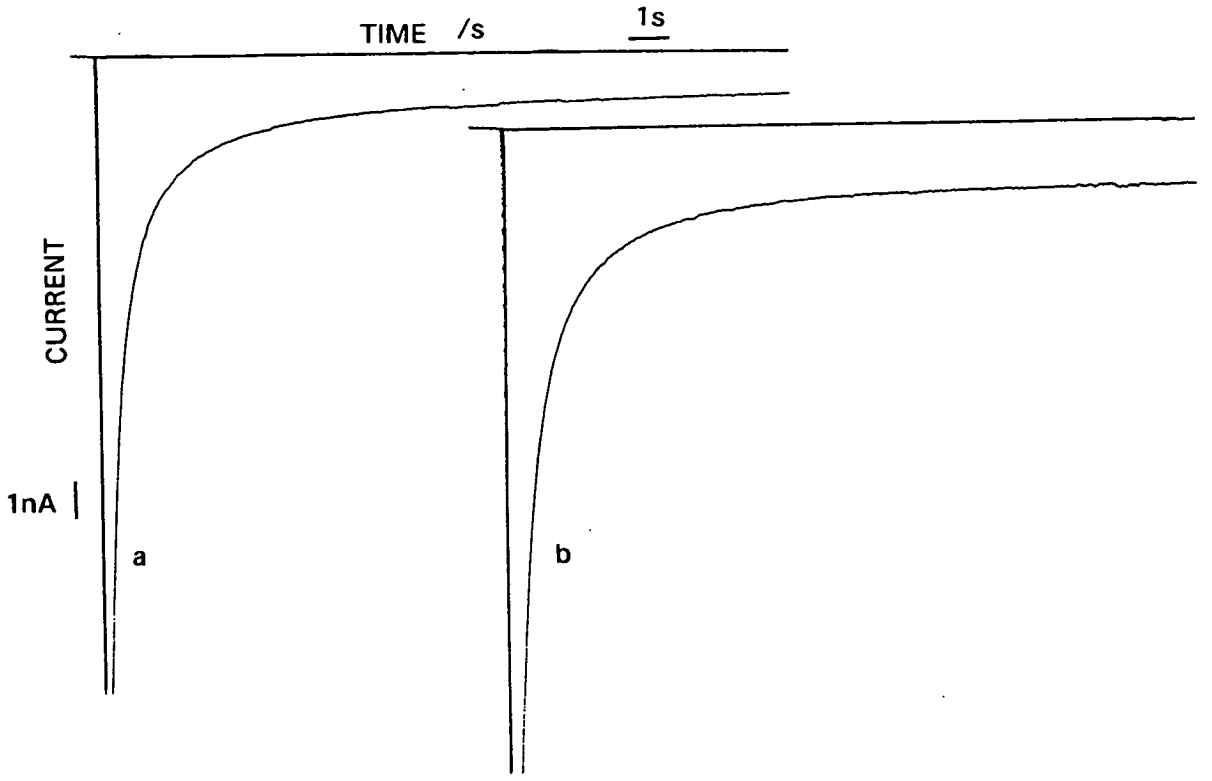

Figure 5.39 Chronoamperometry for the determination of $Fe(CN)_6^{3-}$ in aqueous KCl (1.3M). Potential step +0.5V to 0.0V vs. SCE. a. background, b. 0.97µM.

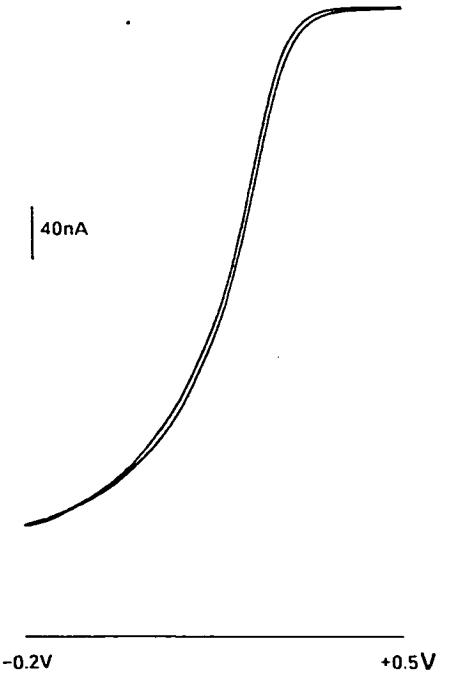

Figure 5.40 Cyclic voltammetry of potassium ferricyanide (1.18mM) in aqueous KCl (1.3M) at a submicron band electrode, w=10nm, l=28.6mm. Polyimide laminate with 1µm negative photoresist , potential sweep +0.5V to −0.2V vs. SCE, v=10mV s^{-1}.

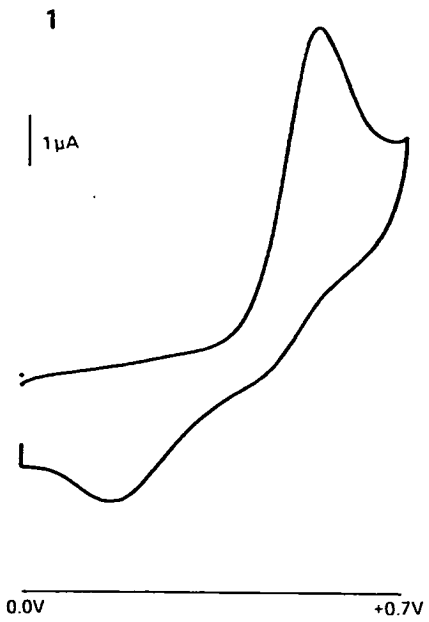

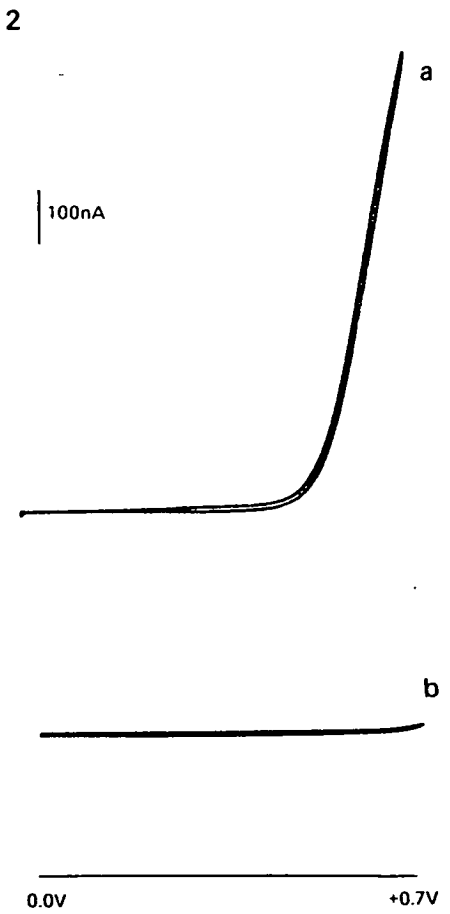

Figure 5.41 (1) Cyclic voltammetry for the oxidation of quinol (2.6mM) in acidic KCl (1.0M) solution, at a gold disc electrode 1mm dia. Potential sweep from 0.0V to +0.7V vs. SCE, v=10mV s^{-1}

(2) Cyclic voltammetry for the oxidation of quinol, conditions as for fig. 5.10 (1) using a gold band electrode w=100nm l=11mm. (a) quinol 2.6mM, KCl 1.0M, HCl 0.1M, (b) KCl 1.0M, HCl 0.1M.

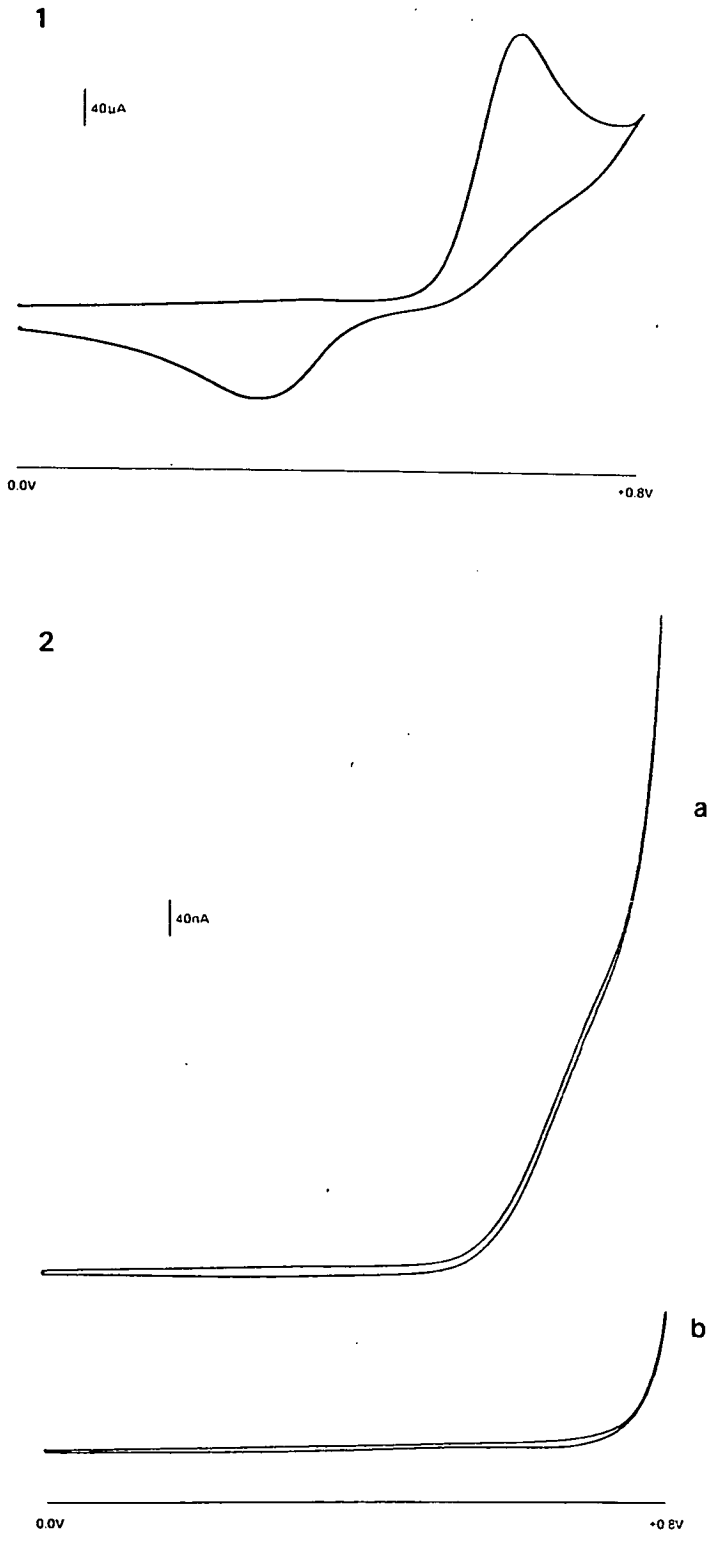

Figure 5.42 1. Cyclic voltammetry of catechol (1.14mM) in aqueous KCl (1.0M), pH 1, at a gold plate electrode, 6.6mmx2.3mm, v=10mV s^{-1}, potential sweep 0.0V to +0.8V vs. SCE.

2. details as for (1) using 100nm Au band electrode, l=9mm.

a. catechol, b. KCl (1.0M), pH=1.

TABLE 5.6 CYCLIC VOLTAMMETRY DATA FOR POTASSIUM FERRICYANIDE AT GOLD SUBMICROMETER BAND ELECTRODES.

w /nm	l /mm	Area /μm^2	i_c nA, E=0.0V	i_a /nA, E=+0.5V	i_c/i_a	i_c/Cl /μAmM^{-1}	$E_{\frac{LIM}{2}}$	i_c/CA EXPT.	i/CA THEOR. Am^2mM^{-1}
100	11.6	1160	370	362	1.02	27.1	+0.200	270.6	267.6
50	18.3	915	546	521	1.05	25.3	+0.155	596.7	495.3
10	28.6	28.6	352	352	1.00	10.4	-	1143.8	2111.3

Data taken from figure 5.32.

TABLE 5.7 CYCLIC VOLTAMMETRY FOR THE REDUCTION OF $Fe(CN)_6^{3-}$ (1.0 mM) IN KCL (1.0M) AT A GOLD ELECTRODE. REFER TO FIGURE 5.33.

l/mm	w/mm	AREA/mm^2	$E_{p,c}$/V	$E_{p,a}$/V	ΔE_{pp}	i_c/μA	i_a/μA	i(theor.)
6.5	2	13	+0.190	0.265	0.075	32.6	33.0	30.5

5.3 AMPEROMETRIC RESPONSE OF DUAL MICROCYLINDER ELECTRODES.

5.3.1 A SINGLE MICROCYLINDER ELECTRODE: THE ISOLATED MICROCYLINDER ARRAY ELECTRODE.

5.3.1.1 CYCLIC VOLTAMMETRY.

Over recent years the amperometric properties of single microwire electrodes have been characterised as mentioned previously. Here a brief description of the amperometric response in terms of the diffusion field will be attempted. The analysis equally applies to a device consisting of an arrangement of microscopic cylinder electrodes into a parallel array where diffusion processes at individual microelectrodes are considered isolated.

Figure 5.43 shows the cyclic voltammetric behaviour of a microscopic platinum wire electrode for the oxidation of $Fe(CN)_6^{4-}$ in aqueous KCl solution. For an electrode of this dimension, r=12.5μm, peaked i-E characteristics are observed at sweep rates above 5mV s^{-1}. The behaviour of a carbon fibre electrode, r=3.4μm, for the oxidation of catechol in phosphate buffer pH=7, shows steady state current behaviour at sweep rate 10mV s^{-1}, see fig. 5.44. Thus it is possible to obtain a steady state current by slow sweep rate voltammetry, although convectional effects possibly contribute to the sigmoidal i-E wave at slow sweep rate.

5.3.1.2 CHRONOAMPEROMETRY.

An empirical expression (eqn.5.1) was presented by Aoki et al. [32] for the chronoamperometric response of microcylinder electrodes. The equation has general application and is considered here.

$$i = nFDCl(1/\sqrt{\pi\theta}+0.422-0.0675\log(\theta\pm 0.0058(\quad (\log(\theta)-1.47)^2) \qquad (5.1)$$

The chronoamperometric (from eqn. 5.1) data for the oxidation of $Fe(CN)_6^{4-}$ at Pt wire electrodes, r=250μm and 12.5μm, given in figure 5.45 show the effects of electrode dimension on the i-t response. Electrodes of microscopic size generate higher current density than a macroscopic wire owing to the larger δ/r ratio affording greater flux linkage per unit area for the microscopic case. The data also serve to show the insensitivity of the current density with electrode radius.

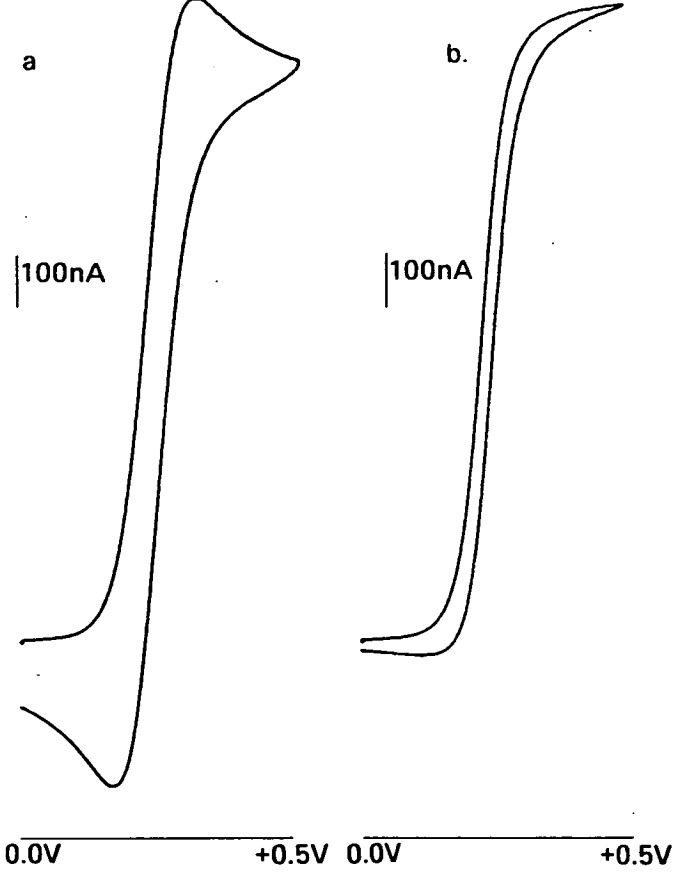

Figure 5.43 Cyclic votammetry for the oxidation of $K_4Fe(CN)_6$ (0.89mM) in aqueous KCl (0.7M) at a platinum microcylinder electrode, r=12.5μm, l=13mm. Potential sweep from 0.0V to +0.5V vs. SCE. a. 20mV s^{-1} b. 5mV s^{-1}.

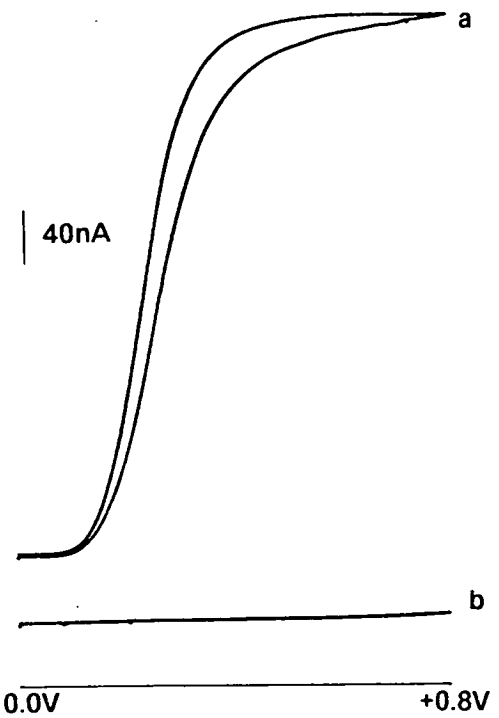

Figure 5.44 a. Cyclic voltammetry for the oxidation of Catechol (1.14mM) in aqueous Na_2HPO_4, NaH_2PO_4 (0.2M,pH=7) at a carbon fibre electrode, r=3.4μm, l=1.2mm (preconditioned fibre). Potential sweep 0.0V to +0.8V vs. SCE, v=10mV s^{-1}.

b. cyclic voltammetry for aqueous Na_2HPO_4,NaH_2PO_4 (0.2M,pH=7), conditions as for a.

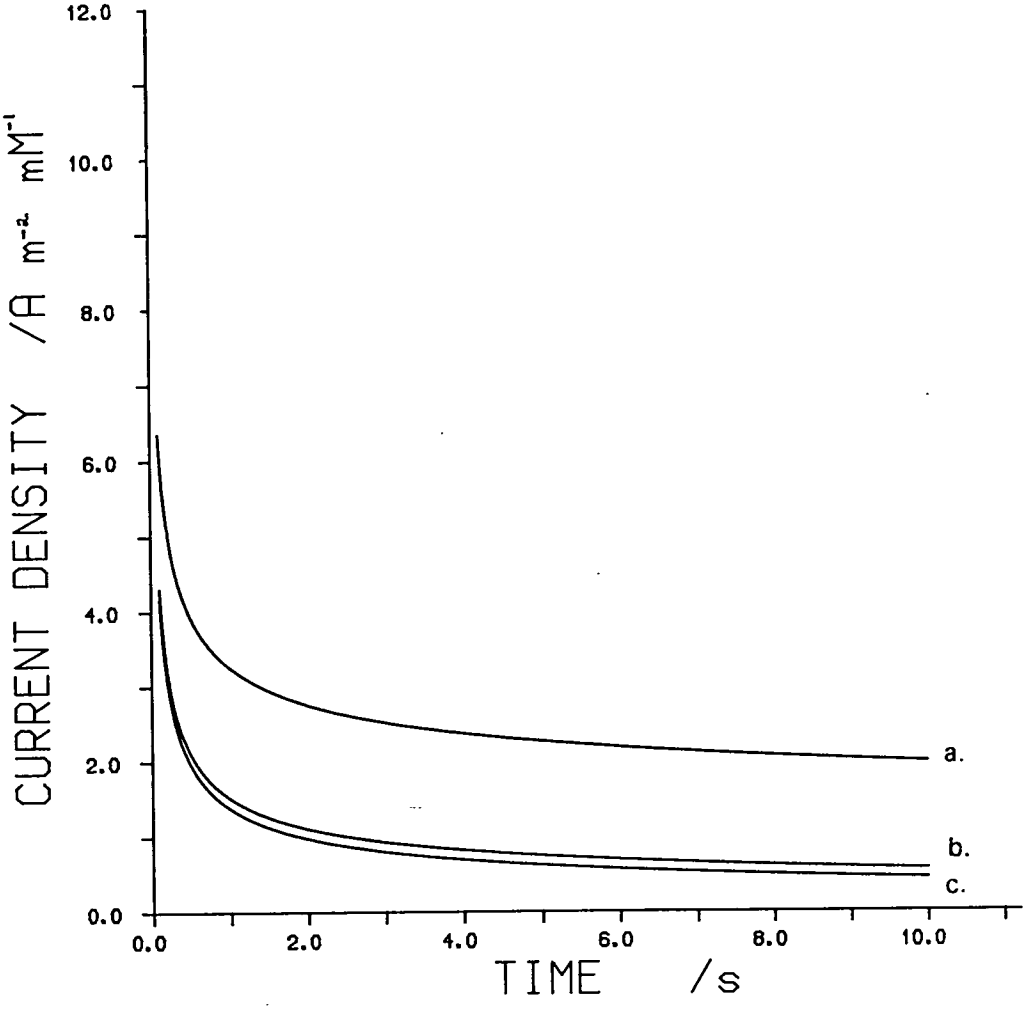

Figure 5.45 Theoretical current-time curves for microcylinder electrodes. Data is calculated from eqn.(5.1) taking $D=6.4\times10^{-10}m^2\ s^{-1}$. a. r=12.5μm, b. 250μm c. Cottrell curve.

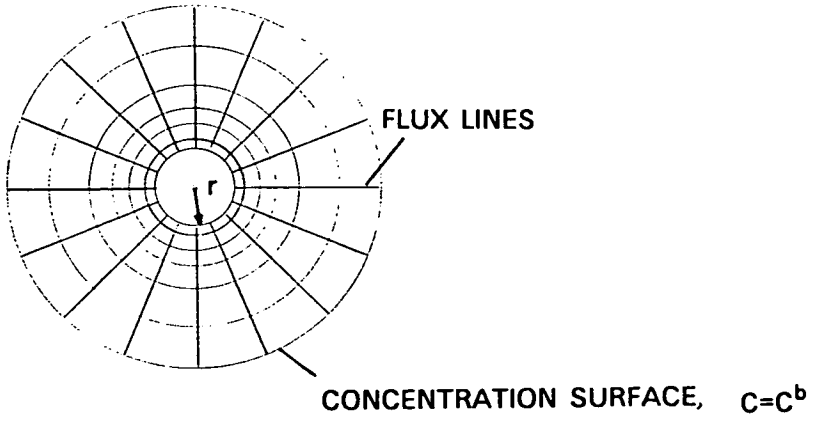

Figure 5.46 Diffusion field at a given time for a microcylinder electrode illustrating the radial flux lines and concentric circular concentration surfaces.

5.3.1.3 DESCRIPTION OF THE DIFFUSION FIELD AT A MICROSCOPIC CYLINDER ELECTRODE.

The time dependent behaviour of the diffusion current at single or isolated microcylinder electrodes follows a short time Cottrell response when the diffusion layer is small relative to the electrode radius; during this phase the curvature of the electrode has no influence on the mass transport process. At a later time, dependent on r, the i-t response deviates from linear behaviour as radial flux becomes important. From fig. 5.45, it is seen that the deviation occurs at shorter time for the microscopic electrode. The diffusion pattern at microscopic cylindrical electrodes at some instant in time is illustrated in figure 5.46 showing the geometrical nature of the concentration and flux surfaces. Surfaces of equiconcentration lie concentric to the electrode, while lines of flux project radially from the electrode into a mature diffusion field. For this field pattern the total volume occupied by the diffusion layer after several seconds electrolysis greatly exceeds that of the microelectrode.

5.3.2 MICROCYLINDER ELECTRODE: EFFECTS OF AN INERT MICROSCOPIC OBSTRUCTION.

The diffusion current at a micrometer scale electrode is sensitive to geometrical form of the environment. This is the case since the current-time characteristic alters with the changing geometry of the diffusion field at a microelectrode. How sensitive the electrode is to such effects will depend on the environmental inflence (size, geometry and distance from electrode) as well as the geometrical nature of the diffusion field. The simplest case of diffusion field modulation in this way occurs for macroscopic electrodes arranged in a thin layer cell. Once the expanding linear field reaches the cell wall the mass flux will rapidly decrease and exhaustive electrolysis ensues.

For a microcylinder electrode, once the diffusion field reaches an inert surface the field will deform from purely cylindrical geometry to a more complex form unique to the new environment. Correspondingly the i-t response will alter from that of an isolated cylinder. A simple model for this effect is a microcylinder electrode placed near an inert plane. In this instance however, the diffusion field induced at a microwire electrode is interupted by an inert microscopic object of cylindrical geometry lying parallel, i.e. the second electrode of the dual wire device at open circuit. Diffusional transport

problems such as this, where the flux has both time and multi-dimension space dependence are complex and require the application of numerical techniques for solution. However, a qualitative picture of the diffusion field can be appreciated by consideration of events leading to the changes in flux and concentration surfaces. Figure 5.47 are representations of the diffusion field at a microscopic cylindrical electrode and object system. Until the diffusion field impinges on the object, the i-t response is identical with an isolated electrode. Once contact is made, and the field progresses over the inert cylinder, the concentration of species between the electrode and object is disproportionally depleted. This thin layer effect invokes the condition;

$$\partial C/\partial \theta \neq 0$$

i.e. concentration gradients are set up in the θ co-ordinate in response to this depletion. The new concentration gradients will tend to distort the original cylindrical concentration field geometry. The outcome of such time dependent effects on the diffusion current is a complex function of electrode and inert cylinder radii and separation. Figure 5.48 shows the i-t data for an electrode-obstruction system applicable here, where w_g=2.7µm and 13.5µm. The data demonstrates the diffusion current dependence on the spacing distance, and suggests that current enhancement occurs with a reduction in electrode separation.

5.3.3 DUAL MICROCYLINDER ELECTRODES: COMMON APPLIED POTENTIAL.

5.3.3.1 CYCLIC VOLTAMMETRY.

Cyclic voltammetry of $Fe(CN)_6^{3-/4-}$ at a platinum dual microcylinder electrode are shown in figures 5.49-5.51. For device PT2 (cf. table 3.2), where w_g=36µm, the individual wire electrodes demonstrate similar voltammetric behaviour in terms of wave features, peak current and potential, as listed in table 5.8. The difference observed in $i_{p,a}$ for this device, 5.2nA, lies within fabrication error of ±10%. Agreement between the i-E response of closely spaced microwires is an indication of a reasonable fabrication method. The effects on the voltammetric wave of a second microcylinder electrode positioned parallel and at a microscopic distance (36µm) is seen in fig. 5.49c. The i-E wave has pronounced peak characteristics in addition to giving rise to a larger peak current. Reference to table 5.8 shows the increase in $i_{p,a}$ is less than twice the

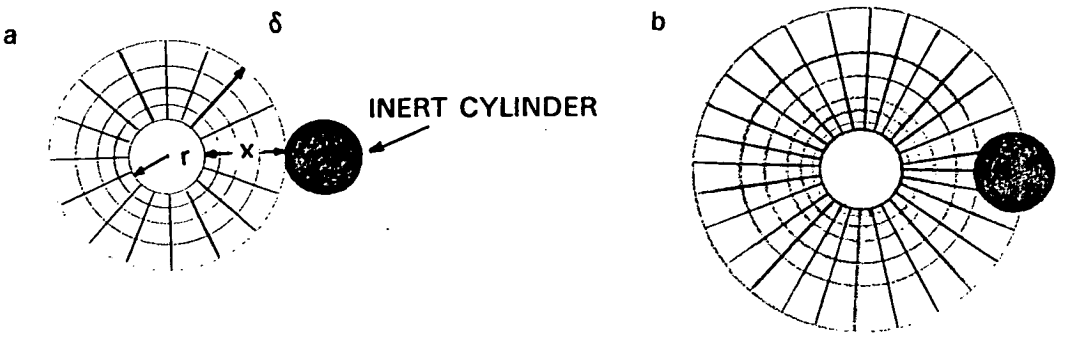

Figure 5.47 Diffusion field at a microcylinder electrode. a. before field interaction with an inert parallel cylinder, $\delta \leqslant x$, b. condition for $\delta > x$.

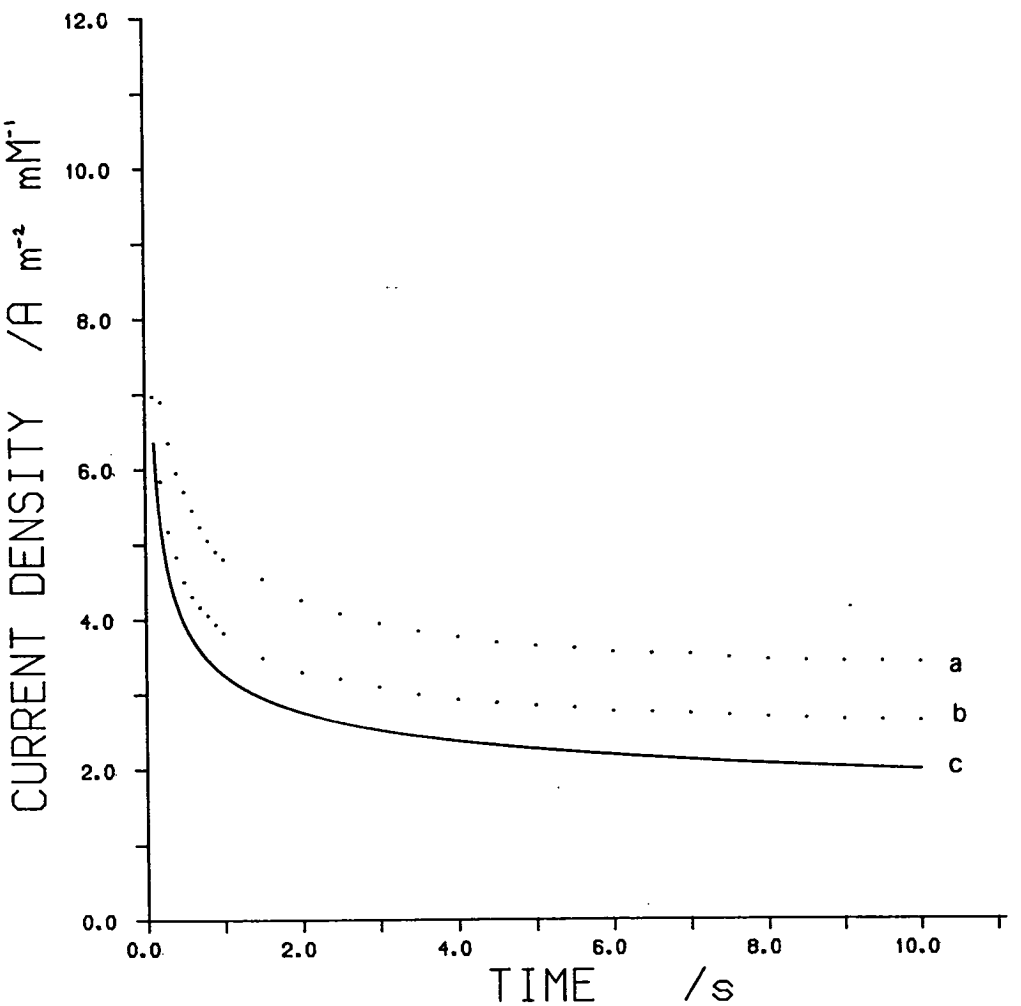

Figure 5.48 Chronoamperometry for the oxidation of $K_4Fe(CN)_6$ (1.0mM) in the KCl (1.0M) at a Pt wire electrode, r=12.5μm. Potential step 0.0V to +0.5V vs. SCE. a. w_g=2.7μm b. w_g=13.5μm

c. Data taken from eqn.(5.1) for electrode radius 12.5μm and D=6.4 $\cdot 10^{-10} m^2 s^{-1}$.

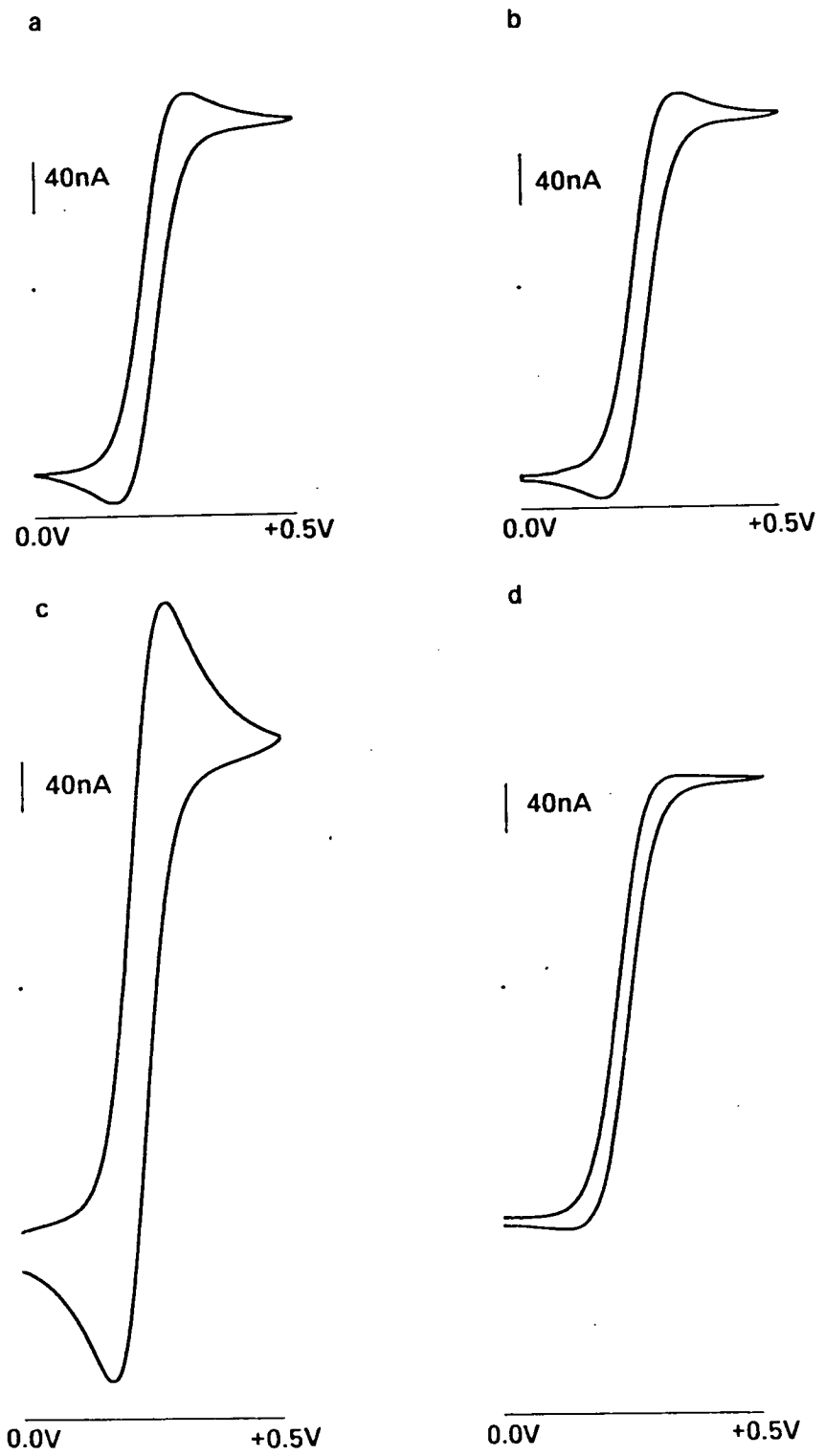

Figure 5.49 Cyclic voltammetry for $K_3Fe(CN)_6$ (1.0mM), $K_4Fe(CN)_6$ (1.0mM) in KCl (1.0M) at Pt dual microcylinder electrodes, r=12.5µm and w_g=36.3µm, l=0.65mm. Potential sweep 0.0V to +0.5V vs. SCE. v=10mV s^{-1}. a. single wire working electrode (electrode 1), b. single wire working electrode (electrode 2), c. dual wire working electrode, d. anode-cathode.

single electrode value. In comparison with electrode 2 of this device, the peak current is increased by 59%. Hence a twofold increase in electrode area for closely spaced microwires does not lead to a doubling in voltammetric peak current.

Table 5.8 also shows the effect of reduced w_g on the voltammetric characteristics of dual microwire electrodes. The single and dual wire operation of device PT3, where w_g=2.7μm, are shown in fig. 5.50. In this instance the peak current enhancement is only 12.8% indicating that the dual electrode behaves essentially has one microwire electrode.

The voltammetric behaviour of closely spaced carbon fibre electrodes for the oxidation of ferrocene carboxylic acid and catechol in phosphate buffer are shown in figures 5.52 & 5.53. The cyclic voltammetry of $FeCp_2COOH$ at a preconditioned dual carbon fibre device, r=3.4μm, w_g=7μm shows that for the dual wire electrode the i_p is less than double that of single wire operation (30.7% increase).

5.3.3.2 CHRONOAMPEROMETRY.

Chronoamperometry for $Fe(CN)_6^{3-/4-}$ at dual parallel wire electrodes are given in figures 5.54–5.56. Figure 5.55 a&b shows the i–t response for device PT5 (r=12.5μm, w_g=13.5μm). The significant response features include the time dependence and deviation from single wire operation leading to a decrease in current density. For instance, after 5s electrolysis the current density of the dual wire electrode drops by 14.4% of a single wire electrode. The chronoamperometric data also show the time scale (200–300ms) upon which deviation from single wire behaviour occurs. A decrease in inter-electrode distance exacerbates these differences. For a dual microcylinder electrode with w_g=2.7μm, the change in current density at t=5s for the dual wire is now 43.6% and current deviation appears on a very short time scale (<100ms). Similar behaviour is found at dual carbon fibre electrodes for the oxidation of $FeCp_2COOH$, see figure 5.57.

5.3.3.3 DIFFUSION FIELD AT A DUAL MICROCYLINDER ELECTRODE.

To illustrate the effects of electrode separation on the current-time response of dual microcylinder electrodes attention is drawn to the series of

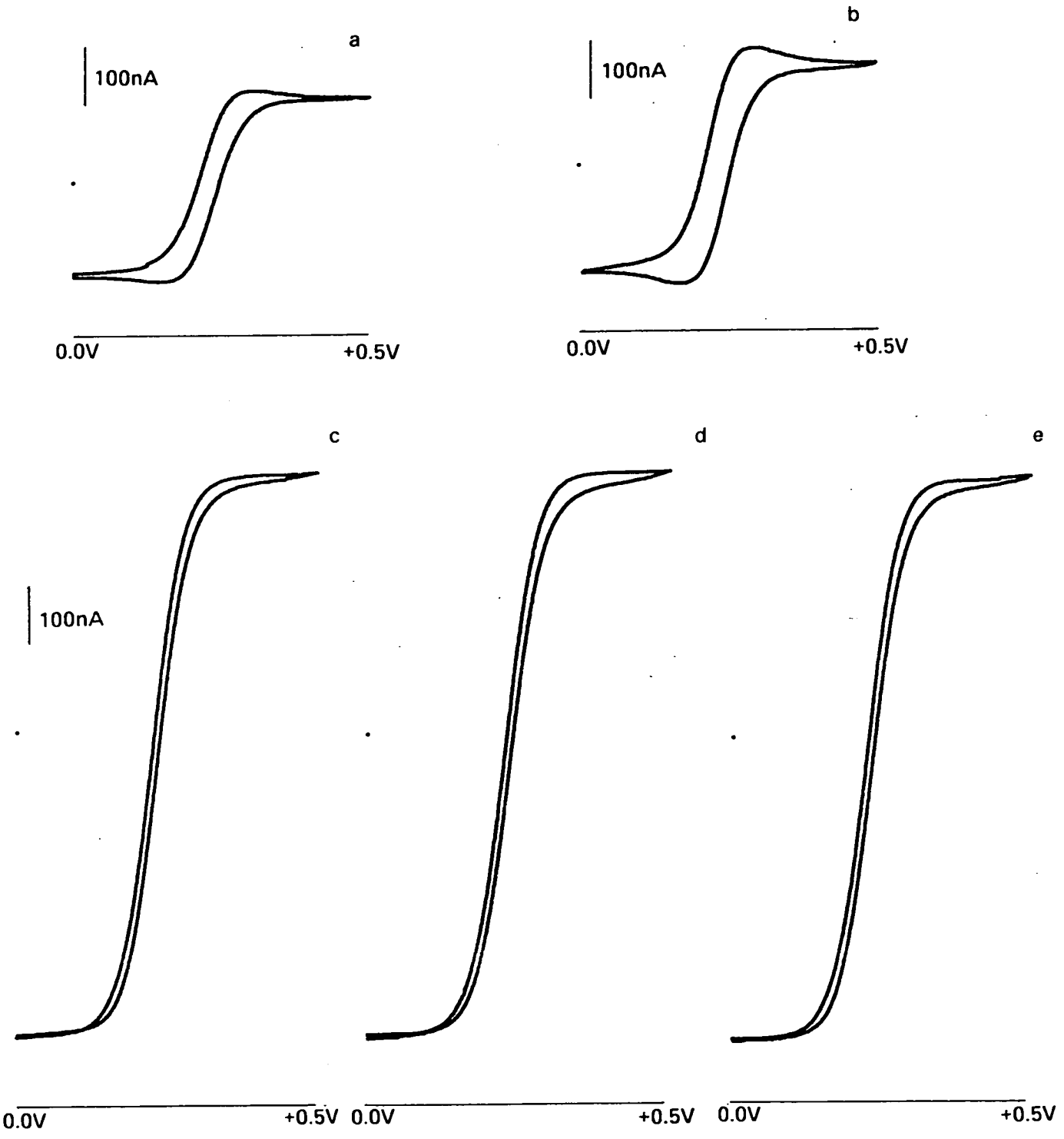

Figure 5.50 Cyclic voltammetry for $K_3Fe(CN)_6$ (1.0mM), $K_4Fe(CN)_6$ (1.0mM) in KCl (1.0M) at Pt microcylinder electrodes, r=12.5µm, w_g=2.7 µ m and l=0.6mm. Potential sweep 0.0V to +0.5V vs. SCE. v=10mV s^{-1}. a. single wire working electrode, b. dual wire working electrode, c-e anode-cathode, repeat scans.

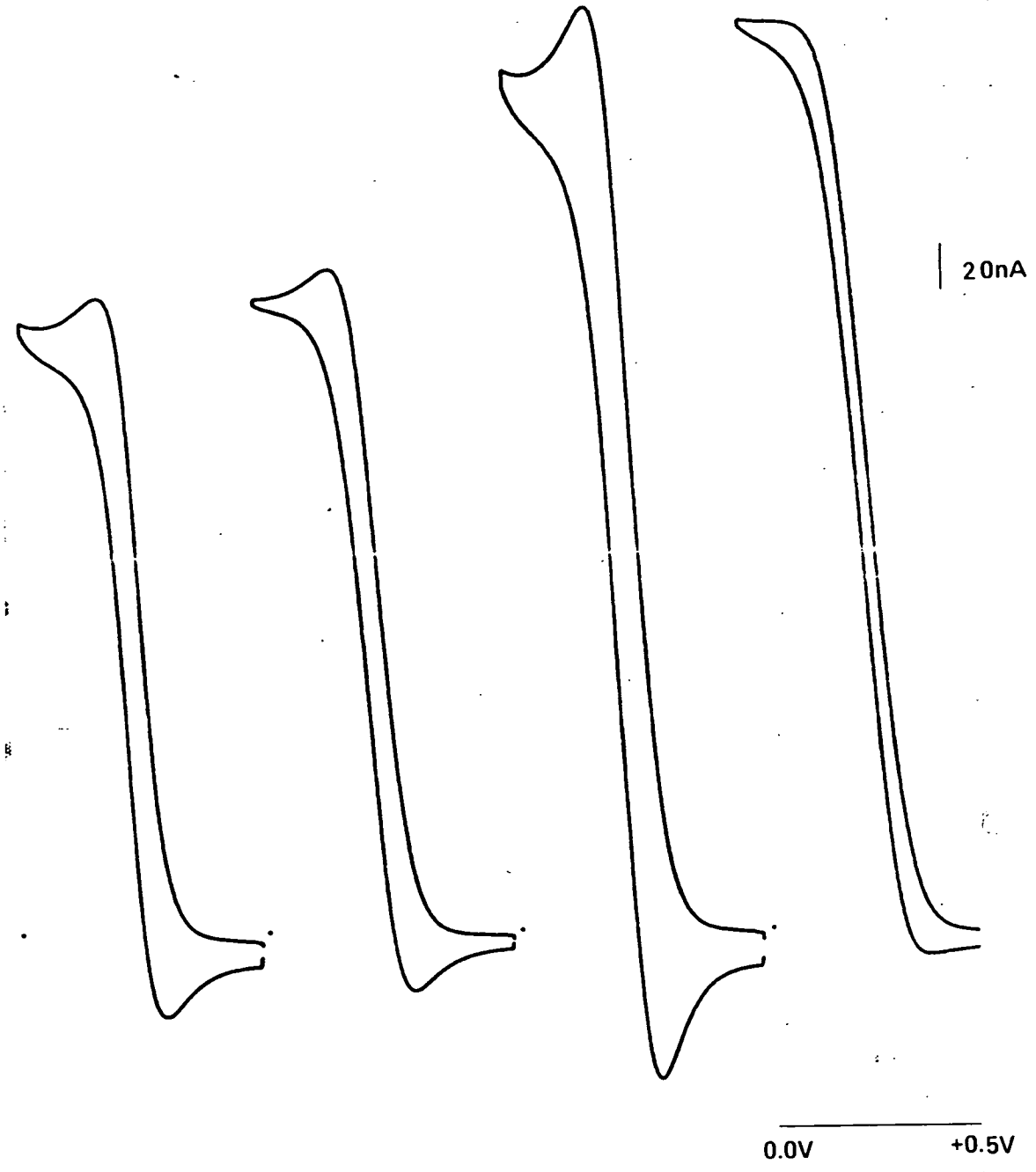

Figure 5.51 Cyclic voltammetry for $K_3Fe(CN)_6$ (1.0mM) in KCl (1.0M) at Pt dual microcylinder electrodes, r=12.5μm, w_g=14μm and l=1.8mm. Potential sweep +0.5V to 0.0V vs. SCE. v=20mV s^{-1}.

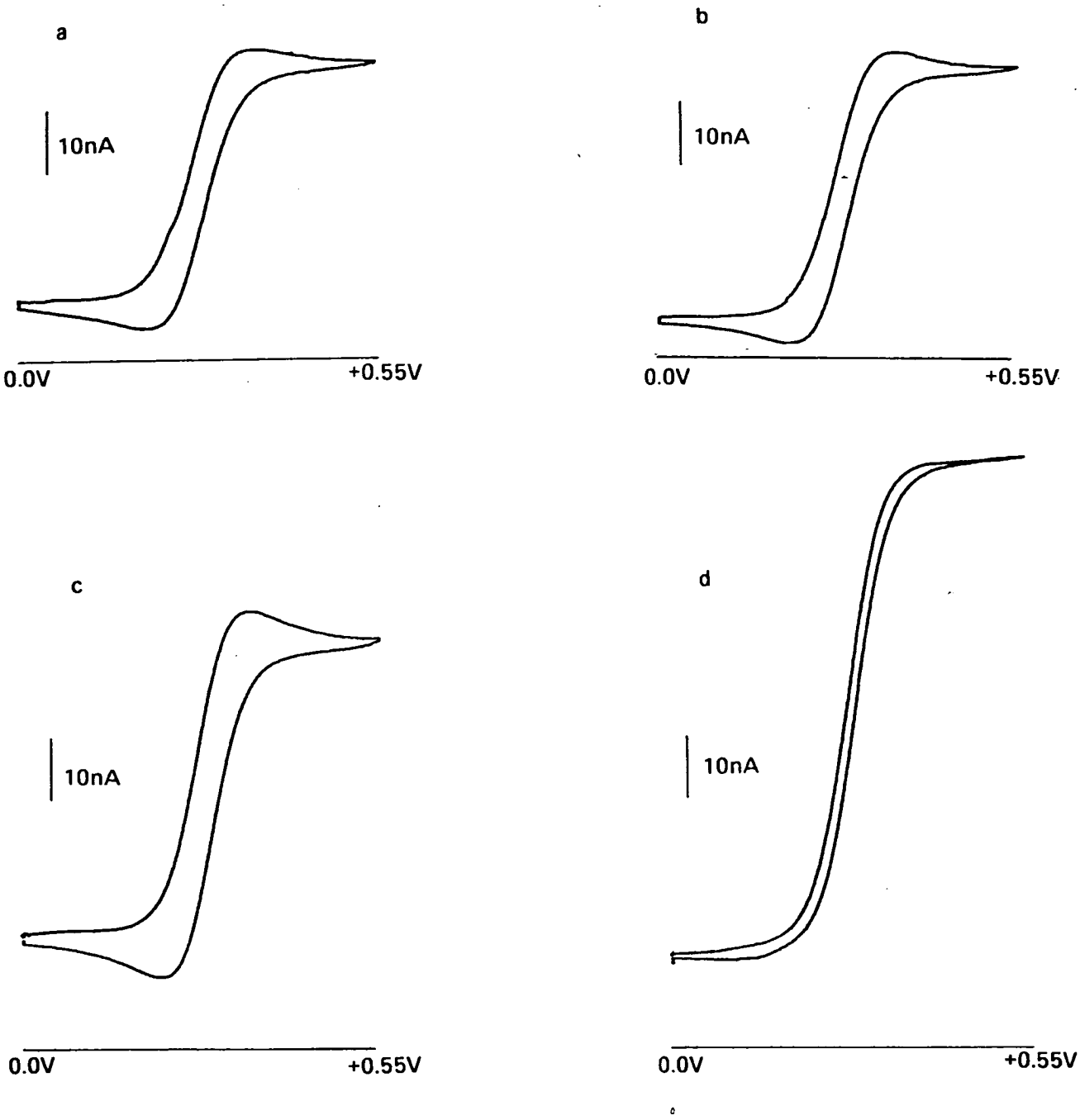

Figure 5.52 Cyclic voltammetry for ferrocene carboxylic acid (0.7mM) in Na_2HPO_4, NaH_2PO_4 (0.2M) pH=7 at dual carbon fibre electrodes. radius 3.4µm, w_g=7µm and electrode length 1.0mm. Potential sweep 0.0V to +0.55V vs. SCE, v=10mV s^{-1}. a. single fibre working electrode (electrode 1), b. single fibre working electrode (electrode 2), c. dual fibre electrode, d. anode-cathode.

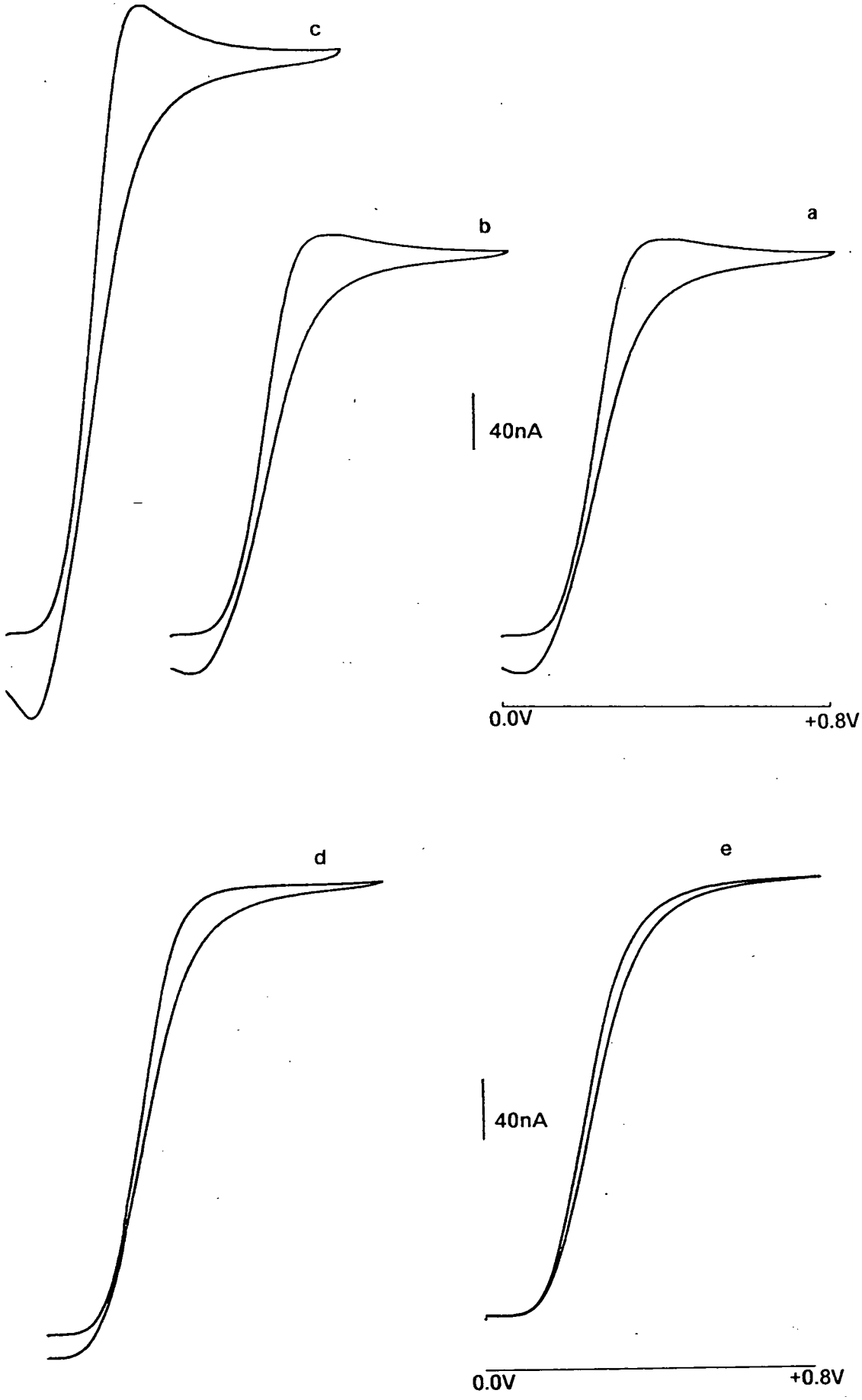

Figure 5.53 Cyclic voltammetry of catechol (1.1mM) in phosphate buffer solution as for fig. 5.52 at dual carbon fibre electrodes, radius 3.4µm, w_g=17µm and l=1mm. Potential sweep 0.0V to +0.8V vs. SCE, v=100mV s^{-1}. a. single fibre electrode (electrode 1), b. single fibre electrode (electrode 2), c. dual fibre electrode, d. anode and cathode, e. as for (d) with v=10mV s^{-1}.

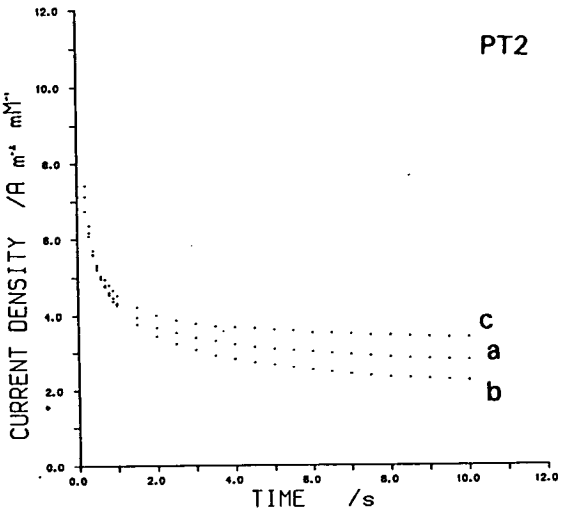

FIG. 5.54

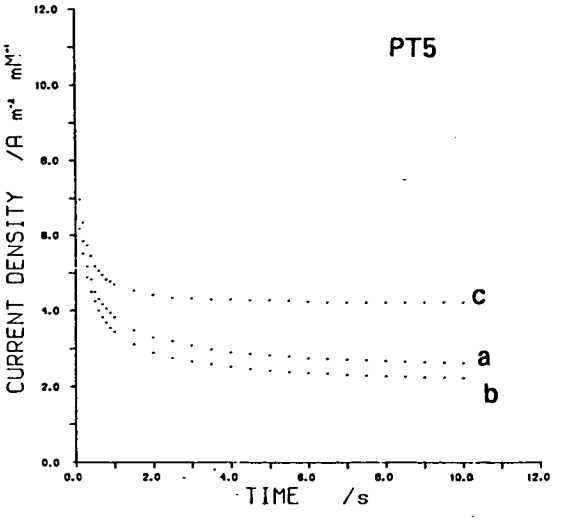

FIG. 5.55

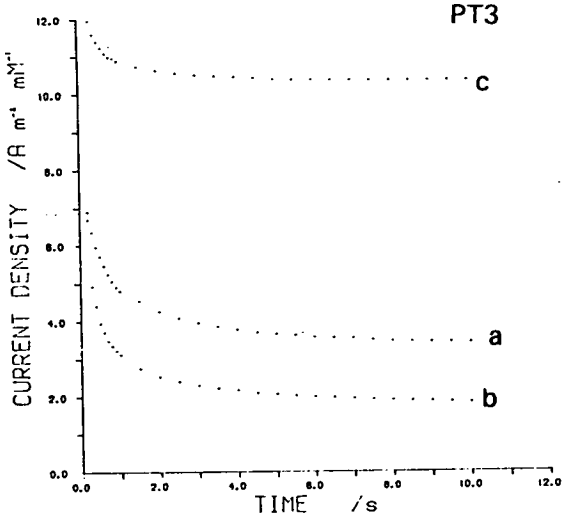

FIG. 5.56

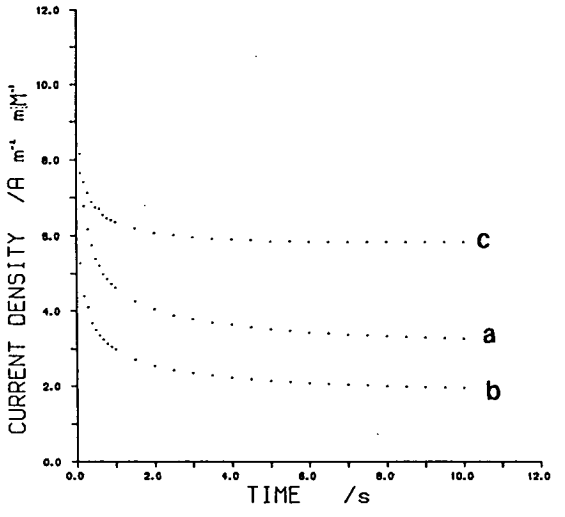

FIG. 5.57

Figure 5.54-5.56 Chronoamperometry for $Fe(CN)_6^{3-/4-}$ (1.0mM) in KCl (1.0M) at Pt dual microcylinder electrodes. Potential step from 0.0V to +0.5V vs. SCE a. single wire, b. dual wire, c. anode-cathode. For device dimensions refer to table 3.2 .

Figure 5.57 Chronoamperometry for $FeCp_2COOH$ (0.66mM) in Na_2HPO_4, NaH_2PO_4 (0.2M) pH=7 at a dual carbon fibre anode and cathode. r=3.4µm, w_g=7µm, l=1mm.

a. dual fibre, b. single fibre, c. anode-cathode.

illustrations in figure 5.58. This provides a qualitative picture of the interacting diffusion fields and the consequent effects on electrode flux.

For widely spaced microcylinder electrodes, the cylindrical diffusion fields at individual electrodes will be unaffeced by events at other electrodes in the array. The microelectrodes then behave as isolated systems and their response will conform to that of a single cylinder. As the electrode separation is reduced to a dimension corresponding to the size of the diffusion field, the effects of field interaction become apparent. The time scale for this diffusional interaction is dependent on the species involved (factors affecting D), but also on the geometry of the electrode (r and w_g), and reflects the decrease in species concentration in the region between the wire electrodes. At the instant of diffusion field contact the flux lines deviate from radial symmetry to a more complex form, depleting the concentration below bulk value. As this interaction evolves, the number of lines of flux linking the diffusion layer surface with the electrode decreases below that for isolated electrodes as the diffusion field changes geometry from cylindrical to approximate elliptic cylinder. The overall effect of diffusion field interaction, leading to a specific i-t response, is dependent on electrode radius and spacing. Therefore three chronoamperometric time phases may be realised for dual microcylinder electrodes; an initial short time Cottrell response, the duration of which is a function of r, a 'cylindrical' phase, where the response is identical to an isolated electrode, and which continues until individual diffusion fields converge. The duration of this second phase is a function of r and w_g. The final phase represents changes in the field geometry and is a function of device specific dimensions.

5.3.4 DUAL MICROCYLINDER ELECTRODES: DIFFERENTIAL APPLIED POTENTIAL.

5.3.4.1 CYCLIC VOLTAMMETRY.

The voltammetric characteristics for a reversible redox species at a dual microcylinder device operated as an anode and cathode pair are presented in figures 5.49-5.53. These voltammograms illustrate the effects of placing redox recycling electrodes at close proximity with the production of an amplified steady state response. The votammetric data given in table 5.8 shows the dependence of the steady state current on electrode separation. For a decrease in electrode spacing from 13.5µm to 2.7µm, a 2.7 fold increase in

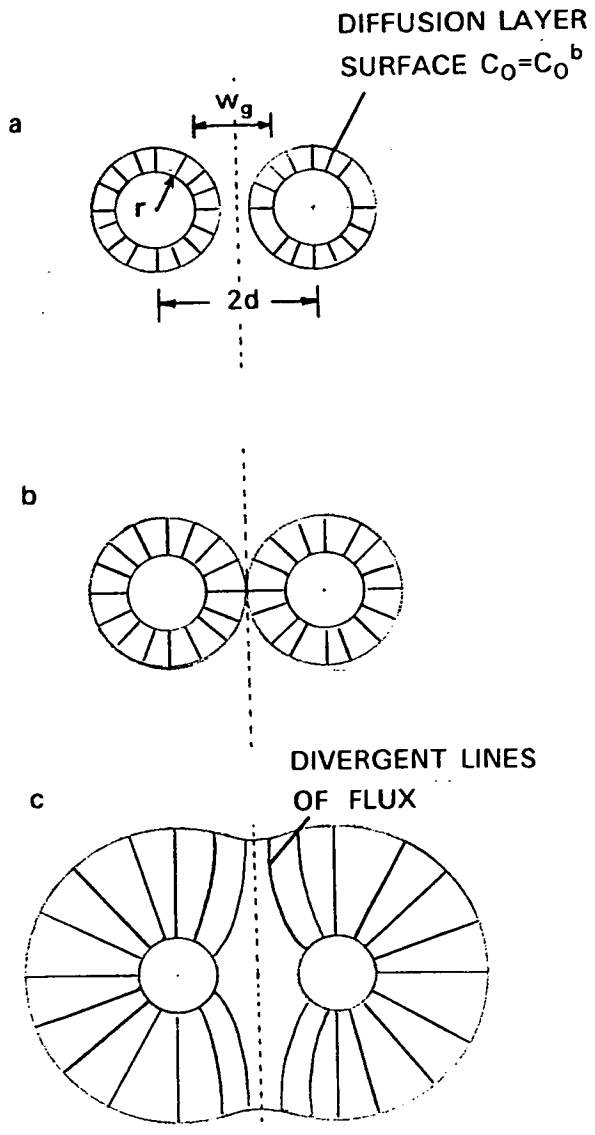

Figure 5.58 Illustration of the diffusion field at dual microcylinder electrodes . a. isolated fields, b.& c. field contact and interaction (shielding).

limiting current is found.

5.3.4.2 CHRONOAMPEROMETRY.

Current amplification and i-t response changes are also shown in figures 5.54-5.56. The chronoamperometric curves for three devices operating in anode-cathode mode with variable spacing shown in figure 5.59 illustrate the effects of the spacing parameter on diffusion current, both in terms of magnitude and speed of response, eg. a response time of ca. 2s is found for a device with 12.5μm radius and w_g=2.7μm.

Figure 5.60 shows the long electrolysis time behaviour (3min.) of a dual microcylinder anode-cathode compared with a single microcylinder electrode of the same radius. This data demonstrates the inherent stability of the feedback current response at dual microcylinder electrodes. Convection has little influence on the recycling diffusion field on account of its small size.

A qualitative representation of the chronoamperometric curves for a dual microcylinder device and an isolated microcylinder electrode for an electrolyte containing O and R forms of a reversible redox species is given in figure 5.61. Until $t=\tau_1$, the i-t response of both devices is identical as a result of the limited extension of the diffusion field, i.e. $\delta<w_g/2$. The current-time curve show that the system approaches steady state after a certain electrolysis time $t=\tau_2$, corresponding to complete diffusion field interaction and the establishment of a total feedback diffusion process. The current response, as a function of time over the interval τ_1 to τ_2, is dependent on the changing condition of field interaction. This is accompanied by simultaneous and adjusting contributions from bulk solution and the recycling electrode. The transient duration $\tau_2-\tau_1$, is a function of electrolytic and device variables.

5.3.4.3 VERIFICATION OF THE STEADY STATE CURRENT EXPRESSION FOR A MICROCYLINDER ANODE-CATHODE DEVICE.

The equation formulated in chapter 2 for the steady state diffusion current at a dual microcylinder anode-cathode device (eqn. 2.81) is compared with experimental chronoamperometric data for a series of Pt devices with variable spacing in table 5.9. Steady state current density plotted as a function of the geometric parameter, $1/\cosh^{-1}(d/r)$, as shown in fig. 5.62. The experimental

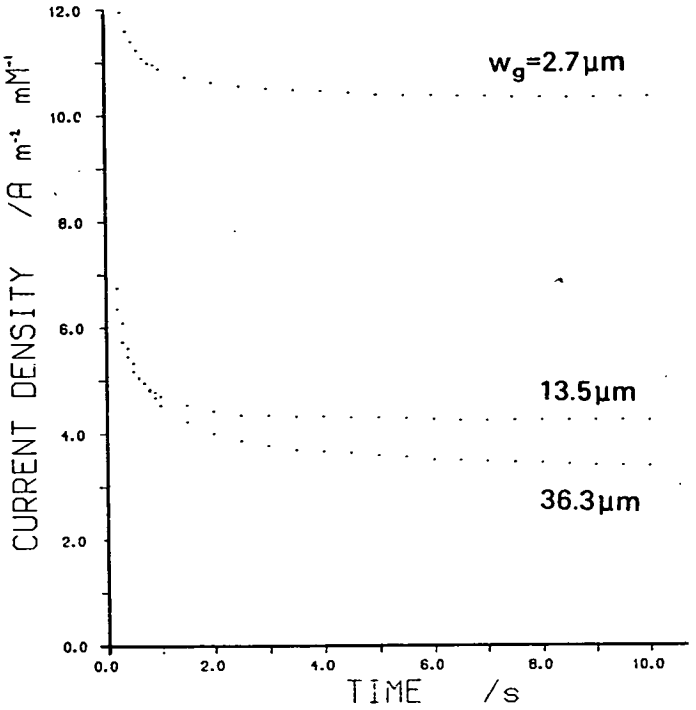

Figure 5.59 chronoamperometry at dual microcylinder anode-cathode devices. Conditions as in figs 5.54 to 5.56.

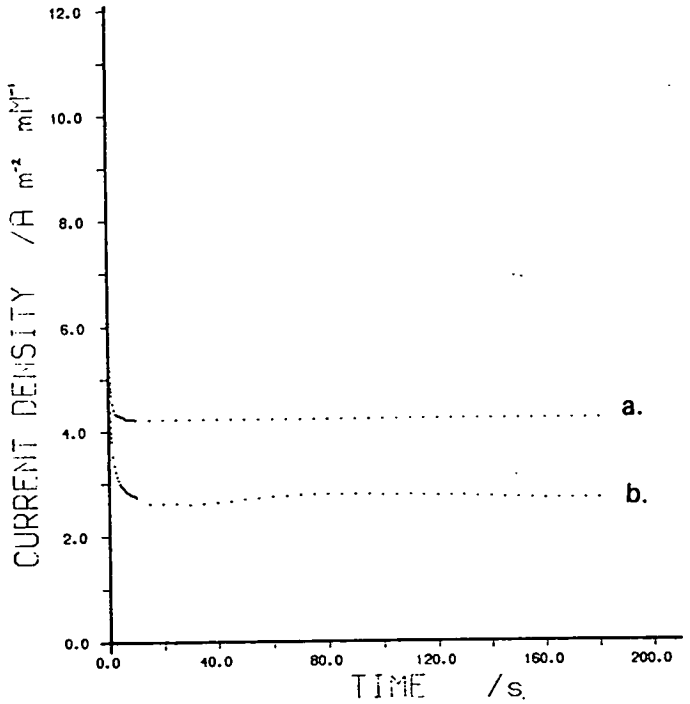

Figure 5.60 chronoamperometry for the oxidation of $Fe(CN)_6^{4-}$ (1.0mM) in aqueous KCl (1.0M) at Pt microcylinder electrodes. a. dual microcylinder electrodes, r=12.5µm, w_g=13.5µm. b. single microcylinder electrode, r=12.5µm.

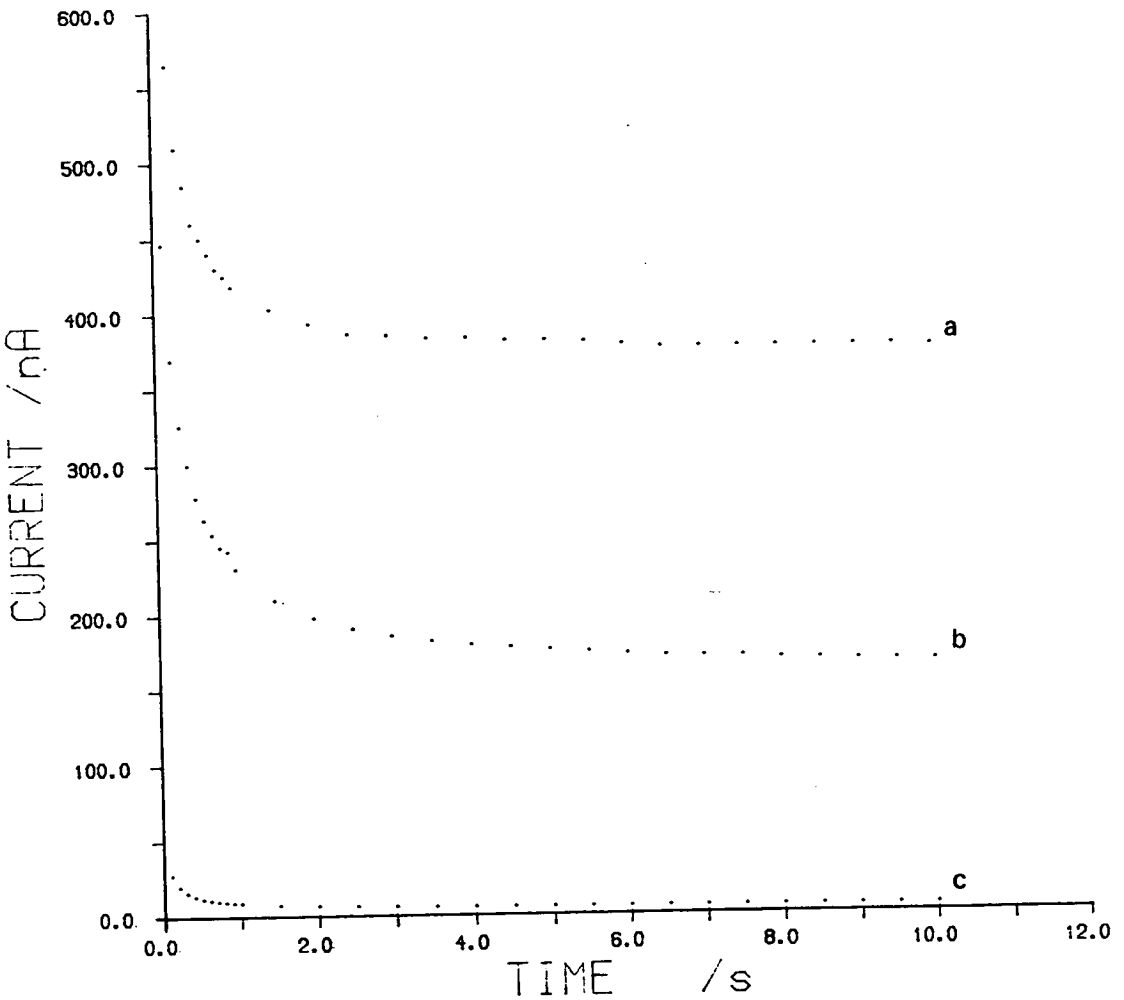

Figure 5.65 Chronoamperometry at a dual Pt microcylinder anode-cathode device. r=12.5µm, w_g=13.5µm, l=0.55mm. a. $Fe(CN)_6^{3-/4-}$ (1.0mM), b. $Fe(CN)_6^{3-}$ (1.0mM), c. support electrolyte KCl (1.0M)

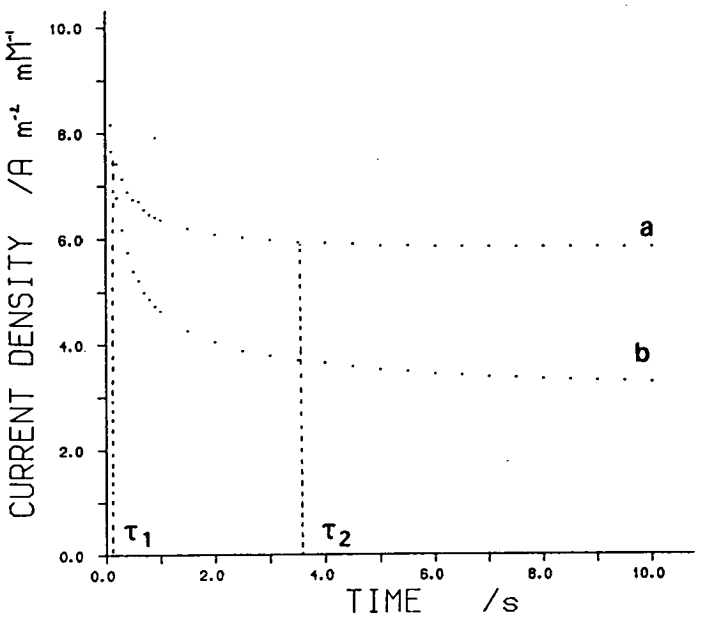

Figure 5.61 chronoamperometry at microcylinder electrodes. a. dual microcylinder anode-cathode, b. isolated microcylinder.

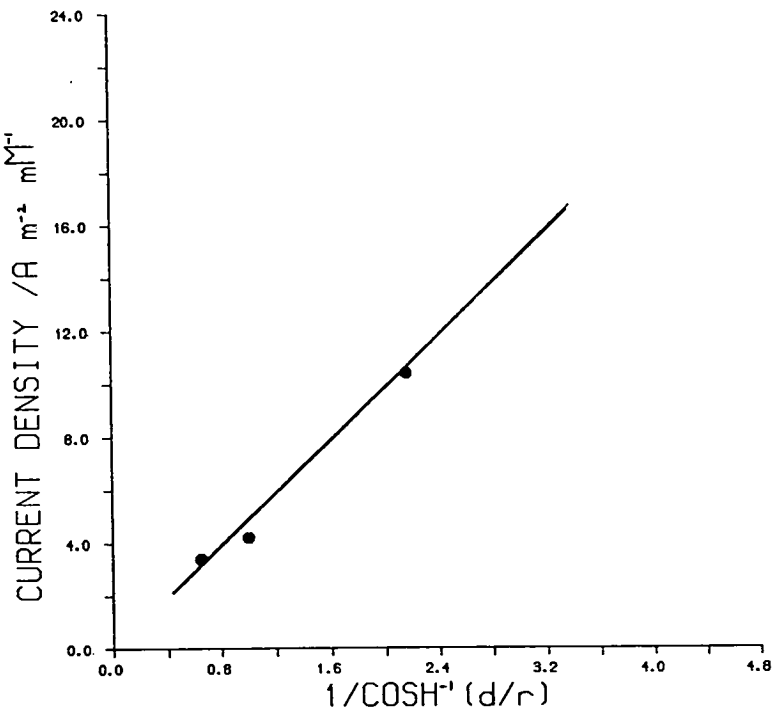

Figure 5.62 Plot of steady state current density against the geometric parameter for dual microcylinder anode-cathode devices. Solid line is the theoretical data, points are for devices PT2, PT3, PT5 using data from fig. 5.59.

data shown here are in general agreement with theoretical values, which for the dual microcylinder device is a general analytical solution. An error analysis for assessment of the quality of the theoretical model is hindered by the errors introduced at fabrication. For the dual microcylinder devices studied the experimental data agreed within ±15% of theory.

Diffusional recycling of redox species such as catechol, noradrenaline and ferrocene carboxylic acid was effected using a dual carbon fibre anode-cathode, i.e. for only one form of a redox couple initially present. For a device with fibre radius 3.4μm, spacing 17μm and length of 1mm, a virtual steady state response was attained after several seconds electrolysis with noradrenaline. For this system the current at t=10s was 201nA mM^{-1}, while the theoretical current was 190nA mM^{-1}. The voltammetric limiting current data for catechol and ferrocene carboxylic acid are also in good agreement with the theoretical expression.

5.3.4.4 INTERPRETATION OF AMPEROMETRIC BEHAVIOUR OF THE MICROCYLINDER ANODE-CATHODE DEVICE.

The geometric parameters important to the form of the diffusion current response with time for a dual microcylinder anode-cathode include the respective radii, r_a and r_c and the electrode spacing. The approach to steady state by a recycling mechanism at microcylinder electrodes is a complex time dependent diffusional transport problem, that will require the application of numerical modelling for elucidation. However, a qualitative consideration of relevant field dynamics with respect to the device dimensions can be informative.

The operation of a dual microcylinder anode-cathode for diffusional recycling of a reversible redox species may be considered for two cases distinguished by the initial conditions: a. one form of a reversible redox couple is present or b. both forms of a reversible redox couple are present. The mechanism of feedback diffusion between microcylinder electrodes is most readily appreciated for the second case, where $C_O=C_R$, and for a symmetrical device, $r_a=r_c$. After a certain electrolysis time τ_1, dependent on device geometry, (r,w_g) the cylindrical diffusion fields of each electrode converge at $w_g/2$ as depicted in figure 5.63. At this instant linkage of flux lines occurs along the axis -XOX, i.e. at this moment there exists a single line of feedback flux

between the microcylinder electrodes. The value of the concentration at point X=0, Y=0, is then maintained at the bulk value and is the begining of the establishment of a Nernst plane, where,

$$C_O^{X=w_g/2} = C_R^{X=w_g/2} = C_{O/R}^{b}$$

As the diffusion field develops with time more flux lines become linked, increasing the quantity of species undergoing recycling in proportion to the bulk diffusion transport. Increased flux linkage has the effect of deviating the radial bulk flux pattern to a circular inter-electrode flux. This has the effect of increasing flux density over that of the isolated wire case. Total flux linkage is completed at time τ_2. In this simplified model of inter-electrode diffusion, this will occur when the diffusion field extends over the whole device region enclosing both electrodes, that is, for $\delta=w_g+2r$. This corresponds to the total flux recycling, where contributions from bulk solution are now absent and a state of constant current is observed. Analogous with microband electrodes, the feedback model for dual microcylinders may include the establishment of a Nernst concentration surface where the concentration at a plane $w_g/2$ is maintained by the feedback mechanism at bulk concentration,see fig. 5.64. Therefore it can be appreciated for dual microcylinder anode-cathode devices that the time response and level of steady state current are a function the electrode size and separation since these affect the position of the Nernst plane.

Figure 5.65 gives the chronoamperometric response of device Pt5 and compares the behaviour of two systems. The O/R system where both forms of a reversible redox couple are initially present at equiconcentration, in this case $Fe(CN)_6^{3-/4-}$, and the O system, where $Fe(CN)_6^{3-}$ only is present. It will be observed that the steady state diffusion current in the O/R case is twice the O case this is a consequence of the value of the Nernst plane which is $C_O^b/2$ for the O only system. Most interestingly, the time response is different for the two experiments. With the O/R system a steady state response is established at ca. 2s, while for the O system the condition of steady state current is observed only after 6.5s. This difference in the onset time (or response time) for a steady state current reflects the different transient diffusion processes which occur at dual microcylinder anode-cathode devices, and is directly analogous to the microband electrodes as discussed earlier.

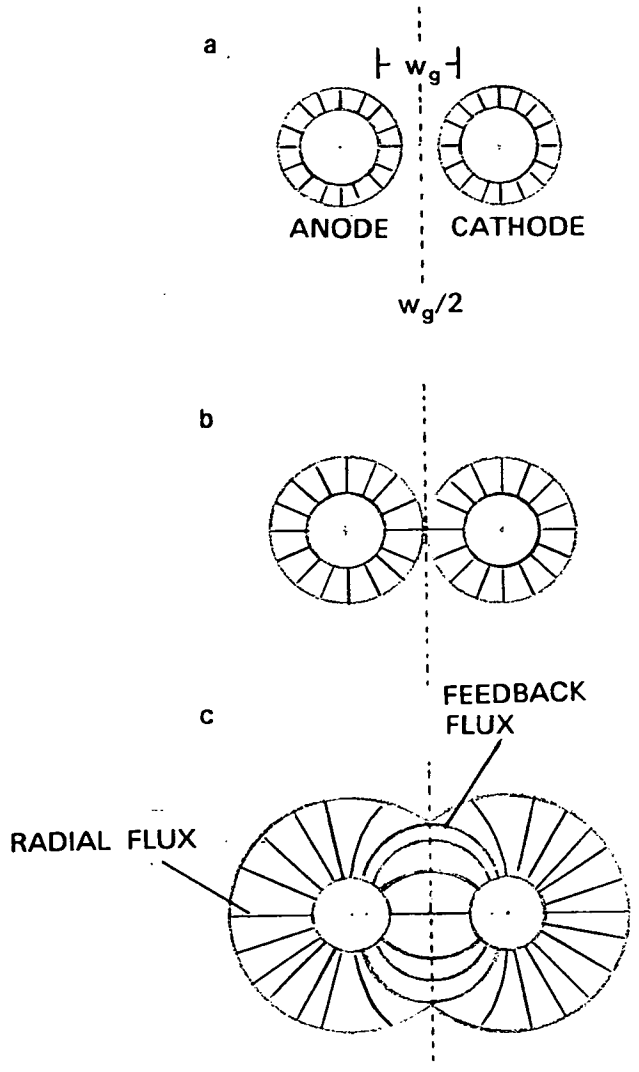

Figure 5.63 Illustration of the diffusion field at a dual microcylinder anode- cathode device. a. isolated fields, b.&c. field interaction (feedback diffusion).

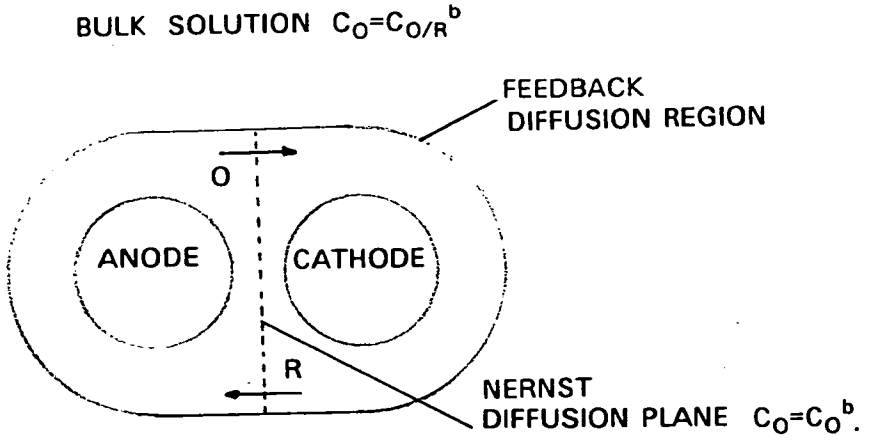

Figure 5.64 Feedback diffusion region at a dual microcylinder anode and cathode.

TABLE 5.8 CYCLIC VOLTAMMETRY DATA FOR DUAL MICROCYLINDER ELECTRODES.

	SINGLE ELECTRODE OPERATION										DUAL ELECTRODE OPERATION									
	ELECTRODE 1					ELECTRODE 2					ANODE OR CATHODE					ANODE AND CATHODE				
	$i_{p,a}$ /nA	$i_{p,c}$ /nA	$i_{p,a}/i_{p,c}$	i_{p-p} /nA	$E^{o\prime}$ /mV	$i_{p,a}$ /nA	$i_{p,c}$ /nA	$i_{p,a}/i_{p,c}$	i_{p-p} /nA	$E^{o\prime}$ /mV	$i_{p,a}$ /nA	$i_{p,c}$ /nA	$i_{p,a}/i_{p,c}$	i_{p-p} /nA	$E^{o\prime}$ /mV	$i_{s.s,a}$ /nA	$i_{s.s,c}$ /nA	i_a/i_c	$E^{o\prime}$ /mV	
Pt2	289.2	282.0	1.03	325.2	+206	294.4	288.0	1.02	318.4	+213	470.4	458.4	1.03	616	+203	352.0	306.0	1.15	+223	
Pt3						313.0	310.0	1.01	330.0	+210	353.0	343	1.03	403.0	+210	953.0	915.0	1.04	+230	
#	39.0	38.6	1.01	44.6		42.6	41.5	1.03	46.5		51.0	49.0	1.04	58.6		74.0	75.0	0.99		

Data for a dual carbon fibre device, r=3.4μm and w_g=7μm.

TABLE 5.1. COMPARISON OF EXPERIMENTAL AND THEORETICAL STEADY STATE CURRENT AT PLATINUM DUAL MICROCYLINDER ANODE AND CATHODE DEVICES.

DEVICE	EXPERIMENTAL		THEORETICAL		% DIFFERENCE
	i/C /nA mM^{-1}	i/CA /A m^{-2} mM^{-1}	i/C /nA mM^{-1}	i/CA /A m^{-2} mM^{-1}	
[1]Pt1	1627	2.1	1468	1.9	+10.8
Pt2	171.4	3.4	163.2	3.2	+5.0
Pt3	486.9	10.4	502.8	10.7	-3.2
[1]Pt4	395	2.8	408.9	2.9	-3.4
Pt5	182	4.2	214.0	5.0	-15.0

1. Ferricyanide only, theoretical value taking $D=7.6\times10^{-10} m^2\ s^{-1}$

Theoretical data calculated from eqn.(2.62) taking $D=6.4\times10^{-10} m^2\ s^{-1}$

CHAPTER 6

APPLICATION OF MICROBAND AND CYLINDER ARRAY ELECTRODES TO ELECTROANALYSIS.

6.1 MEASUREMENT OF REDOX SPECIES.

The application of ensembles of regularly arranged microscopic band or cylinder electrodes in a common potential mode for the determination of redox species will require the optimisation of bandwidth/radius and spacing with due consideration to assay procedure. Microdetectors/sensors composed of such microelectrode assemblies are well suited for low volume (µl) trace analysis (< µM) of redox species owing to a combination of attribues including, small size, and favourable current-time characteristic leading to high sensitivity and detectability. However, it would be important for a given application to maximise detection parameters within the practical limitations imposed by microfabrication and analytical constraints.

The chronoamperometric signal for an array of band or cylinder microelectrodes will vary as a function of time. Furthermore, signal sampling (in quasi steady state analysis) should be made before diffusion field interaction in order to preserve the response of individual microelectrodes. It has already been mentioned for submicroscopic band electrodes that the sensitivity, i/C, per unit area is greatly superior to macroscopic electrodes. These electrodes offer some of the best analytical characteristics for chronoamperometry. Table 2.1 shows theoretical chronoamperometric data for submicroscopic band electrodes of 1mm band length. Taking a bandwidth of 100nm as discussed in chapter 2, bands must be arranged with band gap, ca. 600nm to avoid diffusional interaction on the time scale $\leqq$10s. Therefore, a detector of size 1mm^2 could house 1429 bands set with 600nm separation. Such a detector would then provide a quasi-steady state current of 38.3nA µM^{-1} at t=10s, see fig. 6.1. Allowing for the submicromolar determination of analyte by chronoamperometry.

6.2 MEASUREMENT OF REVERSIBLE REDOX SPECIES.

Arrays of microelectrodes operated in a differential potential mode for the detection of reversible redox species must be arranged in close proximity for the optimisation of the amperometric signal, i.e. sensitivity and response time. Theoretical and experimental studies on the steady state current response of amperometric interdigitated devices of regular geometry have developed to the extent that a clearer understanding of the analytical potential of this form of amperometric detector is now possible.

The chronoamperometric signal characteristics for a large scale interdigitated microband device have been extolled in chapter 5. The main analytical features of this device are;

a. the generation of a steady state signal.

b. response time of ca. 2s, for experiments with equiconcentration of O and R.

c. current (sensitivity) of ca. 11nA μM^{-1}.

d. linear concentration range from 1µM to 1mM.

e. detection limit at the high nanomolar level (100nM).

Since this device has a total sensing area of 20.6mm^2; the current normalised for a 1mm^2 device is ca. 0.5nA μM^{-1}

Small scale devices have now been fabricated and their chronoamperometric response characterised. Aoki et al. [21,22] have shown for a device of dimensions, w_e=5µm, w_g=5µm, l=2mm, that the steady state current after t=10s was 23.2µA mM^{-1} when using ferrocene as a model redox species. For a 1mm^2 detector, this corresponds to a sensitivity of 15.5nA μM^{-1}. The device described by these workers had a response time of less than 1s.

Niwa et al. [40] extended this study with the fabrication of micrometer bandwidth devices with 0.5µm band gap. The amperometric signal is very impressive with a response time of the order of 20–30ms for w_e=5µm and w_g=0.5µm. The i/C for this device occupying 2mm^2 was 110.5µA mM^{-1}, with collection efficiency ca. 100%. The current delivered by a 1mm^2 device, 55nA μM^{-1}, is in stark contrast to that for large scale devices as reported here. These workers went on to show for a device with collector bandwidth, 2µm,

and generator bandwidth, 3μm, with band gap of 0.5μm and a total area of $1mm^2$, a current of 87.5nA μM^{-1} could be obtained for steady state amperometry.

Table 6.1 compares the theoretical performance of various interdigitated devices in terms of assay parameters important to microanalysis. It can be appreciated from this data (calculated using eqn. 2.62) that the highest sensitivities are achieved for the submicroscopic devices. For a device with bandwidth of 100nm and band gap 10nm, the current delivered for a $1mm^2$ device would be 431.2nA μM^{-1}, easily allowing the determination of low nanomolar concentration of analyte. It is interesting to consider the level of current delivered by an interdigitated microdetector of total area of $1\mu m^2$ and consisting of bands 100nm in bandwidth and band gap 10nm. By eqn.(2.62) such a device would give a steady state current of 0.38pA μM^{-1}, which is readily detectable with low bias current FET ammeters.

The levels of feedback current attainable with microcylinder anode and cathode were shown in table 5.10. The experimental data indicates that for a device of radius 12.5μ and w_g=2.7μm and of length 100μm, the current was 81.2nA mM^{-1}. Table 6.2 further illustrates the sensitivity achieved by such microdevices. The data here is calculated from eqn.(2.81) and considers the current delivered by microcylinders of radius 3.4μm separated by a microscopic spacing. The theoretical current which can be expected from a device of 100μm in length and 3μm electrode gap is 33.4pA μM^{-1}. Hence the application of dual microcylinders as microsensors in feedback voltammetry will require sensitive current measurement of pA or fA signals.

Owing to the special diffusion current characteristics of interdigitated devices there exists a number of opportunities for analytical application, and some are listed below. Only the extension to immunoassay will be considered here with allusion to the band geometry. The application of the dual microcylinder anode-cathode device for in vivo analysis is also discussed.

a. immunological assay.

b. enzyme electrodes.

c. amperometric titration.

c. in-vivo amperometry.

d. amperometric detectors in flow systems.

e. oxygen measurement.

6.2.1 A HOMOGENEOUS COMPETITIVE BINDING IMMUNOASSAY FOR LOW MOLECULAR MASS LIGANDS.

Interdigitated microband array electrodes are especially suited as amperometric measuring devices for homogeneous immunoassay. What will follow is a brief description of an area of analytical immunology applicable to the operation of interdigitated electrodes.

Research into electrochemical detection for immunological assay has emerged throughout the 1980s in line with the popularity of the "biosensor" in a concerted effort to move the immunoassay from radioisotopic and spectroscopic methods to simpler assay protocol.[47,48].

Highly sensitive analytical methods are necessary however for application to immunoassay. Listed in table 6.3 are the plasma and/or serum concentration levels for some commonly assayed biochemicals. An assay for testosterone for example would need to measure over a range 3nM to 50nM to determine abnormal physiological changes of the hormone.

Immunoassay by electrochemical measurement offers interesting alternatives to the older detection systems. In this instance the immunological reaction, i.e. binding of the antibody with antigen (ligand), is monitored by electrical perturbation of a sensing surface, viz electrode. The electrical signal changes in response to ligand concentration which is a function of ligand binding. Immunoassay using amperometry at solid electrodes is applicable to a wide range of low molecular mass ligands (haptens). This technique pertains to electroactive ligands, either naturally occurring such as thyroxine, morphine or via. redox labelling.

Amperometric electrodes are intrinsically appropriate as measuring devices for homogeneous immunoassay since the diffusion limiting current is a function of the physicochemical nature of the species. The principle of the immunoassay lies in signal discrimination as a consequence of a difference in diffusivity

between bound electroactive ligand and free ligand. This can be most appreciated by considering the molecular size of ligand species with respect to binding proteins. Macromolecules such as globular proteins are typically 10A to 100A diameter, with a diffusion coefficient of the order, $5x10^{-11}m^2\ s^{-1}$. In contrast for the ligand species (3A), diffusion coefficients are of the order $5x10^{-10}m^2\ s^{-1}$.

The relationship between molecular size and the diffusion coefficient of a spherical macromolecule is given by the Stokes-Einstein equation (6.1),

$$D = kT/6\pi r\eta \qquad (6.1)$$

where, D, is the diffusion coefficient of a spherical molecule of radius, r. η is the viscosity of the medium, k is the Boltzmann constant. From eqn. (6.1), any increase in molecular size will have a reciprocal effect on the diffusion coefficient, a process which occurs when antibody binds with antigen.

The principle of the homogeneous assay is represented by the following reaction scheme,

$$Ab + Ag + Ag^L \rightleftharpoons AbAg + AbAg^L$$

where Ab is antibody, Ag, antigen and L a labelling agent. For homogeneous analysis there is no separation step for the measurement of free Ag^L, hence the method should contain a discriminating factor.

For chronoamperometry at macroscopic electrodes, the diffusion current, i, is described by the Cottrell equation (6.2),

$$i = nFD^{1/2}C/(\pi t)^{1/2} \qquad (6.2)$$

In the case of macroelectrodes, analytical sensitivity is dependent on $\sqrt{D}$, and is a varying function of time. Hence for a competitive binding assay, where binding protein is limiting, the signal to background current ratio is governed by the following relation,

$$i^f/i^b = C_{Ag}{}^L/C_{AbAg}{}^L.f(D^f/D^b) \qquad (6.3)$$

and for macroelectrodes,

$$f(D^f/D^b) = \surd D^f/D^b \quad (6.4)$$

Where the superscripts f and b refer to free and bound labelled ligand respectivity.

The background current in this sense is considered only from bound redox labelled ligand.

Considering an assay system at equilibrium, where $C_{AbAg}{}^L = C_{Ag}{}^L$, and $D_{AbAg} = 5x10^{-11}m^2\ s^{-1}$, $D_{Ag} = 5x10^{-10}m^2\ s^{-1}$.

then, $i^f/i^b = \surd 10$ (6.5)

The essential advantage in utilising interdigitated devices as measuring systems in homogeneous amperometric immunoassay is the proportionality that exists between the diffusion current and diffusion coefficient.

Therefore, $i^f/i^b = C_{Ag}{}^L/C_{AbAg}{}^L.D^f/D^b$ (6.6)

and for the conditions stated above,

From, $i^f/i^b = 10$ (6.7)

Hence for interdigitated devices there is an improvement in signal to background ratio over that for conventional electrodes. This identity, together with the sensitivity enhancement and steady state response form the basic strategy for the application of interdigitated microband array electrodes in homogeneous amperometric immunoassay, refer to figure 6.2.

The binding protein and ligand system proposed for this work was Avidin and biotin respectively. This will be summarised in appendix 3.

6.2.2 DUAL MICROCYLINDER ANODE-CATHODE: A DEVICE FOR IN VIVO MEASUREMENT OF REVERSIBLE REDOX SPECIES.

The utilisation of the feedback mechanism in connection with oxygen measurement has already been mentioned in the literature [41]. The aim here is to briefly show the applicablity of the dual wire design in microsensor for

measurement of oxygen in localised or microscopic environments. A schematic diagram is shown in figure 6.3 illustrating how the principle of operation relies on the balanced consumption and regeneration of oxygen at a close spaced anode and cathode within a compartmented region. The electrodes are potentiostated such that the anodic and cathodic currents are equal, in this way once equilibration of oxygen has occurred within the device and its environment, the O_2 level within the device remains constant. This would allow for stable and continuous monitoring experiments to be performed within microenvironments.

Species such as dopamine are present in neuronal tissue at submicromolar concentration with ascorbate at a much higher level, 500µM. While the catecholamine is reversible on carbon based electrodes, ascorbate behaves irreversibly in terms of redox electrochemistry. Furthermore, the voltammetric oxidation waves for these compounds at physiological pH occur at very similar potentials. Other complicating factors exist for the selective measurement of dopamine in the presence of ascorbate, possibly the most important is the reduction of the quinoid form of dopamine, cf. figure 6.4.

Difficulties such as these together with the unfavorable low concentration of dopamine and the nature of the measuring site, an intercellular region, make for a formidable analytical problem. The application of dual carbon fibre electrodes as a microsensor device for the in vivo monitoring of catechols is illustrated by figure 6.5. The electrodes are suitably polarised for the oxidation (+0.2V) and reduction (−0.3V vs. Ag/AgCl) of the catechol couple. The principle of operation relies on the "collection" of the quinoid form by the cathode before the follow up ascorbate reduction reaction as proceded. This is equivalent to saying that the diffusion distance of the quinoid species (w_g) must be short relative to a reaction layer thickness. This method of monitoring therefore relies on the placement of a recycling electrode within the diffusion field of a generator electrode [42].

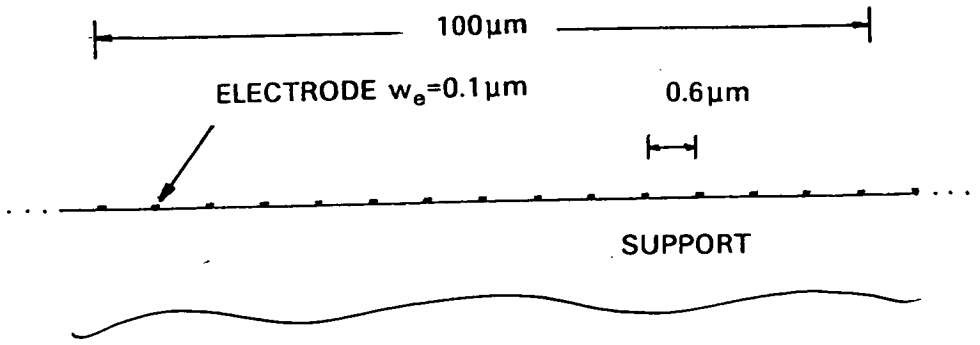

Figure 6.1 Isolated submicroscopic microband array electrode.

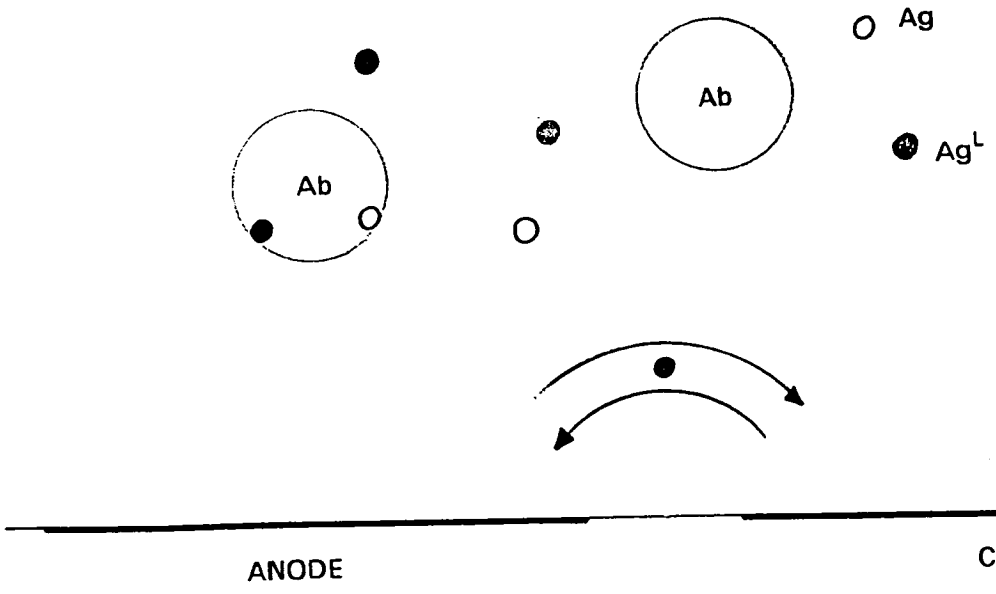

Figure 6.2 Illustration of a homogeneous amperometric immunoassay utilising interdigitated microband array electrodes as the detection system.

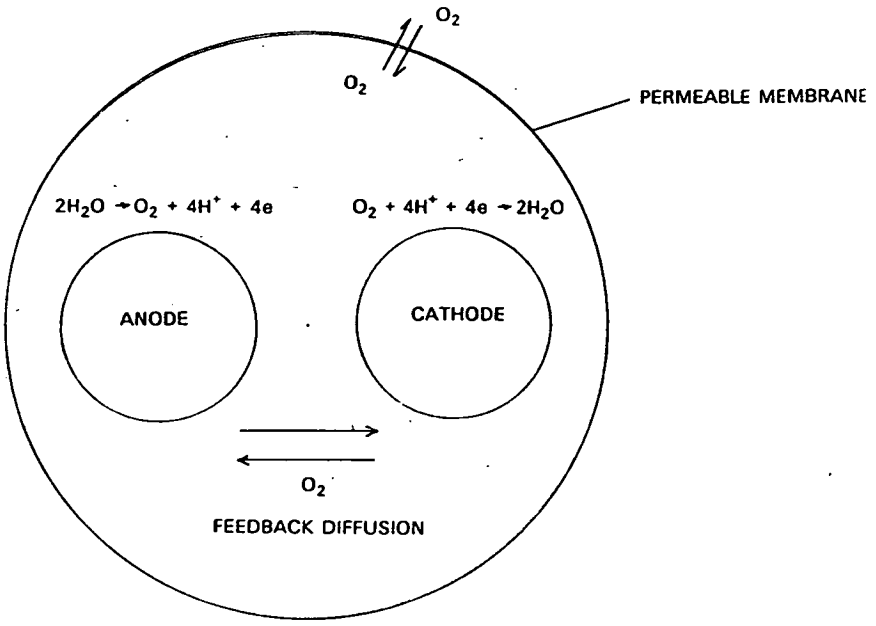

Figure 6.3 Oxygen measurement at a platinum microcylinder anode and cathode.

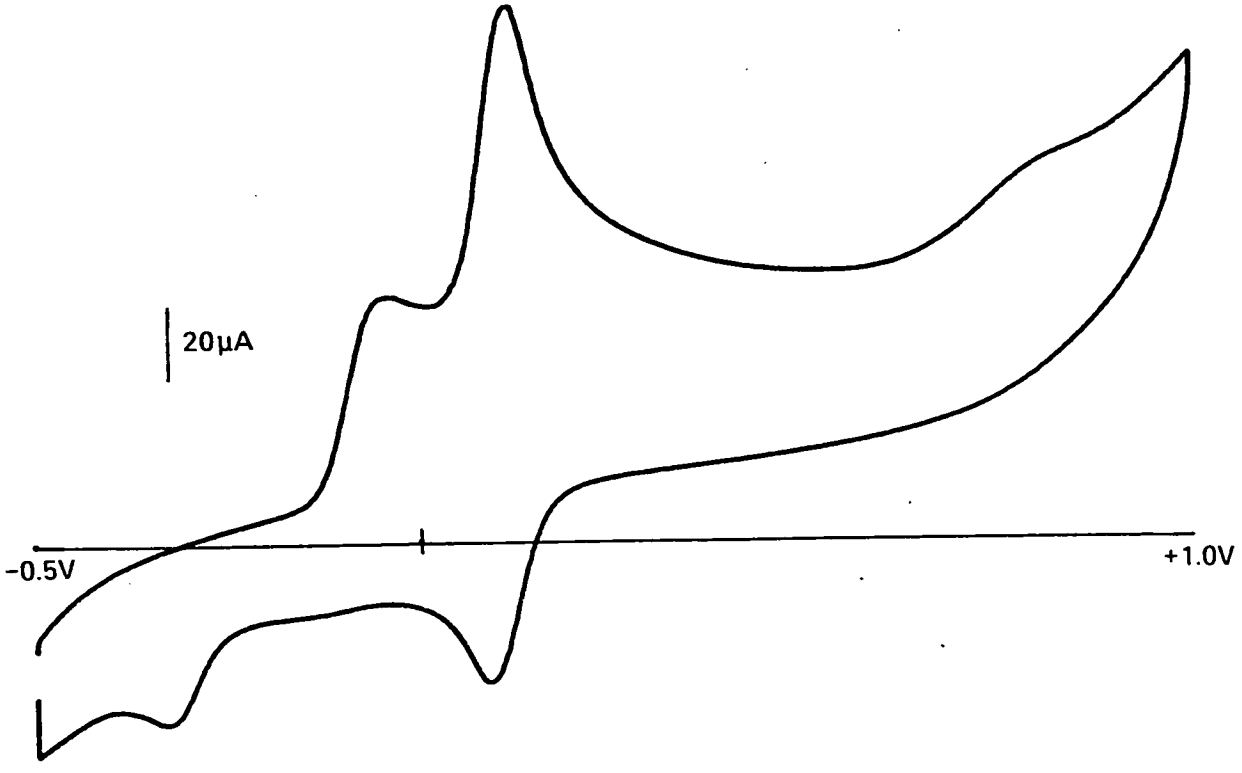

Figure 6.4 Cyclic voltammetry at pyrolytic carbon disc (4mm dia.) electrode for ascorbic acid (1mM) and dopamine (1mM) in aqueous NaCl (140mM) and phosphate buffer (0.02M, pH=7.4). Potential sweep from −0.5V to +1.0V vs. Ag/AgCl. v = 50mV s^{-1}.

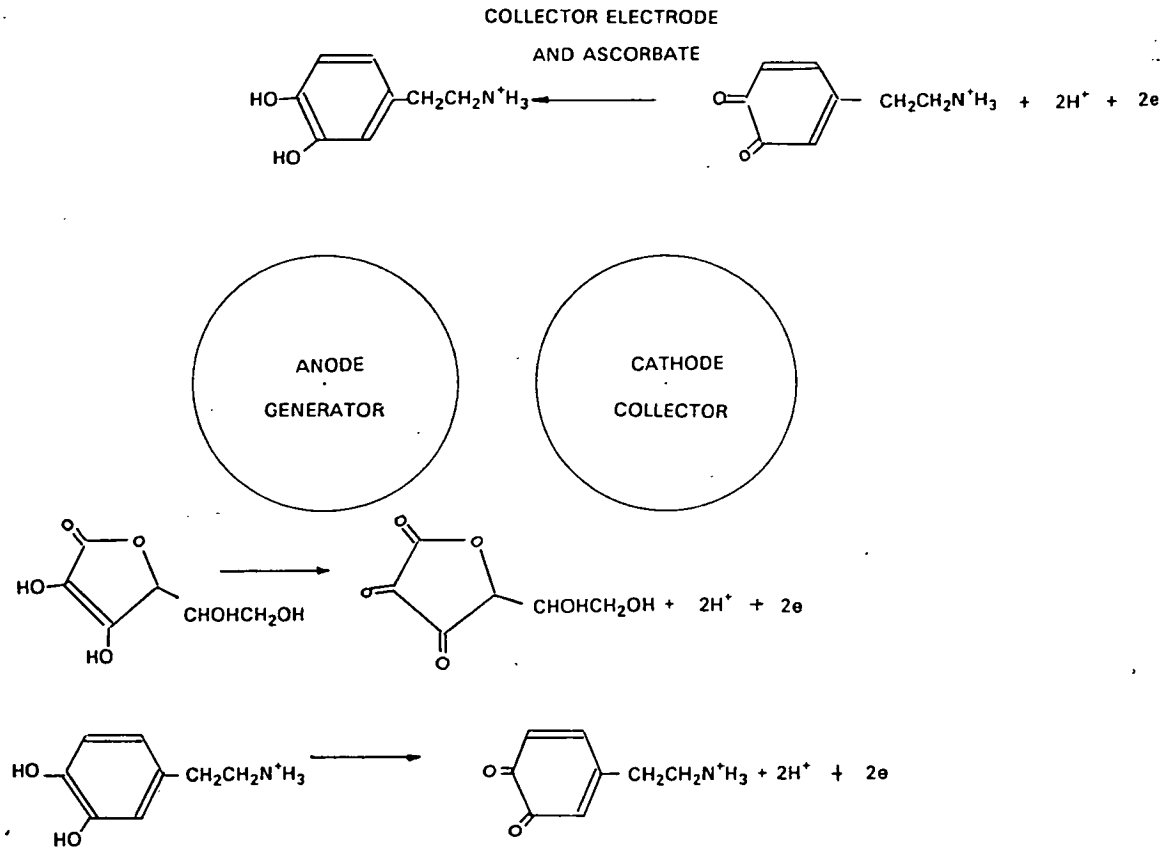

Figure 6.5 Determination of catecholamines in the presence of ascorbate at a carbon fibre anode and cathode.

TABLE 6.1 ASSAY PARAMETERS FOR INTERDIGITATED MICROBAND ARRAY ELECTRODES.

		macroscopic electrode	interdigitated microband array electrodes								
CURRENT RESPONSE		decay: $i=f(t^{-1/2})$	← steady state current →								
			← a →		← b →		← c →		← d →		
DETECTOR AREA /mm^2		1	1	1	1	1	1	1	1	1	1
BANDWIDTH /μm		-	95	10	10	5	5	2	0.1	0.1	0.1
BAND GAP /μm		-	18	10	2	2	0.5	0.5	0.1	0.05	0.01
NUMBER OF GENERATOR BANDS		-	4	25	41	71	100	250	2500	3333	4545
NUMBER OF COLLECTOR BANDS		-	5	25	42	72	100	250	2500	3333	4545
ASSAY VOLUME /μl	<μl	1	1	1	1	1	1	1	1	1	1
SENSITIVITY i/C /nA μM^{-1}		0.54#	0.31	1.5	3.1	4.2	9.5	17.6	101.1	180.4	431.2
RESPONSE TIME		← several seconds →			<1s	← 10s ms →					

a. Large scale interdigitated device

b. small scale interdigitated device

c. undulating interdigitated device

d. submicroscopic interdigitated device

Data calculated from eqn.(2.62) taking $D=5\times10^{-10}m^2\ s^{-1}$.

t=5s

TABLE 6.2 THEORETICAL STEADY STATE CURRENT AT MICROSCOPIC DUAL MICROCYLINDER ELECTRODES.

r /μm	w_g /μm	l /μm	i/C /pAμM^{-1}
3.4	7.0	100	22.7
3.4	3.0	100	33.4

Taking n=1 and D=10x10^{-10}m^2 s^{-1}.

TABLE 6.3 BLOOD CONCENTRATION OF BIOLOGICAL SUBSTANCES.

SUBSTANCE	CONCENTRATION /μM
ACTH (P)	3-15pM
Insulin (S or P)	40-190pM
Testosterone (P)	male 10-40nM
Thyroxine (S)	60-150nM
T3 (S)	1.2-3.1nM
Bilirubin (S)	3-20μM
IgA (S)	6-20μM
IgD (S)	0-1.7μM

P = Plasma, S = Serum. N. Engl. J. Med., 298 (1978) 34.

APPENDIX 1

J. Electroanal. Chem., 266 (1989) 227–238
Elsevier Sequoia S.A., Lausanne – Printed in The Netherlands

Interdigitated microband electrodes: chronoamperometry and steady state currents

B.J. Seddon and H.H. Girault *

Department of Chemistry, University of Edinburgh, West Mains Road, Edinburgh EH9 3JJ, Scotland (Great Britain)

M.J. Eddowes

Thorn EMI, Central Research Laboratories, Dawley Road, Hayes UB3 1HH (Great Britain)

(Received 5 December 1988; in revised form 6 March 1989)

ABSTRACT

The chronoamperometric response of an interdigitated microband electrode is reported. For the electrode design considered, a steady state current density of 2.3 A m mol^{-1} is observed within 2 s, allowing the amperometric measurement of analyte concentrations down to the low micromolar range.

An explicit finite difference method is used to model the current–time response of the device operated as a system of closely spaced band electrodes and as an alternate anode–cathode system.

An analytical expression is presented for the steady state current to an interdigitated microband electrode in terms of the geometric parameters, bandwidth and bandgap. The current density calculated from this expression is consistent with simulated and experimental data, and predicts a magnitude of kA m^{-2} mol^{-1} for submicroscopic interdigitated electrodes.

INTRODUCTION

Electroanalytical techniques in the past have relied mainly on hydrodynamic methods (e.g. polarography, rotating disc or wall–jet electrodes) to obtain amplified steady state currents for the amperometric determination of analyte.

Another approach to the generation of steady currents in static solution is the use of the special mass transport characteristics of microelectrode systems. Recent moves to take advantage of microelectrode properties have led to the development of a new class of amperometric sensors with improved signal to noise characteristics and shorter response times [1,2].

Recent studies of regular arrays of microdisc and microband electrodes have shown that easily measurable currents (μA) can be obtained together with a high current density. In particular, it has been demonstrated that interdigitated microband electrodes where anodes and cathodes are arranged as alternate fingers of the

0022-0728/89/$03.50

array can perform electrolysis with the generation of enhanced steady state currents [3]. In this case, the steady nature of the current has been assigned to the proximity of the anode and cathode which causes reactants of one electrode reaction to be generated mainly at the closely located counter electrode rather than being transported from the bulk of the solution. This inter-electrode diffusion process is equivalent to a phenomenon of "feedback diffusion" and offers a further means of increasing mass transport to a microband electrode.

Published work on interdigitated band electrodes has been concerned with sensor applications [4]; in particular the flow cell characteristics of these devices has received much attention [5]. The geometry of closely spaced band electrodes further allowed kinetic studies of homogeneous reactions which were essentially carried out in the past with rotating ring–disc methodology [6]. Also, the electrochemical properties of conducting films synthesised across a micrometer band gap have been investigated with interdigitated band electrodes, mainly to study their conductivity properties [7].

Parallel band electrodes may be operated in two different ways: (i) all bands set at the same potential; (ii) interdigitated anodes and cathodes. In the former, it has been shown that diffusion field overlapping results in a diminished current density compared to that of a single microband electrode, whereas in the latter a steady state current response is obtained owing to feedback diffusion effects.

The purpose of the present work is to establish the properties of the steady state currents obtained with interdigitated microband electrodes in relation to the geometric dimensions of the device. Further, a discussion is presented for parallel microband electrodes, illustrating the importance of band separation on current density.

EXPERIMENTAL

The interdigitated microband electrode used in the present study is a two-electrode device consisting of an array of interlaced microbands. Each gold electrode has ten microbands (95 μm $\times$ 10.0 mm); microbands are separated by an insulating gap 18 μm wide as illustrated in Fig. 1. Standard photolithographic techniques were used to fabricate 20 devices on three inch silicon wafers. Electrical insulation was achieved by a SiO_2 layer and gold adhesion was improved using a polyimide or chromium sub-layer. Array dimensions were measured by scanning electron microscopy: bandwidth 95 $\pm$ 1 μm, bandgap 18 $\pm$ 1 μm.

Chronoamperometry was performed using a waveform generator (HiTek PPR1, England) and a home-built picoammeter based on a high input impedance FET operational amplifier (Burr-Brown OAP 104) in a two-electrode arrangement. Potassium ferricyanide and potassium ferrocyanide (BDH) were of analytical grade. Micromolar solutions in 0.5 *M* KCl supporting electrolyte were freshly prepared.

Digital simulation was used to model the current–time response of a microband array electrode and interdigitated microband electrodes. For this, Fick's diffusion equation was solved in two dimensions subject to boundary conditions imposed by

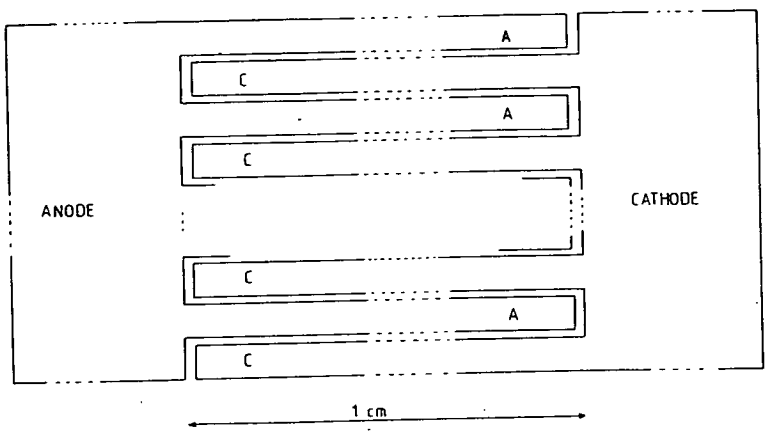

Fig. 1. Schematic diagram of the interdigitated electrode used.

the amperometric technique and the electrode geometry. An explicit finite difference approach with uniform cartesian coordinates was used [8]. All programs were written in standard Fortran and executed on the mainframe computer of the Edinburgh University Computing Service. Two-dimensional concentration profiles were plotted by means of a Symvu graphics package. Chronoamperometry at a single microband electrode was used to verify the accuracy of the simulation model before application to microband arrays.

THEORY: STEADY STATE CURRENT AT PARALLEL ANODE AND CATHODE

Let us consider a parallel anode and cathode as illustrated in Fig. 2 and further assume that both electrode reactions are ideally reversible and purely diffusion

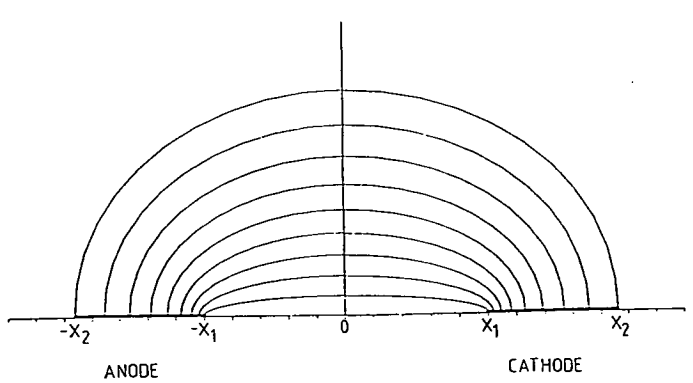

Fig. 2. Cross-section through an anode–cathode repeating band assembly (interdigitated band electrode), showing lines of flux between neighbouring electrodes.

controlled. At the steady state the boundary conditions for the oxidized species can be written as:

Cathode: $X_2 < X < X_1$ $\qquad c_O = 0$

Anode: $-X_2 < X < -X_2$ $\qquad c_O = 2c^b$

assuming that at $t = 0$, the reactant concentrations are equal:

$$c_O = c_R = c^b$$

where the subscripts O and R refer to the oxidised and reduced species, respectively.

We shall further assume the equality of the diffusion coefficients of the oxidized and reduced species. The diffusion equation at steady state simply reads

$$\frac{\partial^2 c_O}{\partial X^2} + \frac{\partial^2 c_O}{\partial Y^2} = 0 \tag{1}$$

and the steady state current per unit length is given by

$$i = \int_{X_1}^{X_2} nFD\left(\frac{\partial c_O}{\partial Y}\right)_{Y=0} \mathrm{d}X \tag{2}$$

In order to integrate eqn. (2), we can make the following change of variables

$$x = \cosh u \cos v \tag{3}$$

$$y = \sinh u \sin v \tag{4}$$

where x and y are dimensionless distances defined by

$$x = X/X_1 \tag{5}$$

$$y = Y/X_1 \tag{6}$$

and v is the dimensionless concentration defined by

$$v = \frac{\pi c}{2c^b} \tag{7}$$

The lines of flow between the cathode and the anode can be approximated by ellipses, as illustrated in Fig. 2, whereas the equipotential lines are represented by hyperbolas given by

$$\frac{x^2}{\cos^2 v} - \frac{y^2}{\sin^2 v} = 1 \tag{8}$$

Differentiation of eqns. (3) and (4) leads to the following identity

$$\left(\frac{\partial u}{\partial x}\right)_{\substack{y=0 \\ 1>x>x_2}} = \left(\frac{\partial v}{\partial y}\right)_{\substack{y=0 \\ 1>x>x_2}} \tag{9}$$

where x_2 is equal to X_2/X_1, from which the current can be expressed by

$$i = \frac{2nFDc^b}{\pi} \cosh^{-1}\left(\frac{X_2}{X_1}\right) \tag{10}$$

A similar derivation for the analogous problem in heat conduction has been published previously by Carslaw and Jaeger [9].

It can be seen from eqn. (10) that in order to optimize the current density, I, of parallel microband electrodes, one has to maximise the value of the following function;

$$I = \frac{2nFDc^{b}}{\pi(X_2 - X_1)} \ln\left[\frac{X_2}{X_1} + \left(\left(\frac{X_2}{X_1}\right)^2 - 1\right)^{1/2}\right] \tag{11}$$

In the case of interdigitated band electrodes, it should be noted that the distance $X_2 - X_1$ represents only half the width of the electrode because of the symmetry involved.

RESULTS AND DISCUSSION

The interdigitated band electrode expression (11) can be used to calculate the theoretical current density for any regular array of parallel anodes and cathodes.

Table 1 compares steady state current values calculated for an interdigitated band electrode either by using eqn. (11) or from computer simulation to experimental data. The experimental data are lower than the theoretical value and this can be explained by the fact that the insulation of the contact pad carried out by painting an insulating layer overspills on the bands themselves and consequently decreases the effective area.

The simulated current, on the other hand, overestimates the theoretical value and this may result from the simplicity of the explicit two-dimensional square cartesian grid used.

Although current density enhancement for electrodes of this dimension is not great (2.3 A m mol^{-1}) compared to the Cottrell current, it can be noted that a disc electrode of equal diameter of 95 μm would generate a steady state current density of only 2.0 A m mol^{-1}. Further, the equation predicts for a device constructed at the limit of conventional photolithography (bandwidth and bandgap 2 μm) that a limiting current density of 47 A m mol^{-1} should be observed (see Table 2).

For a device of bandwidth 0.2 μm and bandgap 1 μm, the current density increases significantly to 290 A m mol^{-1}. If one envisages the construction of even thinner electrodes [10] the increase is even more spectacular. Figure 3 shows the

TABLE 1

Steady state current density per unit concentration at an interdigitated microband electrode

Current density/A m mol^{-1}		
Theoretical	Experimental	Simulation
2.48	2.33	2.90

TABLE 2

Comparison of steady state current at an interdigitated microband electrode and at a microdisc electrode

(Bandwidth/ Disc diameter)/μm	Bandgap/μm	Current density /A m mol^{-1}		Steady state current	
		Band	Disc	Band [b] /μA mol^{-1} m^3	Disc /nA mol^{-1} m^3
95	18	2.5	2.0	21.9	13.9
2	2	61.5	93.4	446.5	0.29

[a] Calculated for an interdigitated band electrode with ten anode/cathode strips. $D = 7.6 \times 10^{-10}$ m^2 s^{-1}.

effect of submicrometer band separation on current density of a 50 nm bandwidth device and illustrates that a current density of about 2000 A m^{-2} mol^{-1} could theoretically be achieved with this new type of device.

Before discussing the amperometric properties of interdigitated electrodes in static solution it is worth considering the fundamental properties of a single microband electrode and those of a set of parallel microband electrodes held at a common potential.

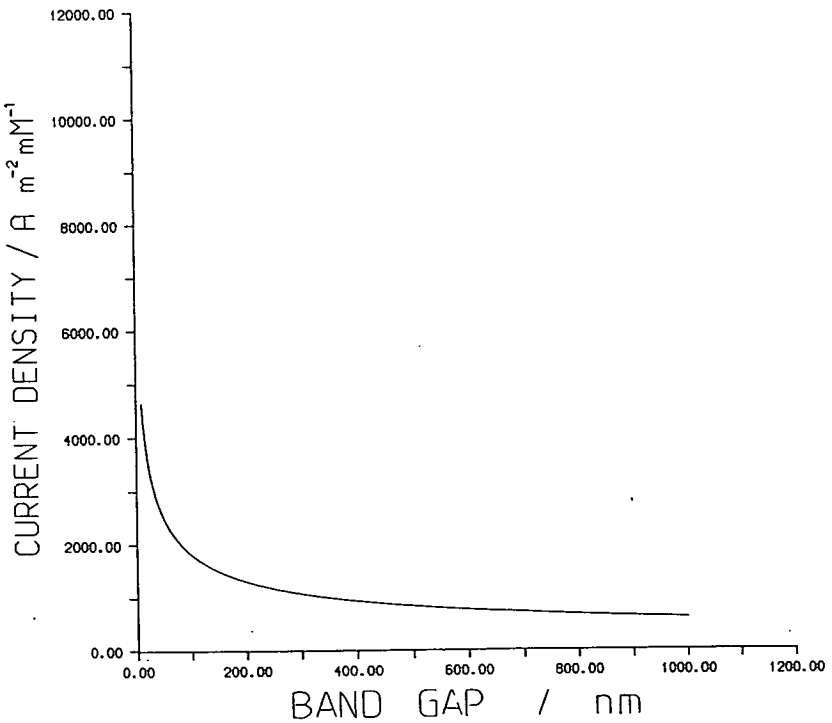

Fig. 3. Data from analytical expression showing current density as a function of band gap for a 50 nm bandwidth interdigitated band electrode.

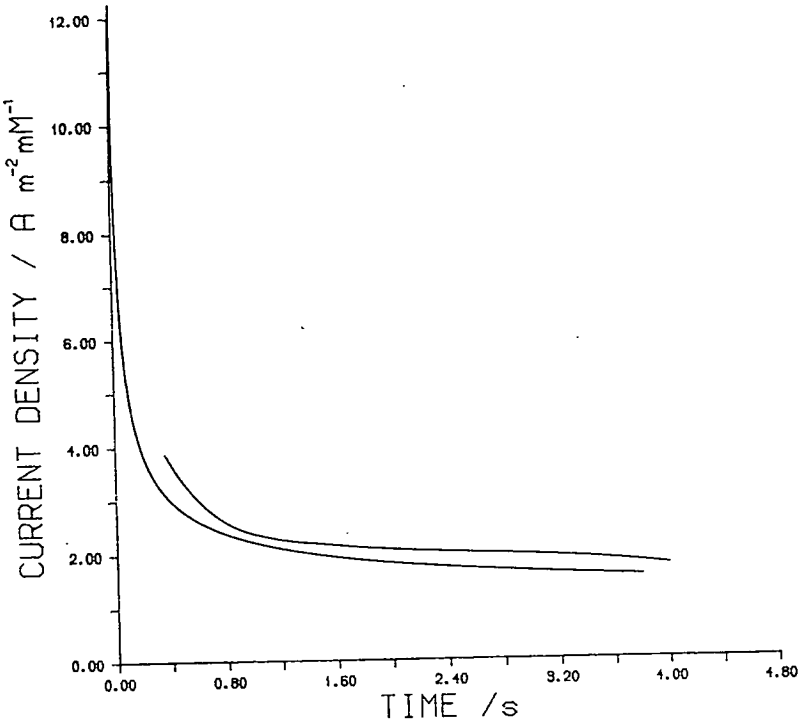

Fig. 4. Comparison of experimental with simulation $i-t$ data for a single microband electrode (68 μm bandwidth). Experimental data (upper curve) taken from ref. 11. Potential step -0.1 to $+0.6$ V vs. SCE; 0.5 m*M* $K_4Fe(CN)_6$ in 0.5 *M* KCl.

The simulated chronoamperometric response of a band electrode is compared with experimental data in Fig. 4. The main feature of this result is that no steady state current can be reached with the single microband electrode. For microbands smaller than 10 μm, the current decay follows (at long times) a $1/\ln(t)$ relationship as a consequence of the cylindrical diffusion pattern. However for bands of ca. 100 μm, the non-linear component of diffusion is relatively small (Fig. 5) and essentially an ovoid diffusion pattern is envisaged.

When all the bands of a parallel 95 μm wide band electrode array are kept at the same potential, the current–time response obtained shows that a mutual interference of the diffusion shells occurs with time, as depicted in Fig. 6. This phenomenon, referred to as shielding [12], can be illustrated by two-dimensional concentration profiles. It can be seen from Fig. 7 that shielding takes place as soon as the concentration between two adjacent bands falls below the bulk value. At longer times, this concentration approaches the surface concentration on the electrode and the microband array electrode behaves as a uniform planar electrode.

Figure 8 shows how the current density sampled, after 1 s, depends on the microband separation for a 95 μm wide microband array electrode. For closely

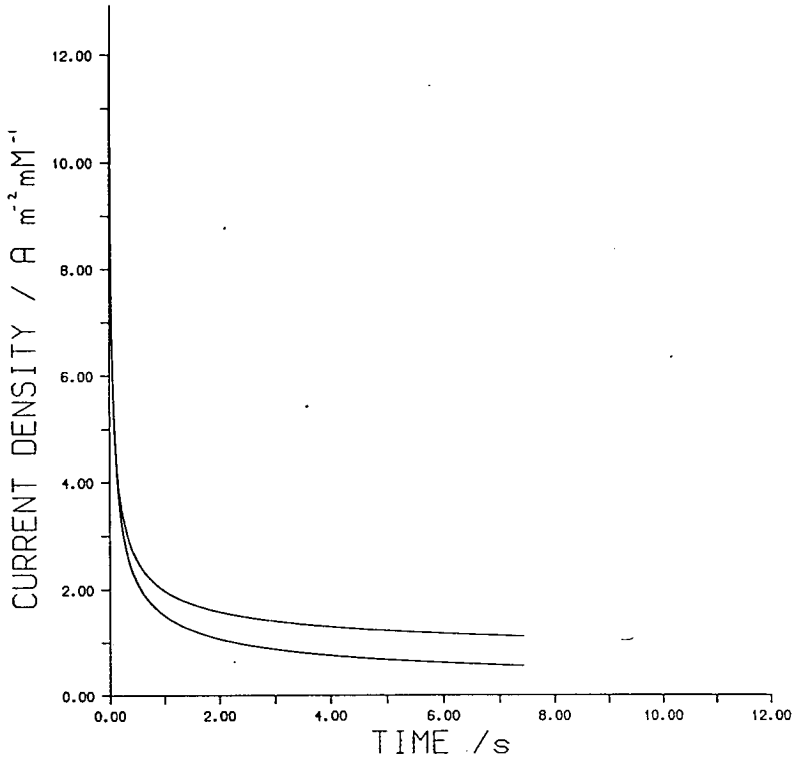

Fig. 5. Current–time simulation data for a 95 μm band (upper curve) compared with the theoretical Cottrell plot.

spaced bands (< 10 μm) the array current density after 1 s is essentially that of a macroscopic planar electrode. The current density at this microband array electrode becomes independent of band separation when the bandgap is greater than 120 μm.

The amperometric characteristics of interdigitated electrodes are different from those of a set of parallel electrodes as shown in Fig. 6 in the sense that narrow band gaps generate an amplified current response.

For a 95 μm wide band electrode separated by a 18 μm gap, the time taken to establish the constant current is about 2 s. Despite its relative simplicity, the computer model also generates steady state currents comparable to experimental data and it can therefore be used to study the influence of a band gap on both the response time and the current density. The latter can also be compared to the value obtained from the analytical expression given by eqn. (11).

The influence of the band gap was studied. The simulation model predicts that the time taken to attain a steady state (response time) increases with gap size. This is accompanied by a lower current density as a consequence of diminished feedback diffusion.

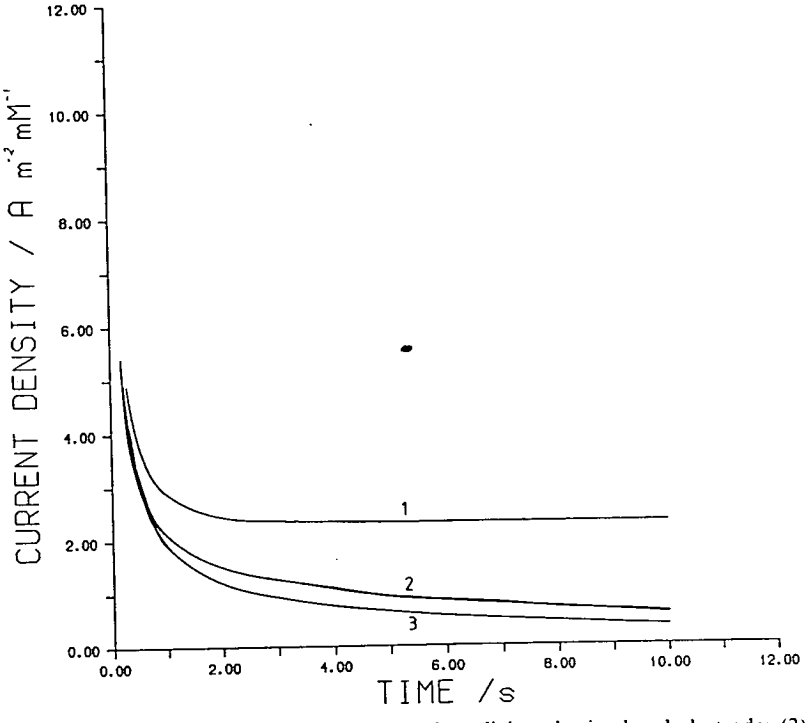

Fig. 6. Experimental current–time data: (1) interdigitated microband electrode; (2) one band array as working electrode; (3) both band arrays as working electrode. Potential step −0.5 to −0.3 V vs. $Au/Fe(CN)_6^{3-/4-}$; 1 m*M* $K_3Fe(CN)_6$ + 1 m*M* $K_4Fe(CN)_6$ in 0.6 *M* KCl.

Computer simulation is also a useful tool to illustrate the attainment of a steady state current with interdigitated systems. With conventional electrodes such as the rotating disc electrode, a steady state current is obtained by fixing the "Nernst plane" ($c = c^b$) at a fixed distance from the electrode. It can be seen from Fig. 9 that with interdigitated systems the "Nernst plane" is no longer parallel to the electrode but perpendicular to the plane of the anode and cathode and located at equal distances from the two electrodes. It can therefore be seen that reducing the band gap is equivalent to reducing the distance between the "Nernst plane" and the electrodes, consequently giving rise to higher currents. Whereas for conventional electrodes the current is proportional to δ^{-1}, where δ is the Nernst layer thickness, for interdigitated band electrodes the current is linked to the band gap by eqn. (11).

The high current density obtained with interdigitated microband electrodes allows us to use them as amperometric sensors and preliminary results using a 95 μm wide electrode separated by a 18 μm gap have shown that the device answers linearly to concentrations down to the micromolar range, as shown in the calibration plot given in Fig. 10. The detection limit for these devices was found to be 50 n*M*.

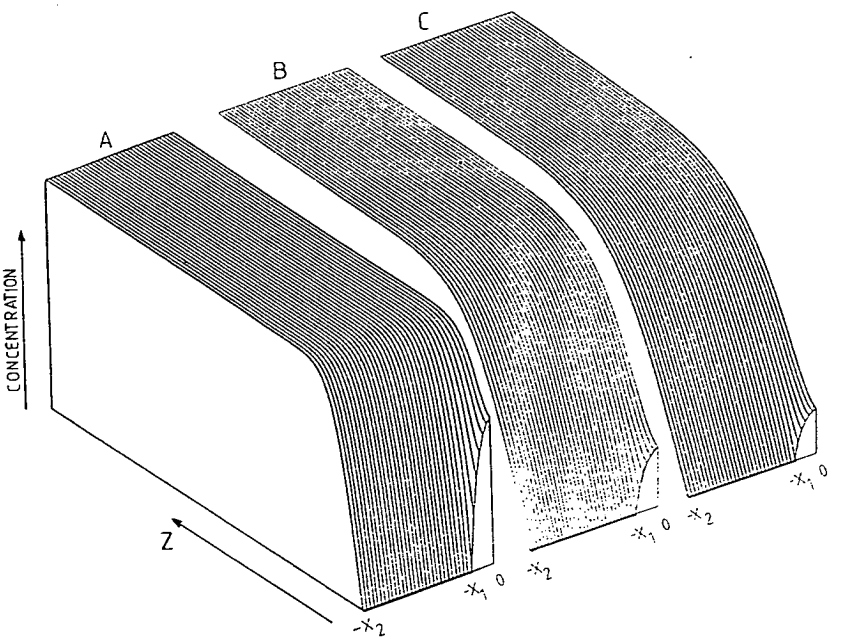

Fig. 7. Development of two-dimensional concentration profiles for a potential step experiment at closely spaced multiple band assembly. Bandwidth 95 μm, bandgap 18 μm. (A) After 82.5 ms; (B) after 412.5 ms; (C) after 825 ms.

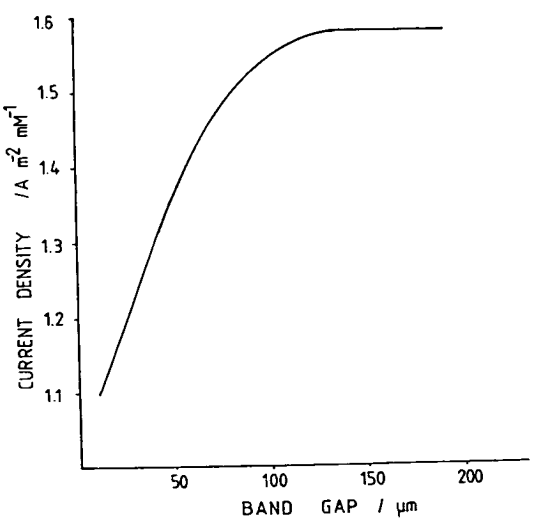

Fig. 8. Simulation data for closely spaced bands showing current density (after 1 s) as a function of bandgap.

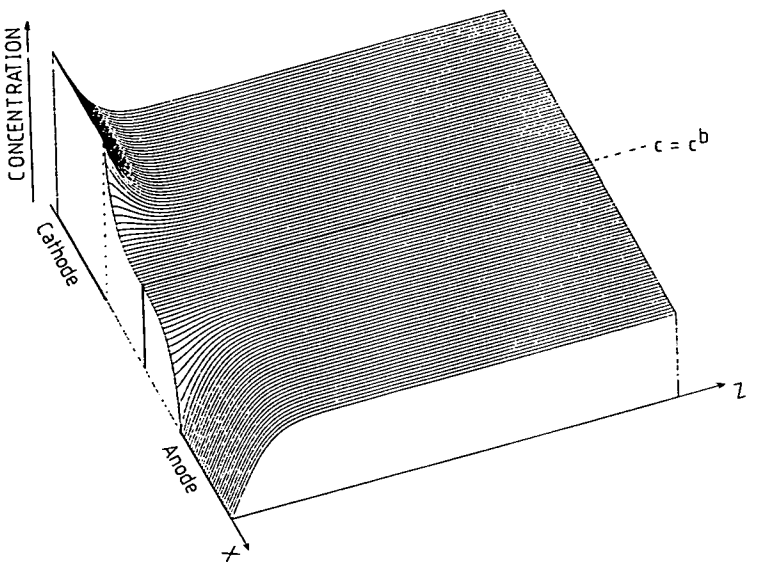

Fig. 9. Two-dimensional concentration profiles for a potential step experiment at an interdigitated band electrode.

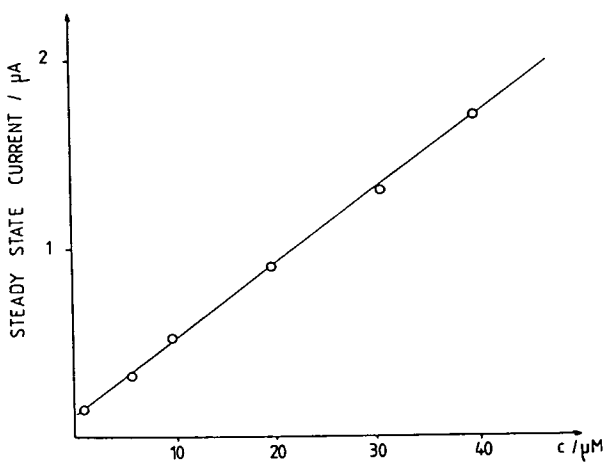

Fig. 10. Limiting current–concentration plot for the interdigitated microband electrode described in the text. $K_3Fe(CN)_6$, $K_4Fe(CN)_6$ (equimolar) in 0.6 *M* KCl.

CONCLUSIONS

The steady state current characteristics of interdigitated band electrodes have been studied by chronoamperometry and computer simulation. The observation of a constant current response for reversible redox systems at interdigitated microband electrodes opens up new areas of opportunity for the design of amperometric chemical sensors. Devices operating with improved analytical sensitivity as a consequence of the enhanced steady state current density, the short response time and high signal to noise ratio are very desirable features for amperometric transducer systems.

From this study it is considered that interdigitated microband electrodes can form the basis of many practical sensor devices.

The analytical expression for the steady state "feedback" current illustrates the important geometrical considerations for the electrode device in terms of current density improvement. The equation predicts massive enhancement of current density for submicrometer interdigitated band electrodes. The construction of devices with dimensions less that 1 μm is now presently being explored in our laboratory [10] with new fabrication techniques based on thin film technology.

The simulation model was helpful in demonstrating dynamic consequences of band gap variation, the response time for the onset of the steady state current being inextricably linked to the distance through which redox species diffuse.

ACKNOWLEDGEMENTS

The authors wish to thank Thorn EMI Central Laboratories for their financial and technical backing. One of us (B.J.S.) expresses his thanks to the SERC for a CASE postgraduate studentship.

REFERENCES

1 M.P. Bennetto, D.R. DeKeyzer, G.M. Delaney, A. Koshy, J.R. Mason, L.A. Razack, J.L. Stirling and C.F. Thurston, Int. Anal., 1 (1987) 22.
2 D.E. Tallman and D.E. Weisshaar, Anal. Chem., 55 (1983) 1146.
3 L.B. Anderson and D.G. Sanderson, Anal. Chem., 57 (1985) 2388.
4 B.C. Tofield, J. Chem. Soc. Faraday Trans., 92 (1986) 1117.
5 L.E. Fosdick, J.L. Anderson, T.A. Baginski and R.C. Jaeger, Anal. Chem., 58 (1986) 2750.
6 A.J. Bard and T.V. Shea, Anal. Chem., 59 (1987) 2101.
7 C.E. Chidsey, B.J. Feldman, C. Lundgren and R.W. Murray, Anal. Chem., 59 (1986) 601.
8 D. Britz, Digital Simulation in Electrochemistry, Springer-Verlag, Berlin, 1981.
9 H.S. Carslaw and J.C. Jaeger, Conduction of Heat in Solids, Oxford University Press, London, 1959.
10 A. Firth, B.J. Seddon and H.H. Girault, in preparation.
11 K. Aoki and H. Matsuda, J. Electroanal. Chem., 230 (1987) 61.
12 A.J. Bard, J.A. Crayston, G.P. Kittlesen, T.V. Shea and M.S. Wrighton, Anal. Chem., 58 (1986) 2321.

APPENDIX 2

```
1     C  SIMULATION OF CHRONOAMPEROMETRY FOR A TWO DIMENSIONAL DIFFUSION
2     C  MODEL OF REVERSIBLE  REDOX SPECIES AT TWO ADJACENT MICROBAND
3     C  ELECTRODES (CATHODE/ANODE): THE INTERDIGITATED MICROBAND ARRAY
4     C  ELECTRODE.
5     C
6     C  AN EXPLICIT FINITE DIFFERENCE METHODE IS USED WITH UNIFORM
7     C  SPACE GRID.
8     C
9           DIMENSION NOCONC(201,201) ,OOCONC(201,201) ,X(201) ,CURREN(1000)
10         £, T(10000)
11    C
12          CHARACTER*6 ONAME
13          CHARACTER*6 CNAME, TNAME
14          CHARACTER*2 NUMFIL
15          REAL LAMBDA,NONT,NONW,NOCONC,OOCONC
16          INTEGER XLIM,XDIM
17          ONAME='T£OO'
18           CNAME='T£CURR'
19          TNAME='T£ROOT'
20    C
21    C  SET THE PARAMETERS
22    C
23          LAMBDA=0.25
24          NT=10000
25          WIDTH=30
26          XLIM=11
27          XDIM=2*XLIM+1
28          DIMW=47.5E-6
29          DIFCO=7.0E-10
30          F=9.64846E4
31    C
32    C  CALCULATION OF ITERATION CONSTANTS DX & DT
33    C
34          NONT=1./NT
35          DX=SQRT(NONT/LAMBDA)
36          NONW=DX*WIDTH
37          DELTA=DIMW/NONW
38          TIME=DELTA**2/DIFCO
39          DT=TIME/NT
40          FACTOR=(F*DIFCO)/(DELTA*WIDTH)
41          NX=10./DX+0.5
42          IF(NX.GT.150) NX=150
43          NINT=NT/10
44          INT=0
45          ICOUNT=10
46    C
47    C  INITIALISE THE 2D CONC. SPACE FOR RED. & OX. SPECIES
48    C  PRIOR TO ELECTROLYSIS
49    C
50          DO 100  I=1,XDIM+1
```

```
51          X(I)=(I-1)*DX
52          DO 95 J=1,201
53          OOCONC(I,J)=1.
54          NOCONC(I,J)=1.
55      95  CONTINUE
56      100 CONTINUE
57      C
58      C  INITIALISE THE 2D CONC. SPACE FOR RED. & OX. SPECIES
59      C  AT START OF ELECTROLYSIS
60      C
61          DO 105 I=1,WIDTH
62          OOCONC(I,1)=2.
63          OOCONC(XDIM+1-I,1)=0.
64      105 CONTINUE
65      C
66      C  START OF TIME ITERATION
67      C
68          DO 200 IT=1,NT
69          NXX=IT+1
70          IF(NXX.GT.NX-WIDTH) NXX=NX-WIDTH+1
71          DO 110 IN=1,WIDTH
72          NOCONC(IN,1)=2.
73          NOCONC(XDIM+1-IN,1)=0.
74      110 CONTINUE
75      C
76          IF(NXX.GT.XLIM-WIDTH) GOTO 1001
77          DO 120 I=WIDTH+1,WIDTH-1+NXX
78          NOCONC(I,1)=OOCONC(I,1)+LAMBDA*(OOCONC(I-1,1)+
79         £OOCONC(I+1,1)+OOCONC(I,2)-3.0*OOCONC(I,1))
80          NOCONC(XDIM+1-I,1)=OOCONC(XDIM+1-I,1)+LAMBDA*
81         £(OOCONC(XDIM+1-I-1,1)+
82         £OOCONC(XDIM+1-I+1,1)+OOCONC(XDIM+1-I,2)-3.0*OOCONC(XDIM+1-I,1))
83      120 CONTINUE
84      1001 CONTINUE
85      C
86          IF(NXX.LE.XLIM-WIDTH) GOTO 1002
87          DO 121 I=WIDTH+1,XLIM
88          NOCONC(I,1)=OOCONC(I,1)+LAMBDA*(OOCONC(I-1,1)+
89         £OOCONC(I+1,1)+OOCONC(I,2)-3.0*OOCONC(I,1))
90          NOCONC(XDIM+1-I,1)=OOCONC(XDIM+1-I,1)+LAMBDA*
91         £(OOCONC(XDIM+1-I-1,1)
92         £+OOCONC(XDIM+1-I+1,1)+OOCONC(XDIM+1-I,2)-3.0*OOCONC(XDIM+1-I,1))
93      121 CONTINUE
94      1002 CONTINUE
95          DO 160 J=2,NXX
96          NOCONC(1,J)=OOCONC(1,J)+LAMBDA*(OOCONC(1,J-1)+OOCONC(1,J+1)
97         £+OOCONC(2,J)-3.0*OOCONC(1,J))
98          NOCONC(XDIM,J)=OOCONC(XDIM,J)+LAMBDA*(OOCONC(XDIM,J-1)+
99         £OOCONC(XDIM,J+1)+OOCONC(XDIM-1,J)-3.0*OOCONC(XDIM,J))
100         IF(NXX.GT.XLIM-WIDTH) GOTO 1003
101         DO 150 I=2,WIDTH-1+NXX
102         NOCONC(I,J)=OOCONC(I,J)+LAMBDA*(OOCONC(I-1,J)+
103        £OOCONC(I+1,J)+OOCONC(I,J-1)+OOCONC(I,J+1)-4*OOCONC(I,J))
104         NOCONC(XDIM+1-I,J)=OOCONC(XDIM+1-I,J)+LAMBDA*
105        £(OOCONC(XDIM+1-I-1,J)+
106        £OOCONC(XDIM+1-I+1,J)+OOCONC(XDIM+1-I,J-1)+OOCONC(XDIM+1-I,J+1)-
107        £4*OOCONC(XDIM+1-I,J))
108     150   CONTINUE
109     1003  CONTINUE
110         IF(NXX.LT.XLIM-WIDTH) GOTO 1004
```

```
111           DO 122 I=2,XLIM
112           NOCONC(I,J)=OOCONC(I,J)+LAMBDA*(OOCONC(I-1,J)+OOCONC(I+1,J)
113          £+OOCONC(I,J-1)+OOCONC(I,J+1)-4.0*OOCONC(I,J))
114           NOCONC(XDIM+1-I,J)=OOCONC(XDIM+1-I,J)+LAMBDA*(OOCONC(XDIM-I,J)
115          £+OOCONC(XDIM+2-I,J)+OOCONC(XDIM+1-I,J-1)+OOCONC(XDIM+1-I,J+1)
116          £-4.0*OOCONC(XDIM+1-I,J))
117     122   CONTINUE
118     1004  CONTINUE
119           IF(NXX.LT.XLIM-WIDTH) GOTO 131
120           NOCONC(XLIM+1,J)=OOCONC(XLIM+1,J)+LAMBDA*(OOCONC(XLIM,J)
121          £+OOCONC(XLIM+2,J)+OOCONC(XLIM+1,J-1)+OOCONC(XLIM+1,J+2)-
122          £4.0*OOCONC(XLIM+1,J))
123     131   CONTINUE
124     160   CONTINUE
125     C
126           DO 180 JJ=1,201
127           DO 170 II=1,XDIM
128           OOCONC(II,JJ)=NOCONC(II,JJ)
129     170   CONTINUE
130     180   CONTINUE
131           INT=INT+1
132           IF(INT.LT.NINT) GOTO 199
133           INT=0
134     C
135           WRITE(NUMFIL,201) ICOUNT
136     201   FORMAT(I2)
137           ONAME(5:6)=NUMFIL
138           OPEN(UNIT=12,FILE=ONAME,STATUS='NEW',ACCESS='SEQUENTIAL',
139          £FORM='FORMATTED')
140           DO 90 I=1,XDIM
141           DO 89 J=1,130
142           WRITE(12,9996) NOCONC(I,J)
143     9996  FORMAT(1H ,F10.6)
144     89    CONTINUE
145     90    CONTINUE
146           CLOSE(UNIT=12)
147           ICOUNT=ICOUNT+1
148     199   CONTINUE
149           T(IT)=IT*DT
150            CURREN(IT)=0.
151            DO 222 I=XDIM,XDIM-WIDTH,-1
152            CURREN(IT)=CURREN(IT)+NOCONC(I,2)
153     222   CONTINUE
154            CURREN(IT)=FACTOR*CURREN(IT)/DX
155     200   CONTINUE
156           OPEN(UNIT=13,FILE=CNAME,STATUS='NEW',ACCESS='SEQUENTIAL',
157          £FORM='FORMATTED')
158           WRITE(13,3100)(T(I),CURREN(I), I=1,NT,10)
159     3100  FORMAT(2F15.6)
160           CLOSE(UNIT=13)
161           OPEN(UNIT=14,FILE=TNAME,STATUS='NEW',ACCESS='SEQUENTIAL'
162          £,FORM='FORMATTED')
163            WRITE(14,450)((1./SQRT(T(I))),CURREN(I), I=1,NT)
164     450    FORMAT(2F15.6)
165            CLOSE(UNIT=14)
166           STOP
167           END
```

APPENDIX 3

AVIDIN-BIOTIN: A MODEL SYSTEM FOR THE ASSESSMENT OF AMPEROMETRIC IMMUNOASSAY.

The binding protein-ligand system, avidin and biotin is well known in various biochemical disciplines. It has been used extensively over recent years in histological studies where the strong binding of the protein to the ligand is utilised.

This well characterised system was selected as a model for studying the analytical performance of interdigitated electrodes under immunoassay conditions. The measurement of unbound biotin at interdigitated microband array electrodes relies on labelling the biotin molecule with a reversible redox moiety. The labelling strategy considered was complexation of histidyl-biotin with pentacyanoferrate(111) as shown below.

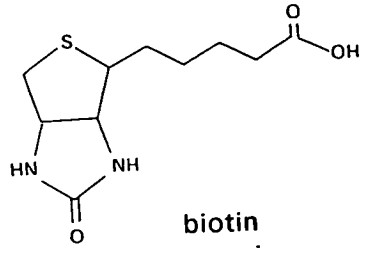

biotin

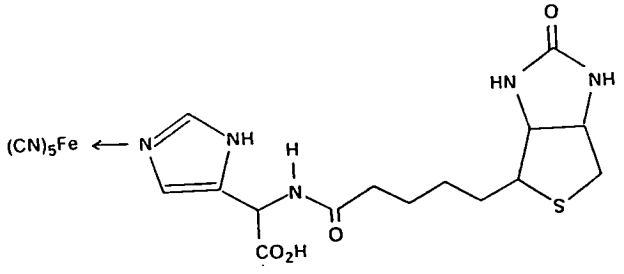

The following labelling route was proposed,

$$\text{biotin} \xrightarrow[\text{reduced P}]{SOCl_2\ 20\ C} \text{biotinCOCl} \xrightarrow[\text{histidine}]{<5\,^{\circ}C\ DMF} \text{histidyl-biotin}$$

$$\text{histidyl-biotin} + Fe(CN)_5(NH_3)^{3-} \xrightarrow{\text{aqueous}} Fe(CN)_5\text{-histidyl-biotin}$$

REFERENCES

1. Saito,Y., Rev. Polarog., 14 (1967) 168-175.

2. Saito,Y., J. Appl. Physiol., 23 (1967) 979

3. Saito,Y., Rev. Polarog., 15 (1968) 177-187.

4. Wehmeyer,K.R., Deakin,M.R., Wightman,R.M., Anal. Chem., 57 (1985) 1913-1916.

5. Aoki,K., Tokuda,K., Matsuda,H., J. Electroanal. Chem., 225 (1987) 19-32.

6. Aoki,K., Tokuda,K., Matsuda,H., J. Electroanal. Chem., 230 (1987) 61-67.

7. Aoki,K., Tokuda,K., J. Electroanal. Chem., 237 (1987) 163-170.

8. Thormann,W., Arn,D., Schumacher,E., Sep. Sci. Technol., 19 (1985) 995-1011.

9. Wohltjen,H., Anal. Chem., 56 (1984) 87A-103A.

10. Miasik,J.J., Hooper,A., Tofield,B.C., J. Chem. Soc. Faraday Trans. 82 (1986) 1117-1126.

11. Mansfield,F., J. Electrochem. Soc., 135 (1988) 1354.

12. Anderson,J.L., Moldoveanu,S., J. Electroanal. Chem., 185 (1985) 239-252.

13. Anderson,J.L., Fosdick,L.E., Baginski,T.A., Jaeger,R.C., Anal. Chem., 58 (1986) 2750-2756.

14. Anderson,J.L., Moldoveanu,S., Ou,T.Y., J. Electroanal. Chem., 247 (1988) 1-16.

15. Reilley,C.R., McDuffie,B., Anderson,L.B., J. Electroanal. Chem., 12 (1966) 477-494.

16. Wrighton,M.S., White,H.S., Kittlesen,G.P., J. Am. Chem. Soc., 107 (1985) 7373-7380.

17. Anderson,L.B., Sanderson,D.G., Anal. Chem., 57 (1985) 2388-2393.

18. Wrighton,M.S., Shea,T.V., Kittlesen,G.P., Crayston,J.A., Bard, A.J., Anal. Chem., 58 (1986) 2321-2331.

19. Bard,A.J., Shea,T.V., Anal Chem., 59 (1987) 2101-2111.

20. Bartelt,J.E., Deakin,M.R. Amatore,C., Wightman,R.M., 60 (1988) 2167-2169.

21. Niwa,O., Morita,M., Tabei,H., Aoki,K., J. Electroanal. Chem., 256 (1988) 269-283.

22. Aoki,K., Tanaka,M., J. Electroanal. Chem., 266 (1989) 11-20.

23. Seddon,B.J., Eddowes,M.J., Girault,H.H.J., J. Electroanal. Chem. 266 (1989) 227-238.

24. Laitinen,H.A., Kolthoff,I.M., J. Phys. Chem., 45 (1941) 1061-1079.

25. Davies,P.M., Brink,F., Rev. Sci. Insts., 13 (1942) 524- 533.

26. Kinoshita, K., Carbon: electrochemical and physicochemical properties, Wiley 1988.

27. Jorgenson,J.W., St.Claire,R.L., J. Chromatog. Sci., 23 (1985) 186-191.

28. Jorgenson,J.W., Guthrie,E.J., Knecht,L.A., J. Am. Chem. Soc., 56 (1984) 479.

29. Wightman,R.M., Deakin,M.R., Kovach,P.M., J. Phys. Chem., 90 (1986) 4612-4617.

30. Kovach,P.M, Caudill,W.L., Peters,D.G., Wightman,R.M., J. Electroanal. Chem. 185 (1985) 285-295.

31. Aoki,K., Honda,K., Tokuda,K., Matsuda,H., J. Electroanal. Chem., 182 (1985) 267-279.

32. Aoki,K., Honda,K., Tokuda,K., Matsuda,H., J. Electroanal. Chem., 186 (1985) 79-86.

33. Amatore,C.A., Deakin,M.R., Wightman,R.M., J. Electroanal. Chem., 206 (1986) 23-36.

34. Kaneko,H., Aoki,K., J. Electroanal. Chem., 247 (1988) 17-27.

35. Jost,W., Diffusion, Academic Press Inc., N.Y. 1952.

36. Crank,J., The Mathematics of Diffusion, Oxford University Press, 2Ed., London, 1965.

37. Ruis,A., Polo,S., Llopis,Y.J., An. Fis. Quim., 45 (1949) 1029-1046.

38. Carslaw,H.S., Jaeger,J.C., Conduction of Heat in Solids, Oxford University Press ,2Ed., 1959.

39. Isachenko,V., Osipova,V., Sukomel,A., Heat Transfer, Mir Publications, Moscow, 1965.

40. Niwa,O., Morita,M., Tabei,H., J. Electroanal. Chem., 267 (1989) 291-297.

41. Phelan,D.M., Taylor,R.M., Fricke,S., Intern. Lab., 12 (1982) 60-75.

42. Stewart,A.A., Ph.D. Thesis, Edinburgh University, 1990.

43. Plotnik,I., Solid State Technology, Jan. (1989) 102.

44. Harris,K., Solid State Technology, Jan. (1989) 100.

45. Pang,S.W., Goodhue,W.D., Geis,M.W., J. Electrochem. Soc. Solid State Science and Technology, June (1988) 1526-1529.

46. Bard,A.J., Faulkner,L.R., Electrochemical Methods, Wiley 1980.

47. Heinemen,W.R., Halsall,H.B., Anal. Chem., 57 (1985) 1321A-1331A.

48. Bataillard,P., Anal. Chem., 60 (1988) 2374-2379.

49. Adams,R.N., Electrochemistry at Solid Electrodes, Dekker, 1969.